

UNIVERSITE DE LIMOGES

Ecole Doctorale Sciences et Ingénierie pour l'Information, Mathématiques

FACULTE DES SCIENCES ET TECHNIQUES

Equipe de recherche XLIM MINACOM

Année : 2013

Thèse N° 73-2013

Thèse

pour obtenir le grade de

DOCTEUR DE L'UNIVERSITÉ DE LIMOGES

Discipline : Electronique des Hautes Fréquences et Nanotechnologie

présentée et soutenue par

Pierre FRANCK

le 17 décembre 2013

Mesoscopic electromagnetic model of carbon-nanotube arrays and scalable technological processes: application to the fabrication of novel antennas

Thèse dirigée par Dominique BAILLARGEAT, co-dirigée par Beng Kang TAY, évaluée par :

Christian PERSON	Prof., LabSTICC-ENST, Brest	Président
Luca PIERANTONI	Prof., Univ. Poli. delle Marche, Ancona	Rapporteur
Frédéric NGUYEN VAN DAU	Dir., UMR137 CNRS/Thales, Palaiseau	Rapporteur
Jean-Paul MARTINAUD	Thales Systèmes Aéroportés, Elancourt	Examineur
Rose-Marie SAUVAGE	DGA/DS/MRIS, Bagneux	Examinatrice
Philippe COQUET	Prof. et dir. CINTRA, Singapour	Examineur
Beng Kang TAY	Prof., Nanyang Tech. Univ., Singapour	Examineur
Dominique BAILLARGEAT	Prof. et dir. XLIM, Limoges	Examineur
Julien PERRUISSEAU-CARRIER	Prof., EPFL, Lausanne, Suisse	Invité
Charlotte TRIPON-CANSELIET	MdC, UPMC L2E, Paris	Invitée

to Aliénor, my love and fellow PhD globe-trotter,

to my parents and family for their love and support,

Acknowledgements

First and foremost I shall thank Professor Dominique BAILLARGEAT for offering me the opportunity to pursue this PhD at CINTRA and XLIM under his advised guidance and for ensuring all conditions were met to make it an interesting and enjoyable, if intense, experience. He has been an invaluable scientific advisor and mentor while giving me great latitude and support in my research. He also knew to find arrangements to allow me to conduct my research in Singapore on a French PhD funding. As CINTRA's first director he lead us to where it stands now, four years later, with many connections, ongoing collaborations, arrangements, access to a variety of facilities in NTU and a Nespresso machine. Thank you, Dominique.

Many thanks go to my co-supervisor Professor TAY Beng Kang who gave me the opportunity to collaborate with the Nanoelectronics Materials & Devices Research Group he leads in NTU EEE. In particular he associated me to the team working on the Nano Antenna Array project. This was an enriching research experience in a Singaporean context along a structured and ambitious project in a multidisciplinary and multicultural team with access to many facilities. Frequent review deadlines had to be met with fixed deliverables agreed upon with the funding agency. I was honored he entrusted me to report on the modeling and design work during the reviews.

I shall subsequently thank my direct collaborators, Dr LI Hong, Ray YAP Chin Chong, CHOW Wai Leong, LU Congxiang, TAN Dunlin, TAN Chong Wei, Christophe BRUN and Professor Philippe COQUET for sharing their knowledge and know-how. They taught me a lot and their hard work on the project was a decisive asset for the successful fabrication of the antenna prototypes. I shall also thank Professor ZHANG Qing for granting me access to his CVD equipment, Hasman Bin Hassan and Dr Tony TSANG Siu Hon for technical help, Dr David HEE (Thales Singapore) for interesting exchanges on antennas.

I would also like to thank Professor Cesare SOCI for giving me access to his laboratory and equipment, inviting me to discuss research plans, and offering valuable advice and suggestions. Special thanks go to WANG Zilong who helped me carry out the photocurrent measurements and CHIN Xin Yu for sharing some of his electrode designs.

I would also like to express my gratitude to the DGA and CNRS for funding me over the course of my PhD work and my successive DGA correspondents Pascal MAIGNE and Rose-Marie SAUVAGE.

I gratefully acknowledge the members of my jury I have not yet mentioned, Christian PERSON, Jean-Paul MARTINAUD, Julien PERRUISSEAU-CARRIER, Charlotte TRIPON-CANSELIET with a special mention for my two reviewers Luca PIERANTONI and Frédéric NGUYEN VAN DAU, for the time and attention they have dedicated to the evaluation of the work reported in this thesis.

I also wish to thank the people in XLIM who made this specific arrangement possible, in particular Marie-Laure GUILLAT, Nadine SEGUIN and Dominique CROS. I thank Michel AUBOURG for providing EMXD and some related assistance and Damien PASSERIEUX for discussing and conducting RF measurements on the antenna prototypes. Finally I thank all

the welcoming and interesting people who took some time with me in XLIM in the occasion of my different stays, Stéphane BILA, Karim LOUERTANI and Aurelian CRUNTEANU from MINACOM, Thierry MONEDIERE, Marc THEVENOT and Cyril DECROZE from OSA, and the PhD students in MINACOM.

I would like to thank my colleagues in CINTRA for the moments shared: the seniors Xuan Quyen DINH, Edwin TEO, Christophe COUTEAU and Heinrich DIESINGER, the would-be seniors but not just yet Aurélien OLIVIER and Sébastien PACCHINI, our admin angels Jessie QI Jia and Coralie HUNSICKER, my fellow PhD students and friends, Donny LAI and Riko MADE (and their lovely wives Joyce and Ratih), Loïc LOISEL (and Juliette), XU Naiyun, Charles ALTUZARRA, Christophe WILHELM, Zeineb BEN AZIZA, Olivier COMETTO and interns from the successive batches Philippe CASTERA, Romain DUBREUIL, Mathieu BERGONT, Agnès MESSANVI, Camille DEGARDIN, Etienne RODRIGUEZ, Brioux DURAND, Mathieu COMETTO, David PEYROT, Eino PERREAU.

I want to thank the great friends we made in Singapore, Thomas and Cécile, Sylvia, Florian and Florence, Miyuki, Leng, Harish, Joe, Sebastian and Jackie, Tom and Emily, Jun, Yin Ting, Audoin, Aziza and Manu, Mathilde, Claire, Lucille, Roman, Samuel, Annelaure, Massy, Jo Pei Hua, Yingying, Stéphane and everyone I may have missed. I should not forget to mention my two Singaporean friends and my Malaysian Chinese friend from London who helped me decide on taking up this opportunity without having ever been to Singapore and South-East Asia, Clement an entrepreneur roller-skater globe-trotter, who was also one of my first guides to Singaporean life and culture, and my friends and fellow optics students in Imperial, Lijian and Yan Woon. Thanks to all my fellow Erasmus Mundus students and to the inline-skating communities in London and Singapore for driving my international appetite further. Thanks to Kim for organizing great improv' workshops where I have met so many fun and fun-loving people.

I send many thanks and love to my dear friends in France for having been present each time I came back the Nirvanouilles, Rémy, Jean, Jules and Aurélien, Cocotte, Alexandre, Damien, Jérôme, Jojo, Max, Babs, Lauriane, Coco and to my friends from Supoptique and Alunissons that I would have liked to see more and hope to catch up with when I am back in France.

Last but not least I have my dear Aliénor and our families to thank. Thank you Aliénor for following me all the way to Singapore and picking up hazardous hobbies – inline skating, scuba diving, jumping on kangaroo stilts and hydrofluoric-acid etching among others – to stay with me. Thank you for putting through the long working hours, the awfully-packed agenda, and my constant travel queries. Sharing these three years, our life in Singapore and our trips with you made them so much more thrilling, fulfilling and delightful. You have been present at the more difficult times too and I owe you my deepest apologies for having had you spend our two-week-long “holiday” in an indefinitely parked campervan while I was completing this thesis. Thanks for sticking through.

Cathy, Stéphane, merci de nous avoir fait confiance et de m'accueillir avec tant d'amour et de naturel dans votre formidable famille. Merci aussi pour toutes vos petites et grandes attentions culinaires pour le glouton que je suis. Smi, merci d'être venue nous rendre visite avec Fred, heureux que nous ayons pu partager ces beaux moments ensemble, et merci à Goran, Greg et toi de m'accueillir à bras ouverts et de vous occuper si bien de moi quand je débarque à Limoges qui en a pris un tout autre charme. Merci Guillaume de transformer la

tête d'ampoule en mousse girl quand il le faut et de me faire rêver avec tes engins tout-terrain. Merci enfin à Jelena et Srđan pour leur accueil chaleureux quand nous arrivons à Paris et pour avoir lancé la nouvelle génération avec le petit Zlatan que j'ai vraiment hâte de rencontrer. Merci Papy et Jeanine pour votre simplicité et bonne humeur et de prendre soin d'Aliénor quand je ne suis pas là.

Pôpa, Maman, merci pour tout, merci de m'avoir offert une si belle vie et d'avoir ouvert les portes qui m'ont conduit jusqu'ici. Je vous doit tout : le goût pour la science, la soif d'innovation et de culture que vous m'avez communiquée, vos conseils éclairés et votre support moral et financier qui m'ont permis de poursuivre ces études, de voyager et d'y prendre goût, de prendre mon indépendance tout en rentrant toujours avec plaisir au bercail. Merci beaucoup d'être venus découvrir Singapour et faire un petit tour d'Asie avec nous, nous avons vraiment envie de partager ça avec vous.

Merci à mes frères pour les jeux, les bagarres, les bêtises et tout ce que l'on n'apprend que dans une fratrie. Thomas, Chloé, bonne chance pour devenir de « vrais » docteurs, on viendra vous voir en Bretagne, manger du kouign-amann comme des touristes et boire du chouchou comme des vrais. Valentin, bonne chance avec ton business, tu as l'air d'avoir pris le bon raccourci, il va falloir que je te rattrape!

Grazie a voi Nonno e Rossana per tanta gentilezza e generosità, e grazie di accoglierci ogni volta così bene e con tanto naturale a casa vostra. Spero di vedervi più spesso l'anno prossimo quando saremo tornati a Parigi. Un pensiero per i miei carissimi cugini italiani, ora sarò davvero « dottore »!

Merci Tatine, Mamie, Nanou, Marc, Christine, Gaston, Benoît, Isa, François, Béné, Laurence, Thomas, Claire, Habib, Vincent, Thibaut, Anne-Laure, Jérôme et tous les cousins de Barr pour tant de beaux moments en famille.

Thanks to all my cousins in the US, in particular Cathy, Ernest, Lisa, Jeff, Shelli, Linda and Aldo for so much love and hospitality. Thanks for the great and fun times and sharing all the best things New York and California have to offer. Hope to see you more as we move closer! Camille, Caitlin, Judah, Thomas when are you coming to visit us?

In short thanks to all of you that have made these three years so rich and fulfilling!

Contents

Contents.....	7
Introduction	9
Chapter I) Carbon nanotubes for antenna applications.....	15
I.A) Structure.....	15
I.B) CNT fabrication methods.....	17
I.C) Optical and optoelectronic properties	17
I.D) Applications in electronics and RF.....	19
I.E) Optical control.....	20
I.F) Methodology	20
Chapter II) Carbon nanotube modeling	25
II.A) Existing models, usage and necessity of a new approach	25
II.B) Effective medium approach.....	43
II.C) Implementation and validation	61
II.D) Conclusion on simulation techniques.....	73
Chapter III) Development of CNT-based electronics fabrication techniques	79
III.A) Conventional fabrication techniques.....	79
III.B) CVD growth of CNTs	89
III.C) Structures fabrication	103
III.D) Considerations for experimentally-realizable CNT antennas	107
Chapter IV) Resonant electrically-short CNT antennas	111
IV.A) Trade-offs and tools	111
IV.B) THz characterization and THz FSS	137
IV.C) Prototypes from lattice-aligned metallic SWCNTs on quartz	139
IV.D) Prototypes from vertically-grown CNTs	159
IV.E) Mask design.....	181
IV.F) Fabrication and characterization.....	190
IV.G) Conclusion on CNT-based antenna design.....	195
Chapter V) Initial characterization towards optical control	197
V.A) Photocurrent samples: sorting metallic and semi-conducting CNTs	197
V.B) Measurement and characterization	207
V.C) Clues for analysis and design	228
Chapter VI) Conclusion and outlook	233
VI.A) Summary of the main achievements	233
VI.B) Conclusions on CNT-based antennas	236
VI.C) Outlook on related slow-wave technologies	237
Bibliography	241
Appendices	257
Detailed Table of Contents	281
List of Figures.....	289
List of Tables.....	301
List of Equations.....	303
Abstract	309

Introduction

Since the advent of modern computing, the quest for reduced dimensions in electronics has led us to probe ever smaller scales. In recent years, as the physical limits of conventional fabrication techniques are becoming more and more stringent, potential next generation materials, techniques and technology have attracted much attention for “more Moore”. Quasi-one-dimensional nanotubes and nanowires and more recently two-dimensional materials (starting from graphene) are of particular interest owing to their inherent nanometric scale and extraordinary physical properties. They have been explored as possible replacement of silicon in transistors and a team has recently demonstrated performances surpassing state-of-the-art technology using carbon nanotubes [1], [2] while another team has developed imperfection immune designs with a sufficient yield to allow the demonstration of a first 96-transistor carbon-nanotube computer [3]. A number of research grants and projects have been attributed, start-ups founded and a patenting anything CNT has been ongoing for the last decade. Graphene is also a good illustration of the importance accorded to carbon-nanomaterials. A.K. Geim and K.S. Novoselov have been granted the 2010 Nobel prize in Physics in a record time of less than 6 years for physically isolating graphene while, in 2013, the European Union has set up a research initiative, the Graphene Flagship, which will receive 1 billion euros in funding over ten years to investigate new applications and industrialization of graphene and other 2D materials. Samsung [4] and recently Sony [5] have demonstrated large-scale roll-to-roll CVD production of predominantly single-layer graphene. Singapore is also massively investing in nanotechnology with, for instance, a Graphene Center newly opened in National University of Singapore (NUS) and a few recipients of a NRF (National Research Foundation) Fellowship each receiving research grants of up to S\$3 million over five years to conduct research in NUS, Nanyang Technological University (NTU) or Singapore University of Technology and Design (SUTD).

Most of the focus has been put on the development of devices, often overlooking the problem of their integration with micro- and macro-world technologies. Lithography contacting of these nanodevices is difficult to scale and decreases the achievable density. Furthermore ohmic contact to nano-objects is still, to-date, difficult to achieve and displays high variability and, for high-frequency electronics, the large impedance mismatch between 50- Ω microelectronics and k Ω nanodevices is an issue (cf. e.g. [6]). Wireless communication

with these devices could be an alternative. Indeed single-wall carbon nanotubes (SWCNTs) have been foreseen as interesting candidates for antenna applications. They are predicted [7], [8] to display a high kinetic inductance, leading to slow propagation of electromagnetic waves along their axis. The existence of the kinetic inductance has been verified experimentally [9]. Since a reduced propagation velocity implies a shorter wavelength at a given frequency, this would allow the design of resonant antennas much smaller than with usual materials – about fifty-fold in the case of a dipole with arms made of a single SWCNT each [10]. Bundled CNTs may however be necessary to overcome certain experimental challenges such as high contact resistance at CNT-metal junctions [11], poor efficiency of single-tube devices or to match the impedance of the antenna with that of the fabricated device. The antenna link would in the latter case act as an impedance transformer. Additionally, owing to their reduced size and high operating frequency range, CNT-based nano-antennas are a potential candidate for wireless chip-to-chip and on-chip communications – an emerging interconnect concept [12].

Here we thus explore the use of CNTs in the design and fabrication of novel antennas. As stated, they could help improve the performance of electrically-small antennas but may also allow the development of novel structures such as optically-controlled reflectarrays. In certain applications such as biomedical devices (stomach scanner pill, implementable devices), wireless sensor networks, or on-chip communication the final size of the antenna is limited by physical constraints such as the final size of the pill to swallow or the available footprint on the chip. The first solution is to work at higher frequencies – thus reducing the physical size of resonant antennas. At 3GHz, the smallest resonant antenna, a quarter-wave monopole is about 2.5mm long while it is ten times shorter at 30GHz. Nevertheless either for interoperability reasons, technology availability or due to absorption bands in the surrounding medium (air, water, animal flesh...) the operating frequency used will sometimes correspond to a wavelength such that resonant antennas will have larger than permissible dimensions. In this case electrically-small antennas will be used. CNT-based antennas can resonate at smaller dimensions [10] and will radiate more efficiently for the same dimensions than a usual metal in a non-resonant antenna configuration. Additionally, the use of CNTs could add agility to these small antennas or to more classic designs disposed as arrays or reflectarrays. Indeed photocurrent has been measured in CNTs [13]–[15] and might allow laser activation or modulation of single radiators in an array for beam shifting for instance.

Short resonant CNT antennas were introduced by G.W. Hanson in [10] in 2005 and followed by a few other studies [16]–[20]. The idea has gained in popularity and momentum with several major research institutions and industrials. In a presentation in 2007, researchers from the American research institute MITRE Corporation proposed [21], [22] to research CNT-based optically actuated RF switch for reconfigurable apertures and CNT-based electrically small and highly efficient antennas to create improved antennas for netted sensors, handheld radios and covert devices. Thales engineers also studied potential applications of the kind [23], [24], and a DGA-DSTA SAFARI agreement was made to fund and support collaboration between French and Singaporean partners on such a project. Related patents have been filed in the past few years [22], [24]–[26]. In 2012, Nokia’s Voutilainen et al., evaluated bundles of CNTs could potentially be used for gigahertz–terahertz antennas, micrometer-millimeter-long interconnections, and low-performance analog transistors [27]. In 2013, Samsung granted support to a joint Spanish-American team for the development of algorithms applicable to the high data rates expected with THz graphene antennas [28].

The research reported in this thesis was co-funded by the French Ministry of Defense agency Direction Générale de l’Armement (DGA), as civilian research, and the French National Center for Scientific Research, Centre National de la Recherche Scientifique (CNRS). I was administratively attached to XLIM, a joint CNRS-Université de Limoges research institute (UMR 7252) where I completed most administrative procedures and trainings required for the PhD defense and had insightful discussions on antenna and RF engineering. XLIM gathers 460 researchers, staff and PhD students exploring disciplines ranging from information technology and mathematics to optics, electromagnetics and electronics engineering. There are six departments and I was attached to MINACOM (Micro and Nanotechnologies for Optoelectronic and Microwave Components) on campus de la Borie, 123 avenue Albert Thomas, Limoges.

However I spent more than 90% of the three years of my PhD studies in Singapore. Indeed the research was led in CINTRA, CNRS International-NTU-Thales Research Alliances. CINTRA is located on the campus of Nanyang Technological University (NTU) in Singapore and is a CNRS Mixt International Unit (UMI 3288) i.e. a research unit out of France formed in collaboration with academic and industrial partners here NTU and Thales. NTU trains 33,000 undergraduate and postgraduate students and with about 16,000 students and almost 2,000 faculty and staff members its College of Engineering is the largest in the

world. A young university, NTU ranks in the top 100 and top 50 in most international education rankings and has been consistently rising. Thales is a multinational company with 67000 employees globally and activities in the defense, security, space, aerospace and ground transportation industries.

Most of the people I collaborated with and of the laboratories and equipment I used in NTU are attached to the school of Electronical and Electronics Engineering (EEE) in the Microelectronics division and to the School of Physical and Mathematical Sciences (SPMS). I also interacted with people from the School of Mechanical and Aerospace Engineering (MAE) and the School of Material Science and Engineering (MSE). My research was supervised by Professor Dominique Baillargeat, director of CINTRA from 2009 to 2013, director of XLIM since 2013 and professor in RF engineering at Université de Limoges. I was co-supervised by Professor Beng Kang Tay, Program Director for the Nanoelectronics Materials & Devices Research Group concurrently holding the appointment of Associate Dean for Research at the College of Engineering of NTU the entity supervising the Engineering schools.

I collaborated with a Singaporean team and a French team that were respectively funded by the Singaporean defense ministry (DSTA, DRTech) and the French defense ministry (DGA) under a SAFARI Singaporean-French bilateral agreement. The French team included a partner from the Laboratoire d'Electronique et d'Electromagnétisme (L2E), Université Pierre et Marie Curie (UPMC), in Paris, A. Prof. Charlotte Tripon-Canseliet, the principal investigator (PI) from Institut d'Electronique de Microelectronique et de Nanotechnologie (IEMN, UMR 8520), in Lille, Prof. Didier Decoster, later joined by Prof. Philippe Coquet who is now director of CINTRA, and partners from Thales Airborne Systems (TAS), in Elancourt, Jean Chazelas and Jean-Paul Martinaud. The PI for the Singaporean team was Prof. Beng Kang Tay with Prof. Dominique Baillargeat, Prof. Hong Wang and Prof. Qing Zhang as partners. The team included two post-doctoral researchers Dr Hong Li and Dr Yuming Wu and a few PhD students, Chin Chong Yap, Wai Leong Chow, Chong Wei Tan, Dunlin Tan, Cong Xiang Lu. Another PhD student from XLIM was working in CINTRA, Christophe Brun.

After a brief introduction to essential notions, this PhD thesis proceeds along the four intertwined axes of research that were explored before formulating final conclusions and recommendations.

In Chapter I), we briefly introduce the notions on carbon nanotubes, their structure and properties that will be needed along this thesis.

In Chapter II), we review the available simulation techniques for CNTs then derive an original mesoscopic model for the electromagnetic properties of aligned arrays of nano-elements with a special focus on CNTs.

In Chapter III), we describe the fabrication techniques applied in and developed for the fabrication of CNT-based devices. The conventional techniques are briefly described with an emphasis on their use in CNT-based fabrication then the CNT-specific processes adopted and studied such as CVD growth and solution processing are exposed.

In Chapter IV), we combine modeling, analysis, simulation and fabrication to design and fabricate CNT-based monopole antenna prototypes. We first use the EM model and simulation techniques developed in Chapter II) to study monopole and dipole antennas based on experimentally-relevant but simplified structures. Then, to allow rational design, we derive an analytical model for CNT-based monopole antennas from transmission line theory. Finally, based on these tools and the fabrication techniques from Chapter III) we design and fabricate CNT-based electrically-short resonant monopole antenna prototypes.

In Chapter V), we conceive, fabricate and characterize samples to study photocurrent in CNTs. The fabrication discussion is extended to favoring semi-conducting behavior in CNTs and samples are realized accordingly where technically possible. DC photocurrent is measured under varied illumination and bias parameters and some trends are revealed.

Finally, in Chapter VI) we draw conclusions on the results obtained throughout this thesis and formulate recommendations for future work in all aspects.

Chapter I) Carbon nanotubes for antenna applications

Carbon nanotubes (CNTs) are one of the most popular and well-studied nanostructures known to date. If the first observation of CNTs may date back to 1952, they have been brought to wide attention in 1991 after Sumio Iijima (NEC laboratory in Tsukuba) reported their observation by high resolution transmission electron microscopy [29]. The remarkable properties of carbon nanotubes (CNTs) have since then raised much interest in the various fields of science and technology. Applications ranging from solar energy harvesting [30], [31] and display technology [32] to drug delivery [33] are under investigation. In particular, CNTs are envisioned as a new material for electronics for their high conductivity, physical strength, high aspect ratio, lightness [34]. They could solve some problems encountered in further miniaturization of state-of-the-art electronics such as electromigration, heat dissipation, and scalability. Unique properties are also predicted such as a propagation velocity between 50 and 100 times lower than that of light in vacuum [10], [16], [35] thus allowing scaling down wavelength dependent components such as antennas by this same ratio.

This PhD thesis will focus on this slow-wave effect and on potential photocurrent generation in CNTs to assess their interest in the design of novel small and agile antennas. This chapter is a brief summary of some minimal necessary background on CNTs in the scope of the thesis.

I.A) Structure

Single-wall carbon nanotubes (SWCNTs) can be seen as rolled-up sheets of graphene i.e. a monolayer hexagonal lattice of carbon atoms. They can be uniquely described by an double index or chiral vector (n,m) that corresponds to the way the graphene sheet is rolled up i.e. the angle it makes with the vectors of the lattice and how tight the CNT is rolled up. According to this index, a SWCNT may be metallic (no bandgap) or semiconducting (diameter dependent bandgap). Three types of CNTs can be distinguished (cf. Fig. 2). The only truly metallic CNTs are the armchair $n=m$, rolled along vector \mathbf{a}_2 on Fig. 1. For zigzag (rolled along vector \mathbf{a}_1) and chiral SWCNTs there are two cases: if $n-m=3j+1$ or $3j+2$ then the CNTs are semi-conducting. However, if $n-m=3j$ tubes, the bandgap is sufficiently small that they behave as metals at ambient temperature. They are semimetallic tubes usually referred to as being simply metallic CNTs. In this case, from Fig. 1, or the 3-congruence, it is simple to

conclude that, if all chiral vectors have the same probability, there should be 1/3 metallic SWCNTs and 2/3 semiconducting. Common CNT production methods usually have a narrow diameter distribution but chiral vectors of semiconductor and metal SWCNTs are equivalently distributed. A number of purification or growth techniques to enrich CNTs in semiconducting CNTs exist and are discussed in section V.A).

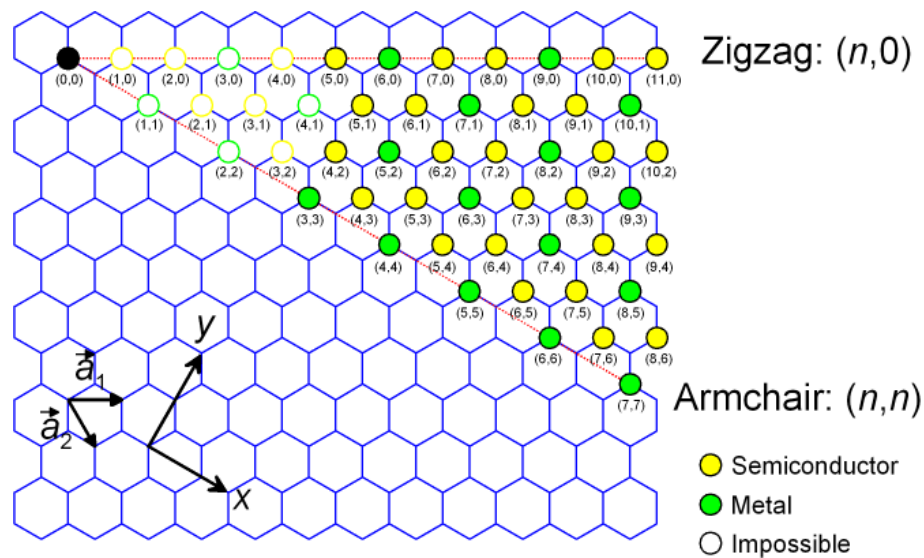


Fig. 1. Chiral vector of CNTs (adapted from www.sanken.osaka-u.ac.jp).

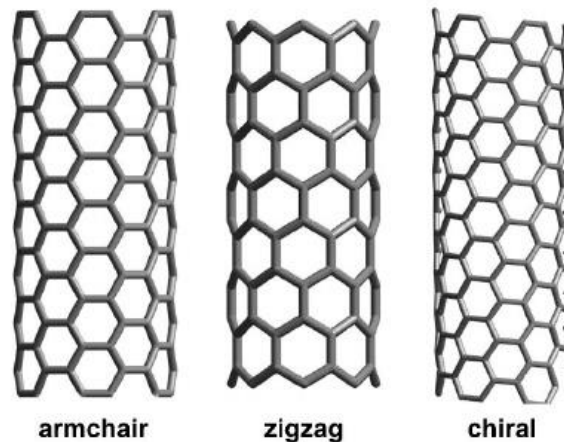


Fig. 2. Structure of the three main types of SWCNTs.

Source: <http://coecs.ou.edu/Brian.P.Grady/images/nanotube.jpg>

Multi-wall carbon nanotubes (MWCNTs) are concentric shells like Russian dolls made of SWCNTs. They come in a variety of diameters, number of shells etc.

CNTs can display huge length-to-diameter aspect ratios since the diameter varies from 1nm to a few tens of nm but lengths up to half a meter have been reported [36]. Usual lengths vary from less than a micrometer to hundred micrometers depending on the fabrication technique and application.

I.B) CNT fabrication methods

There are three common CNT fabrication techniques. Arc discharge, as used by Sumio Iijima [29] is simple, inexpensive and produces CNTs of high quality but short and random sizes and further purification is usually required. Laser ablation or vaporization, developed in 1995 in the group of Richard Smalley at Rice University, has a higher yield and produces mostly disordered SWCNTs with a good control over diameter and few defects. It is however more expensive than arc discharge and the last method, chemical vapor deposition, actually adapted to CNTs two years earlier. This process is easy to integrate for industrial and large scale process, and can produce the longest CNTs by far [36] it has good yield and aligned arrays can be produced and even patterned before growth. We focus on this production method which is described in more details in section III.B). Work on field emission from CNTs led to the demonstration of large arrays of standing CNT rods, 5 μ m-wide, 25 μ m-long [37] that could be interesting for antenna arrays. One challenge of patterned CVD growth is that it is a high-temperature process so the structures should be able to sustain the corresponding temperatures. Solutions to reduce the temperature at the level of the substrate have been developed such as top-heating (optical [38], [39]).

I.C) Optical and optoelectronic properties

Visually CNTs present two extreme appearances. When grown or coated in horizontal layers they are so transparent that they are used as transparent electrodes as a replacement of Indium Tin Oxide (ITO) for anything from displays to solar cells where transparency is key to performance. However in the form of vertically aligned arrays, CNTs appear an intense black; they act as a light trap so much so that they could be used as stray light absorbers in spatial detectors as proposed by a team of engineers at NASA's Goddard Space Flight Center [40]–[42].

SWCNTs present a chirality-dependent bandgap [43]–[45] as shown on Fig. 3. The bandgap is actually only diameter dependent once only semi-conducting CNTs are considered. The bandgap is inversely proportional to the diameter as can be seen from the Kataura plot on Fig. 4 reproduced from [44]. To determine the CNT types in a sample (usually solution-prepared CNTs) optical absorption spectroscopy can be performed and the absorption peaks analyzed through the Kataura plot. Another optical property of CNTs

leading to both a characterization method and applications is their photoluminescence which can be mapped as shown on Fig. 5 and described in [45].

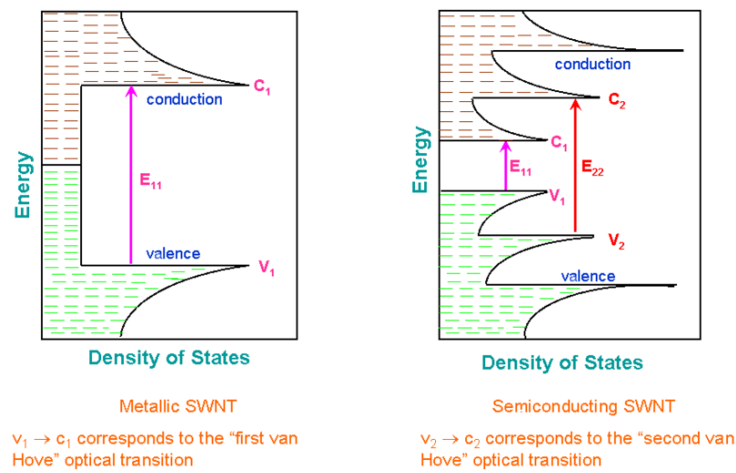


Fig. 3. Density of states in SWCNTs and bandgaps E_{11} and E_{22} between van Hove singularities. Source: Wikipedia

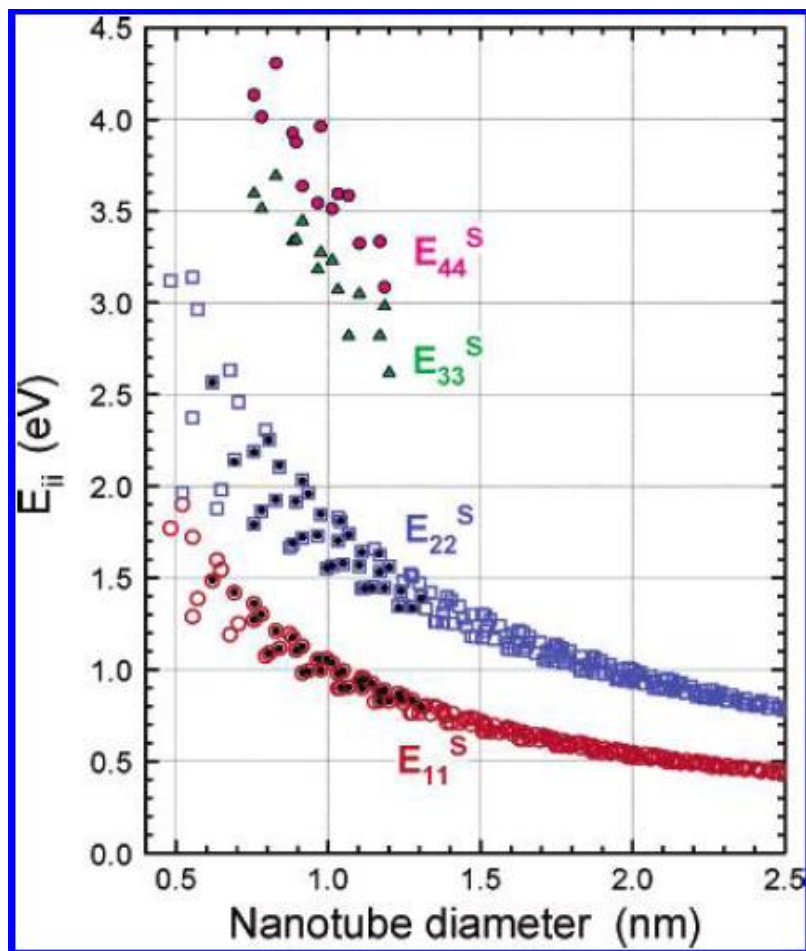


Fig. 4. Kataura plot from [44] (R. B. Weisman et S. M. Bachilo, 2003)

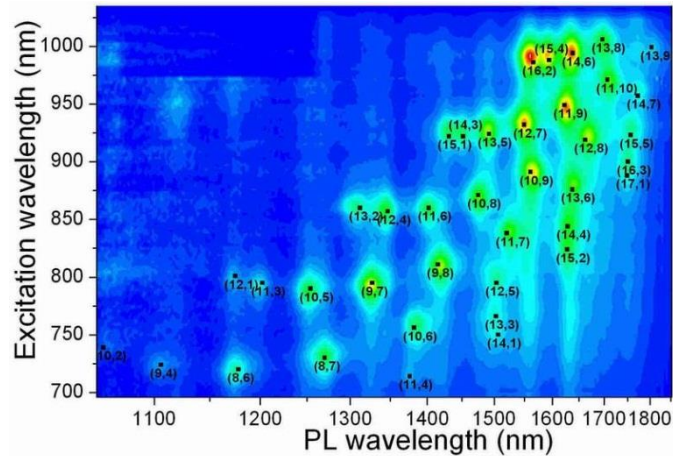


Fig. 5. Typical photoluminescence map of a CNT sample. Source: Wikipedia.

I.D) Applications in electronics and RF

Most research on CNTs for electronics was led on transistors. Recent advances show that CNTs might become a viable alternative to silicon both because they can display superior performance [2][46] and because they can now be integrated with sufficiently reasonable yield to fabricate a first “computer” [3]. Other applications include interconnects and shielding from electromagnetic interference for electromagnetic compatibility (EMI/EMC).

Some ingenious but rather anecdotic demonstrations of radio receivers from CNTs were reported. Rutherglen and Burke used a CNT as an AM demodulator in an otherwise classical circuit, arguing that its non-linear IV response made it a good rectifier [47]. Concurrently, also from UC, Jensen et al. used a combined NEMS-field-emission approach [48]; the field emission from a CNT is modulated by the vibrations induced by incoming radio waves on its charged tip – and only for the frequency corresponding to its tunable flexural resonance. Finally Kocabas et al. demonstrated a normal circuit with CNT transistors [49].

Apart from these, there have been only few measurements of CNT-based resonant antennas reported and they fall under three categories. The first one is antennas that either use the CNTs as a normal conductor [50]–[53] and work at about the same frequency they would have if made of metal or antennas that use them in exotic ways like the NEMS antenna described in [48]. The second type uses CNTs as load for otherwise classical antennas [54], [55]. These antennas are usually designed to operate at technologically current frequencies (e.g. 2.4GHz) and do not provide us with much information on the practicality of the

electrically-short resonant antennas we seek. The third category is optical [56], [57] and terahertz measurements on short CNTs. These give us more practical information for the application of electrically-short resonant antennas. We discuss the results in section IV.B).

I.E) Optical control

One of the interesting novelties CNTs could bring to antenna design is optical switch or modulation of the response of components, in particular beam-stirring for reflectarray antennas. Alternative technologies include vanadium dioxide (VO_2) [58]–[61], III-V nanowires [62] or photoconductive polymers. Photoconductive-polymer-coated CNT FETs have also been reported [63]. Optically controlled reconfigurable reflectarray antennas are a desirable technology as can be observed from the several patented concepts reviewed in [64], [65].

Beam-stirring with graphene in the (low) THz range was proposed using geometries such as high-impedance surfaces (HIS) [66], leaky wave antennas [67], and reflectarray elements [68], [69]. It has yet to be demonstrated experimentally.

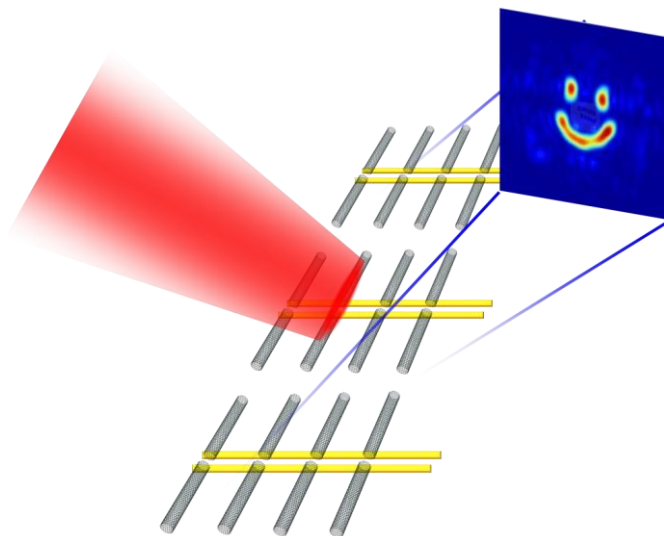


Fig. 6. Optically-controlled RF-beam stirring would allow the definition of multiple beams and beamshapes with applications in radar, monitoring, or secured transmission by path hopping.

I.F) Methodology

Designing and realizing CNT-based antennas is a complex task. Because the application of CNTs to RF is still rather fresh [70] and advanced CNT growth is still a

sensitive process, it requires the development of tools and techniques for every step from CNT modeling to CNT-based device simulation to fabrication and characterization (cf. Fig. 7). As we explain in the next paragraphs, all these aspects are tightly intertwined and cannot be dealt with separately. It is thus important to master them all – especially in the case of tuned resonant structures like antennas. The following chapters are arranged around the progress made on these four axes. We will here outline the permeability and mutual influence of these aspects and how they can be seen as a self-consistent iterative process.

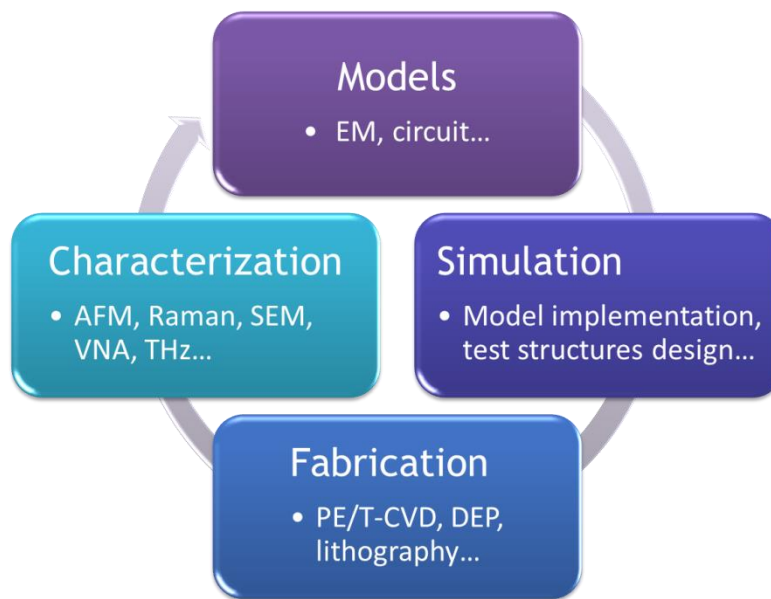


Fig. 7 Interrelated conception aspects of an antenna

In order to take advantage of the attractive electromagnetic properties of carbon nanotubes (CNTs), models and simulation techniques have been developed that account for them. The EM model developed in Chapter II) provides a method to bridge the gap there used to be between simulation and fabrication capabilities by adopting a mesoscopic approach.

Test structures and designs have been devised based on existing fabrication techniques and model predictions. In turn, parametric simulation studies of the designs were led to determine the requisites on fabrication techniques limits and variability (Chapter III).

This set clear goals to develop specific recipes and processes susceptible to yield reproducible high-quality small-diameter CNT growth (Chapter III). CNTs were grown by chemical vapor deposition (CVD); horizontally aligned on quartz and vertically aligned.

The investigation of lattice-aligned CVD growth on quartz and spray techniques were also motivated by the additional characterization techniques they would allow – such as transmission spectrophotometry, SNOM or THz spectrometry. Closing the loop (cf. Fig. 7), physical characterization of the CNTs combined to their RF response provides information to refine our CNT EM model – while the RF response interpretation relies on initial simulation.

On a parallel loop, photocurrent studies were undertaken to provide an empirical input to the modeling and design of light-modulated CNT-based components. Indeed in this case, the variety of CNT materials in the available studies made it difficult to assess the potentialities theoretically.

Let us proceed along the loop, starting from CNT modeling. To design antennas from CNT arrays while taking advantage of their properties, a suitable electromagnetic model and straightforward simulation techniques are needed.

Chapter II) Carbon nanotube modeling

We are interested in the use of carbon nanotubes (CNTs) and nanowires (NWs) for passive microwave and millimeter-wave electronics. This chapter aims at enabling much simpler and more efficient EM analysis of materials encapsulating nanotubes or nanowires to provide useful information needed for the design of mesoscopic electronic devices. These may find applications in the likes of antennas, resonators, interconnects, electromagnetic compatibility and interaction (EMC/EMI) as shielding or free-space THz elements such as polarizers, frequency selective surfaces (FSS), notch filters.

We start by reviewing the available methods to simulate CNTs and CNT-based electronics and find that our RF electronics application lies in a modeling gap between quantum mechanical (QM) solvers and analytical modeling on one side and circuit modeling on the other. This leads us into adopting a new mesoscopic approach to the electromagnetic modeling of nanotubes and nanowires in arrays or bundles of arbitrary shape and size [71], [72]. The derived model enables feasible and efficient EM analysis of electronic designs incorporating these novel materials. Furthermore, it can be seamlessly implemented in most commonly available EM simulation software – thus allowing engineers and researchers to focus on the novelty of the materials without having to learn to work in a new environment.

A general and straightforward approach to derive anisotropic bulk conductivity from single-element models is exposed. The specific model for single-wall carbon nanotubes is then adapted from an authoritative discrete semi-classical model. Both bulk and discrete models are subsequently implemented in two different 3D EM solvers. Through simulation of single- and bundled-SWCNT structures, we demonstrate the near equivalence of both models in transmission as well as in radiation. Finally we demonstrate the full EM simulation and retrofitting of experimental data of devices integrating carbon nanotubes.

As a conclusion, some possible complementary uses of different modeling techniques with our model are described.

II.A) Existing models, usage and necessity of a new approach

To take advantage of the most interesting electronic properties of CNTs a comprehensive model is required. Because we are dealing with molecular electronics,

classical electromagnetics (EM) provide an incomplete description. Let us review the available simulation methods.

A full quantum mechanical (QM) treatment is the most accurate method. It can be achieved relying on Density Functional Theory (DFT) but, most of the time, it is unpractical for the design of electronic components which rely on multi-scale electronics. To deal with the scale mismatch between electrodes and CNTs, a solution is to jointly solve EM and QM equations in a custom code. However, this remains computation-intensive and limited to nanoscopic CNT regions thus not applicable to large CNT arrays.

Two other approaches allow semi-classical treatment of CNTs behavior with common engineering techniques. Complex EM properties derived from Boltzmann's equation and the tight-binding approximation can be used in classical EM methods while most transport effects may also be described with distributed circuit elements. We will treat these techniques more extensively as they will serve as a base to our simulation platform.

II.A.1) Density Functional Theory

Density Functional Theory (DFT) is one of the most accurate methods to simulate carbon nanotubes electrical behavior. It provides a full *ab initio* quantum treatment of the structure by iteratively solving the interrelated electron density function and single-particle potential. A solution relying on this type of approach is SIESTA [73]. To compute transport in a molecule between two semi-infinite electrodes, DFT needs to be combined to the non-equilibrium Green's function (NEGF) [74]. For instance, TranSIESTA interfaces SIESTA and the NEGF to allow for a self-consistent calculation of the density matrix under external bias [75]. We illustrate schematically these algorithms in Fig. 8.

DFT only works for a static external potential but can compute quantum capacitance and inductance related to the density of states. Additionally there exist DFT-based methods to calculate frequency-dependent permittivity [76] and research on applying these to compute a frequency-dependent response is ongoing in Prof. Haibin SU's group at NTU/CINTRA. An extended theory for time-dependent response exists, Time-Domain Density Functional Theory (TDDFT, [77]).

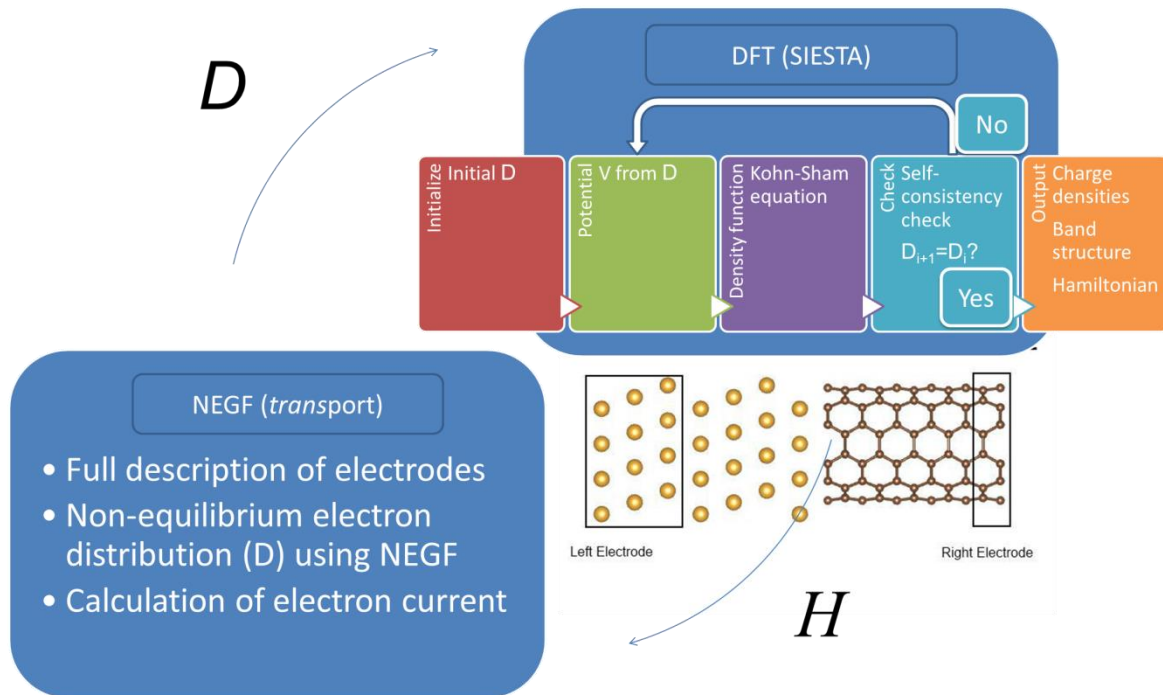


Fig. 8 Block diagram of a self-consistent DFT-NEGF algorithm like TranSIESTA. The DFT algorithm computes the Hamiltonian. It is fed to the NEGF algorithm which in turn computes the electron distribution and passes it to the DFT algorithm.

These self-consistent methods are mainly limited by their iterative steps that require a good initial guess for the density function and make the process computation-intensive – even more so for TDDFT. Structures are thus limited to few few-nanometer-long CNTs and very close-by metal electrodes atoms. A typical system calculated using SIESTA/TranSIESTA, with one 2-nm-long CNT – too short for antennas but long enough for a QM contact modeling – between two gold leads takes 3~4 hours for one I-V point with 24 CPUs in NTU’s HPC. The required memory per CPU is around 1GB – this being largely dependent on the number of atoms and the desired accuracy.

II.A.2) Combined Maxwell-Schrödinger approach

In [78], [79], L. Pierantoni et al. describe a method to self-consistently solve Maxwell equations and the Schrödinger equation – hence providing a full QM treatment of CNTs while keeping a comparatively lighter classical EM treatment of CNT surroundings. The principle is to discretize and solve the 3D domain by a transmission-line-matrix (TLM) technique then to solve the Schrödinger equation on a 1D chain between two nodes of the 3D matrix by a finite-

difference time-domain (FDTD) method (cf. Fig. 9 and Fig. 10). Alternative algorithms have been proposed in [80]–[82] to cut computational cost.

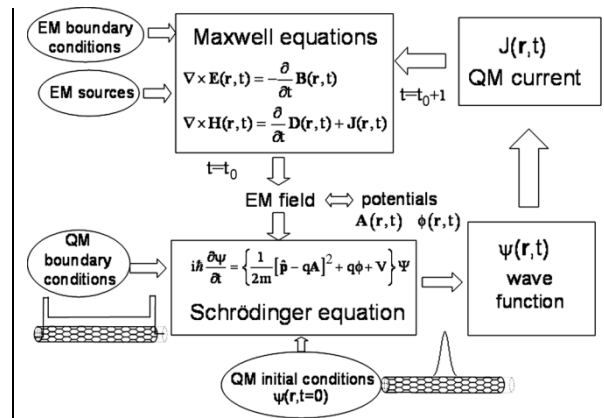
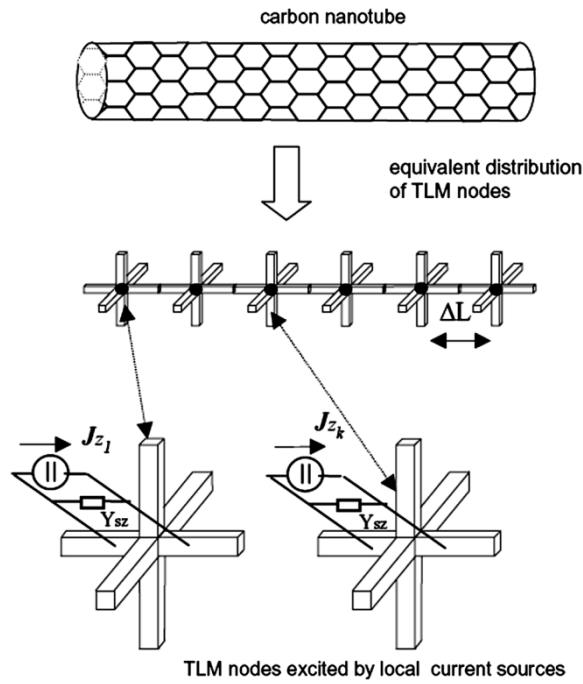


Fig. 9 Block diagram of the self-consistent QM-EM loop – reproduced from [79].

Fig. 10 The CNT is discretized in 1D FDTD with nodes connecting to those of the 3D TLM discretized environment – reproduced from [79].

Although elegant, this method is not straightforward to integrate with common engineering tools and rather requires the development of a tailored simulator – making it necessary for the user to adopt a new tool. More importantly, it is better suited to problems with a single to a few short CNTs or similarly small quantum domain as in a nano-transistor, a nano-diode or, recently, a graphene nanopatch [83] – quite opposed to the numerous long CNTs needed for low-impedance antennas at technologically relevant frequencies.

II.A.3) Effective surface conductivity

The effective impedance boundary conditions introduced in 1999 by G.Y. Slepyan and S.A. Maksimenko in [7] offer an interesting solution. The CNT's quantum properties are modeled by an equivalent complex conductivity on a hollow tube (cf. Fig. 11) derived in the semi-classical approximation based on the Boltzmann kinetic equation and tight-binding theory.

In most cases, this approach combined to an appropriate integration technique may be sufficient and more versatile. A circular-cross-section metallic single-wall CNT (m-SWCNT)

of radius smaller than 3.39nm is described as a hollow tube with a Drude-like complex surface conductivity derived following semi-classical equations [7] for all chiralities and rewritten by G.W. Hanson [10] as:

$$\sigma_{CNT,surf} \simeq \frac{2e^2 v_F}{\pi^2 \hbar a (\nu + j\omega)} \quad (1)$$

where a is the radius of the CNT, ω is the angular frequency, $e \approx 1.602 \cdot 10^{-19} \text{C}$ is the elementary charge, $\hbar = h/2\pi$ with $h \approx 6.626 \cdot 10^{-34} \text{ J}\cdot\text{s}$ the Plank constant, $\nu = \tau^{-1}$ is the relaxation frequency and v_F is the Fermi velocity in CNTs. The latter is given by $v_F = 3\gamma_0 b/2\hbar$ with $b=0.142\text{nm}$ and γ_0 the overlap integral. Both $\gamma_0 \approx 2.5\text{-}3.1 \text{ eV}$ [84] and $\tau \approx 3 \cdot 10^{-12}\text{s}$ (low frequencies) – 10^{-13}s (IR below optical transitions) [85] are phenomenological constants [17], [86] that may vary depending on the frequency band.

We shall note that this conductivity derives from an analytical estimate of a more complex formula encompassing all SWCNTs and in particular zigzag semiconducting SWCNTs (sc-SWCNTs) [7]. G.Y. Slepyan et al. provide numerical estimates for sc-SWCNTs and show their conductivity is smaller than that of m-SWCNTs of similar diameter by a few orders of magnitude for typical SWCNT diameters. This is discussed further in section II.B.3).

Both the analytical simplification and the numerical estimates account for intraband motion only. Thus they hold up to the optical transition limit as equivalent to a more rigorous quantum mechanical approach. The frequency limit is estimated at tens of terahertz [84] or analytically [7]:

$$\omega < \begin{cases} \frac{3\gamma_0 b}{2\hbar a} = \frac{v_F}{a} & \text{for metallic SWCNTs} \\ \frac{\gamma_0 b}{2\hbar a} = \frac{v_F}{3a} & \text{for semiconducting SWCNTs} \end{cases} \quad (2)$$

Beyond these limits, M.V. Shuba and the previous authors described similar approaches to derive more rigorous effective boundary conditions in cases such as MWCNTs, and including tunneling and interband transitions [7], [18], [20]. A discussion of the respective approximations of Boltzmann/Maxwell and Schrödinger/Maxwell (previous section) treatments can be found in introduction of [87].

With regards to the circuit model discussed in section I.A.1.1), G.W. Hanson noted [87] that the above formula overlooks the local diffusion – equivalent to the quantum capacitance – and presented an amended version of his formula:

$$\sigma(q, \omega) = \frac{\sigma(\omega)}{1 - \xi q^2} \quad (3)$$

with

$$\xi = \frac{v_F^2}{v^2 u(u - j)} \quad (4)$$

and q the spatial wavenumber. However no general expression for q is provided which makes the implementation impractical. As will be shown by circuit considerations this effect is actually quite negligible for externally coupled CNT structures (cf. section I.A.1.1)).

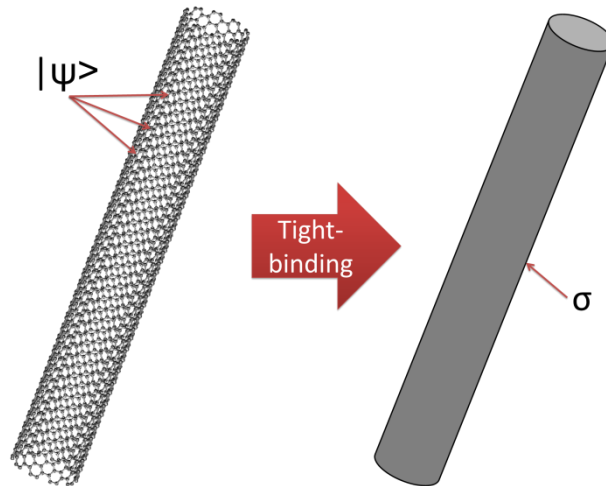


Fig. 11 Using tight-binding theory or similar approaches, a SWCNT may be approximated as a hollow cylinder with effective complex conductivity σ . This then allows a classical EM treatment of the problem.

As one of the first investigations of CNT use as antennas, G.W. Hanson used the method of moments (MoM) to solve the case of a dipole antenna made of two identical metallic SWCNTs modeled by equation (1) [10]. The MoM is classically used for thin-wire antennas but does not provide much versatility and is restricted to simple ideal cases. Therefore a realistic feed of the antenna cannot be studied using this technique.

To address this issue and allow the use of CNTs in common engineering tools, we integrated the hollow-tube model in finite-element (FEM) electromagnetic (EM) solvers to study transmission and radiation in SWCNTs [88], [89]. In HFSS, a commercial distribution edited by Ansys [90], the dipole case was reproduced using two cylinders linked by a 50-ohm lumped port. A complex surface impedance (5) based on [7] was applied to the cylinders. In EMXD, an FEM EM solver developed at XLIM by Michel Aubourg, a senior researcher, the implementation is similar but the surface impedance has to be returned by an .exe file to the solver rather than directly providing the formula (cf. Appendix 2).

$$\begin{aligned} Z_{CNT,surf} &= \frac{1}{\sigma_{CNT,surf}} = \frac{\pi^2 \hbar a}{2e^2 v_F} (v + j\omega) \\ &= 2\pi a \frac{h v}{8e^2 v_F} \left(1 + j \frac{\omega}{v}\right) \end{aligned} \quad (5)$$

Following our technique, tens of tubes can be studied but, as explained in II.A.5), meshing issues are encountered when multiple scales become involved. Some multiscale simulation techniques such as the mixed FEM/IE engine for radiator and surrounding that should be released with HFSS 15 could help in cases limited to few CNTs but the problem remains for simulation of a large number of CNTs. It is thus still not an efficient technique for CNT-based microwave devices.

II.A.4) Circuit model

A simple and intuitive model for CNTs is based on distributed circuit elements derived from the Luttinger liquid model [91], [92]. The application of Luttinger liquid formalism to SWCNTs was introduced and experimentally supported by M.W. Bockrath [93], [94] in 1999. The resulting description in terms of distributed circuit elements was then extended by P.J. Burke into transmission line formalism for the case of metallic SWCNTs [8], [95]. Additional refinements and scope broadening to MWCNTs and bundles can be found in [96]–[98].

We will cover the case of the SWCNT extensively as this gives us a first grasp of the underlying physics and design considerations for CNT-based RF devices. Furthermore the transmission-line analysis is extended to monopoles and dipoles of SWCNTs in section IV.A.1.3).

II.A.4.1) Lumped-element circuit model for a transmission line

Following classical microwave theory [99], a transmission line can be described as a series of lumped two-port segments of infinitesimal length Δz as illustrated Fig. 12. This description accounts for the conductors' total per-unit-length series resistance (R) and inductance (L) as well as their mutual coupling and dielectric loss – in the dielectric separating the conductors – through per-unit-length shunt capacitance (C) and conductance (G) respectively.

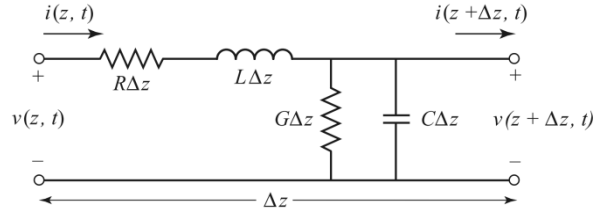


Fig. 12 Transmission line. Lumped-equivalent circuit from [99].

Analytical studies starting from the *telegrapher equations* are derived for $\Delta z \rightarrow 0$. For circuit simulation, for instance using Agilent's Advanced Design System (ADS, [100]), lumped blocks repeated with an appropriate Δz need to be used. The typical condition is $\Delta z \ll \lambda$ where λ is the wavelength of the wave under consideration in the transmission line. Commonly, R , L , C , G are coined distributed circuit elements as opposed to lumped elements and Δz is dropped in the distributed circuit representation for the sake of simplicity.

Let us recall here some of the main results from the transmission line formalism [99]. The *telegrapher equations* (6) and (7) are obtained by applying Kirchhoff's voltage and current laws to the circuit of Fig. 12 then dividing by Δz and taking the limit $\Delta z \rightarrow 0$.

$$\frac{\partial v(z, t)}{\partial z} = -Ri(z, t) - L \frac{\partial i(z, t)}{\partial t} \quad (6)$$

$$\frac{\partial i(z, t)}{\partial z} = -Gv(z, t) - C \frac{\partial v(z, t)}{\partial t} \quad (7)$$

If we consider the sinusoidal steady-state with cosine phasors, we obtain:

$$\frac{dV(z)}{dz} = -(R + j\omega L)I(z) \quad (8)$$

$$\frac{dI(z)}{dz} = -(G + j\omega C)V(z) \quad (9)$$

By solving equations (8) and (9) simultaneously, one finds the wave equations for voltage and current as:

$$\frac{d^2V(z)}{dz^2} - \gamma^2V(z) = 0 \quad (10)$$

$$\frac{d^2I(z)}{dz^2} - \gamma^2I(z) = 0 \quad (11)$$

where

$$\gamma = \alpha + j\beta = \sqrt{(R + j\omega L)(G + j\omega C)} \quad (12)$$

is the complex propagation constant. Solutions to (10) and (11) can be found in the form:

$$V(z) = V_0^+ e^{-\gamma z} + V_0^- e^{\gamma z} \quad (13)$$

$$I(z) = I_0^+ e^{-\gamma z} + I_0^- e^{\gamma z} \quad (14)$$

Now, if we derive (13) and combine it with (8) then (14) we realize that:

$$\frac{\gamma}{R + j\omega L} (V_0^+ e^{-\gamma z} - V_0^- e^{\gamma z}) = I(z) = I_0^+ e^{-\gamma z} + I_0^- e^{\gamma z} \quad (15)$$

Hence we can define the *characteristic impedance* of the transmission line, Z_C , as relating the voltage and current on this line:

$$Z_C \equiv \frac{V_0^+}{I_0^+} = \frac{-V_0^-}{I_0^-} \quad (16)$$

And we have the following general expression for the characteristic impedance:

$$Z_C = \frac{R + j\omega L}{\gamma} = \sqrt{\frac{R + j\omega L}{G + j\omega C}} \quad (17)$$

The wavelength on the line and the phase velocity are given by [99]:

$$\lambda = \frac{2\pi}{\beta} \quad (18)$$

$$v_p = \frac{\omega}{\beta} = \lambda f \quad (19)$$

In the lossless case ($R = G = 0$),

$$Z_c = \sqrt{\frac{L}{C}} \quad (20)$$

$$v_p = \frac{\omega}{\beta} = \frac{1}{\sqrt{LC}} \quad (21)$$

$$\lambda = \frac{1}{f\sqrt{LC}} \quad (22)$$

The main advantage of the circuit approach to analytical modeling of CNTs is that the classical derivations from the telegrapher equations can be readily applied once the circuit elements are known. In section IV.A.1.3) we derive the full expression of β in the general lossy case before applying it to the SWCNT bundle problem.

I.A.1.1) Metallic SWCNT

When set in a waveguide configuration – such as parallel wires or a wire and a ground – metallic SWCNTs may be described using transmission line formalism by adding specific lumped and distributed components deduced from the Luttinger liquid formalism [8], [94] for one-dimensional electron gases (1DEG).

M.W. Bockrath introduced the concept of a kinetic inductance, L_{k1} , and quantum capacitance, C_{Q1} , by considering the Lagrangian of charges in an m-SWCNT [94]. The kinetic inductance arises from the kinetic energy needed to promote an electron above the Fermi level (opposes the change in current). The quantum capacitance, originally termed compressibility for electron gases, results from the potential energy (Fermi level) increase when adding an electron to the system. Following [92], in ballistic regime, the DC conductance of a spinless 1D channel ohmically-contacted to a 3D system is h/e^2 (Plank constant over the square of the elementary charge). This can be modeled at AC as split in two lumped contact resistances [8], one at each end of the channel, of value R_0 – sometimes referred to as the resistance quantum

since it corresponds to the resistance of a channel with two spins. M.W. Bockrath also discussed tunneling into a CNT in his thesis.

$$L_{K1} = \frac{h}{2e^2v_F} \quad (23)$$

$$C_{Q1} = \frac{2e^2}{hv_F} = \frac{1}{v_F^2 L_{K1}} \quad (24)$$

$$R_0 = \frac{h}{2e^2} \quad (25)$$

where, as in section II.A.3) and the rest of this thesis, $e \approx 1.602 \cdot 10^{-19}C$ is the elementary charge, $h \approx 6.626 \cdot 10^{-34} J.s$ is the Plank constant and $v_F = 3\gamma_0 b/2\hbar$ is the Fermi velocity in CNTs with $b=0.142nm$ and γ_0 the overlap integral.

These quantities are calculated for a single spinless mode. However an m-SWCNT has four modes: two channels arising from the lattice degeneracy multiplied by two electron spin states. These four channels should intuitively behave as four quantum wires in parallel linked externally through a common electrostatic capacitance. After careful treatment, reported in Appendix 1, this proves to be correct.

Hence, an m-SWCNT presents the following distributed elements:

$$L_K = \frac{1}{4} L_{K1} = \frac{h}{8e^2v_F} = \frac{R_0}{4v_F} \quad (26)$$

$$C_Q = 4C_{Q1} = \frac{8e^2}{hv_F} = \frac{4}{R_0v_F} \quad (27)$$

$$R_C = \frac{R_0}{4} = \frac{h}{8e^2} \quad (28)$$

$$R_Q = \frac{R_0}{4} \frac{1}{MFP} = \frac{h}{8e^2} \frac{1}{v_F\tau} = \frac{R_0}{4v_F\tau} \quad (29)$$

where L_K , C_Q and R_C are the effective distributed kinetic inductance, distributed quantum capacitance and lumped 3D-to-1D contact resistance (one on each side for an ohmically-contacted CNT in ballistic regime). A distributed resistance R_Q is introduced to account for losses in non-ballistic regime. In non-ballistic regime, the average length between collisions is called Mean Free Path (*MFP*). Provided that electrons move at the Fermi velocity v_F in CNTs this defines the plasmon lifetime in CNTs as $\tau = \frac{MFP}{v_F}$ and the relaxation

frequency $\nu = \tau^{-1}$. Assuming scattering at each collision is equivalent to that at an ohmic contact, we obtain (29) – consistent with the definitions in the surface conductivity.

These distributed components are inherent to the 1DEG nature of the m-SWCNT without presupposing a specific configuration – except for the actual existence of a distributed electrostatic capacitance (cf. Appendix 1). In fact they are equivalent to integrating the surface conductivity described in section II.A.3) over the cylinder perimeter to obtain a distributed impedance. One can write [87]:

$$Z_{cn}(q, \omega) = \frac{1}{2\pi a \sigma(q, \omega)} = R_Q + j\omega L_K + \frac{q^2}{j\omega C_Q} \quad (30)$$

with the same definitions for all notations between the conductivity and circuit model. This is even clearer in [101] where the circuit parameters are directly derived from Boltzmann and Maxwell equations – the same used for the conductivity.

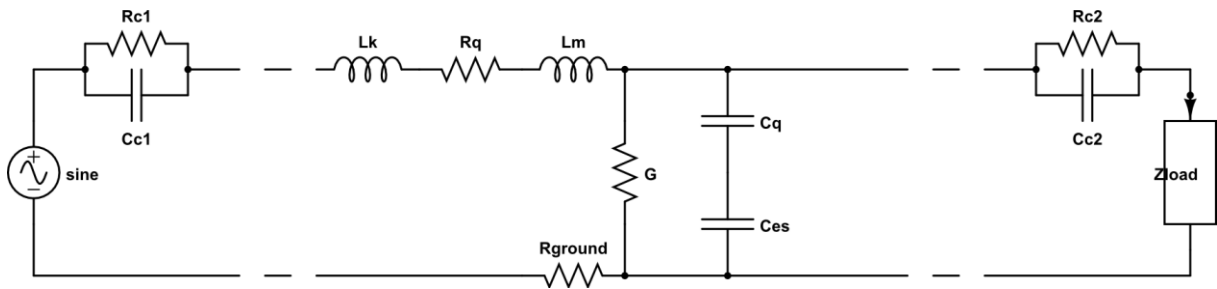


Fig. 13 Effective circuit diagram for a SWCNT contacted at both ends with a source and a load.

By combining this description of the CNT conductor behavior and the description of the geometry of a waveguide through classical elements, we can describe the expected behavior of a guided wave using the transmission line formalism. The waveguide configuration will generally imply a self-inductance of the line and mutual-capacitance of its conductors also referred to as distributed magnetic inductance, L_M , and electrostatic capacitance, C_{ES} . An imperfect ground will be manifested by a distributed resistance, R_{ground} , especially so at higher frequencies due to the skin effect. An imperfect dielectric between the conductors gives rise to a distributed conductance G . Finally imperfect contacts at the end of the CNT will be modeled by lumped resistances R_{C1}, R_{C2} and capacitances C_{C1}, C_{C2} rather than the ideal R_C . Values can be calculated through DFT or similar techniques [102], [103], extracted from published experiments [11], [104], [105] or, preferably extracted from measurements of samples fabricated through the same process that will be used for the

final device. The final transmission line for a SWCNT over a ground is represented Fig. 13. It can be simplified to the RLCG line described in section II.A.4.1) by writing:

$$L = L_K + L_M \quad (31)$$

$$C = \frac{1}{C_Q^{-1} + C_{ES}^{-1}} \quad (32)$$

$$R = R_Q + R_{ground} \quad (33)$$

Expressions for the inductance, capacitance, resistance and conductance in classical configurations [99] applied to an m-SWCNT are given in Table 1. The quantum capacitance is applied only once in the two-wire configuration as asserted without formal demonstration in [16]. The formula for R_{ground} for an m-SWCNT parallel to a metallic wall is intuited from L_M and fitting numerical values calculated with TXline by AWR [106]. It is intended as a tool for assessing the influence of an imperfect ground on the propagation. We write the effective depth of propagation of the EM wave $\delta_{min} = \min(\delta_{skin}, \delta_{ground})$ where δ_{ground} is the thickness of the metallic ground and δ_{skin} the skin depth in the ground.

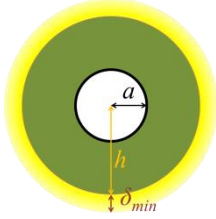
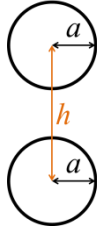
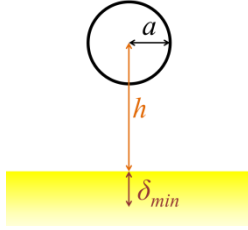
$$\delta_{skin} = \sqrt{\frac{2}{\omega\mu\sigma_{ground}}} \sqrt{\sqrt{1 + \left(\frac{\omega\epsilon}{\sigma_{ground}}\right)^2} + \frac{\omega\epsilon}{\sigma_{ground}}} \quad (34)$$

For $\frac{\omega\epsilon}{\sigma_{ground}} \ll 1$ i.e. $\omega \ll \frac{\sigma_{ground}}{\epsilon} \sim 10^{18}$ Hz for good conductors (copper, gold, aluminium) this simplifies to the better known:

$$\delta_{skin} = \sqrt{\frac{2}{\omega\mu\sigma_{ground}}} \quad (35)$$

In the cases covered in this thesis equation (35) is a perfectly valid approximation for metallic lines because we will study frequencies up to a few terahertz at most. Equation (34) might only be needed in the case of lines made from poor conductors such as semi-conductors or doped polymers. Gold has skin depths of 454, 249 and 144nm at 30, 100 and 300GHz respectively. Hence a 0.5-1 μ m-thick metallization is necessary to reduce losses. Silver, copper and aluminium are similar while nickel, iron, and platinum require about twice these thicknesses.

Table 1. Transmission line parameters for a SWCNT adapting from [99].

	Coaxial	Two-wire	CNT parallel to ground
			
L_M	$\frac{\mu}{2\pi} \ln\left(\frac{h}{a}\right)$	$\frac{\mu}{\pi} \operatorname{arcosh}\left(\frac{h}{2a}\right)$	$\frac{\mu}{\pi} \operatorname{arcosh}\left(\frac{h}{a}\right)$
C_{ES}	$\frac{2\pi\epsilon'}{\ln\left(\frac{h}{a}\right)}$	$\frac{\pi\epsilon'}{\operatorname{arcosh}\left(\frac{h}{2a}\right)}$	$\frac{\pi\epsilon'}{\operatorname{arcosh}\left(\frac{h}{a}\right)}$
R_{ground}	$\frac{1}{\pi\delta_{min}(2h + \delta_{min})\sigma_{ground}}$	0	$\frac{1}{2a\left(1 + \sqrt{\frac{\operatorname{arcosh}\left(\frac{h}{a}\right)}{\pi}}\right)\delta_{min}\sigma_{ground}}$
G	$\frac{2\pi\omega\epsilon''}{\ln\left(\frac{h}{a}\right)}$	$\frac{\pi\omega\epsilon''}{\operatorname{arcosh}\left(\frac{h}{2a}\right)}$	$\frac{\pi\omega\epsilon''}{\operatorname{arcosh}\left(\frac{h}{a}\right)}$
L	$L_K + L_M$	$2L_K + L_M$	$L_K + L_M$
C	$\frac{1}{C_Q^{-1} + C_{ES}^{-1}}$	$\frac{1}{C_Q^{-1} + C_{ES}^{-1}}$	$\frac{1}{C_Q^{-1} + C_{ES}^{-1}}$
R	$R_Q + R_{ground}$	$2R_Q$	$R_Q + R_{ground}$

In Table 2 we give some typical numerical values for a SWCNT transmission line calculated for the case of a SWCNT over a ground plane. The relative spacing and plasmon lifetime – which respectively affect the classical and quantum properties of the line – are varied on a logarithmic scale to cover most possible cases. It can be observed that the kinetic inductance is predominant as it is in all cases 3 to 4 orders of magnitude larger than the magnetic inductance. The quantum capacitance leads to less than 5% variation on the total capacitance making it rather negligible compared to the electrostatic capacitance – as mentioned in section II.A.3). The conductance can be ignored for typical insulators used (air, SiO₂). Finally the ground resistance is 1 to 2 orders of magnitude smaller than the quantum resistance for a single SWCNT. Conclusions on resistance and inductance may change in the case of a bundle however since the quantum resistance and kinetic inductance are then

divided by the number of SWCNTs while the ground resistance and magnetic inductance remain sensibly of the same order.

Table 2. Typical circuit parameter values. We take $\gamma_0 = 2.7$ eV hence $v_F = 8.74 \times 10^5$ m/s. Then we have $L_K = 3.69$ nH/ μ m and $C_Q = 355$ aF/ μ m independently of the two factors varied in the table. For R_{ground} we take $a = 0.7$ nm and $\delta_{min} = 100$ nm.

	F_v GHz	MFP μ m	R_Q k Ω / μ m	R_{ground} k Ω / μ m	L_M pH/ μ m	L_K/L_M	C_{ES} aF/ μ m	C aF/ μ m
τ $= 3 \times 10^{-12}$ s $h/a = 3$	53	2.62	1.23	0.100	0.7	5239	15.8	15.1
τ $= 1 \times 10^{-12}$ s $h/a = 10$	159	0.87	3.69	0.088	1.2	3085	9.3	9.1
τ $= 3 \times 10^{-13}$ s $h/a = 30$	531	0.26	12.31	0.081	1.6	2256	6.8	6.7
τ $= 1 \times 10^{-13}$ s $h/a = 100$	1592	0.09	36.94	0.076	2.1	1743	5.3	5.2

II.A.4.2) MWCNT and bundles

A MWCNT is made of concentric shells of rolled up graphene – in other words, SWCNTs. It can thus be regarded as multiple SWCNT transmission lines in parallel. Each shell will shield its adjacent shells from each other so there is capacitive coupling only between adjacent shells, $C_{coax,i,i+1}$, with the same expression than reported for the coaxial line in Table 1. Similarly, only the external shell is coupled to the ground. Because the shells are only separated by the Van der Waals distance between graphene layers in graphite, $\delta_{graph} = 0.34$ nm, tunneling between adjacent shells can be expected and could be modeled through a conductance G_{tunnel} . Note that there are conflicting reports on such a conductance [107] which is estimated between negligible to 10^{-4} S/ μ m.

Because shells in MWCNT may present diameters exceeding those typical of SWCNTs, the number of electronic subbands participating to conduction can be more than 2. As an approximation to the Fermi distribution at room temperature (300K), Naeemi and Meindl give the number of channels as follows [108]:

$$N_{\text{chan}}(D) = \begin{cases} \frac{2}{3}, & D < 6\text{nm} \\ xD + y, & D \geq 3\text{nm} \end{cases} \quad (36)$$

Where $x = 0.0612\text{nm}^{-1}$, $y = 0.425$. This has less than 15% error for any value of D and includes the fact that only 1/3 of SWCNTs are metallic. The formula is also limited to low voltages as higher voltages allow more subbands to participate in the conduction. In the overlapping 3 to 6nm region the two approximations are almost equivalent.

This approximation includes the statistical 1/3-2/3 ratio and is thus valid for MWCNTs with numerous shells or numerous MWCNTs with various shells. In other cases, based on the curves in [108] and keeping the same 1/3-2/3 pondered average, metallic shells can be modeled using:

$$N_{\text{chan}}(D) = \begin{cases} 2, & D < 6.78\text{nm} \\ xD + y_m, & D \geq 5.85\text{nm} \end{cases} \quad (37)$$

and semiconducting shells as:

$$N_{\text{chan}}(D) = \begin{cases} 0, & D \leq 3\text{nm} \\ xD + y_{sc}, & D \geq 3\text{nm} \end{cases} \quad (38)$$

where $x = 0.0612\text{nm}^{-1}$, $y_m = 1.642$, $y_{sc} = -0.1836$, with 5% error on $N_{\text{chan}}(D)$. Extending the affine approximation of the metallic case down to 3nm is still less than 10% error.

Naeemi and Meindl also note that the MFP is directly proportional to the diameter [108]:

$$\text{MFP}(D) = l_0 D \quad (39)$$

Hence, following our previous derivation, we have for each shell:

$$L_K(D) = \frac{1}{2N_{\text{chan}}(D)} \frac{R_0}{v_F} \quad (40)$$

$$C_Q(D) = 2N_{\text{chan}}(D) \frac{1}{R_0 v_F} \quad (41)$$

$$R_C(D) = \frac{1}{2N_{\text{chan}}(D)} R_0 \quad (42)$$

$$R_Q(D) = \frac{1}{2N_{\text{chan}}(D)} \frac{R_0}{MFP(D)} = \frac{R_0}{2l_0} \frac{1}{D(xD + y)} \quad (43)$$

Finally we can model a MWCNT as proposed in [107], reported in Fig. 14. Note that the shells are represented as all ohmically contacted which is not necessarily the case, especially if a capped MWCNT is contacted by deposition/contact of electrodes after the growth. In the latter case, the lumped R_{mc} should be directly connected to the extremity of the external shell only, like the distributed C_E . Lumped inter-shell capacitances should then be used at both extremities to model the nested caps.

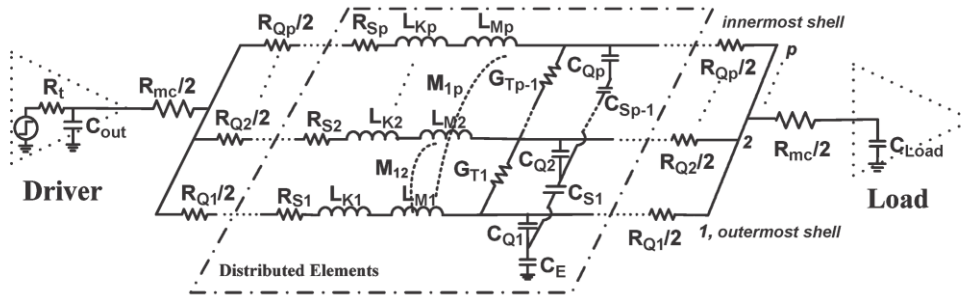


Fig. 14 MWCNT circuit model, reproduced from [107]. R_{mc} is the imperfect contact resistance.

Similarly, bundles of SWCNTs and MWCNTs can be treated as transmission lines in parallel [96], [98], [109]. In most cases, the CNT-to-CNT coupling capacitances require being evaluated with electrostatic solvers. Additionally the complex circuit model can usually not be solved analytically but require numerical treatment as discussed in the next section.

In cases where the CNTs or their shells are all connected at their base and of comparable conductivities, simplifications on the circuit model can be operated. We discuss this in section II.B.3.3).

II.A.4.3) Implementation

The circuit model of CNTs can be used on its own for simple structures or combined to elements calculated by full-EM simulation like capacitance matrices [98] or S-parameters matrices imported in Agilent's ADS [110]. Alternatively, nanoHUB.org references, among other resources, an online tool to calculate electrical properties of MWCNT bundles [111] based on the circuit model as described in [97].

Analytical radiation may be determined [16] in simple cases but this is restrictive and requires much attention to the approximations made in the non-conventional cases dealt with for CNTs. Because the technique inherently neglects radiation [16] it may not be deemed self-consistent to generally apply it to antenna problems [18]. The approximation is justified in the case of high-impedance antennas with low radiation resistance like for a long single SWCNT but at optical frequencies or dealing with a bundle it could imply a non-negligible error. However the description in terms of distributed circuit elements allows straightforward understanding of the underlying physics which may help interpreting results and designs.

II.A.5) Bundle modeling and necessity of a new approach

Previous work [8], [10], [16], [20], [96], [112]–[118] has shown that most applications of CNTs in high-frequency electronics would need to make use of bundled CNTs, as opposed to single CNTs, to overcome problems such as high impedance and poor efficiency. In [20], Shuba et al. concluded that, at similar external radii, bundles of SWCNTs would be a more efficient antenna than a MWCNT or SWCNT. Efforts have been made towards modeling of bundled CNTs but they either rely on a circuit approach [96], [98], [109] or on approaches difficult to apply in modern CAD software or to extend to general cases [17], [19], [119], [120]. To understand the behavior of devices based on this new material and predict their performance, full 3D EM simulation is necessary [121]. It would allow rational design and optimization by taking into account parasitics, integration with other components, shielding. However, simulation of CNT-based devices is made very difficult by three factors: the huge aspect ratio of the CNTs (typically 1000:1 to 10^6 :1), the large quantities involved (from hundreds to millions of CNTs) and the multiple scales involved when connecting CNTs to microelectronics [78], [79]. As a result, most works limit themselves to circuit or hybrid simulation for full structures [9], [78], [79], [98], [114]–[116], [122] which cannot properly model both long-distance propagation in CNTs and coupling in complex structures. Some other works input measured data [52] – or present comparative performance without modeling [123] – which does not allow pre-design. We need a new model. It should solve the meshing issues, be seamlessly integrated in conventional EM simulation tools and based on theoretical grounds to allow parametric performance prediction.

II.B) Effective medium approach

We propose to overcome all the issues outlined in the previous section at once by using a bulk equivalent to arrays or bundles of CNTs. Indeed the typical length of variation of the cross-sectional structure of a bundle is small compared to the wavelengths involved in radiofrequency regime (even up to optical range). Hence you may consider averaging the electrical properties of the nanotubes (NTs) over the volume they occupy. Topological considerations can be dealt with by introducing anisotropic properties. For instance, as shown in Fig. 15, an array of vertically aligned CNTs will be modeled by a bulk material assigned with an averaged CNT conductivity along the vertical axis (\mathbf{z}) and with a conductivity matching the coupling and tunneling effects occurring between CNTs along the two other orthogonal axes. This approach is very versatile as it can accommodate any model of CNT or nanowire (NW) by the derivation technique that will be exposed. It can also be implemented in most EM simulation suites, independently of the solving method and makes analytical solving possible.

From hollow tubes ... to nanowires ... to an anisotropic bulk material

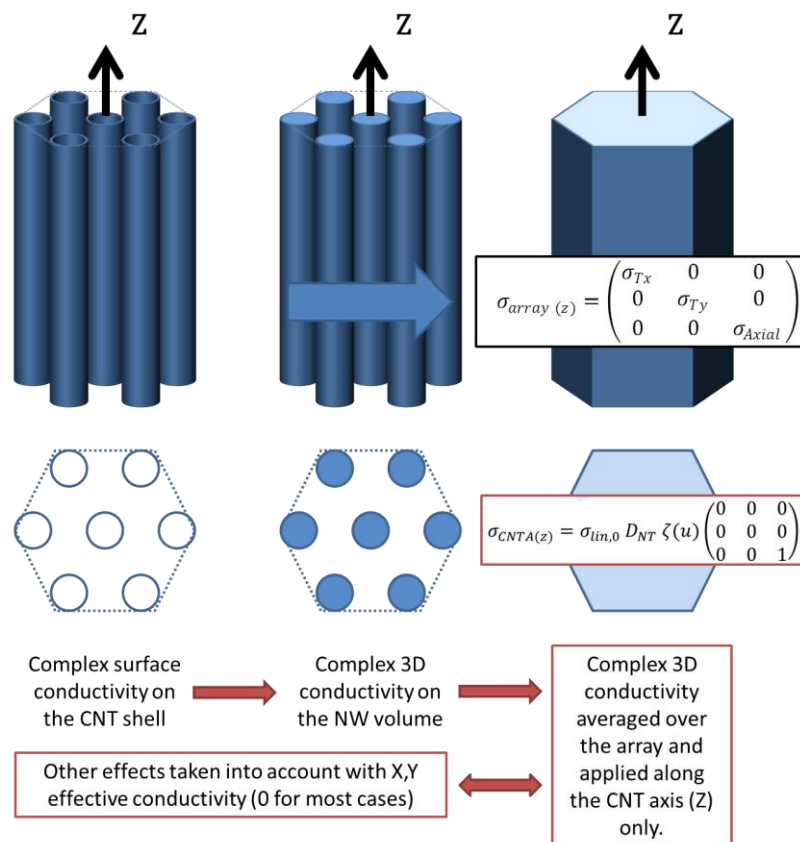


Fig. 15. Schematic illustration of the anisotropic bulk model.

A few didactic steps will lead us to the final model and its application. In section II.B.1) we expose a general anisotropic bulk model for arrays of nanoelements and, in section II.B.2), the method to derive it from a given single element model. In section II.B.3) we derive a practical model for arrays of metallic SWCNTs.

Next, we implement both our model and the one it was derived from in electromagnetic (EM) solvers to validate its equivalence to existing models (section II.C.2)) and its practicality over them. In section II.C.3), full microstructures including CNTs are simulated using our bulk model. Note that, in these simulations, coupling inside the bundle can be ignored – as in most practical situations as will be demonstrated.

II.B.1) Anisotropic bulk model

II.B.1.1) Methodology

We proceed as follows. First, we derive a bulk nanowire (NW, bulk wire) electrically equivalent to a nanotube (NT, hollow tube). CNTs can then be dealt with as any other bulk NW. Secondly we derive bulk electromagnetic properties for arrays of aligned NWs. Finally we apply this general derivation to the case of SWCNTs starting from an existing surface conductivity model.

II.B.1.2) Scale considerations

Typically, if we work at frequencies lower than 3THz, the free-space wavelengths of the fields under consideration are above $\lambda_{0,3\text{THz}} = 100\mu\text{m}$, much greater than the nanometer scale cross-sectional diameters of NTs and NWs. For CNTs however, an interesting predicted property [10] is that there exists an approximate 1:50 ratio between the free-space and the plasmon wavelengths. Numerically we have $\lambda_{p,3\text{THz}} \simeq 2\mu\text{m}$. This is still much greater than the typical diameters of NTs: from a few angstroms to a few nanometers for single-wall carbon nanotubes (SWCNTs) and up to few tens of nanometer for multi-wall CNTs. Note that the radius a of a CNT is given by:

$$a = \frac{\sqrt{3}}{2\pi} b \sqrt{m^2 + mn + n^2} \quad (44)$$

where $b=0.142\text{nm}$ is the interatomic distance in graphene and (m,n) is the dual chiral index of the CNT. Experimentally, the radius of SWCNTs is usually found smaller than $a(m=n=50) = 3.39\text{nm}$.

Hence, in our work we will assume $\lambda_0 > \lambda_p \gg a$ for the fields under consideration which will allow us to work with effective media in the corresponding directions. The eventual upper frequency applicability limit of the approach depends on the typical cross-sectional dimensions of the nano-objects and the dispersion relation of the medium. For SWCNTs it typically holds up to tens of terahertz, which is also the limit of the semi-classical model used in section II.B.3) [84].

II.B.1.3) Bulk nanowire equivalent to a nanotube

In the next section, we assume prior knowledge of bulk conductivity for the nanoelements under consideration. However, when working with NTs, the models have rather been derived as surface properties for hollow tubes – with regard to their physical nature. For instance, in [7], Slepyan, Maksimenko et al. provided a model for SWCNTs of small radii and in [87] Hanson extends it to cover both CNTs and solid NWs. As simple calculus shows, the circuit approach by P.J. Burke [8] is actually equivalent in terms of resistance and inductance [87], [119].

In our work, we derive an equivalent bulk material of electrical conductivity such that a bulk NW and a hollow tube of identic dimensions exhibit the same overall electrical properties. Let a NT be aligned along \mathbf{z} . Since $\lambda \gg a$ and the NT is long with respect to its radius, we can consider the electrical field constant over its cross section. We consider the equivalent bulk NW as the one verifying the same distributed Ohm's law as the NT:

$$I(z, \omega) = \frac{E_z(z, \omega)}{Z(z, \omega)} \quad (45)$$

where $I(z, \omega)$ is the net current across the NT cross-section at z , $E_z(z, \omega)$ is the electrical field component along \mathbf{z} in the NT at z and $Z(z, \omega)$ is its (linear) distributed impedance. Considering equation (45) applied to the NT and to the equivalent NW, we deduce that:

$$Z_{NW,bulk}(z, \omega) = Z_{NT,surf}(z, \omega) \quad (46)$$

Then from relation (46), we set equation (47):

$$\begin{aligned} \iint_{cross-section} \sigma_{NW,bulk}(z, \omega) dA \\ = \int_{c-s\ perimeter} \sigma_{NT,surf}(z, \omega) dl \end{aligned} \quad (47)$$

where $\sigma_{NW,bulk}$ is the bulk conductivity of the equivalent NW and $\sigma_{NT,surf}$ is the surface conductivity of the original NT.

Since the bulk and surface conductivities are supposed constant over the NW and NT cross-section, this results in:

$$\sigma_{NW,bulk} = \sigma_{NT,surf} \frac{P_{NT}}{\Phi_{NT}} \quad (48)$$

where P_{NT} and Φ_{NT} are respectively the perimeter and the area of the cross-section of the NT. Similarly, if the NT was to be filled with a material of conductivity $\sigma_{filling}$ then, by linear combination:

$$\sigma_{NW,bulk} = \sigma_{NT,surf} \frac{P_{NT}}{\Phi_{NT}} + \sigma_{filling} \quad (49)$$

This approach can be adopted to model other conductive nanoelements, for instance graphene nanoribbons, by assigning them a finite cross-section area.

In conclusion, we have introduced a bulk NW equivalent to NTs and both types of nanoelements will thus be treated and addressed as NWs in the rest of the derivation. For simplicity, we will now write σ_{NW} instead of $\sigma_{NW,bulk}$.

II.B.1.4) Array of aligned nanowires

In the next section, we consider an array (or bundle) of NWs aligned along \mathbf{z} (see Fig. 15). We derive its anisotropic effective bulk conductivity σ_{array} . The array is then readily modeled as a block of identical dimensions made of an anisotropic material of conductivity σ_{Axial} along the \mathbf{z} axis and $(\sigma_{Tx}, \sigma_{Ty})$ in the transverse directions – to model any coupling or tunneling between NWs (see Fig. 16):

$$\sigma_{array(z)} = \begin{pmatrix} \sigma_{Tx} & 0 & 0 \\ 0 & \sigma_{Ty} & 0 \\ 0 & 0 & \sigma_{Axial} \end{pmatrix} \quad (50)$$

In the case of isotropic repartition and shape of the NWs in the cross-sectional plane, we have $\sigma_{Tx} = \sigma_{Ty} = \sigma_T$. The definition of two quantities can be useful in cases such as arrays of graphene nanoribbons or anisotropic spacing of the nanoelements.

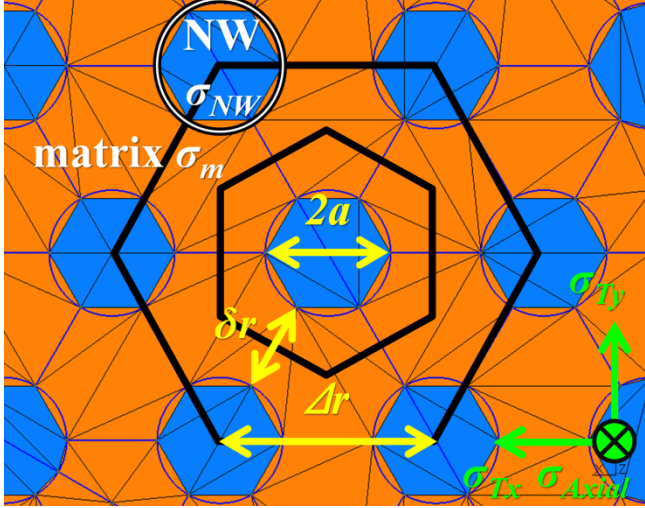


Fig. 16. Cross-sectional cut of a hexagonal array of NWs. In this simple case, NW centers are equidistant and NWs are similar which simplifies geometrical considerations. This cut is a typical inner mesh of the CNT bundles simulated in section II.C.2).

Note that this approach may be applied in two dimensions when interested in a horizontal array of NWs thin with respect to relevant quantities. This has partly been investigated by S. Choi's anisotropic sheet model for horizontally aligned CNTs [124]. He derived his model from the circuit model [8] whereas in our approach, we start from a physical model. Moreover, our approach enables to thicken the sheet so that coupling effects between the NWs and their environment are better modeled.

More complicated situations may also be treated following this anisotropic bulk method by linear combination of the models. Possibilities range from anisotropic embedding media to isotropic tri-dimensional meshes of interconnected NWs. Inter-mode coupling can also be taken into account through the non-diagonal coefficients.

II.B.2) General derivation

II.B.2.1) Axial bulk conductivity

In an array of aligned NWs, the volume fraction of NWs, δ_{NW} , is equal to the proportion of cross-sectional area occupied by the NWs and is given by:

$$\delta_{NW} = \frac{N_{NW}\Phi_{NW}}{\Phi_{bulk}} \equiv \Phi_{NW}D_{NW} \quad (51)$$

where Φ_{bulk} is the cross-sectional area of the array of interest, Φ_{NW} is the cross-sectional area of one NW, N_{NW} is the number of NW in this array, D_{NW} is the density of NW (number of NW per unit area).

Thus, by averaging the conductivity of the NWs and that of the embedding medium (matrix) σ_m , we find the effective axial bulk conductivity σ_{Axial} as follows:

$$\sigma_{Axial} = \sigma_{NW}\delta_{NW} + \sigma_m(1 - \delta_{NW}) \quad (52)$$

Note that, in the special case of aligned CNTs embedded in a dielectric ($\sigma_m = 0$), (49) (51) and (52), simply lead to:

$$\sigma_{Axial} = \sigma_{NT,surf}P_{NT}D_{NT} \quad (53)$$

II.B.2.2) Transverse bulk conductivity

Rather than trying to derive inter-tube coupling from tube-to-tube coupling [16], [98], [118], we will follow effective medium theories (EMT) such as Maxwell Garnett's or Bruggeman's [125]–[127]. As explained in [84], [85], [128], this allows describing the full electromagnetic interaction between inclusions (CNTs) at frequencies ranging from microwave to optical range.

We propose a model for arrays of aligned circular-cross-section NWs. In this case, in the transverse plane, NWs can be considered as circular inclusions in a matrix, provided they are separated or bundled in patches small with respect to the wavelength – which is experimentally correct. Then, following [126], [127] we can find the effective conductivity σ_T :

$$\delta_{NW} \frac{\sigma_{NW} - \sigma_T}{\sigma_{NW} + \sigma_T} + (1 - \delta_{NW}) \frac{\sigma_m - \sigma_T}{\sigma_m + \sigma_T} = 0 \quad (54)$$

where σ_{NW} is the conductivity of the bulk NWs, σ_m is the conductivity of the embedding medium and δ_{NW} is the proportion of cross-section area occupied by NWs. This leads to the second order polynomial equation:

$$\sigma_T^2 + \sigma_T (1 - 2 \delta_{NW}) \Delta\sigma - \sigma_{NW}\sigma_m = 0 \quad (55)$$

with

$$\Delta\sigma = (\sigma_{NW} - \sigma_m) \quad (56)$$

Which, taking $Re(\Delta\sigma) > 0$ has only one physically meaningful root:

$$\sigma_T = \left(\delta_{NW} - \frac{1}{2} \right) \Delta\sigma + \left(\left[\left(\delta_{NW} - \frac{1}{2} \right) \Delta\sigma \right]^2 + \sigma_{NW}\sigma_m \right)^{\frac{1}{2}} \quad (57)$$

For conducting NWs in a poorly conducting matrix i.e. taking $|\sigma_{NW}| \gg |\sigma_m|$, this can be approximated as:

$$\sigma_T = \begin{cases} \frac{\sigma_m}{(1 - 2\delta_{NW})}, & \left(\frac{1}{2} - \delta_{NW} \right) \gg \left| \frac{\sigma_m}{\sigma_{NW}} \right|^{\frac{1}{2}} \\ \left(1 + \left(\delta_{NW} - \frac{1}{2} \right) \left(\frac{\sigma_{NW}}{\sigma_m} \right)^{\frac{1}{2}} \right) (\sigma_{NW}\sigma_m)^{\frac{1}{2}}, & \left| \delta_{NW} - \frac{1}{2} \right| \ll \left| \frac{\sigma_m}{\sigma_{NW}} \right|^{\frac{1}{2}} \\ (2\delta_{NW} - 1)\sigma_{NW}, & \left(\delta_{NW} - \frac{1}{2} \right) \gg \left| \frac{\sigma_m}{\sigma_{NW}} \right|^{\frac{1}{2}} \end{cases} \quad (58)$$

And more particularly if the embedding matrix is perfectly dielectric ($\sigma_m = 0$):

$$\sigma_T = \begin{cases} 0, & \delta_{NW} \leq \frac{1}{2} \\ 2 \sigma_{NW} \left(\delta_{NW} - \frac{1}{2} \right), & \delta_{NW} > \frac{1}{2} \end{cases} \quad (59)$$

This shows an interesting percolation threshold at $\delta_{NW} = \frac{1}{2}$ as illustrated in Fig. 17. Below the threshold, there is no direct transmission but above it, the resulting conductivity is affine to the proportion of NWs with a slope of twice their conductivity. Therefore, only very dense arrays will show effective coupling. For instance, in a hexagonal Bravais lattice, as shown on Fig. 16, the transverse conductivity is only significant if:

$$\left(\delta_{NW} > \frac{1}{2} \right) \Leftrightarrow \left(\frac{\Delta r}{2a} < \sqrt{\frac{\pi}{\sqrt{3}}} \approx 1.35 \right) \quad (60)$$

where a is the radius of the NWs and $\Delta r = \delta r + 2a$ is their spacing, center to center, while δr is the shell-to-shell spacing.

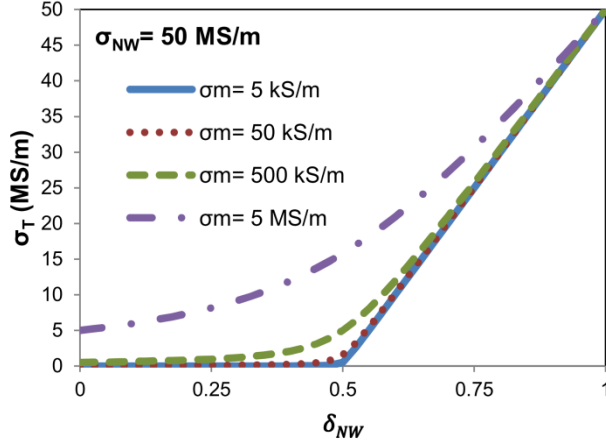


Fig. 17. Transverse conductivity as a function of the fraction of cross-sectional area occupied by NWs for various matrix conductivities. 50MS/m is the DC conductivity of the equivalent NW of a SWCNT of radius 2.4nm (cf. section II.B.3)). It is close to the conductivities of bulk gold and bulk copper. For reference, sea water has a conductivity of 4 S/m, polystyrene 0.1 fS/m and metals from 1 to tens of MS/m. Note the threshold at $\delta_{NW} = \frac{1}{2}$ for relatively low matrix conductivities.

Interpreted otherwise, there is no significant coupling between NWs in a hexagonal Bravais lattice configuration if:

$$\delta r \geq 2 \left(\sqrt{\frac{\pi}{\sqrt{3}}} - 1 \right) a \approx 0.7 a \quad (61)$$

Measurements on CNT composites show a similar percolation threshold [129], [130]. However the differences to the case we describe do not allow numerical comparison.

In the case of SWCNTs grown in arrays, we usually are below the threshold. Typically the diameter is 1nm, and the minimum possible spacing is $0.39\text{nm} > 0.7a$. Hence, in the rest of the chapter, unless mentioned otherwise, since we describe CNT arrays separated by air we will take $\sigma_T = 0$.

II.B.3) Application to carbon nanotubes

II.B.3.1) Metallic SWCNTs

In this section, we apply the methodology exposed in sections II.B.1) and II.B.2) to derive an anisotropic bulk conductivity in the practical case of metallic single-wall carbon nanotubes (SWCNTs). Following G.W. Hanson's interpretation [10] of Slepian and

Maksimenko's semi-classical derivation [7], a circular-cross-section metallic SWCNT of radius smaller than 3.39nm exhibits a surface conductivity equal to:

$$\sigma_{CNT,surf} \simeq \frac{2e^2 v_F}{\pi^2 \hbar a (\nu + j\omega)} \quad (62)$$

And we have:

$$P_{CNT} = 2\pi a \quad (63)$$

where a is the radius of the CNT, ω is the angular frequency, $e \approx 1.602 \cdot 10^{-19} \text{C}$ is the elementary charge, $\hbar = h/2\pi$ with $h \approx 6.626 \cdot 10^{-34} \text{ J}\cdot\text{s}$ the Plank constant, $\nu = \tau^{-1}$ is the relaxation frequency and v_F is the Fermi velocity in CNTs. The latter is given by $v_F = 3\gamma_0 b/2\hbar$ with $b=0.142\text{nm}$ and γ_0 the overlap integral. Both $\gamma_0 \approx 2.5\text{-}3.1 \text{ eV}$ [84] and $\tau \approx 3 \cdot 10^{-12} \text{ s}$ (low frequencies) – 10^{-13} s (IR below optical transitions) [85] are phenomenological constants [17], [86] that may vary depending on the frequency band. We take $\gamma_0 = 3 \text{ eV}$, leading to $v_F = 9.71 \cdot 10^5 \text{ m/s}$, and $\tau = 3 \cdot 10^{-12} \text{ s}$ – as chosen by G.W. Hanson in [10]. This makes comparing numerical results more relevant and straightforward.

Applying (53) we find, for an array of m -SWCNTs of same MFP in a perfect dielectric:

$$\sigma_{Axial} = \frac{8e^2 v_F}{h(\nu + j\omega)} * D_{NT} \quad (64)$$

This can also be written in the form

$$\sigma_{Axial} = \sigma_{lin,0} D_{NT} \zeta(u) \quad (65)$$

Where

$$\sigma_{lin,0} = \frac{8e^2 v_F}{h\nu} = \frac{24e^2 b\pi \gamma_0}{h^2 \nu} = A\gamma_0\tau \quad (66)$$

is the DC linear conductivity over a single SWCNT. It is linearly dependent on the phenomenological values γ_0 and $\tau = \nu^{-1}$. The complex frequency dispersion profile and the normalized frequency are respectively:

$$\zeta(u) \equiv \frac{1 - ju}{1 + u^2} \quad (67)$$

$$u \equiv \omega\tau = \frac{\omega}{\nu} = \frac{f}{F_v} \quad (68)$$

The function $\zeta(u)$ governing the variations of the frequency dependent bulk conductivity is the same as that of the original surface conductivity. Hence, the limitation noted by Hanson for a single CNT [10] that, for $u < 1 \Leftrightarrow f < F_v \simeq 53\text{GHz}$, damping will prevent any resonance from occurring should still hold for bundles.

The transverse conductivity has been derived in the previous section. For the next section, we will consider a non-coupled situation, both to simplify future circuit interpretation of the resulting bundles and because it corresponds to experimental conditions.

Note that the original conductivity (62) and thus the one we derive from it (65) only take into account the resistive and inductive effects in the CNTs. The electrostatic coupling is readily modeled by the EM solvers; however it is not the case for the quantum capacitance introduced by P.J. Burke [8], [16]. In [87], Hanson indicates that this capacitive effect is actually equivalent to using a drift-diffusion model for the generalized Ohm's law. As this is not an option in the solvers we use, HFSS and EMXD, or other commercially available solutions we know of, we will prefer using the amended version of his formula:

$$\sigma(q, \omega) = \frac{\sigma(\omega)}{1 - \xi q^2} \quad (69)$$

with

$$\xi = \frac{v_F^2}{v^2 u(u - j)} \quad (70)$$

and q the spatial wavenumber. However no general expression for q is provided which makes the implementation impractical. We are still investigating this matter. Following Hanson's approximation of q as ten times the wavenumber in vacuum k_0 , the role of the quantum capacitance is 3 orders of magnitude lower than that of the inductance. Similarly, its implementation in a circuit model shows negligible variation in the response of a monopole/dipole as shown in section IV.A.2).

To conclude, an array of CNTs aligned along \mathbf{z} can be modeled as a material exhibiting the following anisotropic conductivity:

$$\sigma_{CNTA(z)} = \begin{pmatrix} \sigma_T(q, \omega) & 0 & 0 \\ 0 & \sigma_T(q, \omega) & 0 \\ 0 & 0 & \sigma_{Axial}(q, \omega) \end{pmatrix} \quad (71)$$

with $\sigma_T(q, \omega)$ and $\sigma_{Axial}(q, \omega)$ the results of the application of (69) to (57) and (65) respectively.

For the reasons given earlier, we will, for the rest of this PhD thesis, neglect inter-CNT coupling and quantum capacitance and consider CNTs in vacuum or in air leading to:

$$\sigma_{CNTA(z)} = \sigma_{lin,0} D_{NT} \zeta(u) \begin{pmatrix} 0 & 0 & 0 \\ 0 & 0 & 0 \\ 0 & 0 & 1 \end{pmatrix} \quad (72)$$

II.B.3.2) Semi-conducting SWCNTs and mixed SWCNT bundles

II.B.3.2.1) General case of mixed SWCNT bundles

Our approach provides a straightforward means to account for aligned arrays and bundles made of a mix of metallic and semiconducting SWCNTs in known proportions – provided a model is available for each. Let us write:

$$\left\{ \rho_{(n,m)} = \frac{N_{(n,m)}}{N_{total}}, \quad (n, m) \in \mathbb{IN}^2 \right\} \quad (73)$$

$$N_{total} = \sum_{(n,m) \in \mathbb{IN}^2} N_{(n,m)} \quad (74)$$

where $N_{(n,m)}$ is the number of (n,m)-SWCNTs in the array with (n,m) the chiral indices. Then, by linear summation of the contributions, we have:

$$\sigma_{Axial} = D_{NT} \sum_{(n,m) \in \mathbb{IN}^2} \sigma_{lin,(n,m)}(\omega) \rho_{(n,m)} \quad (75)$$

which, if we assume a Drude-like behavior of sc-SWCNTs based on the form of the general equation of zigzag SWCNTs [7], becomes:

$$\sigma_{Axial} = D_{NT} \sum_{(n,m) \in \mathbb{IN}^2} \sigma_{lin,0,(n,m)} \rho_{(n,m)} \zeta(u_{(n,m)}) \quad (76)$$

where $(\sigma_{lin,0,(n,m)}, u_{(n,m)})$ are the respective DC linear conductivities and the frequency normalized by respective plasmon relaxation frequencies of the different (n,m)-SWCNTs. For SWCNTs of sensibly similar diameter the MFP is the same, according to equation (39). In this case and in the limits discussed in section II.A.3), we can further write:

$$\sigma_{Axial} = D_{NT} \zeta(u) \sum_{(n,m) \in \mathbb{IN}^2} \sigma_{lin,0,(n,m)} \rho_{(n,m)} \quad (77)$$

where the function $\zeta(u)$ and the normalized frequency remain those defined in equations (67) and (68). The sc-SWCNTs conductivities can be computed numerically from the integral formula in [7] or using DFT methods for instance.

In the case of different diameters D or resistivity, the frequency dependence is not so straightforward because, following [108], we have:

$$F_v(D) = \frac{1}{2\pi\tau(D)} = \frac{v_F}{2\pi\text{MFP}(D)} = \frac{v_F}{2\pi l_0 D} \quad (78)$$

For distributions where the CNTs have very different diameters, it is simpler to work with equation (76) using:

$$\begin{aligned} \sigma_{lin,0,(n,m)} &= \text{MFP}_{(n,m)} \frac{2N_{chan,(n,m)}}{R_0} \\ &= \begin{cases} \frac{2l_0 D_{(n,m)}}{R_0} 2\delta_{m,typ}, & D_{(n,m)} < 3\text{nm} \times (1 + \delta_{m,typ}) \\ \frac{2l_0 D_{(n,m)}}{R_0} (xD_{(n,m)} + y_{(n,m)}), & D_{(n,m)} \geq 3\text{nm} \end{cases} \end{aligned} \quad (79)$$

where $\delta_{m,typ}$ is the Kronecker delta, equal to 1 if the shell is metallic and 0 if the shell is semiconducting. The highlighted diameter condition with overlap for metallic CNTs, defines three categories of SWCNTs by diameter as:

- $\text{IE}_{cst} = \{(n,m) \in \mathbb{IN}^2 \text{ such that } D_{(n,m)} < 3\text{nm}\}$, for which the number of channels is diameter-independent

- $IE_{lin} = \{(n, m) \in \mathbb{N}^2 \text{ such that } D_{(n,m)} \geq 3\text{nm}\}$, for which the number of channels can be considered linear with diameter, and
- $IE_{mix} = \left\{ \begin{array}{l} \{(n, m) \in \mathbb{N}^2 \text{ such that } D_{(n,m)} \in [3, 6\text{nm}]\}, \alpha \lesssim 2 \\ \emptyset, \alpha \gg 2 \end{array} \right\}$ – where α is the ratio of sc-SWCNTs to m-SWCNTs – a subset of IE_{lin} for which the simpler diameter-independent description is valid within 15% error. The case $\alpha = 2$ is the statistical value for unsorted SWCNTs.

For a relatively large number of SWCNTs, for non-preferential processes, the 1:2 statistical m/sc-SWCNTs ratio should be verified and it should be uniform over diameters. Hence, extending these assumptions to any α , for a distribution included in $IE_{cst} \cup IE_{mix}$, one can write:

$$\sigma_{Axial} = D_{NT} \times \frac{4l_0}{R_0(\alpha + 1)} \sum_{\{(n,m)\}} D_{(n,m)} \rho_{(n,m)} \zeta(u_{(n,m)}) \quad (80)$$

For distributions included in IE_{lin} , quite uncommonly large for SWCNTs but treated for the sake of completeness:

$$\sigma_{Axial} = D_{NT} \frac{l_0}{R_0} \sum_{\{(n,m)\}} D_{(n,m)} (xD_{(n,m)} + y) \rho_{(n,m)} \zeta(u_{(n,m)}) \quad (81)$$

where $y = \frac{1}{3}y_m + \frac{2}{3}y_{sc}$ in the unsorted case and $y = \frac{1}{\alpha+1}y_m + \frac{\alpha}{\alpha+1}y_{sc}$ in general. In other cases, the contributions from the categories IE_{cst} and IE_{lin} can be accounted for by linear combination of equations (80) and (81).

Finally, for continuous distributions of diameters – such as a common Gaussian distribution – the sum in (76) can be evaluated analytically or numerically as an integral sum.

II.B.3.2.2) Respective influence of semi-conducting and metallic SWCNTs

Here, we neglect the influence of the diameter on the mean free path and thus assume τ constant for diameters from 0.12 to 6nm. We then proceed to study the relative contributions of m- and sc-SWCNTs numerically through a typical case based on rigorous calculations. The previous approximations are confirmed and a polynomial description for the conductivity of sc-SWCNTs of small diameter is given.

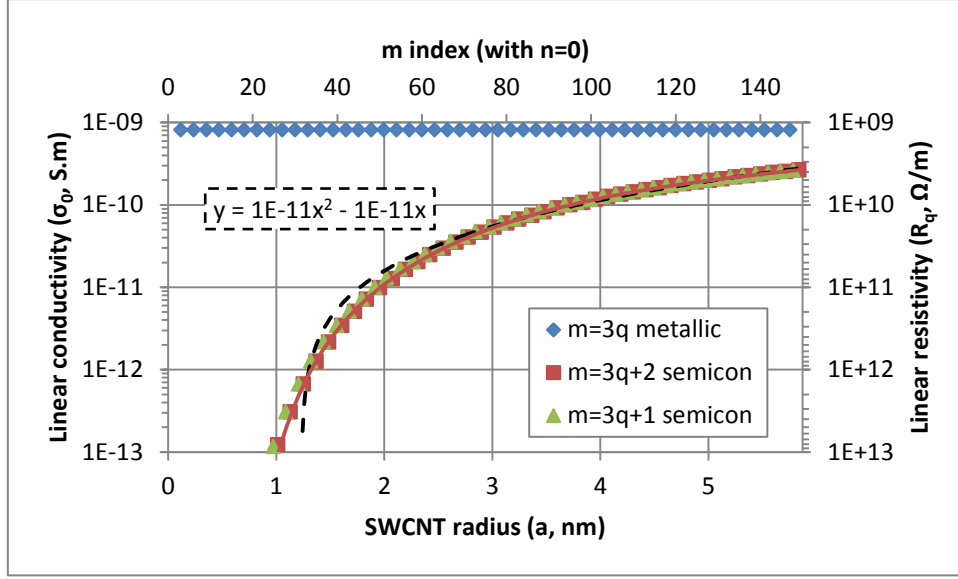


Fig. 18 Linear DC conductivity of zigzag SWCNTs versus their radius. Equivalent linear resistivity and $(m, 0)$ index scales are also indicated. Parameters: $\gamma_0 = 2.7$ eV, $\tau = 3 \times 10^{-12}$ s, $T = 264$ K.

In [7], G.Y. Slepian et al. provide numerical estimates for the conductivity of zigzag sc-SWCNTs, taking $\gamma_0 = 2.7$ eV, $\tau = 3 \times 10^{-12}$ s, $T = 264$ K. On Fig. 18, we use these estimates to plot the DC linear conductivity versus SWCNT radius for all types of zigzag CNTs. This is chosen because, as we have shown in the previous section, metallic CNTs have a radius-independent linear conductivity. On the other hand we show that sc-zigzag SWCNTs conductivity can be correctly approximated by a directly implementable 5th order polynomial of the radius a in the 1 to 6nm range:

$$\begin{aligned} \sigma_{3q+2,lin}(\gamma_0 = 2.7\text{eV}, \tau = 3 \times 10^{-12}\text{s}, a \text{ (in nm)}) \\ \simeq 2 \times 10^{-13}a^5 - 3 \times 10^{-12}a^4 + 2 \times 10^{-11}a^3 \\ - 4 \times 10^{-11}a^2 + 3 \times 10^{-11}a - 8 \times 10^{-12} \end{aligned} \quad (82)$$

A more workable 2nd order polynomial gives a rough estimate from 1.4nm to 6nm:

$$\begin{aligned} \sigma_{3q+2,lin}(\gamma_0 = 2.7\text{eV}, \tau = 3 \times 10^{-12}\text{s}, a \text{ (in nm)}) \\ \simeq 1 \times 10^{-11}a \times (a - 1) \text{ S.m} \end{aligned} \quad (83)$$

while, for metallic SWCNTs:

$$\sigma_{3q,lin}(\gamma_0 = 2.7\text{eV}, \tau = 3 \times 10^{-12}\text{s}) \simeq 8.12 \times 10^{-10} \text{ S.m} \quad (84)$$

and hence,

$$\begin{aligned}
\frac{\sigma_{sc}}{\sigma_m}(\gamma_0 = 2.7\text{eV}, \tau = 3 \times 10^{-12}\text{s}, a \text{ (nm)}) \\
&\simeq 1.25 \times 10^{-2} a \times (a - 1) \\
&\in [7 \times 10^{-3}, 7.5 \times 10^{-2}] \text{ for } a \in [1.4, 3] \text{ nm}
\end{aligned} \tag{85}$$

Therefore, we can conclude that for bundles with sc- to m-SWCNT ratio not in excess of 2 (statistically the case for unsorted SWCNTs) and $a \leq 3\text{nm}$, i.e. $D \leq 6\text{nm}$ it is consistent to model only m-SWCNTs as this should lead to a maximum 15% error in prediction – minimal compared to other experimental uncertainties. For $a \leq 1\text{nm} \Leftrightarrow d \leq 2\text{nm}$ the maximum acceptable ratio leaps to 70 – or 98.6% purity. In these cases the bundle can be modeled following equation (72) by replacing the global (visual) CNT density D_{NT} by an effective m-SWCNTs density $D_{mNT} = \rho_m D_{NT}$.

As a concluding remark for this section, it should be noted that gating, photocurrent and thermal effects cannot be directly simulated with our technique. Rather, these effects should be quantified theoretically or experimentally then implemented as a variation in the effective conductivity.

II.B.3.3) Multi-wall CNTs

The approach can be adapted to deal with MWCNTs with similar distribution schemes among MWCNT types and shells. The conductivity can be derived from the circuit models [107], [108] presented in II.A.4.2) given the equivalence highlighted in equation (30). It can be evaluated analytically if neglecting intershell coupling or numerically otherwise (with ADS [100] or the Carbon Nanotubes Interconnect Analyzer [111]).

In this section, we justify the necessary approximation for analytical solving then present our method of derivation. The DC conductivity is fully evaluated. The more complex calculation for the exact frequency dependence is outlined but not carried out here.

Drawing from II.A.4.2), we know the number of channels per shell to be:

$$N_{\text{chan}}(D) = \begin{cases} 2\delta_{m,typ}, & D < 3\text{nm} \times (1 + \delta_{m,typ}) \\ xD + y_m\delta_{m,typ} + (1 - \delta_{m,typ})y_{sc}, & D \geq 3\text{nm} \end{cases} \tag{86}$$

where $\delta_{m,typ}$ is the Kronecker delta, equal to 1 if the shell is metallic and 0 if the shell is semiconducting and, as previously set, $x = 0.0612\text{nm}^{-1}$, $y_m = 1.642$, $y_{sc} = -0.1836$.

Because MWCNT shells are only separated by $\delta = 0.34\text{nm}$, adjacent shells have similar diameters hence number of channels and conductivity. Actually, the difference in linear DC conductivity for two adjacent shells is given by:

$$\frac{\Delta\sigma_{lin}}{\sigma_{lin}}(D) = \frac{4\left(\frac{\delta}{D} + \left(\frac{\delta}{D}\right)^2\right) + \frac{y}{x}\frac{2\delta}{D^2}}{1 + \frac{y}{xD}} \quad (87)$$

and is less than 20% for metallic shells of diameters above 4nm. Hence, if all the shells at the base of the CNT are connected and excited in common mode, we can neglect the inter-shell conductance and capacitance in first approximation. This is confirmed, in [107], by calculations for an interconnect study rigorously led with the conductance at the maximum expected value and without it and the difference appears rather negligible. Then the linear conductivity of the nanowire equivalent to a MWCNT will be the sum of the linear conductivities of the shells.

$$\sigma_{lin,MW}(\omega) = \sum_{shells} \sigma_{lin,i}(\omega) = \sum_{shells} \sigma_{lin,0}(D_i)\zeta\left(\frac{f}{F_v(D_i)}\right) \quad (88)$$

We will describe a MWCNT by its external diameter D_{max} , its internal diameter $D_{min} \equiv \eta D_{max}$ and its number of shells N_{sh} . Since the spacing between shells is $\delta_{graph} = 0.34\text{nm}$, we have the following:

$$D_{min} + (N_{sh} - 1)(2\delta) = D_{max} \quad (89)$$

$$\begin{aligned} N_{sh} &= 1 + \left\lceil \frac{D_{max} - D_{min}}{2\delta} \right\rceil = 1 + \left\lceil (1 - \eta) \frac{D_{max}}{2\delta} \right\rceil \\ &= 1 + \left\lceil \frac{1 - \eta}{\eta} \frac{D_{min}}{2\delta} \right\rceil \end{aligned} \quad (90)$$

where $\lceil \cdot \rceil$ indicates the integer part (for numerical applications). η varies from 0.35 to 0.8 and can be assumed to be 0.5 in average [108]. Shells are statistically in a ratio of 1:2 metallic to semiconductor. Furthermore this is uniform over diameters. In this case, the average number of channels per shell is as follows [108]:

$$N_{\text{chan}}(D) = \begin{cases} \frac{2}{3}, & D < 6\text{nm} \\ xD + y, & D \geq 3\text{nm} \end{cases} \quad (91)$$

where $x = 0.0612\text{nm}^{-1}$, $y = 0.425$ and there is an overlap of definitions convenient when assuming $\eta = 0.5$. Otherwise, with a $1:\alpha$ ratio, we have on average:

$$N_{\text{chan}}(D) = \begin{cases} \frac{2}{\alpha + 1}, & D \leq 3\text{nm} \\ xD + y, & D \geq 3\text{nm} \end{cases} \quad (92)$$

Where $x = 0.0612\text{nm}^{-1}$, $y = \frac{1.642 - 0.1836\alpha}{\alpha + 1}$. Now, for shells in $\text{IE}_{\text{cst}} \cup \text{IE}_{\text{mix}}$, the DC conductivity can be expressed as:

$$\begin{aligned} \sigma_{\text{lin},0,MW} &= \sum_{i=0}^{N_{\text{sh}}-1} \sigma_{\text{lin},0}(D_i) = \sum_{i=0}^{N_{\text{sh}}-1} \text{MFP}(D_i) \frac{2N_{\text{chan}}(D_i)}{R_0} \\ &= \frac{4l_0}{R_0(\alpha + 1)} \sum_{i=0}^{N_{\text{sh}}-1} (D_{\text{min}} + i2\delta) \\ &= \frac{4l_0 N_{\text{sh}}}{R_0(\alpha + 1)} (D_{\text{min}} + (N_{\text{sh}} - 1)\delta) \\ &= \frac{4l_0 N_{\text{sh}}}{R_0(\alpha + 1)} \frac{(D_{\text{max}} + D_{\text{min}})}{2} \end{aligned} \quad (93)$$

This can also conveniently be expressed as a function of D_{max} and η only:

$$\sigma_{\text{lin},0,MW} = \frac{4l_0 \left(1 + \left[(1 - \eta) \frac{D_{\text{max}}}{2\delta} \right] \right) (1 + \eta)}{R_0(\alpha + 1)} \frac{D_{\text{max}}}{2} \quad (94)$$

It can then be verified that, for $\eta = 1$, we find back the expression of a SWCNT in $\text{IE}_{\text{cst}} \cup \text{IE}_{\text{mix}}$.

For shells in IE_{lin} :

$$\begin{aligned}
\sigma_{lin,0,MW} &= \frac{2l_0}{R_0(\alpha + 1)} \left(x \sum_{i=0}^{N_{sh}-1} (D_{min} + i2\delta)^2 \right. \\
&\quad \left. + y \sum_{i=0}^{N_{sh}-1} (D_{min} + i2\delta) \right) \\
&= \frac{2l_0 N_{sh}}{R_0(\alpha + 1)} \left(\frac{(D_{max} + D_{min})}{2} (xD_{min} + y) \right. \\
&\quad \left. + \frac{(N_{sh} - 1)(2N_{sh} - 1)}{6} x(2\delta)^2 \right) \\
&= \frac{2l_0 N_{sh}}{R_0(\alpha + 1)} \left(\frac{(1 + \eta)}{2} D_{max} (x\eta D_{max} + y) \right. \\
&\quad \left. + \frac{2N_{sh}^2 - 3N_{sh} + 1}{6} x(2\delta)^2 \right)
\end{aligned} \tag{95}$$

This can also be expressed as a function of D_{max} and η only:

$$\begin{aligned}
\sigma_{lin,0,MW} &= \frac{l_0 D_{max}}{R_0(\alpha + 1)2\delta} \left((1 - \eta^2)D_{max} + (1 + \eta)2\delta \right) \\
&\quad \times \left(x \left(\left(\eta + \frac{2(1 - \eta)^2}{3(1 + \eta)} \right) D_{max} + (1 - \eta)2\delta \right) + y \right)
\end{aligned} \tag{96}$$

As expected, for $\eta = 1$, we find back the expression of a SWCNT shells in IE_{lin} :

$$\sigma_{lin,0,MW} = \frac{2l_0 D_{max}}{R_0(\alpha + 1)} (xD_{max} + y) \tag{97}$$

For $D_{max} \gg \frac{2}{1-\eta} \delta \sim 1\text{nm}$, we have:

$$\sigma_{lin,0,MW} = \frac{l_0 D_{max}^2 (1 - \eta^2)}{R_0(\alpha + 1)2\delta} \left(\left(\eta + \frac{2(1 - \eta)^2}{3(1 + \eta)} \right) xD_{max} + y \right) \tag{98}$$

For the average case $\eta = 0.5$, $\alpha = 2$ this means that, for $D_{max} \gg 1.34\text{nm}$:

$$\sigma_{lin,0,MW} = \frac{l_0 D_{max}^2}{R_0 8\delta} \left(\frac{11}{18} xD_{max} + y \right) \tag{99}$$

This is similar to the result in [108] in the long range regime but still different as we did not approximate to an integral sum and only consider the distributed conductivity and model the contact resistance separately. If we assume the relaxation frequency to be the same for all shells, we simply have:

$$\sigma_{lin,MW}(f, D_{max}, \eta) = \sigma_{lin,0,MW}(D_{max}, \eta) \zeta \left(\frac{f}{F_{v,MW}(D_{max}, \eta)} \right) \quad (100)$$

Rigorously, the sum has to be made over the diameters:

$$\begin{aligned} \sigma_{lin,MW}(f, D_{max}, \eta) &= \sum_{i=0}^{N_{sh}-1} \sigma_{lin}(D_i) \\ &= \sum_{i=0}^{N_{sh}-1} MFP(D_i) \frac{2N_{chan}(D_i)}{R_0} \zeta(AD_i) \end{aligned} \quad (101)$$

where we have introduced $A = f \times \frac{2\pi l_0}{v_F}$ and thus $AD = u(D)$. The DC conductivity we calculated is still valid so the final equation will remain in the form:

$$\sigma_{lin,MW}(f, D_{max}, \eta) = \sigma_{lin,0,MW}(D_{max}, \eta) \zeta_2(f, D_{max}, \eta) \quad (102)$$

II.C) Implementation and validation

II.C.1) Implementation

The anisotropic bulk conductivity approach we developed and the model we derived can be implemented virtually in any software that allows the specification of such a quantity, directly or indirectly.

So far, we used two full-wave 3D electromagnetic simulation solutions. One is commercial, Ansoft HFSS 13.0 [90], the other, EMXD, is homemade software developed at XLIM. Both rely on the finite-element method (FEM) for solving the Maxwell's equations in the spectral domain. However the solving method is of no critical importance to the validity and applicability of the model.

EMXD was used to validate the approach since it allows more detailed specification of the electromagnetic properties, including a complex 3x3 anisotropic conductivity.

Coordinately using GMSH [131], an open-source mesh generator supporting ASCII script input, allowed systematic design and refined mesh control.

The model was then implemented into HFSS as a material that can be picked like any other. HFSS is widely distributed and used in the microwave community making the implementation of the model in this suite a significant contribution to the design of CNT-based devices. Design simplicity and the embedded data processing and parametric study abilities make it easier to test various complex structures.

II.C.1.1) Implementation in EMXD

EMXD is a finite-element-method full-electromagnetic 3D simulation solver developed at XLIM by Michel Aubourg. We use it in conjunction with an open-source mesh generator, GMSH [131]. GMSH and EMXD were used in a parametric study to compare the original hollow-tube approach to our effective medium approach because of certain technical specificities.

GMSH requires the user to define every point, line, surface and volume – making it more cumbersome than the latest commercial suites such as HFSS or CST where 3D modeling benefits from numerous standard shapes and transformations. The mesh points along lines also need to be defined by the user where commercial suites offer automatic convergence. However GMSH natively supports ASCII script input which allowed meshing quasi-identical structures with high control and reproducibility to prevent mesh-related artifacts or variations. This is also possible in HFSS/CST with VBA codes or interfacing to Matlab but would require more implementation time and is not guaranteed to provide the same control over the final mesh. This point is only critical when you compare presumed equivalent models – the hollow-tube and effective-medium models in our case.

EMXD supports geometrical symmetry planes rather than the more usual electrical and magnetic planes. Up to three orthogonal planes may be used to reduce the mesh size by a factor 8. It is thus a preferred choice when dealing with large meshes if symmetries can be identified.

The GMSH code for the monopole structures described in section II.C.2) allows the fully-parametric generation of arrays formed by any number of concentric hexagonal layers of aligned hollow tubes. It allows taking into account the symmetry planes for EMXD and

Booleans allow the choice of various options: open/closed tube tips, PML layers, shape of the air box, and, more importantly, equivalent bulk representation of the bundle. The code is not reproduced here as it is 1600 lines-long but a copy is available upon request.

EMXD now natively supports the definition of complex surface impedance – used for the hollow-tube model – and that of a 3D complex conductivity matrix. The numerical values need to be provided by an .exe file to EMXD when EMXD calls it. We reproduced the Fortran codes used to compile such a file in each case in Appendix 2.

II.C.1.2) Implementation in HFSS

Let us write $\varepsilon = \varepsilon' + j\varepsilon''$ and $\sigma = \sigma' + j\sigma''$ the anisotropic (matrices) bulk permittivity and conductivity respectively in the mesoscopic equivalent bulk material.

In HFSS, for a given material, the bulk conductivity σ can be defined as anisotropic (diagonal matrix only) and frequency dependent. However it cannot be given complex values. Moreover relative permittivity is used: $\varepsilon_r = \frac{\varepsilon}{\varepsilon_0}$.

Therefore we shall use the real part of the relative permittivity ε'_r and either the loss tangent $\tan \delta_\varepsilon = \frac{\varepsilon''_r}{\varepsilon'_r}$ or the real part of the conductivity σ' . They can all be defined as anisotropic and frequency dependent.

A generally admitted definition for the complex permittivity is as follows:

$$\varepsilon = \varepsilon' + j\varepsilon'' = K\varepsilon_0 - j\frac{\sigma}{\omega} \quad (103)$$

Comparison of simulation results between EMXD – where there is no ambiguity on defining complex conductivity – and HFSS, as well as the fact that only conductivity or loss tangent can be defined at once (the other quantity being deduced from the one picked), confirmed that this is used in HFSS.

Hence,

$$\varepsilon = \left(K\varepsilon_0 + \frac{\sigma''}{\omega} \right) + j\left(-\frac{\sigma'}{\omega} \right) \quad (104)$$

and therefore

$$\varepsilon_r' = \frac{\varepsilon'}{\varepsilon_0} = K + \frac{\sigma''}{\omega \varepsilon_0} \quad (105)$$

$$\tan \delta_\varepsilon = \frac{-\sigma'}{K\omega\varepsilon_0 + \sigma''} \quad (106)$$

For metallic SWCNTs, applying equation (65), we obtain:

$$\varepsilon_r' = K - \frac{\sigma_{lin,0} D_{NT} u}{\omega \varepsilon_0 (1 + u^2)} = K - \frac{\sigma_{lin,0} D_{NT} \tau}{\varepsilon_0 (1 + u^2)} \quad (107)$$

$$\tan \delta_\varepsilon = \frac{-1}{u \left(\frac{K \varepsilon_0 (1 + u^2)}{\sigma_{lin,0} D_{NT} \tau} - 1 \right)} \quad (108)$$

II.C.2) Theoretical validation

II.C.2.1) Application to dipoles of bundled carbon nanotubes

We propose to validate the equivalence of the anisotropic bulk conductivity model with the surface conductivity on hollow tubes model. To do so we applied both models to a dipole antenna configuration and solved those using both HFSS and EMXD.

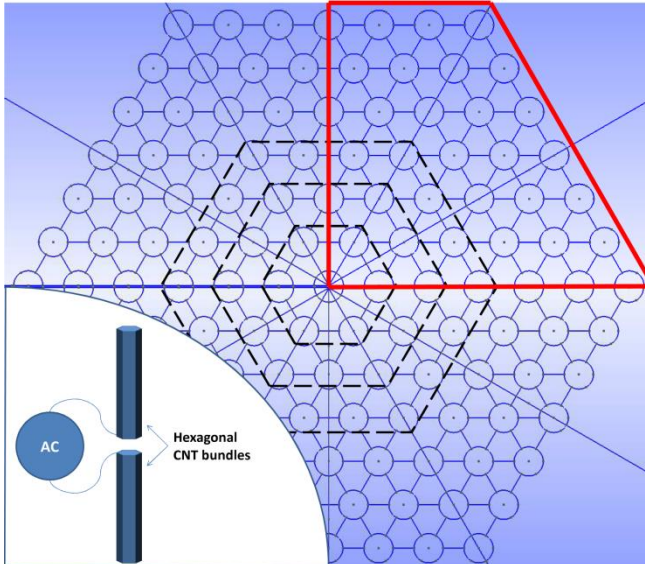


Fig. 19. Hexagonal structure used for the bundle definition ($N=6$). Each circle is the cross section of a CNT. The bundle is made of N concentric hexagonal layers of CNTs arranged around a central CNT. $N=0$ corresponds to a single CNT. $N=1,2,3$ are delimited on this figure. Two bundles are then arranged in a dipole as shown on the inset. An EM equivalent configuration is a monopole over a ground plane. We shall use this last configuration because it saves a factor two on mesh complexity. The resulting input impedance is twice lower.

A systematic study was led for dipoles of bundles of SWCNTs arranged in concentric hexagonal layers with an equilateral triangle lattice (cf. Fig. 19). In order to avoid any inconsistency in mesh generation, the geometrical structure was parametrically coded. It

includes a Boolean allowing switching from the hollow-tubes structure to the equivalent bulk structure, defined as a bulk cylinder of hexagonal cross-section tangent to the external tubes. All mesh conditions being defined similarly, the mesh surrounding the dipole is practically the same for both models making the comparison relevant even if the simulation conditions were to be imperfect.

Finally, compensation techniques have been developed for the hollow-tubes model. Indeed, using FEM, circular tubes need to be approximated by faceted tubes. We have opted for hexagonal tubes which match the perimeter of circular tubes at 95% approximately and allow similar tube-to-tube spacing in all directions allowed by the hexagonal bundle. However the perimeter loss has to be compensated for, either by changing the surface impedance by the same factor or by changing the radius by the inverse factor to obtain 100% of the perimeter. This second option is only applicable if the tube-to-tube spacing and tube radius are not critical. We have shown that it is true for our model as long as the density is low enough. Our simulation results show these two correction techniques are equivalent in the investigated cases.

II.C.2.2) Supporting results

We first validated both approaches by simulating the high-frequency input impedance of single-CNT-arms dipoles (cf. Fig. 19) as solved by Hanson with the method of moments (MoM) [10]. Bulk and hollow single CNTs were simulated under both HFSS and EMXD. As reported Fig. 20, the results agree well with previous predictions. This will allow us to deal with less intuitive structures that cannot be solved through MoM.

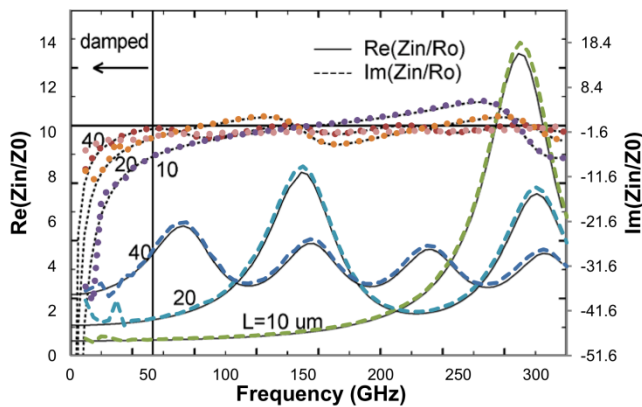


Fig. 20. Input impedance of single-CNT dipole antennas as a function of frequency for various CNT lengths. Our results (color dashed lines and big dots) are superimposed over the reference results (black continuous lines and small-dot lines) from Hanson. Normalized at $Z_0=10\text{k}\Omega$.

Next, we work with the electromagnetically equivalent monopoles to cut the mesh complexity by a factor two – this also divides the input impedance of the antenna by two. The excitation is carried by a 50-ohm lumped port and is swept in frequency. Fig. 21 shows the reflection coefficient $|S_{11}(f)|$ of the monopoles for 0 to 6 layers of CNTs (1 to 127 CNTs) in the case of 40 and 80 μm -long SWCNTs. The dashed curves are the results from the hollow-tube model while the continuous ones correspond to the bulk model. As expected the two models return perfectly matched results both in terms of frequency and amplitude for all 13 configurations tested. This match is especially relevant as we work on resonant structures where the slightest change can be spotted easily. This is supported by Fig. 22, where we show how the correction techniques affect the results. For the two-layer 80 μm -long configuration we also plotted a dotted curve corresponding to simulating distinct bulk nanowires with the corresponding conductivity. This also appears equivalent (Fig. 21), further supporting our approach by validating the intermediary step.

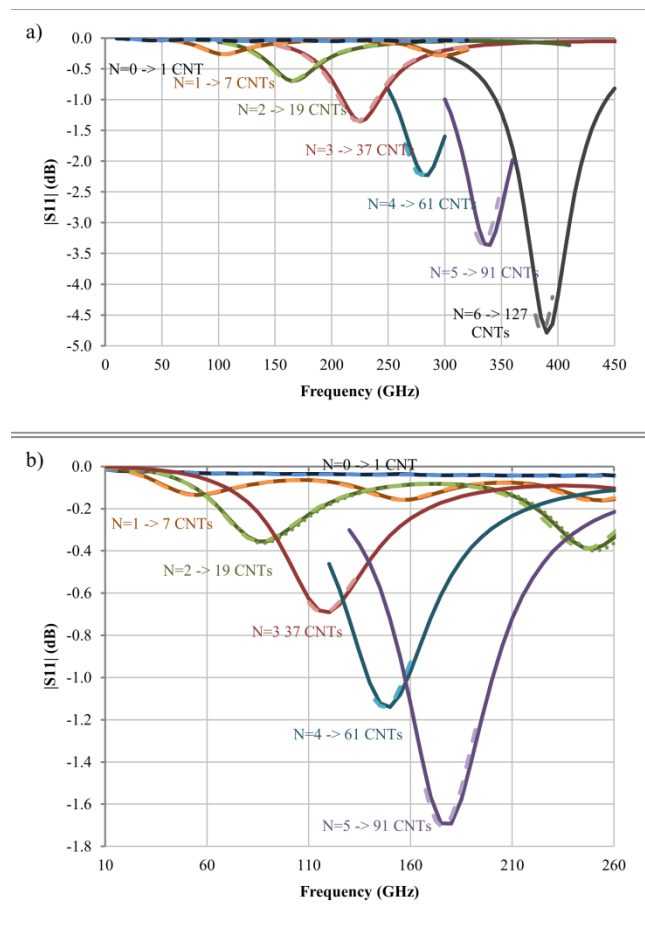


Fig. 21. Reflection coefficient $|S_{11}(f)|$ of the dipoles for 0 to 6 layers of CNTs (1 to 127 CNTs) in the case of 40 (a) and 80 (b) μm -long SWCNTs. The two models show excellent agreement for all 13 configurations although we are studying the very sensitive resonance of a monopole. The CNTs are spaced 8.12nm center-to-center and have a radius of 2.36nm.

Interestingly, as the number of CNTs in the bundle increases, the resonant frequency shifts towards higher frequencies. This is accurately predicted by both models and will be

treated in more details in section IV.A). This kind of effect has been observed at higher frequencies with the different approach developed in [19] for the special case of circular bundles.

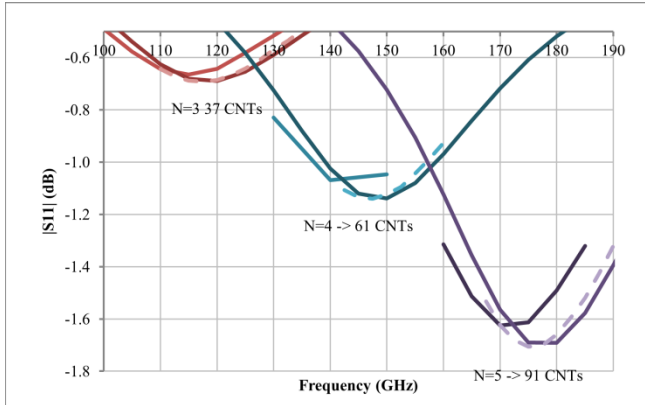


Fig. 22. Sensitivity of the structure. Uncorrected (left-shifted curves) VS corrected hollow-tube model and bulk model. As little as 5% variation on the perimeter of the tubes shows a difference on the resonance, while the bulk model agrees to near perfection to the corrected model.

Another test was conducted and is presented Fig. 23. Bundles of the same external shape and size, made up from the same number of CNTs – and hence having the same D_{CNT} and thus the same bulk equivalent – were simulated with CNTs of various radii – and thus different inter-tube spacing. The variations registered are in the order of the numerical error of the solver as can be seen on the two continuous curves which are two runs for the same bundle with different frequency calculation points. Therefore we can conclude that the nanostructure of the bundle does not affect the result, which validates our approach. Additionally, the near-field emission plots (Fig. 25) show almost no difference between the two models. In fact, the impact of the continuous medium approximation is only seen in the radial section of the bundle itself (Fig. 24). It is also interesting to note that skin effect appears in the bundle for both models (see color version online) which comforts our approach and is in agreement with previous predictions [98].

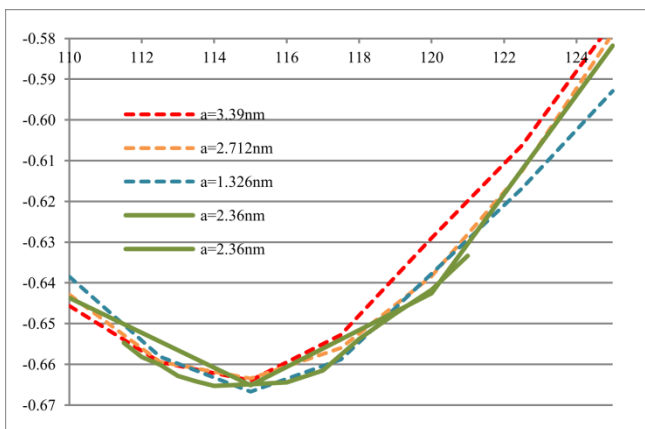


Fig. 23. Adaptation peak as a function of CNT radii with a bundle size kept constant ($L_{cnt}=80\mu m$ $N=3$). Changing the radius of the tubes by a factor two or three does not affect the resonance as long as the bundle global shape and size are maintained. This confirms that all these configurations can be modeled by the same bulk block.

II.C.2.3) Comparative performance

The proposed approach proved not only equivalent, but much more efficient than the hollow-tube model for CAD and simulation. Indeed the solving time and memory use are drastically reduced when using the bulk model. For instance, using two of the four emulated cores of an Intel Core i7 M620, simulating the structure and plotting the field for Fig. 25 at four different frequencies required nine minutes and approximately four hundred megabytes of RAM with the bulk model, seventeen times quicker and 5 times lighter than the 153 minutes and two gigabytes of RAM needed to solve it using hollow tubes. It also avoids producing singularities in the bundle, limits the dynamical range necessary to compute the field and reduces the overall complexity. Using the hollow-tube model, the 127 CNTs configuration exceeded the limits of computation on our laptop – two days for a few frequency points because of the use of swap memory – while the bulk model readily enables us to simulate billions of CNTs.

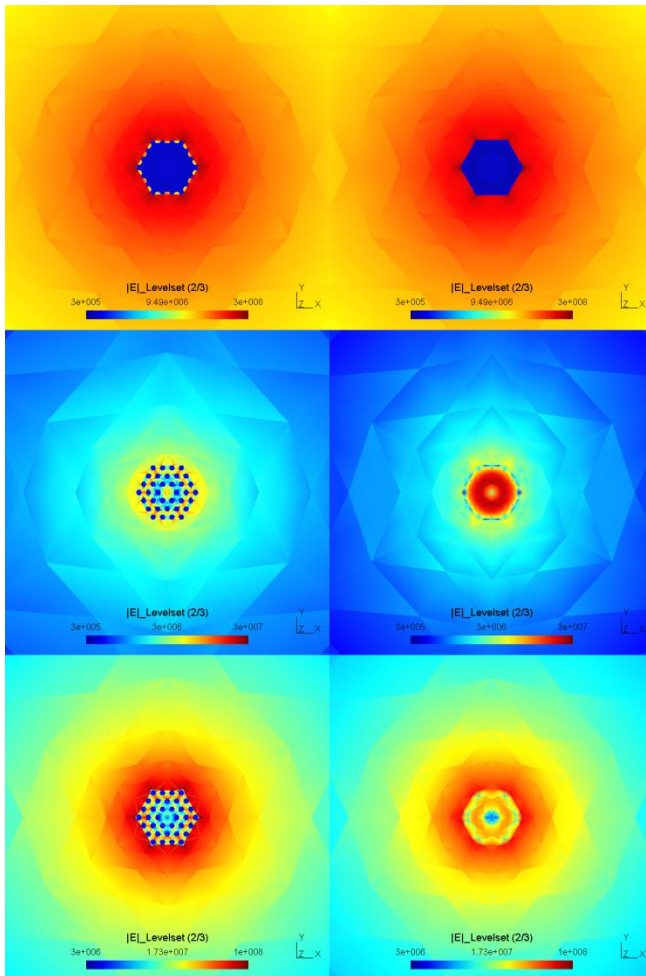


Fig. 24. Electric field magnitude at 120GHz in the cross section (normal to Z axis) of the bundle presented in Fig. 25. Top to bottom: base (metal plane), middle and tip of the bundle. Left: hollow-tube model. Right: bulk model. The scales are logarithmic and identical for tube/bulk comparison but different from top to bottom to stress the field variations in each case. Although the field distribution in the tubes and bulk bundle is different, a skin effect can be observed for both (the field is less intense at the core) and the resulting external fields are similar.

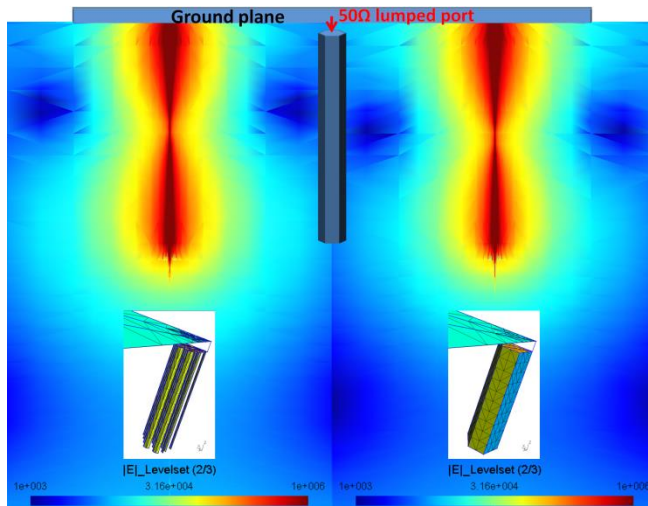


Fig. 25. Electric field magnitude plots for a 3-layer 80 μ m-long bundle of CNTs (half dipole) at 120GHz (close to resonance). Section in the XZ plane. Left: hollow-tube model. Right: bulk model. The insets represent the structures actually simulated (radius magnified by 1000, port length by 10).

II.C.2.4) Conclusion

These simulations thus validate the equivalence of our approach to the hollow-tube model in the frequency range under consideration (below optical transition) and its relevance in addressing the applicability issues of the hollow-tube model in modern CAD software.

II.C.3) Experimental retrofitting

II.C.3.1) Application to a microstructure from literature

II.C.3.1.1) Application to a microstructure

In order to validate the practicality of our approach, we applied the proposed bulk model to a microstructure fabricated and characterized by Yang *et al.* [122]. In this reference, Yang models the CNTs as a simple resistance, incorporated as a cylinder with the corresponding resistivity.

We in turn, reproduced the fabricated structure in HFSS from their supplemental information. It is a simple coplanar waveguide (CPW) with the central line (signal line) cut by a twenty-micrometer gap to impede signal propagation. CNTs are then used to bridge the gap as a means to measure their characteristics. Fig. 27 presents our simulation results (complex S_{21} parameter) for the empty CPW, superimposed over theirs and the measurement data, as a conclusive check for initial match, without any CNT involved.

The next step was to insert the proposed bulk model in the simulation for the structure bridged with CNTs. A contact resistance exists when ohmic contact is established between

CNTs and metal. To model this, where there is surface contact with the bundle, we insert a material of proper conductivity in the Pd-Au thin film constitutive of the signal electrodes (illustrated Fig. 26).

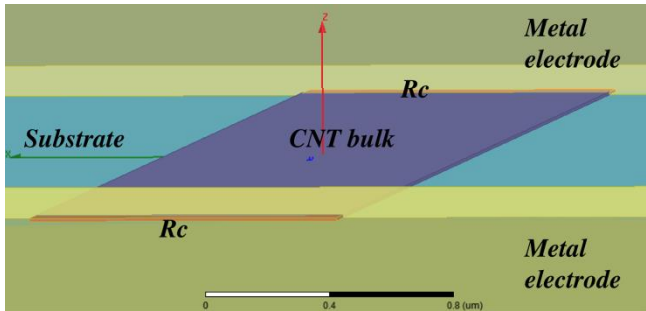


Fig. 26. Bridging the signal line with the CNT bulk model. The yellow boxes are the metallic electrodes. The purple box in the center is the CNT bulk. The red boxes at each end are the material with specific conductivity used to model the contact resistance. They are included in the electrodes and the direct contact of the bundle to the electrodes is only through them. All this lies on a silicon substrate (green).

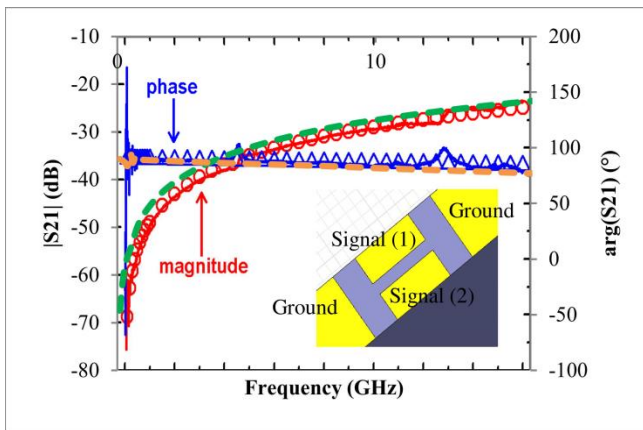


Fig. 27. 20 μm -gap coplanar waveguide structure, from Yang 2011 (cf. inset). Measured (solid lines) and simulated (dashed lines for our results, triangles and circles for Yang's) phase and magnitude of the S21 transmission parameter from one side of the gap to the other for the empty structure. Here the model is not yet under test. The results show good agreement.

Regarding the bundle itself, we needed to use phenomenological constants adapted to the CNTs used by the experimenters – even more so that the tubes properties were different from the first series of sample to the second by a factor 4 approximately. Based on the resistivity tables provided [122], we retained $\gamma_0 = 2.7 \text{ eV}$ and $\tau = 6.97 \cdot 10^{-13} \text{ s}$ for the single CNT and $\tau = 1.84 \cdot 10^{-13} \text{ s}$ for the ten-CNT array. These values match the usual range for CNTs [17], [84]–[86].

From the same tables we deduced a contact resistance of 15.7k Ω for the single CNT and 80.2k Ω per tube for the ten-CNT array. This is in accordance with usual experimental values [11], [132], [133].

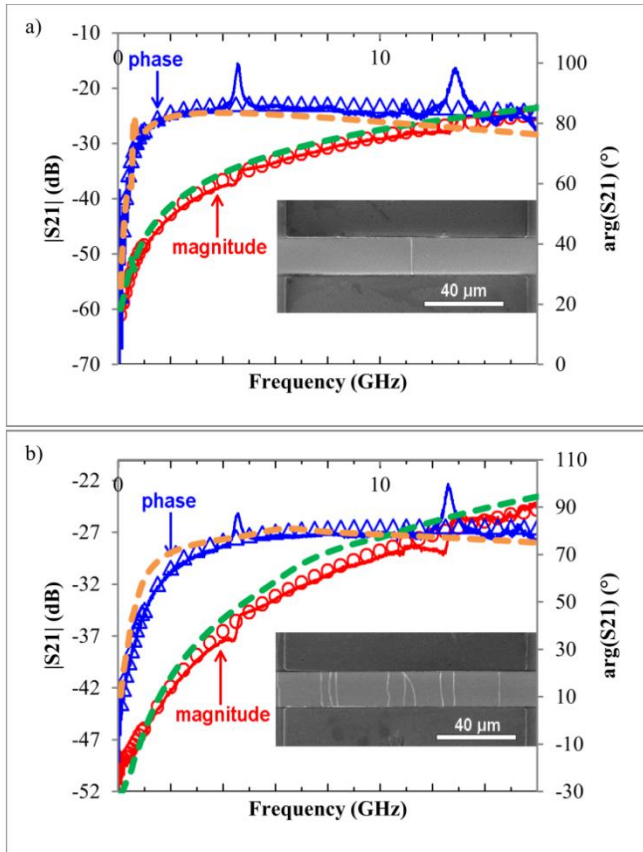


Fig. 28. 20μm-gap CPW with (a) one and (b) ten CNTs as shown on the SEM image in each inset. Measured (solid lines) and simulated (dashed lines for our results, triangles and circles for Yang's phase and magnitude of S21). The results show good agreement both in phase and magnitude.

II.C.3.1.2) Results

Our simulation results match experimental data on both available configurations, as illustrated Fig. 28. As explained in [122] the peaks on experimental data are systematic error from the measurement apparatus and should therefore not appear with the simulated structure. The applicability and reliability of the model are thus confirmed.

To our knowledge, this is the first full EM simulation of a microstructure interacting with a semi-classical model of CNTs. The versatility of our approach and its combined use with CAD software should enable intelligent design of CNT based electronic devices.

Although these are encouraging results that the CNT model we based our work on would be true, higher frequency measurement and careful design will be necessary to find a measurable resonance due to the CNT properties. Measurements of kinetic inductance realized on single CNTs [9], [115] show us that it may be possible.

II.C.3.2) DEP samples

Gold coplanar waveguide lines with an optimized gap were designed on a high resistivity silicon substrate. The gap was bridged with SWCNTs aligned by dielectrophoresis (DEP) with the help of Hong Li and Chin Chong Yap (cf. Fig. 29). The samples were then measured with CPW Infinity probes connected to a Vector Network Analyzer on a Cascade Microtech probe station after TRL calibration.

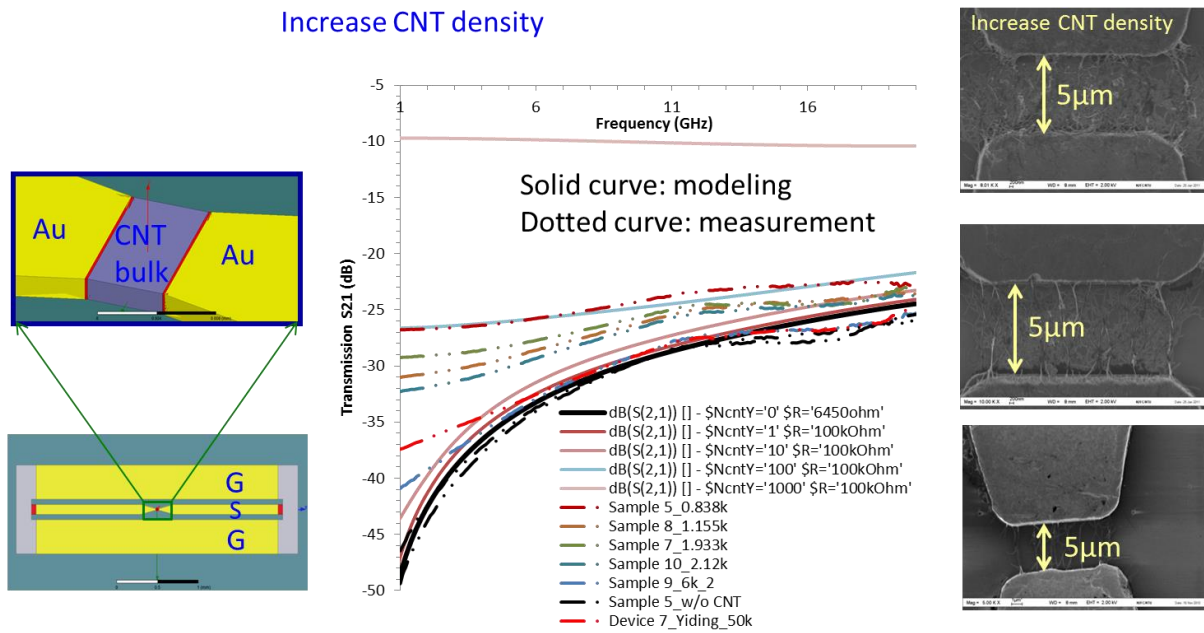


Fig. 29. From left to right: Layout of the simulated and fabricated structure; S21 parameter measured and fitted for different number of CNTs and contact resistances from 1 to 20GHz; SEM images of the CNT bridged gap of a few samples.

The bulk model was used to retrofit the curves with different values of the contact resistance (implemented as the conductivity of the red blocks on Fig. 29) and number of CNTs in the block of CNT bulk (purple). Distinguishing the exact number of CNTs participating in the conduction for these samples was rendered arduous by the bundling of CNTs in ropes.

To help the user analyze the images, a Matlab code was written to enhance the SEM images by post-processing. Options include thresholding, rescaling of gray values and adding artificial colors to artificially extend the dynamics in the image. The code is reported in Appendix 3.

II.C.3.3) Topped-CNT samples

Waileong Chow fabricated samples of topped CNT arrays bridging a CPW gap as shown on Fig. 30. The retrofitting was done with circuit model to save calculation time. Additional verifications were done using the bulk EM model for CNTs. Although retrofitting could also be done using this technique, it makes more sense in terms of required calculations to perform it using a circuit model. However, full-wave simulation allowed us to verify that some assumptions made for the circuit model were correct such as the depth of the layer participating in the conduction (cf. Fig. 31).

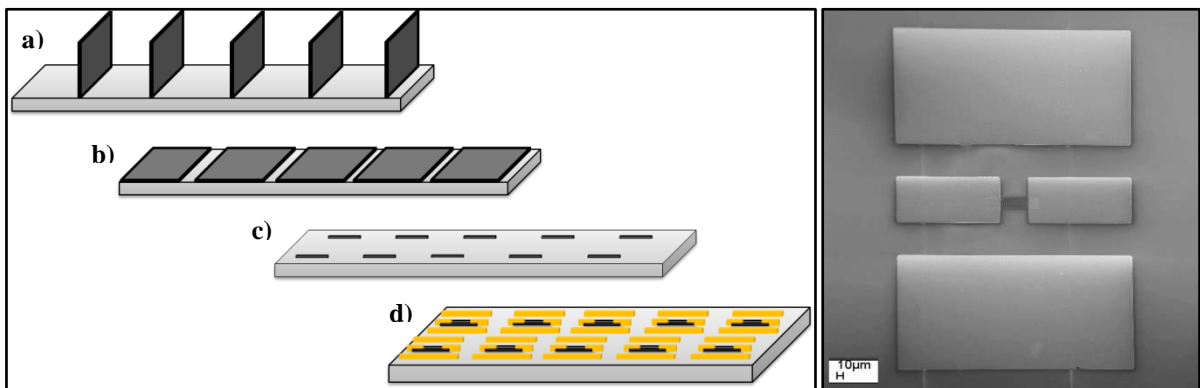


Fig. 30. Wai Leong Chow's fabrication process flow and fabricated structure; right: (a) as-grown vertically aligned CNT film, (b) horizontally aligned CNT film, (c) plasma-etching-patterned horizontally aligned CNT film, and (d) GSG electrodes formed on patterned horizontally aligned CNT film; left: SEM image of the fabricated horizontal CNT film contacted by GSG electrodes.

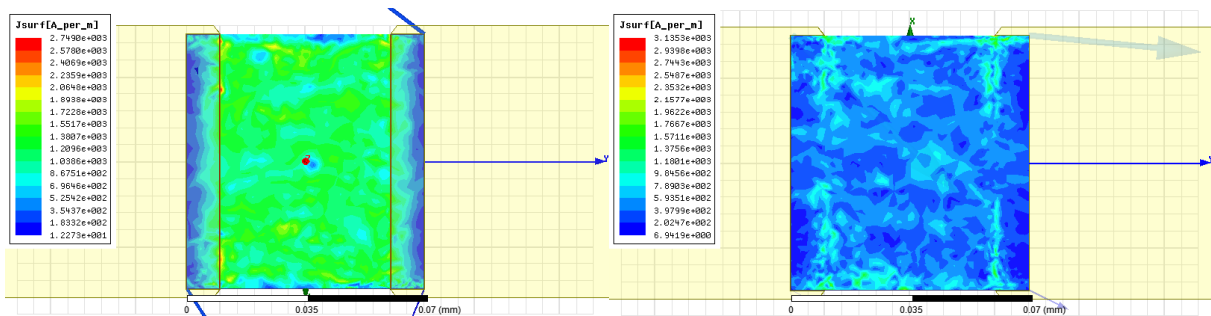


Fig. 31. Top and bottom view of the currents in the topped CNTs showing the prevalence of the top layer in transmission.

II.D) Conclusion on simulation techniques

In this chapter we have exposed a practical approach to modeling large quantities of nano-objects and their integration in micro and nanoelectronic devices at frequencies ranging up to few THz. We have applied this method to find a general form of the proposed anisotropic bulk model. Then we have derived a model for SWCNTs.

This model readily solves most of the problems encountered in CNT simulation and has been implemented in two different simulation solutions. 3D full-wave simulation of up to 127 CNTs has been conducted and proved the equivalence of the model to the more rigorous one it is derived from. These numerical results account for most effects and have been validated by comparison with MoM calculations found in literature.

Finally, the efficiency and practicality of the approach has been proven by the full 3D EM simulation of a microstructure comprising of CNTs as realized and measured experimentally. This new approach to modeling nanotubes and nanowires therefore enables the systematic computer assisted design and performance prediction of high-frequency components and devices based on these novel materials and their composites in commonly used and commercially available simulation solutions.

Although our newly derived bulk approach is the most versatile for RF devices design, it and the pre-existing CNT simulation methods offer various levels of validity range, precision, versatility and performance – as summarized in Table 3. These techniques should be seen as complementary rather than competing. Each is better suited to a certain type of application. The color coding outlines the desired characteristics for our application. To evaluate the performance in terms of computation, we rely on typical calculations for each application.

Table 3. Comparison of techniques of EM simulation of CNTs for antenna design and simulation

Technique	Validity range	Model precision	Versatility	Computational cost	Limitations	Recommended for
Circuit	Below transition, SWCNTs and MWCNTs	Approximate values for components	Need to derive for each structure.	Laptop, quasi instant	No radiation, ideal excitation	Ideal simple structures with arrays: transmission lines, monopoles
Bulk	Below transition, SWCNTs, adaptable to above transition,	Semi-classical + Maxwell	Use any EM solver+3D modeler. Draw a block and assign the appropriate	Laptop/Desktop, rather low memory usage and fast calculation. 1 freq point:	Cannot model nanoshape related effects (field-emission?)	Arrays of CNTs, CNT-based microelectronics and antennas

	MWCNTs		material.	2min, 1CPU, 400MB		
Hollow-tube	Idem	Idem	Idem but tedious for multiple CNTs. Issue with multiple scales (but IE-FEM in HFSS 15 could help).	Laptop/server, high memory usage for each extra CNT. 37 CNTs, 1 freq. point: 38min, 1CPU, 2GB	Size of the structure	Simple structures to validate effective medium assumption
Combined EM-QM	Small atomic structure + classical surrounding	Schrödinger/Maxwell	Need to develop own simulation tool.	Uncommunicated but judged high-cost [81], [82]	Size of the CNT structure	Few-CNT structures with larger environment
SIESTA (based on DFT)	Any small atomic structure but DC although possible techniques for AC	Schrödinger	Code atomic structure. Issue with multiple scales.	Heavy calculation on server (hours on tens of CPUs)	Size of the atomic structure	Few-CNT structures at DC, contact resistance, tunneling
TDDFT	Any small atomic structure	Idem	Idem	Extremely heavy	Idem	Idem but frequency dependent

Most of the time, the best approach will be to combine the simulation methods. For instance, to include effects that cannot be fully analytically studied and implemented in our approach like specific contact configurations, a DFT study of the influence of a few parameters can be done then implemented accordingly.

I did not work on the DFT method myself but collaborated with Tianqi DENG, a doctoral student in the group of Professor Haibin SU, Division of Materials Science in NTU. The goal was for him to study the influence of certain properties of the CNT-metal and CNT-CNT contacts which may require quantum treatment. I would then implement this as a specific material at contacts in FEM simulation – as I have done with the simplified case of Landau-Büttiker contact resistance [92], used in [8] by P.J. Burke, or by fitting with empirical values (cf. section II.C.3)). A typical system calculated using SIESTA/TranSIESTA [73],

[75], with one 2-nm-long CNT – too short for antennas but long enough for a QM contact modeling – between two gold leads takes 3~4 hours for one I-V point with 24 CPUs in NTU’s HPC. The required memory per CPU is around 1GB – this being largely dependent on the number of atoms and the desired accuracy. In contrast, using conclusions drawn from the SIESTA simulation, millions of CNTs long of tens of micrometers placed in a microstructure can then be simulated in matter of minutes on a simple laptop with the bulk approach.

Another example would be the process flow presented in Fig. 32 for the design of a CNT-based antenna using the original hollow-tube model, the bulk model and the circuit model. We have just covered the two first steps of this scheme and will follow the rest of the steps in III.D) to design electrically-short antennas made from SWCNTs. Indeed, the results produced to validate our approach show that a CNT-based antenna resonance needs to be tailored and we will need to systematize our study to draw design rules and trade-offs.

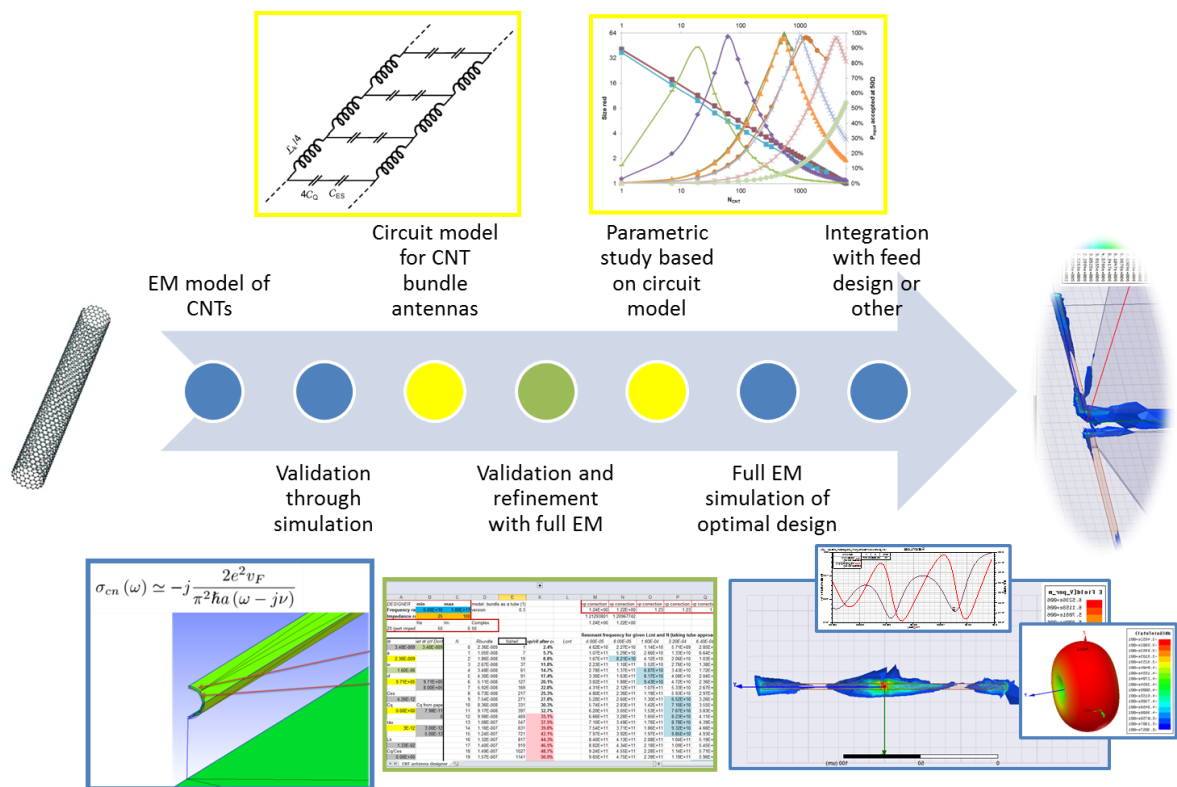


Fig. 32. Multi-model antenna design process flow.

Chapter III) Development of CNT-based electronics fabrication techniques

CNT-based RF devices are still in their prime age and most of the most advanced fabrication techniques each appear to be shared amongst but a few research groups. Indeed instructions and recipes are often published slightly incomplete. Additionally, the sensitivity of CNT-based electronic devices and antennas on the variations of the nature of the CNTs is drastically more stringent than for earlier works on polymer reinforcement or where MWCNTs are used for simple metallic properties or for their high aspect ratio as field-emitters.

Investigating, reproducing and adapting published fabrication techniques is therefore a necessary step to find the suitable material for our application and understand the real underlying technical challenges and opportunities.

We specifically will address the need highlighted by the lower cut-off frequency in the Drude conductivity of CNTs to produce high-quality straight CNTs to enhance the plasmon lifetime. To this end lattice-aligned CNT growth needed to be developed in CINTRA; on top of the increased fabrication and characterization possibilities, when comparing reported values or checking some of the most significant advances in CNT electronics recently [1], [3], this process appears to be the most adapted for high-quality SWCNTs. Vertical arrays and their derivatives remain an interesting proven option for electromagnetic devices although they have mostly been used for their anisotropy and metallic properties (e.g. [134]).

We start by reviewing some conventional fabrication techniques in the scope of CNT-based devices then expose the CNT growth and deposition techniques we developed and used in CINTRA.

III.A) Conventional fabrication techniques

A number of conventional techniques have been studied and mastered with the help and training of the team, colleagues and staff in CINTRA/NTU EEE. This technical experience was an invaluable asset to conceive the advanced designs presented in Chapter

III). The use of these techniques has been explored and tested for various structures integrating CNTs.

III.A.1) Patterning

In our application, patterning techniques are essential for the fabrication of devices following initial designs. The two main features to pattern are the CNTs or their catalyst and the electrodes. The process order determines whether some techniques are applicable or not. For instance, once vertical CNT arrays have been grown they will get denser if submersed in a solution (see e.g. [135]) due to capillary forces. This is inconvenient for structures like the monopole antennas described in section IV.D). Therefore any wet process should be conducted before growth in this case. However for interconnects, dense bundles can be preferred and then, as in the toppled CNT structures described in section II.C.3.3), solvent will be used to make the CNT walls denser and topple them.

III.A.1.1) Selective-masking-based techniques

III.A.1.1.1) Photolithography

Photolithography is a patterning technique based on light-induced chemical differentiation of a polymer – the resist. The resist areas exposed to UV light are easily washed away with the developer (a solvent) contrarily to the unexposed ones – or inversely depending on the use of a positive or negative resist. An optical mask is used for patterning. It is fabricated by direct laser lithography on special metal-covered glass plates. The design is created with CAD software and exported to .gds or a similar file type. The technique is easily scalable. The equipment used is a mask aligner which integrates a UV lamp, a mask holder and a sample holder with relative XYZ tilt motion and two microscopes allowing precise alignment of the patterns on the sample which can be essential for a multistep process.

The theoretical optical resolution limit (diameter of the smallest point resolved) is $2.44\lambda N$. This is $1\mu\text{m}$ for $\lambda=370\text{nm}$ and $N=1.1$. Achievable resolution limit on our equipment is indeed approximately $1\mu\text{m}$. The resolution limit of the mask fabrication facility in NTU is $2\mu\text{m}$ however but $1\mu\text{m}$ -resolution masks can be fabricated by outsourcing. The resolution also depends on the resist and the recipe used. The development is usually done with an approximate time using visual clues. Indeed, unmonitored variations in the mask aligner's UV lamp intensity lead to variations in the process while the unreacted developer concentration in

solution decreases when developing a few samples in a row. Non-transparent substrates such as Si-SiO₂ are more convenient because color changes arise (from green to pink) which are easier to note than slight transmission variations in the case of quartz and resist which both appear uncolored transparent.

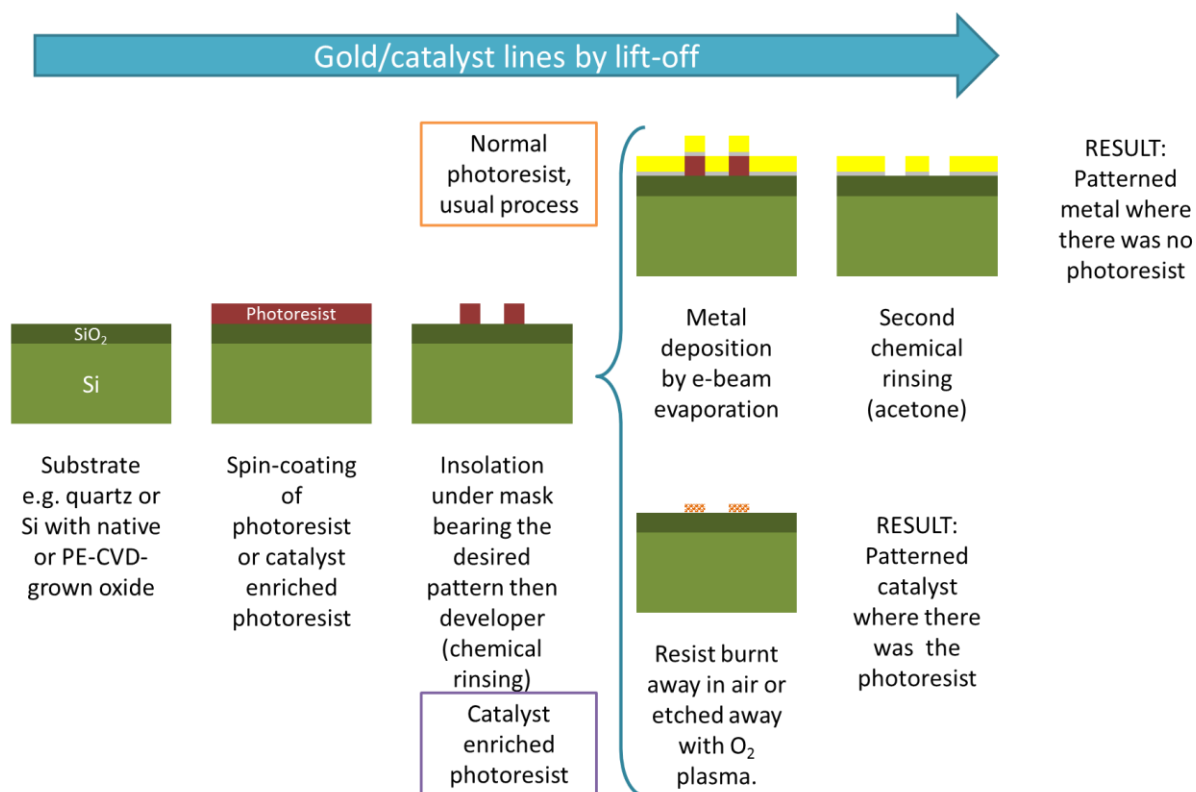


Fig. 33. Two photolithography processes.

The resist we use is AZ-5214. It is very special in that it is a reversible resist – it can be used both as a positive or negative resist depending on the recipe. In the case of electrodes fabrication and catalyst line patterning, we usually use bright-field masks with negative photolithography. For the catalyst experiments described in the next section both negative and positive recipes were used: negative for classical deposition of metal or other catalyst and positive for the direct fabrication of catalyst lines made of enriched resist. Both processes are exposed on Fig. 33. The experimental details can be found in Appendix 5.

III.A.1.1.2) Shadow mask

Shadow masking simply consists in protecting some parts of the sample by affixing a physical mask onto the sample before depositing a new layer by projection (e-beam deposition, spray...). When the mask is removed the pattern is formed. In CINTRA, the supplier we use offers down to 50- μ m resolution on 200 μ m-thick metal masks. One

additional constraint, as compared with photolithography, is the mechanical connection of all parts which makes it unsuitable for CPW structures where the central conductor would have to be manually aligned with respect to the ground unless the mechanical connection is made on a part that can be later removed for instance using gold etchant or cutting the substrate. Shadow masks with much higher precision (equivalent to photolithography or e-beam lithography) can be obtained by using a better laser cutting tool or advanced processes such as a silicon mask with KOH defined thin membrane which is then patterned by resist-based lithography followed by Reactive Ion Etching (RIE) to open the windows.

III.A.1.1.3) Polystyrene beads

Polystyrene (PS) beads could be used to define an array comprising large numbers of vertical CNT bundles with radius smaller than the photolithography resolution limit or a bundle/array of low density thanks to the nanostructure of its cross section. On Fig. 34 we show the typical arrangement of the PS balls after deposition. The shape of the interspaces is defined as a three-pointed star and they form circles with the neighbor interspaces which should yield a high robustness for high aspect ratio structures as we want to achieve for vertical monopoles. The density can be tuned through the radius r of the PS balls deposited; many sizes can be bought ranging from 100nm to micrometers. However the spacing cannot be controlled independently of the size.

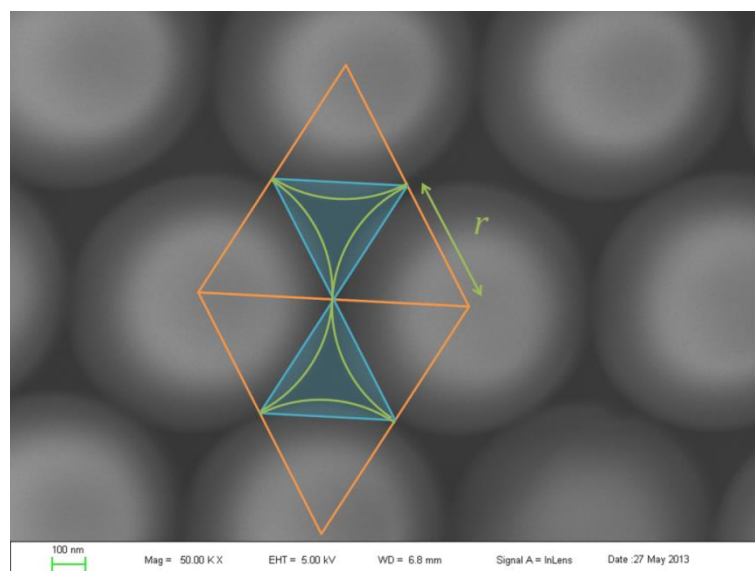


Fig. 34. Polystyrene (PS) balls of uniform radius r can be deposited as a dense monolayer film where they arrange with maximal density in a periodic diamond structure as illustrated here. The area delimited by green lines is not covered and a metal catalyst can then be deposited. SEM image courtesy of Aliénor Togonal (CINTRA).

Alternatively, the beads can serve as a mask for the deposition of a sacrificial layer before removing them and uniformly depositing a metal film. Then by attacking the sacrificial layer, metal would be left only in the disks. In this case spacing and radius of the bundles can be controlled separately. Indeed the center-to-center spacing will be defined by the original radius of the PS balls deposited. However, the balls radius can be reduced by RIE while retaining their original lattice position which would define the eventual radius of the catalyst disks created.

III.A.1.2) Direct writing

III.A.1.2.1) Inkjet

Inkjet printing is a versatile and cheap fabrication method for electronics. It can be used on a variety of substrates including flexible ones (paper, kapton). Interesting concepts have been demonstrated in Manos Tentzeris' group [54], [136], [137]. Recent results include the demonstration of building blocks for phased-array antennas [138], [139].

In CINTRA/NTU EEE a research-purpose inkjet printer can be accessed and offers full control over most printing parameters such as the nozzles used in the cartridge, heating capability for the substrate and the ink or debit control. Lowest reproducible resolutions achieved on metal electrodes are around 25 μ m while custom-made nozzles and wettability studies could allow further refinement. The potential printable materials are unlimited, especially for metals which can be prepared as nanoparticles in solutions then thermally cured after deposition. The number of validated inks sourced in CINTRA is currently limited to two: Sébastien Pacchini who took charge of the equipment uses silver ink (0.5 – 2.10⁶ S/m) and a DWCNT ink from CIRIMAT (CNRS, Bordeaux).

In an effort to fabricate samples to characterize photocurrent in CNTs, we printed microstrip line gaps compatible with a time-domain spectroscopy characterization setup in Cesare Soci's laboratory. The electrodes are made of silver ink and the CNTs from the DWCNT solution from CIRIMAT. Because these could be more suitable for photocurrent CNT inks were also prepared from high-purity semiconducting SWCNTs from NanoIntegris using ethylene glycol then dimethylformamide (DMF) as solvent. These sc-SWCNTs were bought as a flake of condensed short CNTs. A piece of the chip was weighed then put in the solvent. Probe sonication at full power was applied to the ink without any other addition of

surfactant to preserve the electronic properties of the CNTs. However the obtained suspension is not very stable because the CNTs get entangled one with another. After being stored for a while the CNTs aggregate forming a black cloud in solution. Initial tests on printing were inconclusive as too few CNTs were deposited to form a film.

To remedy to this a shortening of (SW)CNTs can be achieved by chemical cutting using a mixture of sulfuric and nitric acid at low temperature as reported in [140] and done at CIRIMAT. This reduces the bundling of SWCNTs in ropes and hence allows an easier dispersion in solvents into a stable solution. It prevents nozzle obstruction, these having 20 μ m-wide openings. However the CNT films rely on intertube tunneling for transmission over distances longer than the CNTs themselves. In this case, the shorter cut CNTs make the film they form less conductive than uncut CNTs deposited with the same density. This is further illustrated in the description of the spray technique that we used with our CNT inks because the nozzle size was better adapted.

III.A.1.2.2) Laser writing

Laser writing and cutting can be used in the fabrication of a variety of structures. In particular the photolithography mask is fabricated by laser ablation of metal in the desired sections of a metal-covered glass plate. The shadow masks are realized by laser cutting. The 50- μ m resolution limit is certainly due to the aspect ratio of the slits and the non-optimal laser cutting process. 100- μ m-thick metal masks exist while ultra-fast (femtosecond) laser cutting would prevent laser energy dissipation through heat and therefore improve the cut quality.

Lasers can also be used to selectively remove CNTs. Here again, the faster the laser the better the cutting. Interesting examples of CNT structures realized by laser ablation of CNTs then densification by capillarity can be found in [135].

III.A.1.2.3) Electron-beam lithography

Electron-beam (e-beam) lithography is often used to realize CNT FETs because it allows finer resolution than commonly available photolithography thanks to the much shorter electron wavelength. It also has the advantage of being a direct -writing technique. Designs can thus be edited almost on the spot which allows rapid prototyping. Although the technique is not viable on an industrial scale, advanced industrial mask aligners allow the fabrication of similar resolutions by the much more productive photolithography.

It uses a photoresist – most often PMMA. Exposure is realized using an electron beam scanned in XY. In NTU, we have access to two different e-beam writers. One is in the Cleanroom 2 in EEE while the other is in a normal lab in SPMS and managed by Prof. Cesare Soci's group. Resolutions down to 15-100nm can be achieved. However the writing area needs to be relatively small because the exposure scan is a long procedure. An additional constraint is the thickness of metal that can be deposited in the windows thus opened. Indeed, for frequencies of a few tens of gigahertz, the skin depth is in order of 1µm and it is difficult to achieve such metallization thicknesses in slots ten times thinner. Usually PMMA is used in thinner layers than AZ is for photolithography. The resolution is also limited by electron diffusion if the resist is thick. Therefore we have preferred to avoid using this technique. If such resolutions were necessary in specific parts of a design, e-beam lithography could be coupled to photolithography to create larger patterns with the latter completed with finer patterns from the former.

III.A.1.3) Stamping

Microcontact printing technique is an application of PDMS soft lithography. This is a straight forward method to fabricate micro/nanostructured surfaces in a scalable way and is roll-to-roll compatible. In this method, a master of PDMS (polydimethylsiloxane) is used as a stamp to print some patterns on the surface of a substrate. An ink (such as CNTs, metal ions in solution, polymers but also proteins, reagents, cells...) is first poured over the surface of the stamp of PDMS. Once coated with a thin layer of ink, the stamp is pressed on the surface of the substrate creating a conformal contact. The ink is then transferred from the stamp to the substrate where direct contact is applied, leaving behind a pattern on the surface of the sample.

Adapting from the already demonstrated transfer technique [141], [142], a PDMS stamp could be patterned with parallel strips to transfer aligned CVD grown CNTs in strips of a desired width. If the length was controlled by catalyst spacing and growth time then the strips would be fully defined. Another technique is to pattern the CNT catalyst by microcontact as reported in [143].

III.A.2) Deposition and coating

Techniques to deposit the various materials in the patterned zones are the next technological step. For metals the three most common techniques are evaporation, sputtering and electroplating. For photoresist and other viscous solutions (e.g. conductive polymers) the usual technique is spin-coating. For CNTs or nanocatalysts in non-viscous solution a few different techniques may be used. Here we review these techniques and their advantages, disadvantages and usefulness in the fabrication of our prototypes.

III.A.2.1) E-beam evaporation and sputtering

The electron-beam (e-beam) evaporation process is a common deposition tool used to coat one side of a sample with a large variety of metals such as gold, nickel, platinum, aluminum, chrome or copper. The sample needs to be loaded in a chamber pumped down to a very low pressure (typically 10^{-6} - 10^{-5} mbar), critical for the electron beam to be sustained. The electron beam is produced by applying a large bias to a heated filament. Several bending magnets are then used to focus and direct the electron beam onto the crucible containing the target metal pellets. The metal heats up and begins to evaporate. A shutter is placed between the sample and the crucible to prevent uncontrolled deposition on the sample during transition phases. Once the desired rate is attained, the shutter is opened, and the surface of the sample is exposed to the evaporating metal. The metal forms a solid layer on the substrate as it touches the surface. A sensor inside the chamber – typically a quartz crystal vibrator exposed to the metal vapor – is used to monitor the deposition rate. Once the deposition is complete, the shutter is closed and the chamber is brought back to atmospheric pressure.

Sputtering deposition is another popular physical vapor deposition technique. In this process, atoms or molecules are ejected from a target material by bombardment with high-energy ions generated inside a plasma. The sample is placed in the path of these ejected particles. The ejected atoms or molecules then condense on the surface of the substrate to form a thin film. One advantage of sputtering deposition is that, being a plasma-based process, it does not require a high vacuum like electron-beam deposition does. However the control over the deposited thickness and the adhesion of the deposited layer may not be as good as that of an e-beam.

E-beam and sputtering evaporation are therefore used alternatively depending on the desired surface quality and deposition rate. 1-to-2-micrometer-thick metal layers as required for RF electronics below 40GHz to prevent skin-effect in good conductors usually require a process time of at least half-a-day. They are also difficult to pattern by photolithography and lift off because their thickness is in the order of that of the photoresist leaving little to no space for the acetone to pass through to the resist and wash it away.

III.A.2.2) Electroplating

Electroplating provides a more effective but less precise way of achieving thick metallization. It allows coating metals on conductive surfaces. For good dielectric substrates such as those used in RF electronics to reduce losses, pre-patterning and thin metal deposition are thus necessary. One additional constraint is that electrical contact needs to be made to any part of the pattern to be coated. Because this is a solution process the contact is usually macroscopic using manually positioned tweezers. This requires the addition in the design of macroscopic pads connected to all parts to be coated and therefore ideally removable.

Electroplating is an electrochemical process – the reversal of the reaction used in batteries. A current is applied between an anode and a cathode in electrolyte solution leading to the attraction of positively charged metallic ions to the cathode where they are reduced by electrons and thus coat the electrode or the sample acting as such. The metallic ions can be simply produced by oxidizing the anode if it is made of the desired metal. Another technique is to use an inert anode and an electrolyte of the desired metal as the solution.

The deposition rate can be controlled by the current and advanced current functions could help improve the otherwise imperfect metal thickness uniformity. However this technique is not suitable for the fabrication of our high-frequency CNT-based antennas. The surface quality of the electrodes in our application is very important for a good vertical CNT growth and at high frequencies where the skin depth comes into play and large roughness at the surface affects the conductivity.

III.A.2.3) Spin-coating

Spin-coating is a very easy and popular method to deposit uniform thin layers of organic materials on the surface of a planar substrate. Short process time and low equipment cost are the main advantages of this technique. We mostly used it for photoresist and modified

photoresist deposition in our experiments. The process is based on the high speed spinning of the substrate to stretch the coating material by centrifugal force. In a first step, the polymer is dispensed onto the surface of the substrate. Then the resin is spread by the spin acceleration followed by spinning at a plateau speed. The thickness of the layer is determined by both the properties of the resin (viscosity, drying rate, surface tension, solid content, wettability) and the spinning conditions (speed, acceleration).

III.A.2.4) Spray coating

A spray gun, or air brush, may be used to coat CNTs (e.g. [144], [145]) onto a substrate. Usually the substrate will be heated around the ebullition temperature of the solvent to guarantee uniform deposition by preventing the coffee-ring effect whereby particles in a solution migrate to the edges of a droplet.

III.A.3) Etching

III.A.3.1) Wet etching

Wet etching is performed by dipping the sample in the appropriate etchant solution – or simply by applying the latter on the former.

Common processes that were investigated and are in use in CINTRA/NTU EEE include KOH etching of silicium wafers (cf. Appendix 8), FeCl_3 etching of copper foils for the recuperation of CVD graphene (after protecting one side with PMMA and proceeding to a dry etch of the graphene grown on the other side to prevent the doubling of graphene layers due to the growth on both sides of the copper foil), HF etch of silicon dioxide and fabrication of silicon nanowires by metal-catalyzed electroless etching (MCEE).

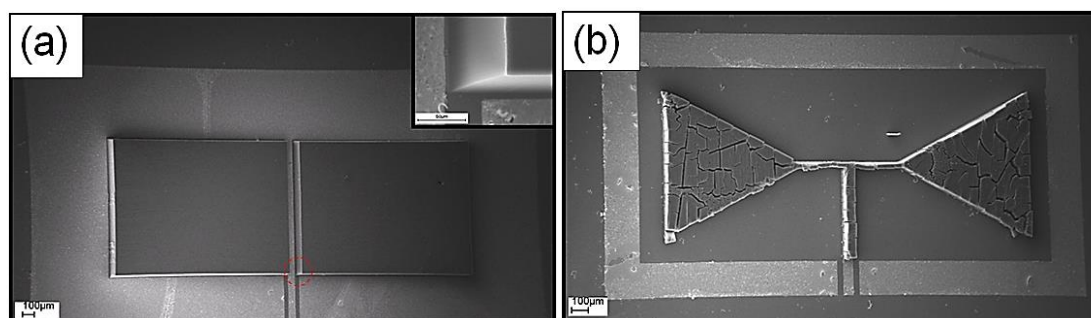


Fig. 35. SEM images of MWCNT grown on (a) slot-type (b) patch-type antenna. Inset of (a) is the enlarged view of the area in the red circle, showing typical growth height of 100 – 150 μm. Samples fabricated by Hong Li and Wai Leong Chow

As part of a series of tests conducted by Hong Li, gold etchant (a mixture of iodine and potassium iodide in water) was used to etch the gold patch of CPW patch antennas before replacing it by CNTs grown by CVD by Wai Leong Chow such as that in Fig. 35 b).

III.A.3.2) Dry etching

Dry etching can be performed using a plasma. This is also called reactive ion etching (RIE). O_2 is typically used to etch resist and polymers. It can also be used to etch CNTs.

III.B) CVD growth of CNTs

In this part we elaborate on the CVD growth processes developed in parallel with the antenna designs exposed in sections IV.B) and IV.D).

III.B.1) Equipment

As explained in introduction (section I.B)) there are several CNT production methods. In our application one of the best solutions is to grow CNTs directly on the sample using Chemical Vapor Deposition (CVD).



Fig. 36. CVD systems in NEL2, School of EEE, NTU

There are three main CNT growth facilities available in CINTRA/NTU through the groups of Prof. Beng Kang Tay and Prof. Qing Zhang. They are situated in the NanoElectronics Laboratory 2 (NEL2) in NTU EEE, as shown on Fig. 36. These are, from left to right, a commercial PE/T-CVD system, the Aixtron BlackMagic II ®, and two home-made quartz tube thermal CVD systems (TCVD2 and TCVD3).

III.B.1.1) Aixtron BlackMagic II

The BlackMagic II ® is a commercial research-purpose reactor distributed by Aixtron and dedicated to the growth of vertical arrays of CNTs. It can grow CNTs in thermal (T) and plasma-enhance (PE) CVD mode and uses an overhead shower to distribute the gas uniformly over the area of its interchangeable 1 inch square and 2 inch round heaters. Bottom and top heater configuration can be adopted with ramp rates up to 1000°C/minute and a maximum temperature of 1000°C. The system mass flow controllers (MFCs) are piloted by computer and so is the heater which allows a fully automated operation of the recipe.

The system is sold as having very reproducible growth and it does its part by reproducing the recipe identically. However, variations in catalyst quality or adjustments to the setup can severely affect the CNT growth and fine tuning is required after this kind of changes.

III.B.1.2) TCVD systems

The TCVD systems rely on a Lindberg/Blue M Mini-Mite tube furnace capable of temperatures up to 1100°C and operated by a programmable microcontroller. A variety of MFCs are installed and connected to a manual control panel, allowing control over the gas mixture. These are relatively cheap systems to build. The furnace costs around USD2000-2500, the MFCs have limited price and are a common piece of equipment that can be recuperated from discarded systems and the only additional cost is simple metal piping and the quartz tubes.

TCVD2 is equipped with a bubbler which enables the use of solution-based catalysts or carbon precursors as illustrated Fig. 37. The gas flow through the system is illustrated Fig. 38 with the corresponding controls. Gas tanks are stored in a bunker outside of the laboratory and all the gas inlets main taps are centralized in a control panel. Once the appropriate taps have been opened the gas recipe is controlled on the selected system. The exhaust can be

connected to an ambient pressure exhaust or to a pump to operate the system under low-pressure or vacuum.

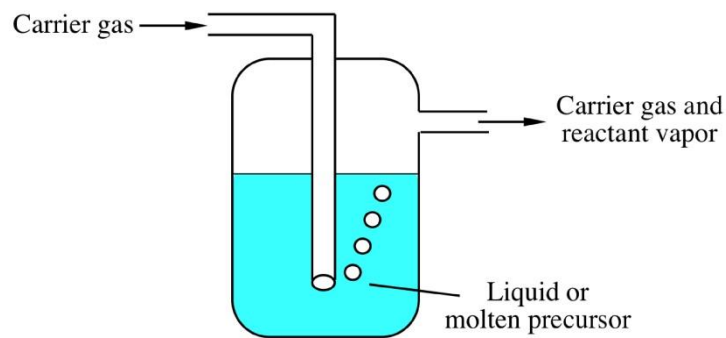


Fig. 37. Bubbler functioning principle

Because the flow may get reversed in the pipes and cause contamination, it is important to successively open the gas taps from the source down to the exhaust. Additionally caution should be exerted not to create excessive pressure in the system, especially in the quartz tube. The heavy and potentially hot metallic connecting parts can fly off in such a case. To remediate to most mistakes, a general solution is to close down the primary taps and pump down the lines then flow the appropriate gases again. To prevent contamination from previous experiments a neutral gas such as N_2 or Ar may be used to flush the system.

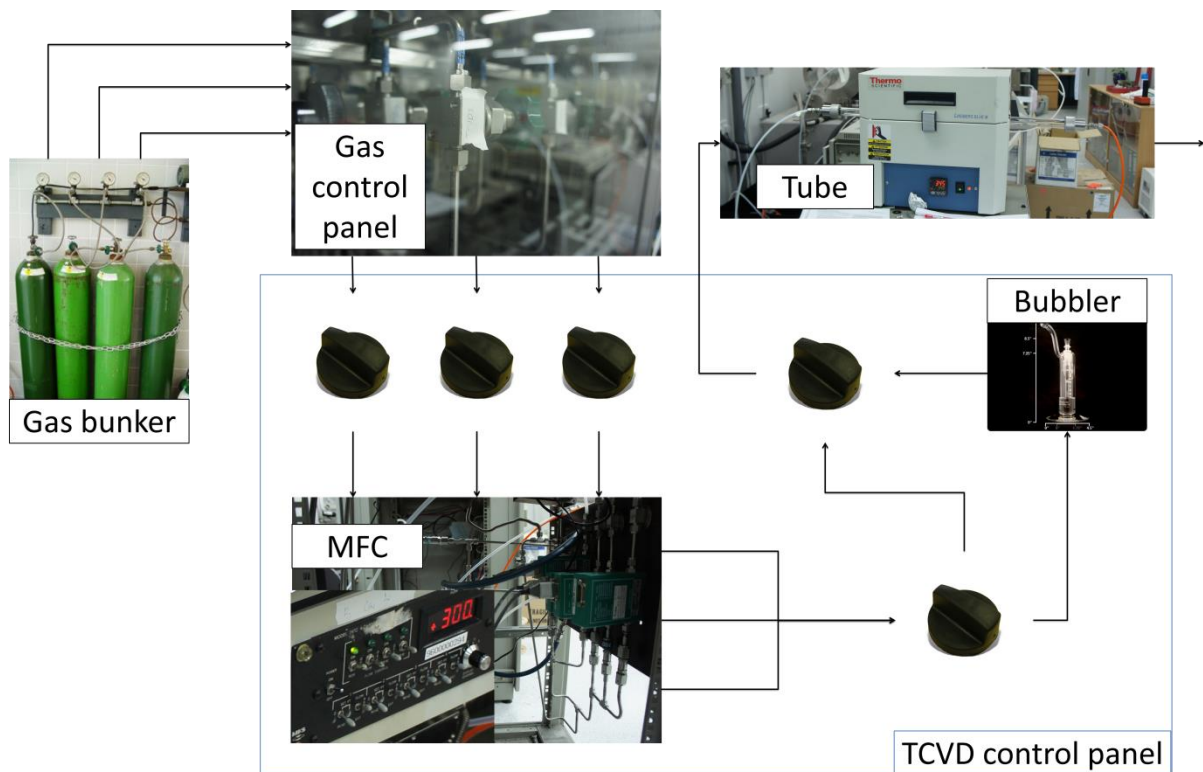


Fig. 38. TCVD gas flow

III.B.2) Growth recipe

The main elements in CNT CVD growth are a carbon feedstock a process to dissociate the carbon feedstock into carbon atoms and a metallic catalyst to adsorb the carbon into carbon nanotubes. Many types of carbon feedstock can be used from gases (CH_4 , C_2H_2) to liquids (ethanol, methanol [146]) or even including pieces of grocery plastic bags [147]. Dissociation is mostly initiated by heat with the standard TCVD where the whole furnace is heated up to temperatures between 800 and 1000°C but also other lower global temperature techniques with localized heating such as RF-plasma based PE-CVD, or top heating based on infrared lamps and laser-excited plasmons [148]–[152] or joule heating. The demonstrated catalysts are mostly metals [153]–[157] with a preference for iron (Fe) and copper (Cu) for SWCNTs and nickel (Ni) for MWCNTs.

III.B.2.1) PE- and TCVD growth of vertical arrays

This growth of vertical arrays can be performed on a variety of substrates including the two we focused on, silicon (usually with a thin layer of oxide) and quartz. Growth on metallization can be performed with an appropriate buffer layer to prevent diffusion in the catalyst but is usually more challenging. Although I was trained on the Aixtron Black Magic system, most growth of vertical arrays for this PhD work was conducted by Chin Chong Yap, Wai Leong Chow and Dunlin Tan as part of the NTU team project Nano Antenna Array. The carbon feedstock used during the growth is C_2H_2 at 150sccm and the growth is conducted at 625°C both parameter having been empirically optimized in a first time.

III.B.2.2) Ethanol TCVD growth of aligned CNTs

This type of growth uses the lattice of the substrate to grow monolayer horizontally-aligned CNTs. It is developed for ST-cut quartz substrate although certain materials such as sapphire have a similar crystal lattice. The CNTs thus produced can however be transferred after growth to a number of substrates.

I fully developed the process and recipe based on available equipment and literature and ran the several initial growths reported here. The starting point was adapting from the recipe reported in [158], [159] and advice from one of the two main authors, Xiehong Cao (under Prof. Freddy Boey and Prof. Hua Zhang), on cutting the quartz.

Ethanol CVD is performed in the TCVD2 quartz tube reactor with bubbler and normal system exhaust (no pump). The system is consistently flushed before each growth process to prevent contamination from other experiments that are run with it. A large flow (1000-2000sccm) of neutral gas (nitrogen (N₂) or argon (Ar)) is passed through the piping without the quartz tube. The tube is then centered in the furnace. The samples are inserted in the middle of the tube on a sample holder – typically a piece of silicon wafer cut to the appropriate dimensions. The quartz tube is then connected between the gas mixer output and the exhaust. The system is flushed once more before initiating the growth process.

There are five main steps in the growth process, as depicted Fig. 39. Under 1000sccm Ar, temperature is quickly ramped-up from 25 to 850°C in TM1. This is followed by a slower ramp-up from 850 to 900°C under 200sccm Ar in TM2 to avoid temperature oscillations when reaching the set temperature plateau and a plateau at 900°C for TM3.1 (2min). The next step is an annealing at 900°C for TM3.2 (20min) under 50sccm Ar and 100sccm hydrogen (H₂). The gas mixture is then changed to 80sccm Ar and 40sccm H₂ and passed through a bubbler filled with ethanol as the carbon feedstock for CNT growth for TM4. The Ar is used as carrier gas while the H₂ ensures the quality of the CNTs by attacking amorphous carbon and imperfect shells and removing them as C_xH_y. At the end of the growth time the samples are cooled down under 1000sccm Ar in TM5.

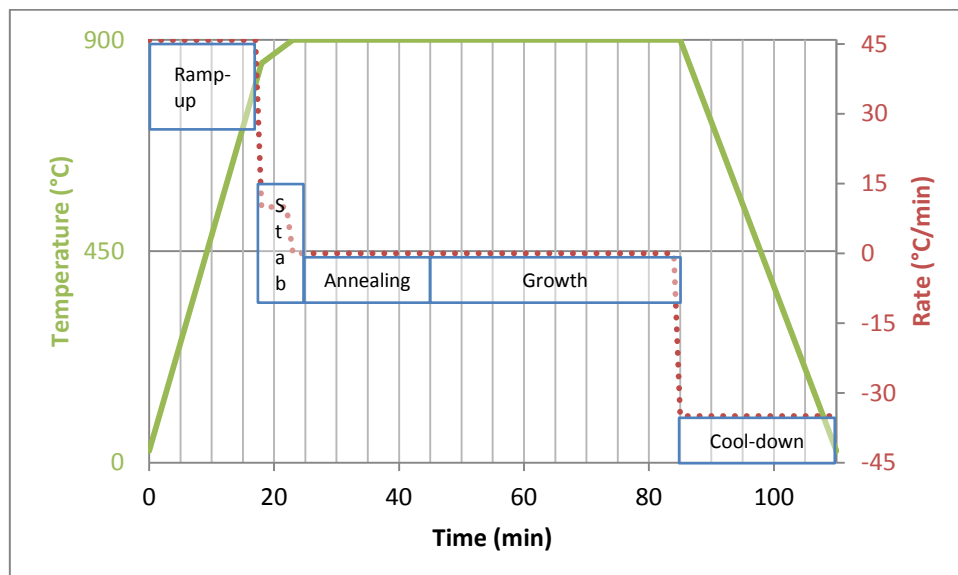


Fig. 39. Ethanol CVD steps.

There are a few points to note about this process. Firstly, depending on the desired cooling rate, opening the furnace and/or ventilating the quartz tube may be required. In our

case, the temperature drops well down to 5-600°C before doing so. Secondly, single-crystal quartz undergoes a phase transformation from alpha quartz to beta quartz at 573°C. This phase transformation needs to be passed at relatively slow heating/cooling rate to prevent fracture for large substrates [142]. This does not affect the growth step of the recipe. It should also be noted that for the minimal set flow rate, 120sccm, in a 1.9-centimeter-diameter tube, the gas flows at 7mm/s at ambient pressure. The flow is thus unidirectional without the pump. Pumping down allows low-pressure growth with possible advantages on the CNT quality but the risk to rarefy the CNT precursors too much for proper growth. Finally, notes on the different runs of the process are reported in Table 10 in Appendix 6. It can be noted that there were variations on the atmosphere used for the flush, ramp-up and cool-down steps as the machine evolved but – because these are neutral phases of the process – the changes apparently did not affect the resulting growth. The last run, E0.09, inaugurated a quite successful step of pre-annealing in air at 700°C which allows burning away any resist left from the photolithography patterning of the catalyst before proceeding to the normal annealing and growth. The Raman spectrum was taken in several points of the substrate for samples extracted from the runs E0.02 to E0.05 which served for device fabrication. The corresponding recipes can be found in Appendix 6 and some of the Raman spectra and an explanation of Raman spectroscopy applied to the characterization of CNTs are reported in section V.B.1.1). It consistently shows a high I_G/I_D such that the defect peak is often below the noise threshold on the horizontal CNTs. On the scratch catalyst zones the D peak is more pronounced but I_G/I_D is still large.

III.B.3) Catalyst study

We investigated various types of catalyst to try to simplify the process and make it cheap and independent of equipment. Indeed the availability of e-beam deposited iron was scarce because iron is only accepted in one or two e-beam evaporators due to oxidation problems. Furthermore the thickness required (1nm) is at the precision limit of the equipment and large variations in thickness and quality can be expected which was a serious issue for the repeatability of vertical CNT growth. We also lead a study on the spacing of catalyst to control CNT density. All the results and SEM pictures that follow are extracted from the same ethanol CVD growth run E0.09 (cf. Appendix 6). This makes them directly comparable. It also validates the versatility of the growth recipe which, without tuning, grows dense horizontal CNT arrays from most catalysts.

III.B.3.1) Scratch catalyst

We first adopted the simplest and cheapest technique that could be found, described in [158], [159], which consists in scratching the substrate with a metallic object. Quartz is harder than metals and small particles deposit while scratching. Scratching with a diamond pen did not return any growth. Scratching with a staple was one of the best growths we obtained although feather knife and needles worked rather well. A reproducible grip on the staple was obtained using a feather knife holder. Scratches were done hand-held and systematically led to CNT growth. A way to systematize the scratching is to use a micromanipulator [158]. We also designed a setup for reproducible parallel scratch lines using a saw laterally as illustrated Fig. 40. The teeth produce equally spaced parallel scratches. The saw can be shifted longitudinally in the air using a microstage then pressed on the sample again before it is laterally shifted to produce additional sets of scratches at a chosen spacing. The use of a commercial CSEM Micro Scratch-Tester was investigated because it seemed the only appropriate way to systematize scratch catalyst. It includes a motorized XYZ platform under an optical microscope with a proper sample holder, and would allow monitored variations of speed and pressure in scratching. However it was not possible to change its diamond tip for a metal one at that time.

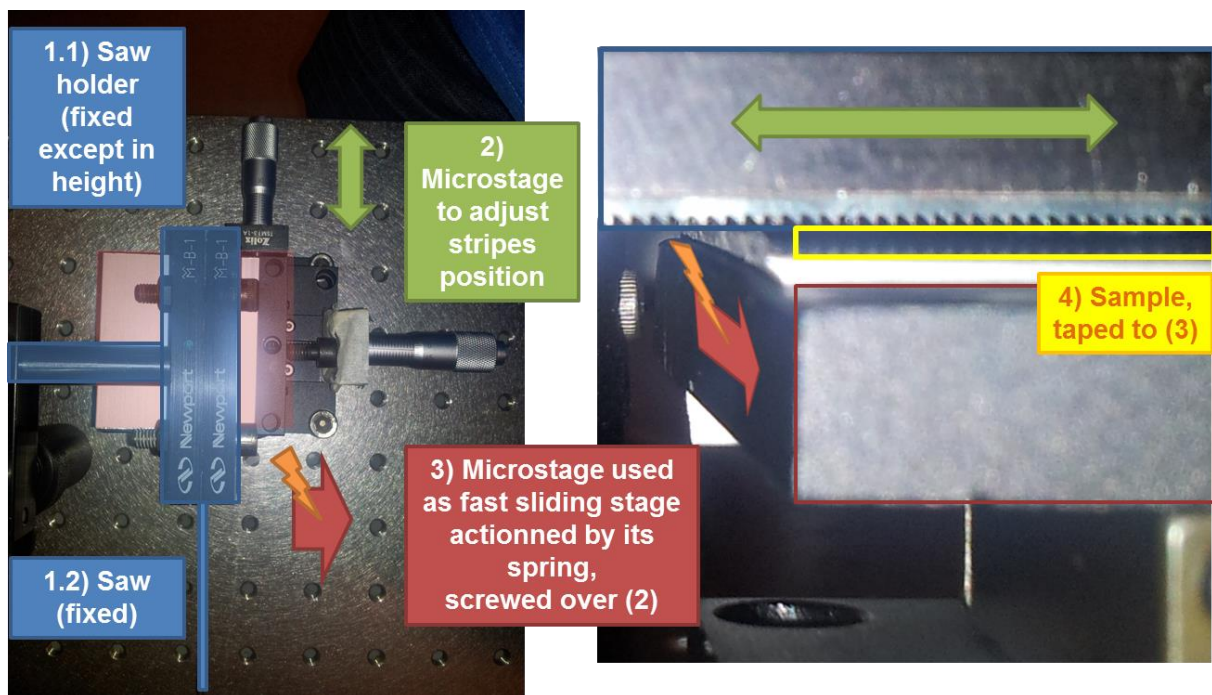


Fig. 40. Saw scratcher.

III.B.3.2) Solution-based catalyst

Solution-based catalyst was investigated as another option for cheap catalyst deposition. Fabrication of well separated copper catalyst nanoparticles was reported by L. Ding using PS-PVP [160] in Jie Liu's group. An alternative developed by W. Zhou in Peter Burke's group [143] was to use photoresist as the embedding polymer to directly pattern this layer.

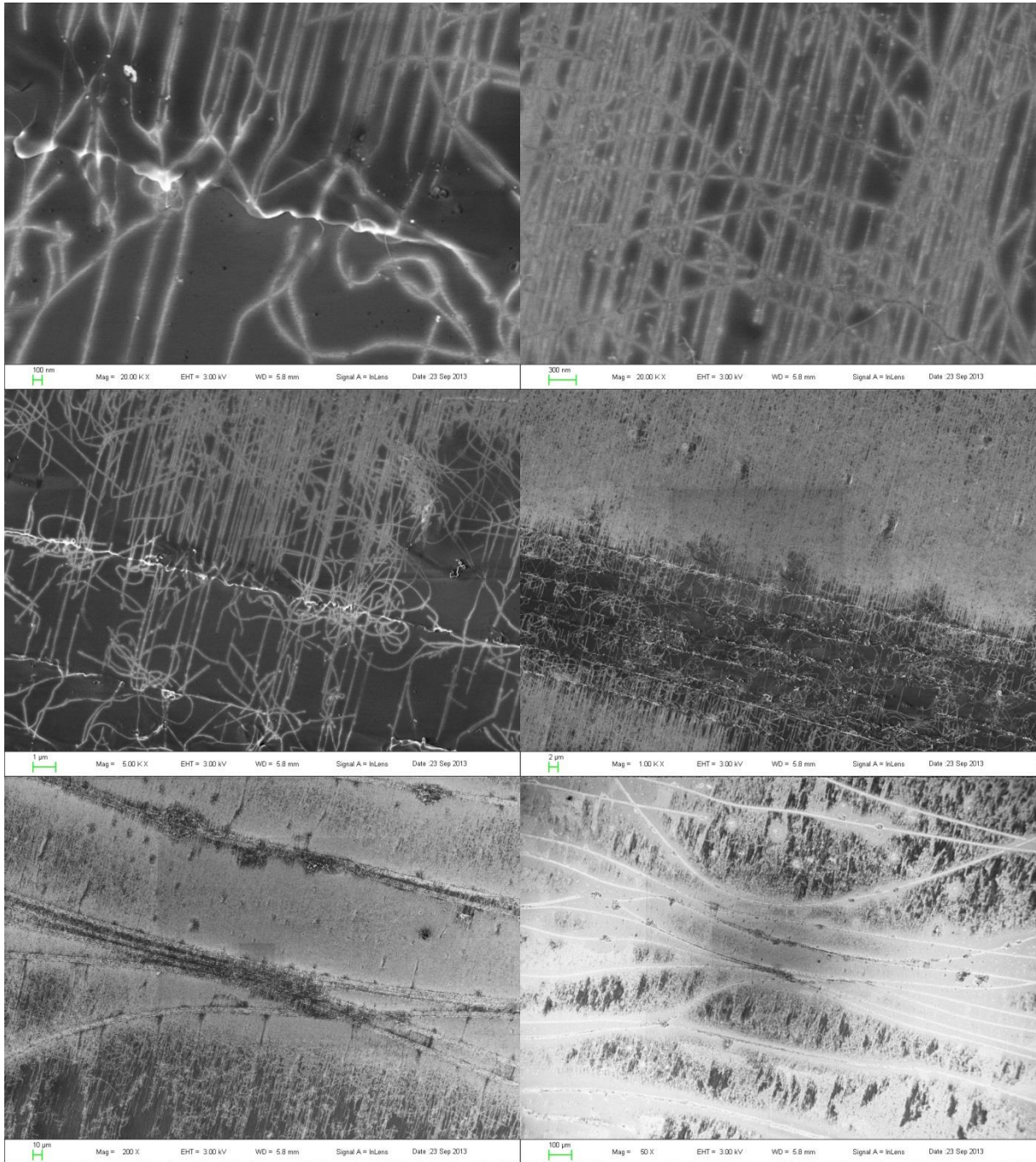


Fig. 41. SEM images of a CNT growth from photolithography patterned AZ+Fe catalyst lines. From 20000x (top images) to 50x (bottom right).

We opted for the latter technique and tried to use FeCl_3 dispersed in the photoresist used in NTU (different from the reported Shipley 1827) to produce well separated iron catalysts. A solution of FeCl_3 in IPA at 5mM was prepared. It was mixed to AZ5214 photoresist to prepare samples with 5 variations of concentration (IPA-Fe:AZ at 1:1, 1:2, 1:3 and 5mM of FeCl_3 directly in photoresist and half this), each repeated twice in a batch. Two batches were prepared by positive photolithography of 5- μm -wide lines of catalyst. All were patterned successfully. However the lines chosen as pattern had too high aspect ratio and would often detach from the substrate and float in the developer solution. Thicker or shorter lines would remedy to this issue.

The results show growth of dense and long aligned CNTs for the different samples. Further analysis will need to be conducted to highlight the differences induced by the concentrations. Fig. 41 shows the typical results obtained: an average density of 10 CNTs/ μm and local densities of 20 CNTs/ μm . The coverage is thus excellent. Because of their high aspect ratio, some of the catalyst lines we fabricated were bent. This is seen on Fig. 41 and highlights that the areas with closest facing catalyst lines have denser CNTs. We proposed to study this in the next section.

III.B.3.3) CNT density control by catalyst lines spacing

Because the CNTs growing from a catalyst line in horizontal CVD seem to have an inverse-law length distribution, we propose to vary the spacing between catalyst lines to tune the CNT density obtained. This will then be applied to the design of CNT strips in section IV.C.2.2.2).

On the fabricated sample here, parallel 6- μm -wide 2.7mm-long catalyst lines are repeated over 0.9mm for each spacing to provide a large statistical sample to check the density for each spacing. The actual catalyst spacing affecting CNT growth in our study is the border-to-border spacing (not center-to-center). We vary it as a geometric progression of common factor $\sqrt{2}$ from 14 μm to 640 μm . The exact parameters are reported in Table 7, section IV.C.2.2.2).

The study was conducted using an ST-cut quartz substrate with 1nm iron catalyst deposited by e-beam evaporation in NTU MAE. The results are presented in Fig. 43 and Fig. 42. Interestingly the catalyst lead to good growth in our process while its quality on samples

produced in the same batch was insufficient for vertical CNT growth. The horizontal CNT growth recipe we use seems again very consistent in growing CNTs from most metal catalyst types. The difference is likely its relative insensitivity to catalyst density while vertical growth needs quite a specific density.

The surface cleanliness of the substrate is of prime importance. Indeed despite long hours in acetone to do the lift-off some resist remained on the substrate on a first try and no aligned CNTs were observed. On the second try, with the same catalyst, we proceeded (process E0.09 – Appendix 6) to an annealing in air at 700°C by leaving one end of the quartz tube open and pumping air with the low-vacuum pump on the other end. The growth was successful. This was actually the same for the photoresist based catalyst lines of the previous section where no prior burning of the resist resulted in no growth, most likely because the catalyst particles were trapped in the resist that would not burn without oxygen.

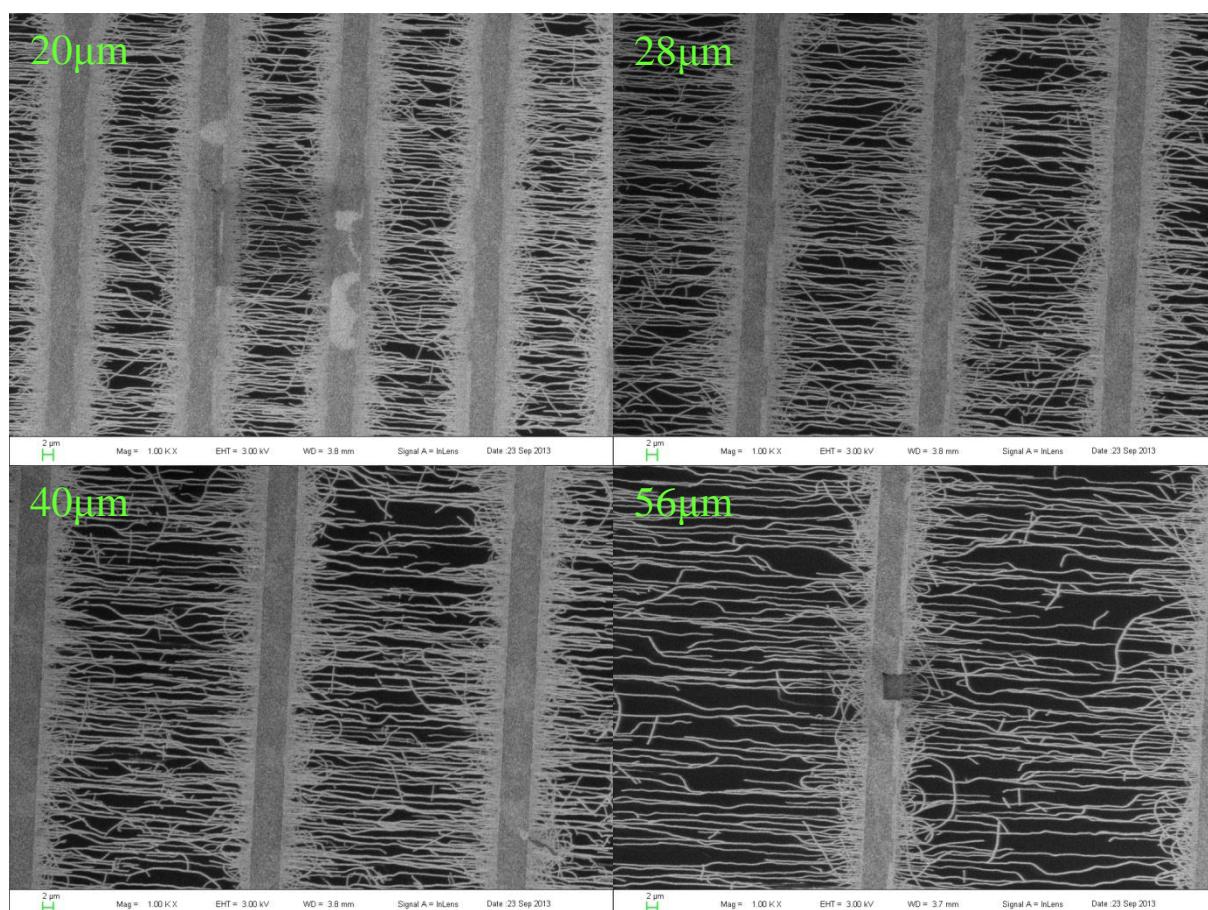
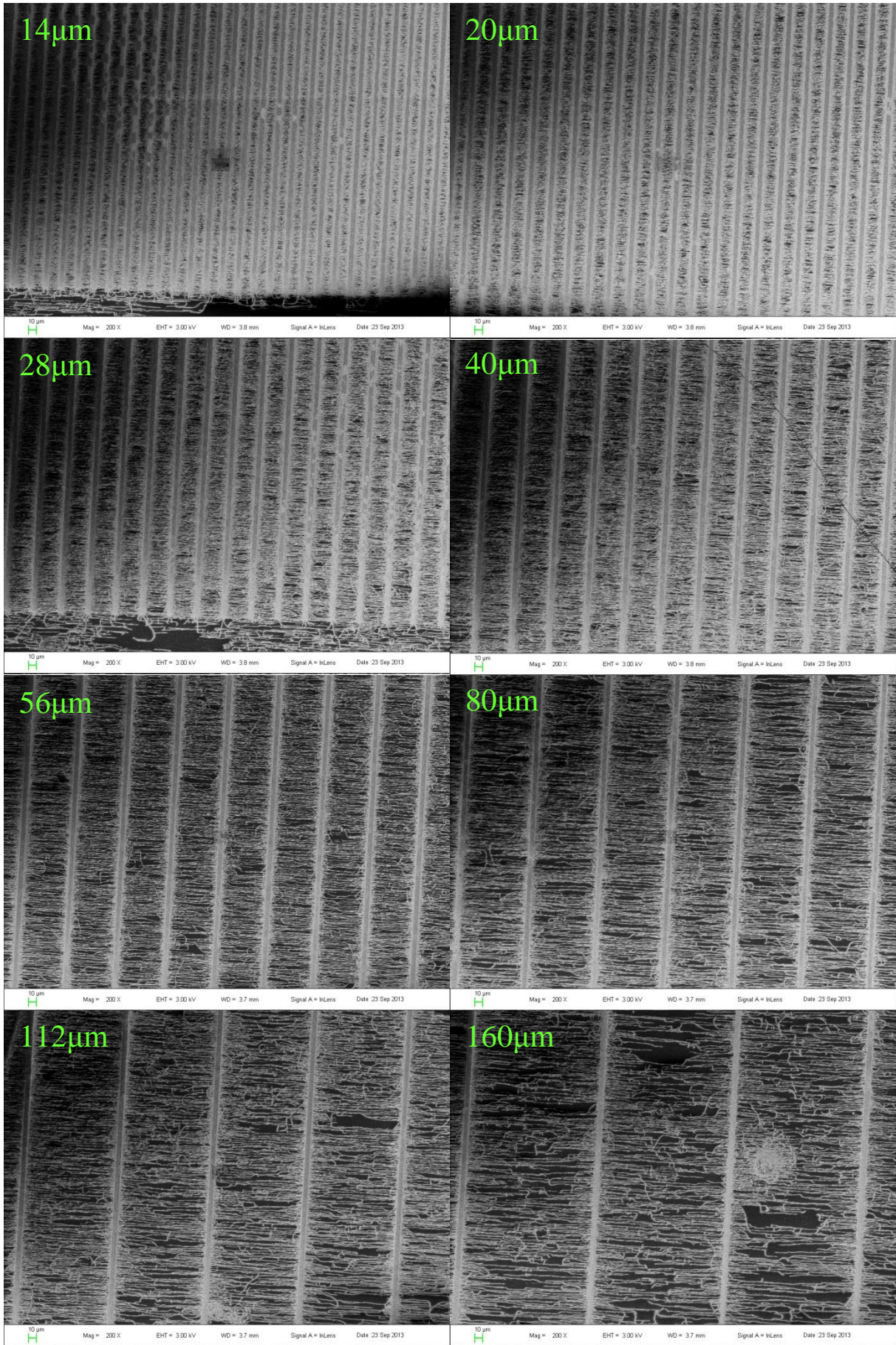


Fig. 42. SEM images of the catalyst lines at 4 consecutive spacing values. Fix zoom, 1000x. The density in the center is visibly decreasing. On each image the catalyst lines are the vertical ones and the horizontal lines are CNTs.



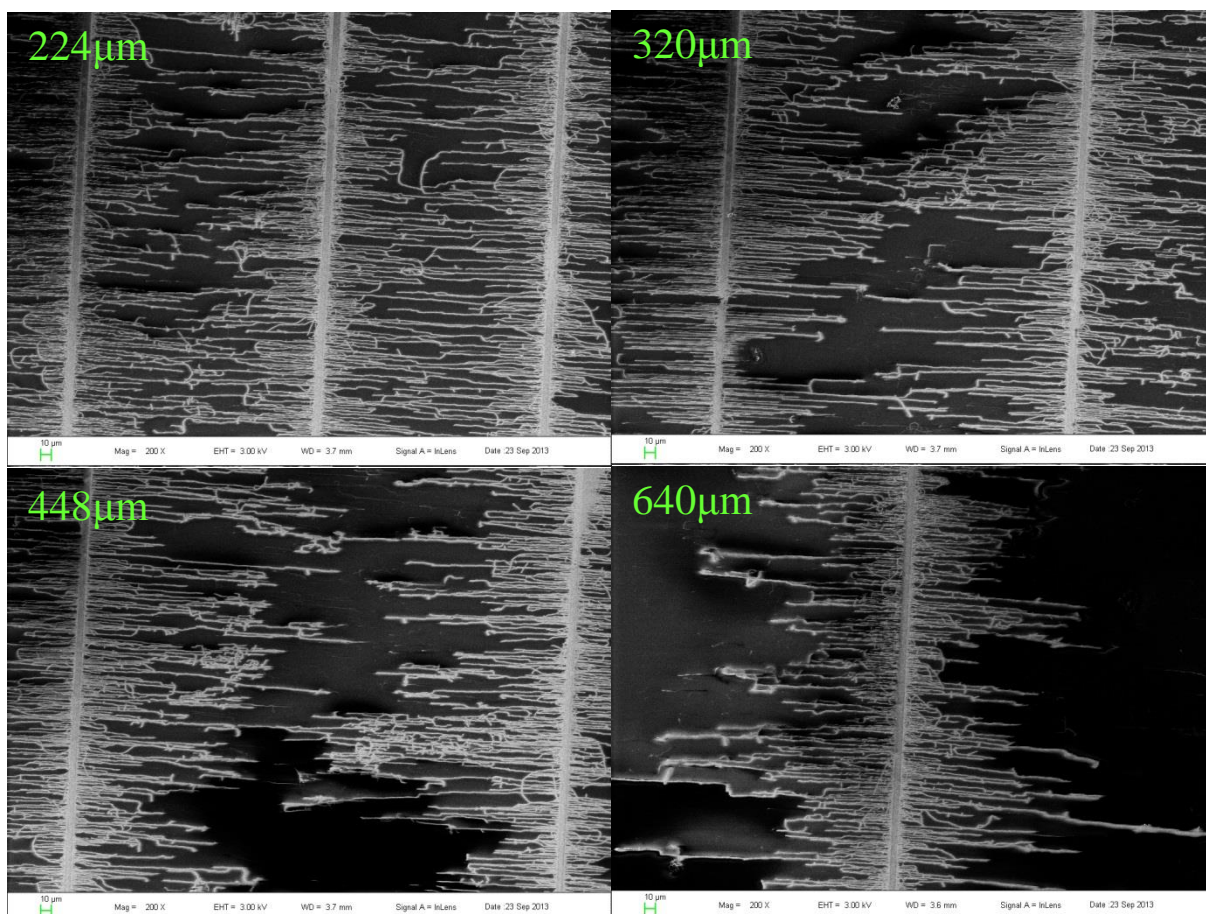


Fig. 43. SEM images of the catalyst lines at the 12 different spacing values (length indicated in green). Fix zoom, 200x. On each image the catalyst lines are the vertical ones and the horizontal lines are CNTs.

The growth result of this spacing study are reported on Fig. 43 for all spacing values at a fixed 200x zoom on Fig. 42 for four consecutive of the smallest values at a zoom of 1000x. The density at the center of the spacing is uniform for each spacing value but is visibly decreasing with increased spacing, as desired. Hence density tuning over a CNT strip will be achievable as designed in section IV.C.2.2.2).

III.B.4) Additional interesting perspectives: combining CNTs and SiNWs

CNT growth was performed on silicon nanowires (SiNWs) fabricated by metal-catalyzed electroless etching by Aliénor Togonal, PhD student at CINTRA/NTU. Two interesting types of structures were obtained. Using gas TCVD with CH_4 as carbon precursor (400sccm) and e-beam or solution deposited iron as catalyst, thick disordered CNT arrays were grown on top of and around the SiNWs (cf. Fig. 44 and Fig. 45). Using ethanol CVD and e-beam deposited iron (1nm), we produced suspended CNTs forming a monolayer net at the tip of the nanowires (cf. Fig. 46). They were found to be high quality SWCNTs from

Raman spectroscopy (cf. Fig. 47). Suspended CNTs are closer to the ideal case of a quantum wire in free space and are reputed to have better optical sensitivity for Raman characterization, photoluminescence and other aspects [161]. They could therefore be used to fabricate photosensors, bolometers, photoswitches or photomodulators. Furthermore SiNWs and CNTs can form a heterojunction [162], [163] and which would be a much more effective photocurrent generator than the CNTs alone.

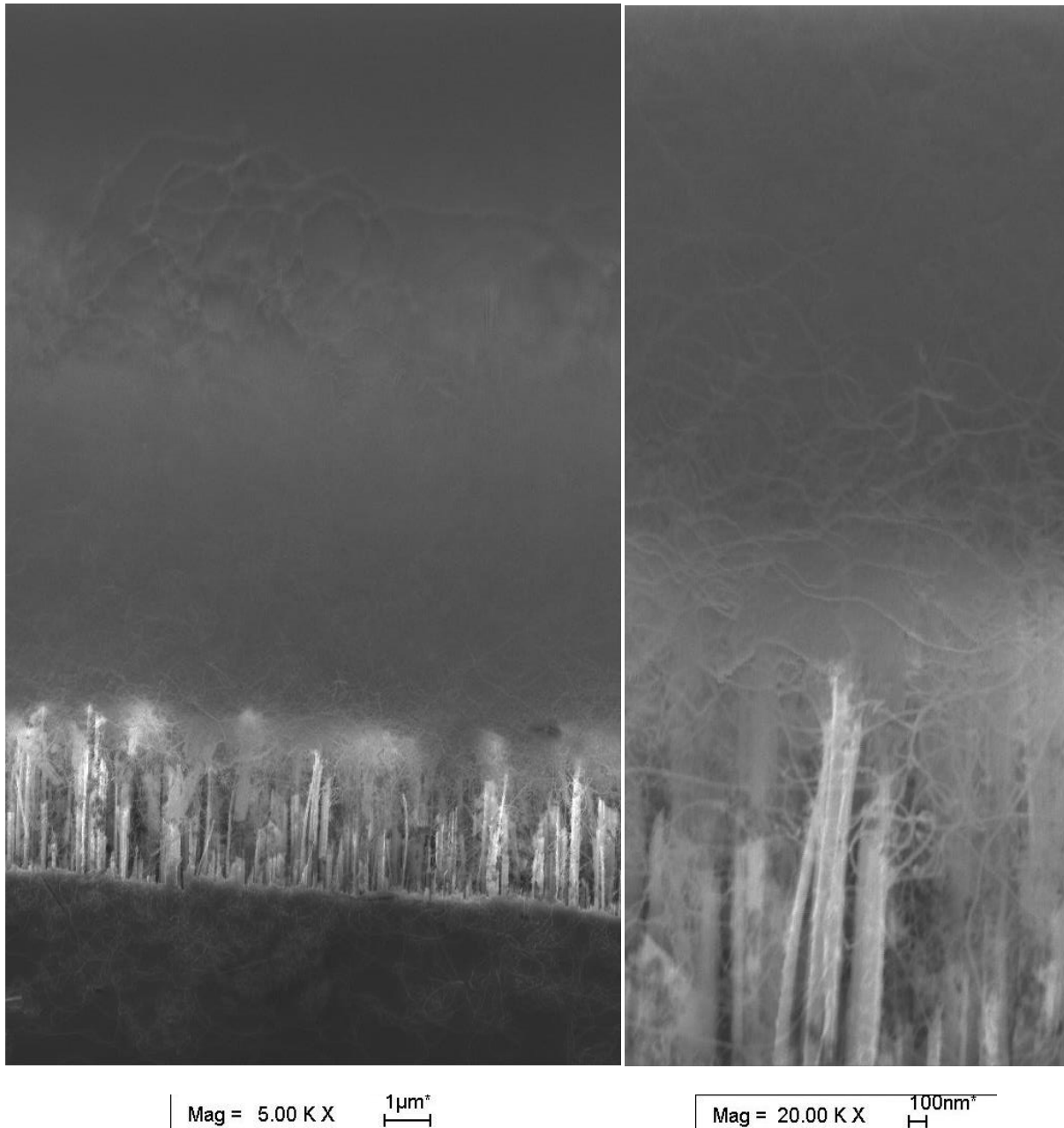


Fig. 44. Thick disorganized CNT film grown by CH_4 TCVD on top of MCEE-fabricated silicon nanowires (sample T0.04B). SEM images zoomed 5000x and 20000x. CNTs are the thin wavy wires and SiNWs the thicker straight vertical pillars.

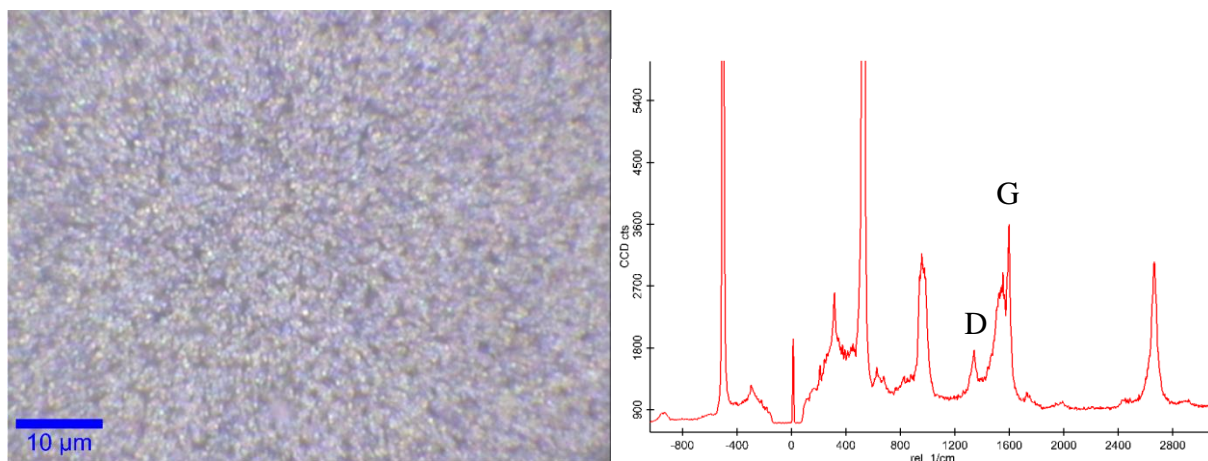


Fig. 45. Optical microscope image and Raman spectrum of sample T0.04B.

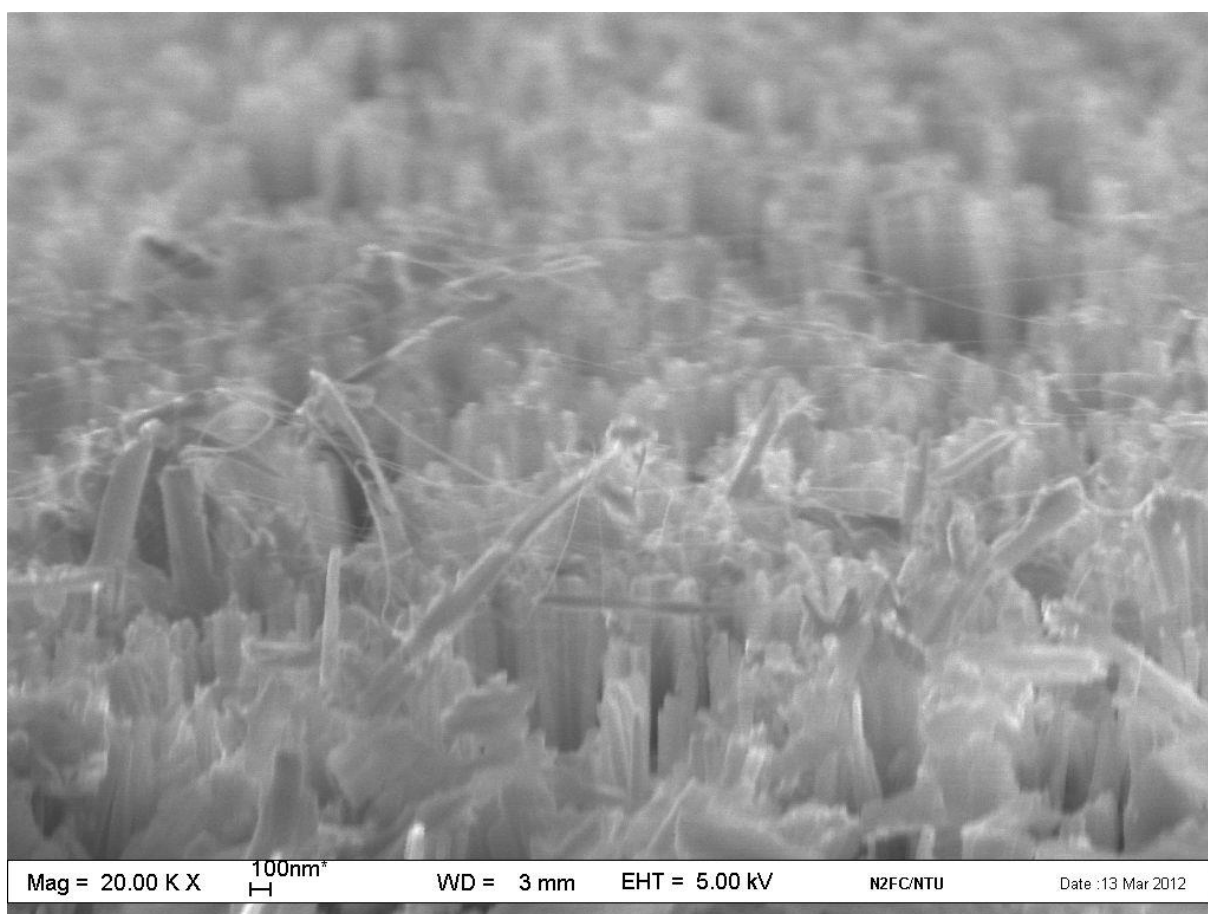


Fig. 46. Suspended SWCNTs (thin horizontal wires) forming a monolayer net at the tip of silicon nanowires (thicker vertical ones). SEM image, sample E0.03B.

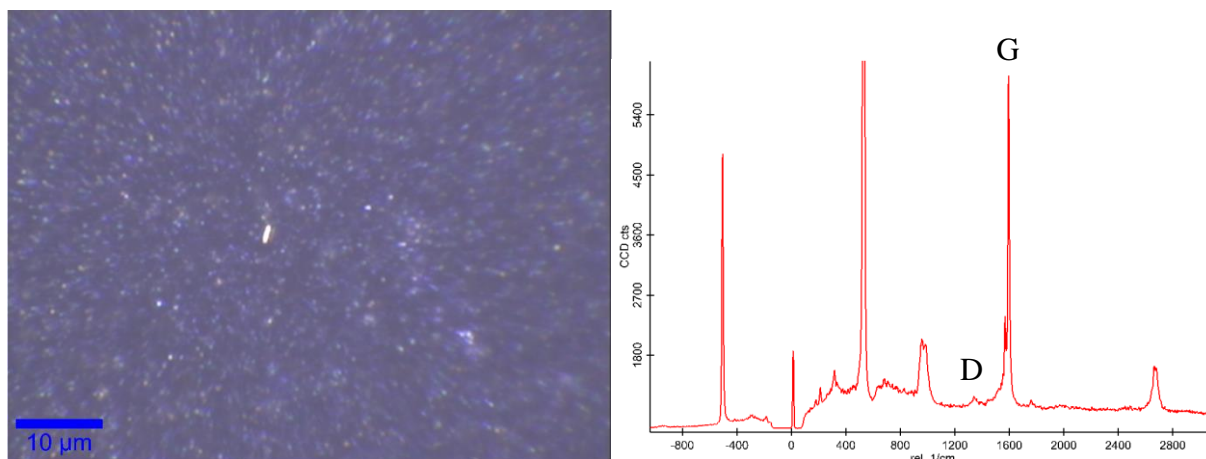


Fig. 47. Optical microscope image and Raman spectrum of sample E0.03B.

III.C) Structures fabrication

A number of structures were fabricated based on the techniques we have exposed: DEP-aligned CNTs in CPW gaps for RF electrical characterization (section II.C.3.2)), sprayed-CNT samples and lattice-aligned CNTs in CPW gap for photocurrent characterization (V.B)). The CNT antenna prototypes fabrication is reported with their design in the respective sections: horizontal monopole based on lattice-aligned CNTs (IV.C.2.2.3)) and vertical and topped monopole antennas IV.D).

III.C.1) DEP-aligned CNTs in CPW gap

Dielectrophoresis (DEP) was used to align CNTs in a CPW gap structure. The process, illustrated on Fig. 48, consists on depositing a droplet of CNTs in solution in the gap between two electrodes and applying an electric field. Metallic CNTs will then preferentially align in the direction of electric field lines. For our samples, as reported in section II.C.3.2), the CNTs bundled in ropes because the gap was 5- μm -long while the CNTs were only 1- μm long or shorter. This can be observed on Fig. 49. On the right side the CNT ropes are seen lying on the substrate while bridging the top of the 1- μm thick metallization on each side of the gap. Ralph Krupke's group has refined the process [164]–[166] which can have interesting applications for short gate transistors or similar applications requiring short CNTs.

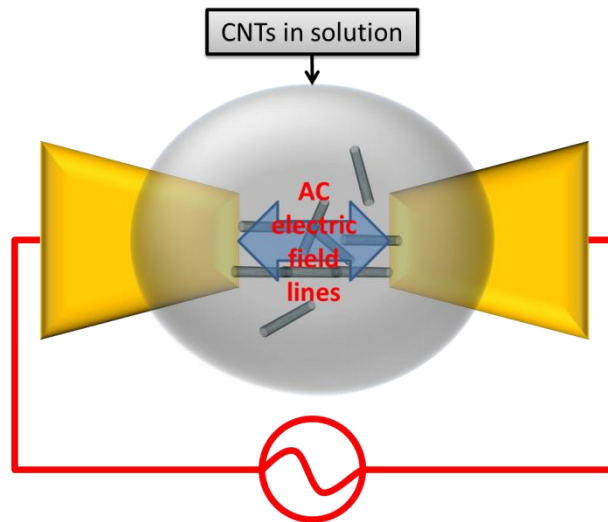


Fig. 48. Dielectrophoresis alignment of CNTs dissolved in solution.

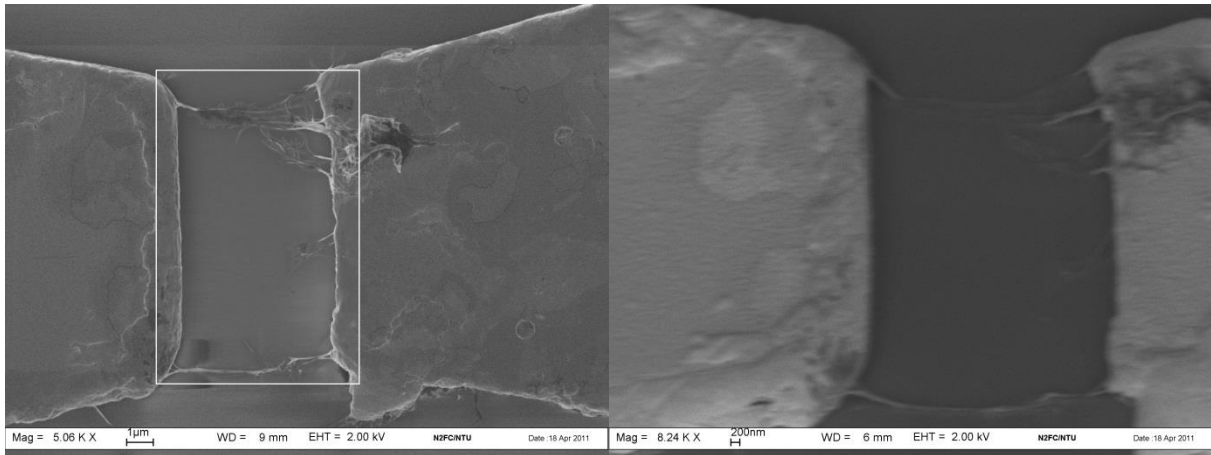


Fig. 49. Top-view (left) and 45°-angle-view of a tapered 5- μm CPW gap characterization structure.

III.C.2) Sprayed-CNT samples

Spray-coating was used to prepare photocurrent samples used in the study, section V.B). As explained earlier, CNT inks were realized by probe sonication of 5mg/L of NanoIntegris 99%-semiconducting SWCNTs flake into two different solvents, dimethylformamide (DMF) and ethylene glycol. The CNT-ethylene glycol solution was sprayed onto microscope coverglass plates and kapton, two cheap transparent highly dielectric substrates, the latter one being flexible as well. A hand-held spray gun connected to a nitrogen bottle served to spray onto the substrate which was simultaneously heated with a heat gun. Approximately 1cm^3 of solution was sprayed at 15cm from the substrate. Despite the high density and coverage of CNTs, the samples remain transparent in the visible range.

Samples were also realized by Paolo Bondavalli (Thales Research and Technology, Palaiseau) on his semi-industrial air-brush setup [145]. The CNTs used are commercially available CoMoCAT CNTs. The huge advantage of the technique over our experimental method is its full repeatability thanks to full control over the deposition parameters. Furthermore the shorter CNTs used form a very clean conformal layer with a few passes as seen on Fig. 50.

The electrodes were to be inkjet-printed on the substrates which would have made an interesting demonstration of cheap-process CNT-based transparent flexible electronics. However due to equipment availability issues, the electrodes were realized by photolithography. 100nm of gold were evaporated. Interestingly, the wet process including rinsing with acetone at lift-off did not seem to damage the CNT film as illustrated on Fig. 51.

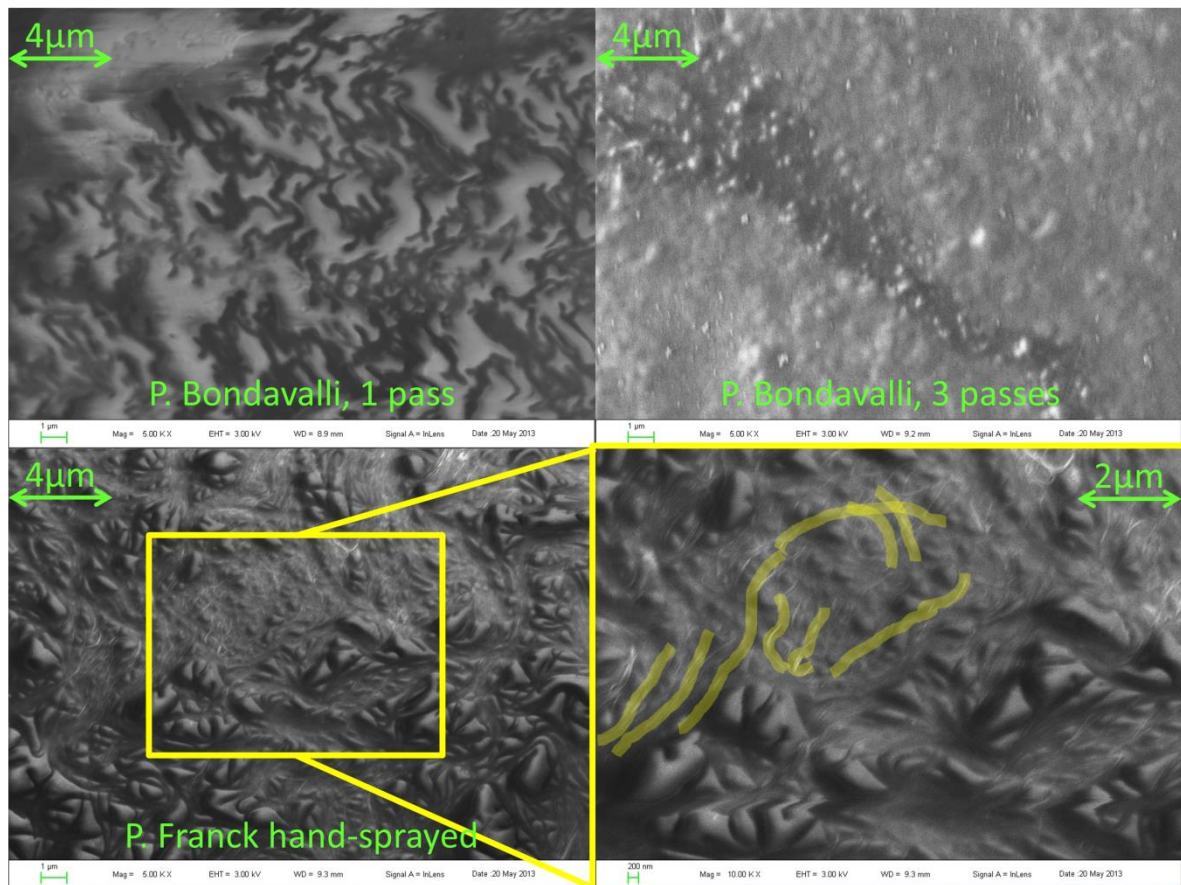


Fig. 50. Sprayed CNTs observed under SEM. Top (5kx): from Paolo Bondavalli, single pass (left) rather uniform but apparently non-continuous film and 3-pass (right) very uniform and continuous. Bottom (5 and 10kx), hand sprayed CNT ink fabricated in CINTRA; long CNTs or CNT ropes can be observed which are not apparent in P. Bondavalli's samples.

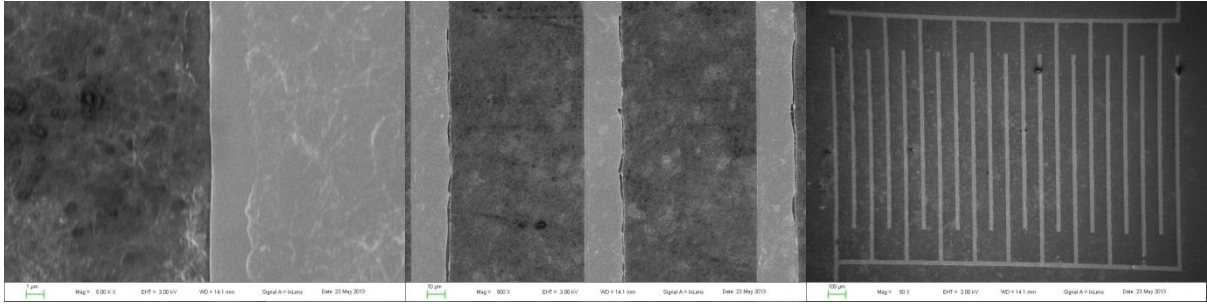


Fig. 51. Gold electrodes fabricated by photolithography on sprayed sc-SWCNTs. From left to right: 5000x, 500x and 50x SEM images. The CNT film appears undamaged by the process.

III.C.3) Lattice-aligned CNTs in CPW gap

The samples, used for photocurrent measurements, were prepared by scratch catalyst and ethanol CVD growth over the entire substrate. The CNT growth direction being known, the scratches for catalyst were made perpendicular to this direction with the precision of a hand-held scratch. For reproducible electrical contact and measurements at RF frequencies, a 50- Ω CPW line with a gap in the middle of the signal line was then patterned by photolithography. The CPW gap pattern was aligned along the CNT direction with its gap placed just above the scratches, the only visible patterns on the otherwise translucent CNT-covered quartz substrate. 100nm titanium (for adhesion) and 1 μ m gold were then deposited to create, after lift-off, the final device. Additional steps of protecting the CNTs in the gap and etching the other CNTs were deemed unnecessary after SEM inspection revealed that no CNT bridged the ground-signal gaps of the CPW thanks to the good alignment realized between the CNTs and the CPW lines. The originally devised process is illustrated on Fig. 52. The actually executed steps are illustrated with images of the experimental outcome on Fig. 53.

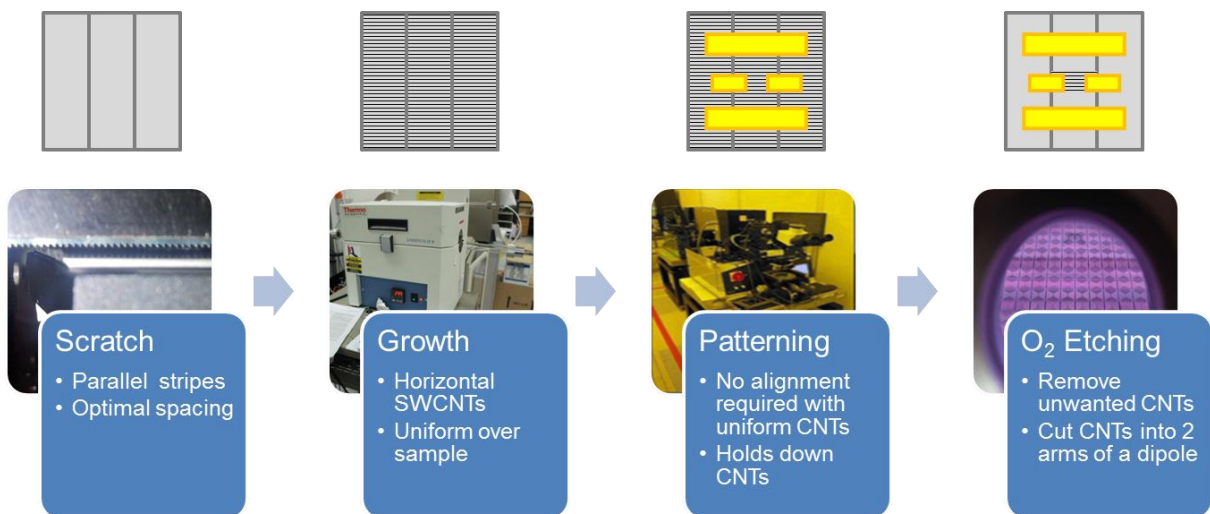


Fig. 52. Steps for the fabrication of CPW gap electrodes over horizontally grown CNTs.

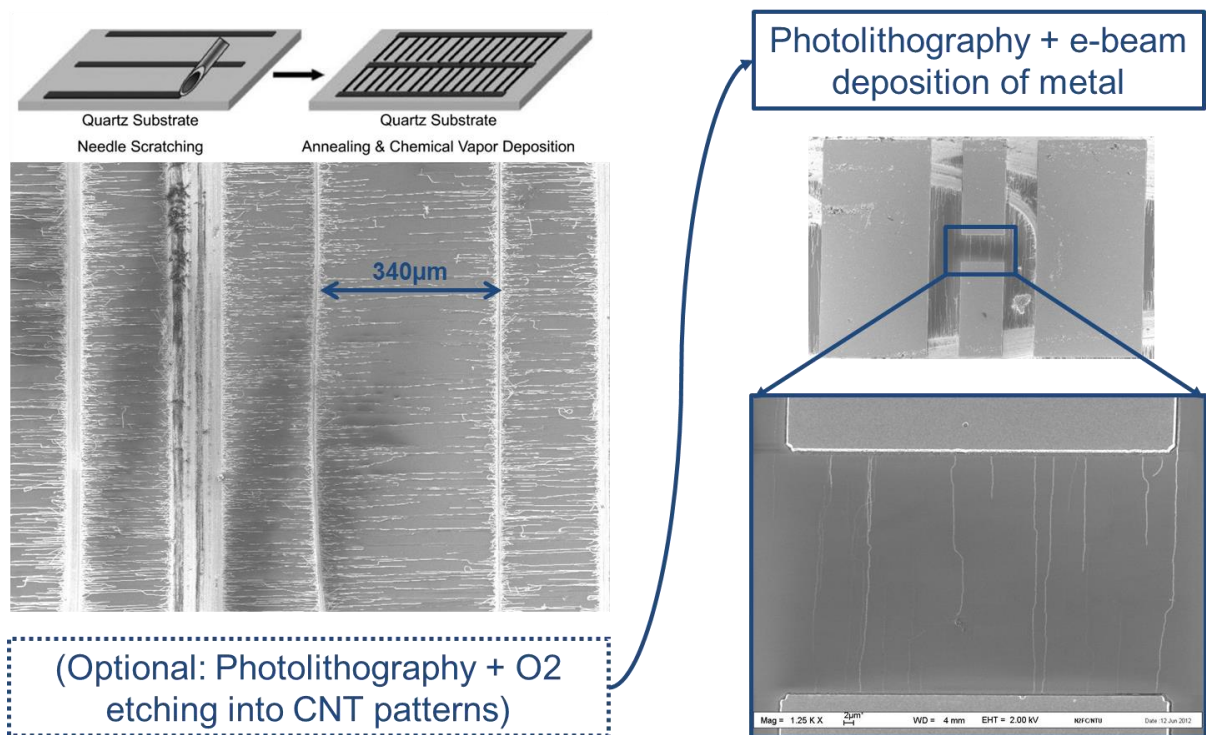


Fig. 53. Same steps illustrated with SEM images of the outcome apart from the skipped step of etching which is also placed in an alternative order.

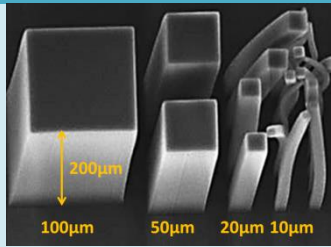
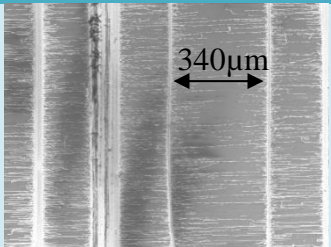
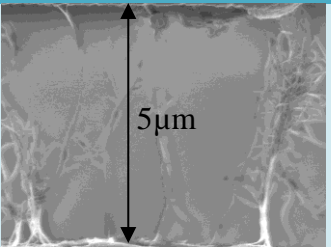
III.D) Considerations for experimentally-realizable CNT antennas

The experimental realization of electrically-short resonant antennas from CNTs is a complex task. The initial results in section II.C.2) and the full study we present in section IV.A) demonstrate the need for SWCNTs that are long (tens to hundreds of micrometers), of high quality ($\tau \geq 1ps$ for plasmon antennas at 160GHz and above) and in specific quantities which takes us to the limits of current CNT fabrication techniques – as we initially reported in [167], [168]. There are a few types of CNT fabrication methods, each with their particular advantages and restrictions. To experimentally observe a size reduction on a resonant antenna, these need to be considered along with simple antenna designs. We will study monopole and dipole antennas where the axial propagation of electrons corresponds best to CNTs. The simplicity of the structure also ensures correct interpretation of the results.

As base material, three types of CNTs can be used. Dense vertical CNT arrays can be obtained by thermal (T) or plasma-enhanced (PE) chemical vapour deposition (CVD); with typical densities of 10^{10} - $10^{11}/cm^2$. Substrate-lattice-aligned horizontal CNTs can also be obtained by CVD on specific substrates such as quartz [169] then, optionally, transferred [141], even at wafer scale [142] ; reported densities range up to 25-50/ μm in peak value [49],

[170] and up to 5 to 10/ μm in average [143], [169], [171] – we have achieved 1/ μm with scratch catalyst so far and 10/ μm with iron catalyst. Finally, solution-processed CNTs can be deposited by a variety of methods rather than in-situ grown. These methods are compared in Table 4 considering aspects relative to the fabrication of CNT monopole antennas. One of the criteria is the minimum number of CNTs achievable by photolithography. This method is preferable for its simplicity and scalability for catalyst and electrode patterning and imposes a lower resolution limit of about 2 μm .

Table 4. Different CNT types for the fabrication of an electrically-short resonant antenna.

	Vertical CVD CNTs	Horizontal CVD CNTs	CNTs in solution
Illustration of typically fabricated arrays in CINTRA			
	PE-CVD grown MWCNT arrays on Si	TCVD grown SWCNTs on ST-cut quartz	5 μm DEP between gold electrodes
Density	100 to 1000/ μm^2	0.1 to 50/ μm	X (pass number for inkjet/spray)
Min(N_{CNT}) by photolithography	300 to 3000	1 to 100	Depends on technique.
Length	10 to 300 μm but aspect ratio <20	5 μm to 0.4cm, dense for < 100 μm	1 μm in average, 0.1 to 5 μm
Quality	SWCNT only: difficult, DWCNT OK. Aligned but wavy, medium-high quality.	High-quality straight to ultra-straight aligned SWCNT. Metallic-semiconducting sorting by electrical breakdown	Random orientation. High quality, chirality/diameter sorting possible.
Robustness	Bad with high aspect ratio	Excellent	Excellent
Characterization	In-situ/Ex-situ (powder/large array)	In-situ (SEM, AFM, Raman)	In-situ/ex-situ
In CINTRA	Well-studied growth	Recently achieved state-of-the-art density with different catalysts	Buy/get CNTs ; inkjet, spray, DEP, drop-casting capabilities

We conclude that only CVD-grown CNTs provide us with the necessary lengths for our application i.e. tens to hundreds of micrometers. Tunneling junction transmission through multiple solution-deposited CNTs would dampen the wave. Vertical CNTs allow the fabrication of long CNTs but, for low N_{CNT} , involve high-aspect-ratio standing structures

difficult to realize. This fabrication process being well mastered in CINTRA, we used it for the design and fabrication of monopole antennas [172], [173] as reported in section IV.D). Additionally methods have been devised to make these antennas more robust. Finally, the lattice-aligned horizontal CNTs seem to be the best logical choice with high-quality ultra-straight SWCNTs easier to connect and characterize. Therefore the first prototypes we describe rely on this type of CNTs (cf. section IV.B)) and efforts were lead to develop this type of growth in CINTRA where there was no prior established process as we have just described in section III.B).

Chapter IV) Resonant electrically-short CNT antennas

As introduced in Chapter I), one of the interesting reasons to investigate CNTs for antenna applications is that they should allow a size reduction for resonant components beyond usual limits by a slow-wave effect. These plasmon resonances however require specific configurations that need to be carefully studied.

Here, we first present the theory and design rules of electrically-short resonant CNT-based antennas by considering ideal cases of monopole and dipole antennas. Then, based on the models and modeling strategies developed in Chapter II), we propose tools to help make the appropriate trade-offs in order to achieve designs meeting specific requirements. Finally we describe the experimental prototypes conceived, designed and realized based on this study and current CNT fabrication techniques. Transmission is investigated in a few configurations and usage recommendations are formulated.

IV.A) Trade-offs and tools

IV.A.1) First observations

IV.A.1.1) Single-SWCNT-arm antennas

Both circuit [16] and EM [10] models have been applied to the study of a dipole made of two metallic SWCNTs. They both conclude that, at a given resonant frequency, these antennas can be scaled down by a factor 50 relatively to the original physical limit. Indeed, P.J. Burke and G.W. Hanson estimate the propagation velocity of EM waves in a single CNT to be about 2% of the speed of light in vacuum [10], [16]. Nevertheless, it is outlined that single tubes present too high impedance and radiate very poorly. The antennas are highly damped [16] and, below a certain frequency, 53GHz, damping will prevent any resonance [10] (cf. Fig. 20).

We shall first compare the radiation properties of a classical electrically-short dipole to those of a resonant CNT dipole to outline what improvement can be expected from the latter. In the usual case of electrically-short dipoles (total length $(2l) < \frac{\lambda}{10}$ where l is the length of a radiating arm and λ the wavelength at operating frequency), the current can be approximated

as a linear taper from its maximal value at the center of the antenna to its minimal value at the edges. Following this, the radiation resistance is found proportional to l^2 [174]:

$$R_{r,l \ll \lambda} = \sqrt{\frac{\mu}{\epsilon}} \frac{\beta^2 (2l)^2}{6\pi} \left(\frac{I_{avg}}{I_0}\right)^2 \approx 80\pi^2 \left(\frac{2l}{\lambda}\right)^2 \left(\frac{I_{avg}}{I_0}\right)^2 \quad (\Omega) \quad (109)$$

where I_{avg} is the amplitude of the average current in the dipole and I_0 is the amplitude of the terminal current of the center-fed dipole. In the case of a short dipole without end-loading, aligned along \mathbf{z} , the current amplitude linearly tapers from I_0 at its center ($z = 0$) to 0 at its ends ($z = \pm l$): $I(z) = I_0 \left(1 - \frac{|z|}{l}\right)$. Therefore $I_{avg} = \frac{1}{2}I_0$ and, in vacuum:

$$R_{r,l \ll \lambda} = 20\pi^2 \left(\frac{2l}{\lambda}\right)^2 \quad (\Omega) \quad (110)$$

For a dipole fifty-fold shorter than the resonant half-wavelength, we have $l = \frac{\lambda}{50}$ and thus $R_{r,l \ll \lambda} = 20\text{m}\Omega$. Another aspect to consider is the losses. Integrating the ohmic losses over the dipole, we find a ohmic resistance linearly proportional to l :

$$R_{loss,l \ll \lambda} = \text{Re} \left(\frac{2l}{3\pi a_{eff}^2 \sigma} \right) = \frac{2l}{3\pi a_{eff}^2} \text{Re} \left(\frac{1}{\sigma} \right) \quad (111)$$

where we have defined:

$$a_{eff} \equiv \begin{cases} a, & a \leq \delta_{skin} \\ \sqrt{(2a - \delta_{skin})\delta_{skin}}, & a \geq \delta_{skin} \end{cases} \quad (112)$$

the radius of the effective cross-section of the wire. We recall equation (35) for the skin depth: $\delta_{skin} = \sqrt{\frac{2}{\omega\mu\sigma}}$. Defining the antenna efficiency as the ratio of the power dissipated in radiation to the total power dissipated (radiation and ohmic), the efficiency quite intuitively improves with increasing l :

$$\eta \equiv \frac{P_{rad}}{P_{rad} + P_{loss}} = \frac{R_{rad}}{R_{rad} + R_{loss}} = \frac{1}{1 + \frac{A(\lambda)}{2l}} \quad (113)$$

where $A(\lambda) = \frac{1}{60\pi^3} \text{Re} \left(\frac{1}{\sigma} \right) \left(\frac{\lambda}{a_{eff}} \right)^2$ (m) is independent of l but a function of λ and the conductivity of the metal.

It is quite the opposite for a resonant CNT antenna. Using a longer resonant CNT at a given frequency will decrease the radiation efficiency. Indeed, the radiated (far-field) electric field is proportional to the coherent sum of the currents on the antenna segments. As explained in [16], for resonant configurations this can be seen as the coherent sum of in-phase and opposite-phase contributions on $\lambda_p/4$ - long segments, where λ_p is the plasmon wavelength i.e. the wavelength when propagating along the CNT in the given embedding medium. At odd resonances, i.e. for $l_{CNT} \approx (2p + 1) \frac{\lambda_p}{4}, p \in \mathbb{N}$ there are $2p$ pairs of opposite current contributions canceling each other out and 2 in-phase segments that emit (cf. cases $\frac{1}{4}\lambda_p, \frac{3}{4}\lambda_p$ on Fig. 54).

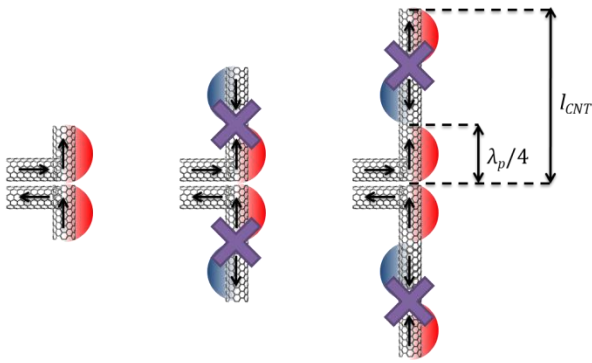


Fig. 54. Current distribution schematic for 3 resonant total lengths: $\frac{1}{4}\lambda_p, \frac{1}{2}\lambda_p, \frac{3}{4}\lambda_p$. Because the far-field is the coherent sum of the contributions, for odd resonances, the emitted field is the same as the first resonance while the even resonances are actually anti-resonances, they do not emit. A CNT dipole about half-plasmon-wavelength-long is thus the most efficient configuration.

Hence there is no additional radiation compared to the half-plasmon-wavelength dipole case. Neglecting losses, the radiation resistance is thus the same. For even, or anti-, resonances i.e. for $l_{CNT} \approx (p + 1) \frac{\lambda_p}{2}, p \in \mathbb{N}$ the radiation is null with $2(p + 1)$ pairs of opposite current contributions canceling each other out (cf. case λ_p on Fig. 54). Hence, as formalized in [16], $R_{rad}(l_{CNT})$ is a periodic function with maximum value at odd resonances rapidly decreasing off resonance and minimum value (0) at even resonances. If the radiation resistance remains unchanged for odd resonances, the losses increase linearly with the length of the CNT. Finally for an odd-resonant CNT dipole, we have:

$$\eta(L_{CNT}) = \frac{R_{rad}}{R_{rad} + R_{loss}} = \frac{1}{1 + \frac{2R_Q}{R_{r,(2p+1)\frac{\lambda_p}{4}}} l_{CNT}} \quad (114)$$

where R_Q is the quantum resistance introduced in section II.A.4) and, as rigorously shown in Appendix 4, for an odd-resonant CNT dipole (i.e. $l_{CNT} = (2p + 1)\frac{\lambda_p}{4}, p \in \mathbb{N}$) sufficiently short (i.e. $(2\pi \frac{(2p+1)\lambda_p}{4} \frac{\lambda_p}{\lambda})^2 \ll 1$) the radiation resistance is:

$$R_{r,(2p+1)\frac{\lambda_p}{4}} = \left(\frac{\lambda_p}{\lambda}\right)^2 \sqrt{\frac{\mu}{\epsilon}} \xi \approx 80 \left(\frac{\lambda_p}{\lambda}\right)^2 \quad (115)$$

For the primary resonance, $l_{CNT} = \frac{\lambda_p}{4}$, recalling equation (109), this is $\frac{80}{\frac{20}{4}\pi^2} \approx 1.6$ times more than the short dipole of the same length, independently of λ_p . This is merely because of the larger average current amplitude over the arms of the antenna for the resonant CNT antenna. Indeed it displays a current distribution from I_0 at its center ($z = 0$) to 0 at its ends ($z = \pm \frac{\lambda_p}{4}$) of the type: $I(z) = I_0 \sin\left(k_p \left|\frac{\lambda_p}{4} - z\right|\right)$ rather than a taper. Hence the radiated power ratio between the two is $\frac{R_{r,(2p+1)\frac{\lambda_p}{4}}}{R_{r,l \ll \lambda}} = \left(\frac{I_{avg,(2p+1)\frac{\lambda_p}{4}}}{I_{avg,l \ll \lambda}}\right)^2 = \left(\frac{4}{\pi}\right)^2 \approx 1.6$. Numerically, for $\lambda_p = \frac{\lambda}{50}$, we thus find $R_{r,(2p+1)\frac{\lambda_p}{4}} = 80 \times \frac{1}{50^2} \approx 32\text{m}\Omega$. However for the third resonance, the CNT antenna already has a radiation resistance $\frac{9\pi^2}{16} \approx 5.6$ times lower than its classical counterpart. Therefore CNT antennas shall be used at their primary resonance which also gives the shortest antennas for a given operating frequency. This reasoning and conclusion apply to bundle-based-antennas as well.

Even so, the advantage of a single-m-SWCNT antenna over the short dipole is still not clear because of the high resistivity of the SWCNT. CNTs are reputed to have excellent conductivity but that is with regards to the volume actually carrying current while, if comparing to nanowires (NW) it is the actual occupied volume that matters. Then the CNTs conductivity would be lower than that of gold nanowires if they had the same conductivity as the bulk material. However, the conductivity in NWs is reduced when the diameter becomes of the order of or lower than the mean-free path in the material, estimated at 40nm for copper and similar for gold [175]. The conductivity is affected as follows:

$$\sigma_0(a) = r(a)\sigma_0 \quad (116)$$

$$r(a) = \left(1 + (1 - p) \frac{MFP}{2a}\right)^{-1} \quad (117)$$

Where p is the specularity parameter for electron reflection from the wire surface [175]. We follow a best case scenario for metallic NWs by taking $p = 0.5$ and disregarding the potential negative effect of grain-boundary scattering.

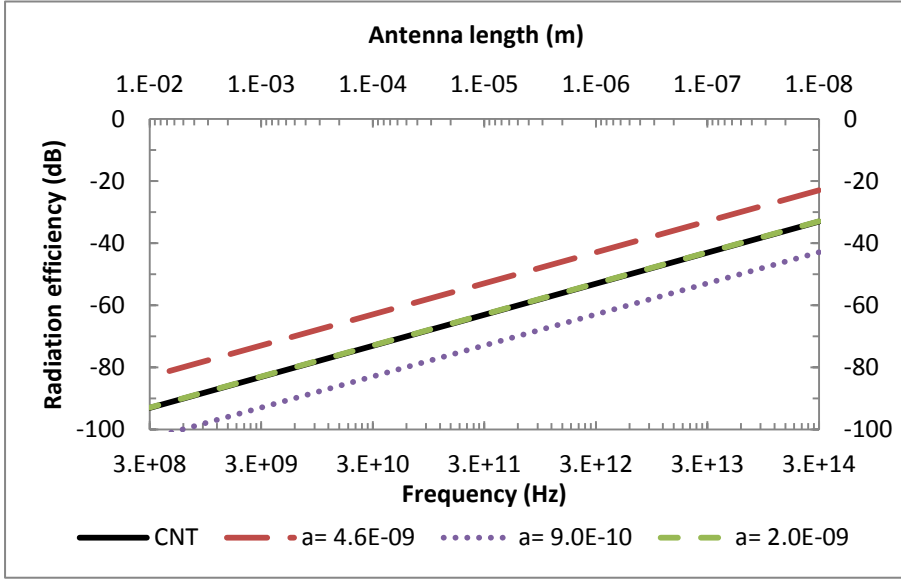


Fig. 55. Radiation efficiency of a $\frac{\lambda}{100}$ dipole with resonant m-SWCNT arms and non-resonant NW arms of various radii. Despite its higher R_{rad} , the SWCNT dipole is only a more efficient radiator than the gold NWs if the latter have a radius $a \leq 2\text{nm}$.

Based on this correction and the previously exposed CNT models, we evaluated the radiation efficiency as a function of frequency for different diameters of NW and a m-SWCNT dipole antenna. This is presented on Fig. 55. We cover the frequency range corresponding to commonly fabricated CNT lengths and assuming a constant size reduction of 50. Actually the 3GHz and 300THz extreme frequencies are one order of magnitude out of range for some of our models but we do not intend to exploit them further as they also correspond to extreme lengths – 1cm and 10nm. Since the radiation resistance is constant with frequency for a given l/λ and is rather small relatively to losses, the efficiency logically progresses at 20dB/decade with frequency i.e. decreasing length and thus losses.

For a radius $a = 0.9\text{nm}$ i.e. a diameter $d = 1.8\text{nm}$, the losses are such in the metal NW that the CNT antenna is 10 times more efficient than the topologically equivalent NW antenna for any frequency. Furthermore, it is more efficient than NWs with radius not in excess of $a = 2\text{nm}$. Hence, for most experimental SWCNTs, at equivalent dimensions or even 2 to 4 times smaller diameter for average SWCNTs, an m-SWCNT antenna is more

efficient than a NW antenna. Nevertheless, if the application does not require an antenna of diameter less than 4nm then a metal rod will be more efficient. For bundled CNTs, the gain in radiation resistance may be better exploited thanks to lower loss.

On Fig. 56 we plot the efficiency as a function of the radius for frequencies from 3GHz to 300THz. For these diameters, even at highest frequencies the skin effect in NWs is still negligible. It starts to matter for radius of 50nm in the terahertz range and not before 0.5 μ m at 300GHz. The $a = 2$ nm cross-over between CNTs and NWs efficiency can be clearly seen for each frequency and we note the very low efficiencies of single m-SWCNTs. At 300GHz a single m-SWCNT has a radiation efficiency of -63dB or 0.00005% - rather the characteristics of an absorber than that of an antenna.

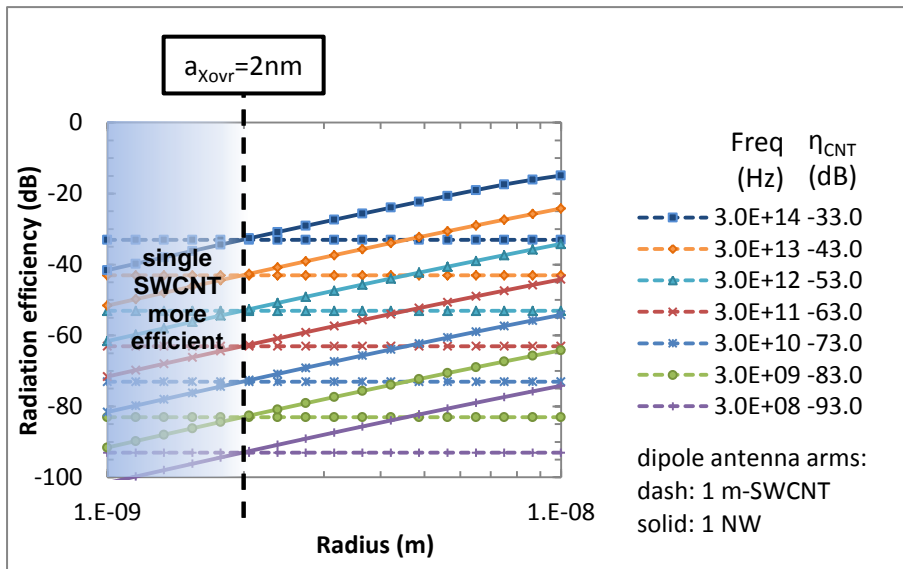


Fig. 56. Radiation efficiency versus diameter for single m-SWCNT and NW dipole antennas.

To improve the radiation efficiency we need to decrease the losses while keeping a short resonant antenna. Indeed the radiation resistance of a resonant CNT antenna is independent of its length while the radiation resistance of a normal short dipole is inversely proportional to the square of the size reduction factor as we saw in equation (110).

The high impedance of single m-SWCNTs is also an issue for integration with conventional technology. Indeed, to avoid impedance mismatch – and thus power transmission issues – with common RF components and circuits, antennas should be designed with a 50 to 75 Ω input impedance whereas the two-CNT dipoles present impedances in the order of tens of k Ω .

IV.A.1.2) Improving performances: MWCNTs and bundles

CNTs with metallic cores [20], [176] or other metal-CNT combinations may be used to decrease the impedance, but they decrease the total inductance even more than the total resistance by adding components (conventional metals) in parallel that present negligible kinetic inductance at these frequencies.

The solution may be to add CNT shells in parallel, be it through bundling or using MWCNTs, which will quite intuitively decrease the total impedance.

For MWCNTs, following equations (40) and (43) the impedance of shells decreases for larger diameters D while the kinetic inductance L_K to resistance R_Q ratio increases linearly with the diameter:

$$\frac{L_K}{R_Q}(D) = \tau(D) = \frac{MFP(D)}{v_F} = \frac{l_0 D}{v_F} \quad (118)$$

where we recall that the mean free path MFP is proportional to the diameter by a constant l_0 and v_F is the Fermi velocity. This is interesting because the plasmon cut-off frequency is shifted lower. Nevertheless each shell will have a different plasmon lifetime $\tau(D)$ which makes the problem counter-intuitive. At intermediate frequencies, a wave may be allowed to resonate on the outermost shells of the MWCNT but not at its core leading to dampening. It is also interesting to note that, because the external shell shields the others, it will be the only shell radiating. Therefore the radiation resistance may be unchanged from the SWCNT case if a plasmon resonance can be created. More likely though, large-diameter MWCNTs will act as classical short dipoles. Few-wall CNTs may strike a balance between decreased inductance-impedance and better reactance/resistance ratio and it would be interesting to try to use them in plasmon resonant structures.

Hanson integrated MWCNTs in his antenna efficiency study in [175] based on the DC conductivity proposed in [108] (cf. section II.B.3.3). Extensive treatment of MWCNTs as antennas and waveguides in the infrared regime was led by M.V. Shuba et al. [20]. The complex phenomena taking place in these structures seem however difficult to take properly into account in an antenna design approach.

Instead we base our study on bundles of SWCNTs (B(SW)CNTs). These can allow us to overcome the problem of the high impedance and low efficiency of single tubes. Methods to synthesize SWCNTs or to sort them by chirality exist and thus allow us to prepare for agile antennas at the same time where we would use sc-SWCNTs as photoswitches for instance. Furthermore, single CNT devices are extremely impractical to fabricate especially with the lengths needed (typically tens of microns). Bundles come closer to experimental reality. The conclusions on BCNTs found in literature being rather scarce and relying on specific structures, it appeared necessary to lead a systematic study of simple antennas as a basis for more complicated design

In section II.C.2.2), and initially in [177], we reported how the resonance frequency of monopoles and dipoles was shifted towards higher frequencies when CNTs were added in parallel. We will now systematize this study.

IV.A.1.3) Effect of bundling and trade-offs

As initially exposed in [89], EM simulation of BCNT-based antennas allows us to study and highlight the trade-offs involved in the design of such antennas.

IV.A.1.3.1) Structure and methodology

For this study, we used EMXD with both the surface impedance model and the effective medium approach, as described in sections II.A.3) (originally in [88]) and II.B). The structure used is the same as the monopole described in II.C.2) but we reiterate and extend the description for convenience.

We study a vertical wire monopole perpendicular to a ground plane excited by a 50Ω lumped port. The wire is replaced by a bundle of CNTs. We use hexagonal bundles as depicted Fig. 19 for mesh efficiency. They are made of hexagonal concentric layers of CNTs. For N_{layers} CNT layers arranged around a central CNT, the total number of CNTs is $N_{shells} = 1 + 3N_{layers}(N_{layers} + 1)$. The monopole configuration being a simple and ideal structure its behavior is well understood and resonances are easily interpreted. When it operates as a quarter wavelength resonator, it is supposedly the smallest resonant antenna configuration for the given frequency. Hence any resonant behavior below this specific frequency shall be due to the specific characteristics of the CNTs. Furthermore the simplicity

of the structure helps keeping the number of mesh elements needed relatively low; this reduces memory use and computation time.

An extensive parametric study of CNT-based monopoles was led with two technologically relevant lengths: 40 and 80 micrometer-long CNTs. These lengths can be realized by in-situ growth. The resulting antennas resonate in the EHF (millimeter) band which would make them measurable with certain VNA setups and terahertz techniques. This also makes them technologically relevant solutions as there is ongoing effort towards EHF and terahertz devices. As will be shown, our conclusions can actually be extended to various lengths.

IV.A.1.3.2) Results

The first observation is that, at a given length, increasing the number of CNTs in the bundle does not only produce the desired effect – namely decreasing the overall impedance by putting impedances in parallel – but shifts the resonance frequency upwards, thus reducing the hypothetical gain in size for CNT-based antennas. Indeed, while decreasing the impedance, we equally decrease the resistance and the kinetic inductance. As a first approximation the resonance frequency is $f_{res} = \frac{v_p}{\lambda_p} \approx \frac{1}{4l_{CNT}} \sqrt{\frac{1}{LC}}$ and increases with decreasing inductance. This is illustrated Fig. 57. Although an input impedance plot would be more general, we chose to plot the return loss normalized at 50Ω because it is more tangible information for antenna design. Note the clear shift in resonance frequency with increasing number of tubes. Coordinately, the return loss at resonance displays a minimum for the configuration where the nearest 50Ω match is realized.

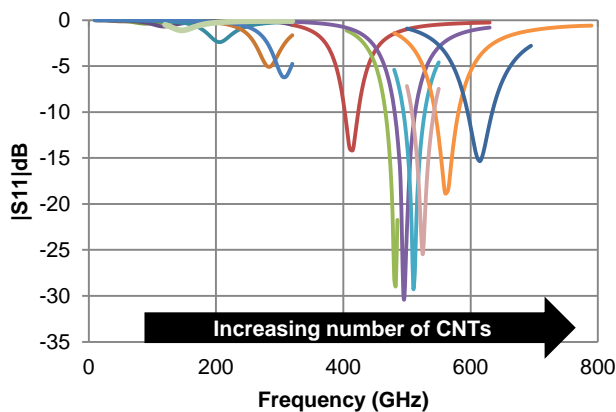


Fig. 57. Return loss plotted against frequency for 80um-long bundled-CNT monopoles with number of CNTs varying from 1 to 2791 (30 hexagonal layers). The best impedance match is achieved with 1261 CNTs ± 100 (20 layers ± 1) while -15dB impedance match is achieved with 721 to 2791 CNTs.

This shift makes designing CNT antennas more complicated than simply adding CNTs in parallel to reach the desired impedance. Nonetheless, this enables tailoring CNT antennas to an impedance match and a resonance frequency as shown in Fig. 58. Indeed, the impedance decreases linearly with the number of tubes whereas, in this configuration and from 1 to a few thousand tubes, the shift of the resonance frequency is well approximated as proportional to $N_{\text{shells}}^{0.44}$. Put otherwise the propagation velocity in a bundle is only multiplied by 2.75 when the number of tubes is increased tenfold (Fig. 59). This observation is independent on the length of the tube and saturates at geometrical resonance. Hence various configurations of tube number and length can be used to obtain the desired input impedance and resonant frequency.

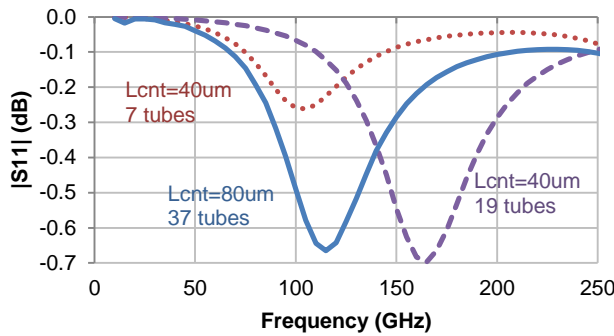


Fig. 58. Return loss for three different configurations of monopole show that similar impedance or operating frequency can be obtained by varying the parameters. However the lower operating frequency with better impedance match is obtained against a doubled size. The high return loss values are due to the normalization at 50Ω for these few-CNTs high-impedance antennas and we are only interested in their relative values here.

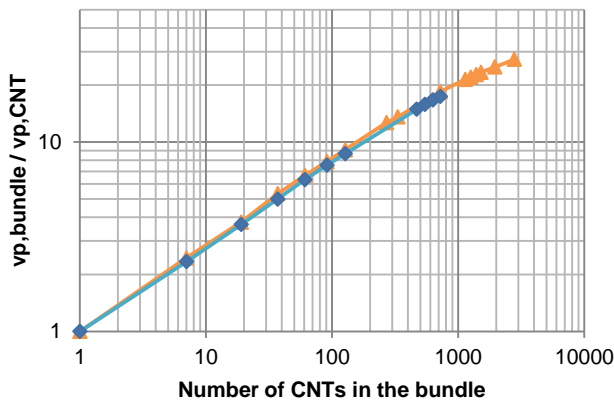


Fig. 59. EM waves propagation velocity ratio between a single tube and a bundle of N tubes. $40\mu\text{m}$ -long (blue diamonds) and $80\mu\text{m}$ -long (orange triangles) bundled-CNT monopoles with varying number of CNTs are used. For both lengths, the velocity ratio rises at 4.4dB/decade .

Still, below the plasma relaxation frequency, $F_v = 1/(2\pi\tau)$, damping will prevent any resonance. Taking a plasmon lifetime $\tau = 3.10^{-12}\text{s}$ [10], we have $F_v = 53\text{GHz}$. This restrains the application of CNT antennas to millimeter and sub-millimeter ranges. As seen with our study, tubes that cannot resonate alone because of a too low fundamental frequency may resonate in a bundle when the frequency has shifted above F_v .

Finally, we summarize the antenna specific performance as a function of the configuration on Fig. 60. There is a clear trade-off between performance and gain in size as compared to a resonant copper antenna in the same monopole configuration. Here we have chosen to plot the percentage of accepted input power rather than the usual return loss in dB to emphasize the acceptably-matched range of configurations rather than the optimal impedance matches. This is plotted for a 50Ω excitation. As seen when comparing the curves for 40 and $80\mu\text{m}$ lengths, selecting higher operating frequencies (e.g. 390GHz rather than 285GHz) and thus shorter CNTs, decreases the impedance, making it possible to use fewer tubes and still have the same impedance match (the accepted power curve shifts to the left). Since the size reduction factor is not dependent on the length of the tubes used but only on their number, this allows for a better gain in size at the same impedance (4.3 instead of 3 in the chosen case for -5dB return loss i.e. 68% of accepted power at 50Ω). The same holds if the matching impedance is increased: the curves will shift to the left. This could either be achieved by impedance matching or using the antennas in an array.

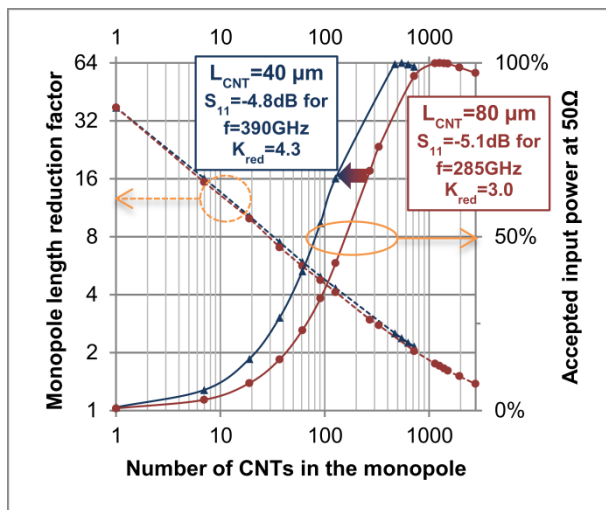


Fig. 60. Size reduction factor K_{red} (compared to a resonant copper monopole) and antenna performance plotted against the number of CNTs in the bundle. Note the shift to the left of the $40\mu\text{m}$ curve with respect to the $80\mu\text{m}$ one. The size gain is only dependent on N_{shells} . By operating at higher frequencies or higher impedance, the relative gain in size is more important for a similar performance.

IV.A.1.3.3) Initial interpretation and conclusions

We have performed 3D EM simulation of CNT-based monopole antennas, thus modeling all the EM effects participating in their resonance. The results show that bundled CNTs allow the conception of tailored antennas in certain ranges of frequency and impedance. We have outlined the key parameters and trade-offs in this simple configuration which should help designing more realistic antenna structures at sizes smaller than the classical physical limit.

In [168], we explain how these trends can be understood through a circuit approach. Indeed using N_{CNT} CNTs in parallel results in dividing the overall impedance and thus the kinetic inductance by N_{CNT} : $Z_{bundle} = Z_{CNT}/N_{CNT} = R_Q/N_{CNT} + j\omega L_K/N_{CNT}$. Neglecting the magnetic inductance and resistance, the propagation velocity along the CNTs can be written:

$$v_{p,bundle} = \frac{1}{\sqrt{LC}} \approx \frac{1}{\sqrt{L_{K,tot} C_{tot}}} \quad (119)$$

and, because the total capacitance has relatively small variations with N_{CNT} , we obtain:

$$v_{p,bundle} \approx \sqrt{\frac{N_{CNT}}{L_K C}} = \sqrt{N_{CNT}} v_{p,CNT} \quad (120)$$

Then at fixed CNT length l_{CNT} the resonance frequency is given by:

$$f_{res,bundle} = \frac{v_{p,bundle}}{\lambda_{p,bundle}} \approx \frac{v_{p,bundle}}{4l_{CNT}} \approx \frac{\sqrt{N_{CNT}}}{l_{CNT}} \frac{1}{4} v_{p,CNT} \quad (121)$$

Hence, in first approximation, the impedance is inversely proportional to N_{CNT} and proportional to l_{CNT} while the resonance frequency is proportional to $\sqrt{N_{CNT}}$ and inversely proportional to l_{CNT} . A trade-off thus needs to be found between size reduction, operating frequency and input impedance (cf. Fig. 60). For an antenna with good size reduction less than 100-1000 CNTs should be used. For it to be well-matched to 50Ω , short CNTs thus need to be used and this leads to working at extremely high frequencies: 200GHz and higher. Lower frequencies and good size reduction are possible at higher impedance.

A more rigorous approach to the circuit model would help us predict the CNT bundle monopole behavior more precisely. We develop it in the following section.

IV.A.2) CNT monopole circuit model

IV.A.2.1) Derivation

Here, from basic transmission line theory exposed in section II.A.4.1), we derive the full expression of $\gamma = \alpha + j\beta$ and Z_C in the general lossy case before applying it to the

SWCNT bundle problem. β gives us v_p while, for a dipole or a monopole with each arm long of l_{CNT} , neglecting the radiation loss, Z_{in} can be calculated as [16]:

$$Z_{in} = Z_C \coth(\gamma l_{CNT}) \quad (122)$$

This is, to our knowledge, the first time the equations for this fully analytical circuit model for bundles of CNTs in monopole or dipole configuration is reported although efforts on the same structures have been described in [109], [119], [124], [178] based on the usual circuit and EM approaches. Our equations can be used analytically or implemented in spreadsheets and simple codes which allows their integration in a design process.

IV.A.2.1.1) Derivation in the general case

Taking the square of equation (12), we have, by:

$$\gamma^2 = (\alpha + j\beta)^2 = (R + j\omega L)(G + j\omega C) \quad (123)$$

Which translates into the set of equations (imaginary and real part):

$$\begin{cases} 2\alpha\beta = \omega(RC + LG) \end{cases} \quad (124)$$

$$\begin{cases} \alpha^2 - \beta^2 = RG - \omega^2 LC \end{cases} \quad (125)$$

The case $\beta = 0$ corresponds to no propagation. For $\beta \neq 0$ we can then write:

$$\begin{cases} \alpha = \frac{\omega}{2\beta}(RC + LG) = v_p \frac{(RC + LG)}{2} \end{cases} \quad (126)$$

$$\begin{cases} 0 = \beta^4 + \beta^2(RG - \omega^2 LC) - \left(\frac{\omega}{2}\right)^2 (RC + LG)^2 \end{cases} \quad (127)$$

Then taking the positive root of the 2nd order polynomial equation in β^2 we find:

$$\begin{cases} \alpha = \omega\sqrt{LC} \frac{K_{RG}}{\sqrt{2(1 + \sqrt{1 + K_{RG}^2})}} \end{cases} \quad (128)$$

$$\begin{cases} \beta = \omega_{RG}\sqrt{LC} \sqrt{\frac{1 + \sqrt{1 + K_{RG}^2}}{2}} = \beta_{lossless} \frac{\omega_{RG}}{\omega} \sqrt{\frac{1 + \sqrt{1 + K_{RG}^2}}{2}} \end{cases} \quad (129)$$

where we have defined a pulsation and unit-less factor as:

$$\begin{cases} \omega_{RG} = \sqrt{\omega^2 - \frac{RG}{LC}} \\ K_{RG} = \frac{1}{\omega_{RG}} \left(\frac{R}{L} + \frac{G}{C} \right) \end{cases} \quad (130)$$

$$\quad (131)$$

Finally we obtain the phase velocity as:

$$\begin{aligned} v_p &= \frac{\omega}{\beta} = \frac{1}{\sqrt{LC}} \frac{\omega}{\omega_{RG}} \sqrt{\frac{2}{1 + \sqrt{1 + K_{RG}^2}}} \\ &= v_{p,lossless} \frac{\omega}{\omega_{RG}} \sqrt{\frac{2}{1 + \sqrt{1 + K_{RG}^2}}} \end{aligned} \quad (132)$$

and the wavelength as:

$$\begin{aligned} \lambda_p &= \frac{2\pi}{\beta} = \frac{v_p}{f} = \frac{1}{\frac{\omega_{RG}}{2\pi} \sqrt{LC}} \sqrt{\frac{2}{1 + \sqrt{1 + K_{RG}^2}}} \\ &= \lambda_{p,lossless} \frac{\omega}{\omega_{RG}} \sqrt{\frac{2}{1 + \sqrt{1 + K_{RG}^2}}} \end{aligned} \quad (133)$$

Note that the characteristic impedance can also be reformulated to see the effect of the losses compared to the lossless case as:

$$Z_C = \sqrt{\frac{R + j\omega L}{G + j\omega C}} = \frac{\omega_{RG}}{\omega} \sqrt{\frac{L}{C}} \sqrt{\frac{1 + j \frac{\omega}{\omega_{RG}^2} \left(\frac{G}{C} - \frac{R}{L} \right)}{1 + \left(\frac{G}{\omega C} \right)^2}} \quad (134)$$

For $\frac{G}{\omega C} < 1$, we can also use the slightly more compact form:

$$Z_C = \frac{\omega_{RG}}{\omega} \sqrt{\frac{L}{C}} \sqrt{\frac{1 - j \frac{\omega}{\omega_{RG}^2} K_{RG}}{1 - \left(\frac{G}{\omega C} \right)^2}} \quad (135)$$

which separates into real and imaginary parts as follows:

$$\left\{ \begin{aligned} Z_{Cr} &= \frac{\omega_{RG}}{\omega} \sqrt{\frac{L}{C}} \sqrt{\frac{1 + \sqrt{1 + \left(\frac{\omega}{\omega_{RG}} K_{RG}\right)^2}}{2 \left(1 - \left(\frac{G}{\omega C}\right)^2\right)}} = Z_{C,lossless} \frac{\omega_{RG}}{\omega} \sqrt{\frac{1 + \sqrt{1 + \left(\frac{\omega}{\omega_{RG}} K_{RG}\right)^2}}{2 \left(1 - \left(\frac{G}{\omega C}\right)^2\right)}} \end{aligned} \right. \quad (136)$$

$$\left\{ \begin{aligned} Z_{Ci} &= -\sqrt{\frac{L}{C}} \frac{K_{RG}}{\sqrt{2 \left(1 + \sqrt{1 + \left(\frac{\omega}{\omega_{RG}} K_{RG}\right)^2}\right) \left(1 - \left(\frac{G}{\omega C}\right)^2\right)}} \end{aligned} \right. \quad (137)$$

It can be verified that all these expressions give the expected simplified values in the case of negligible losses (cf. previous chapter). Indeed, for $R \ll \omega L$ and $G \ll \omega C$, we have:

$$\left\{ \begin{aligned} \omega_{RG} &= \omega \sqrt{1 - \left(\frac{R}{\omega L}\right) \left(\frac{G}{\omega C}\right)} \approx \omega \end{aligned} \right. \quad (138)$$

$$\left\{ \begin{aligned} K_{RG} &\approx \left(\frac{R}{\omega L} + \frac{G}{\omega C}\right) \ll 1 \end{aligned} \right. \quad (139)$$

The application to CNTs is simply done by replacing L, C, R, G by the expressions given in the previous chapter according to the geometrical configuration chosen.

IV.A.2.1.2) Case of negligible conductance

In the cases we deal with, R cannot be neglected but for CNTs in air or a good dielectric embedding medium, even at the smallest frequencies of interest, we have $G \ll \omega C$ and thus:

$$\left\{ \begin{aligned} \omega_{RG} &\approx \omega \end{aligned} \right. \quad (140)$$

$$\left\{ \begin{aligned} K_{RG} &\approx \frac{R}{\omega L} \end{aligned} \right. \quad (141)$$

Consequently the attenuation constant and wavenumber are given by:

$$\left\{ \begin{array}{l} \alpha = \omega\sqrt{LC} \frac{\frac{R}{\omega L}}{\sqrt{2\left(1 + \sqrt{1 + \left(\frac{R}{\omega L}\right)^2}\right)}} \end{array} \right. \quad (142)$$

$$\left\{ \begin{array}{l} \beta = \omega\sqrt{LC} \frac{\sqrt{1 + \sqrt{1 + \left(\frac{R}{\omega L}\right)^2}}}{2} \end{array} \right. \quad (143)$$

Hence, the expressions of the phase velocity, wavelength and characteristic impedance simplify as:

$$v_p = \frac{\omega}{\beta} = \frac{1}{\sqrt{LC}} \sqrt{\frac{2}{1 + \sqrt{1 + \left(\frac{R}{\omega L}\right)^2}}} \quad (144)$$

$$\lambda_p = \frac{v_p}{f} = \frac{1}{\frac{\omega}{2\pi}\sqrt{LC}} \sqrt{\frac{2}{1 + \sqrt{1 + \left(\frac{R}{\omega L}\right)^2}}} \quad (145)$$

and:

$$Z_c = \sqrt{\frac{R + j\omega L}{j\omega C}} = \sqrt{\frac{L}{C}} \sqrt{1 - j\frac{R}{\omega L}} \quad (146)$$

We can separate real and imaginary parts as follows:

$$\left\{ \begin{array}{l} Z_{cr} = \sqrt{\frac{L}{C}} \sqrt{\frac{1 + \sqrt{1 + \left(\frac{R}{\omega L}\right)^2}}{2}} \end{array} \right. \quad (147)$$

$$\left\{ \begin{array}{l} Z_{ci} = -\sqrt{\frac{L}{C}} \frac{\frac{R}{\omega L}}{\sqrt{2\left(1 + \sqrt{1 + \left(\frac{R}{\omega L}\right)^2}\right)}} \end{array} \right. \quad (148)$$

Finally, the wave amplitude attenuation over a propagation of a quarter-wavelength (one-way trip on a monopole or the arm of a dipole while neglecting the radiation resistance) is given by:

$$A(\lambda_p/4) \equiv \frac{V(\lambda_p/4)}{V(0)} = e^{-\alpha \frac{\lambda_p}{4}} = e^{-\frac{\pi}{2} \frac{\frac{R}{\omega L}}{1 + \sqrt{1 + (\frac{R}{\omega L})^2}}} \quad (149)$$

IV.A.2.2) Implications for the design of CNT-based antennas

We use the line parameters we derived for the general case of lossy lines to discuss the implications for BCNT antenna design.

IV.A.2.2.1) Moderate and low-loss regime

I.A.1.1.1.1) Definition

In all these expressions, it can be verified that for $\left(\frac{R}{\omega L}\right)^2 \ll 1$ or, equivalently, for $\omega^2 \gg \left(\frac{R}{L}\right)^2$ the equations of the phase velocity and wavelength are the same as those of the lossless case with minimal error:

$$v_p = \frac{\omega}{\beta} \approx \frac{1}{\sqrt{LC}} \left(1 - \frac{1}{8} \left(\frac{R}{\omega L}\right)^2\right) \approx \frac{1}{\sqrt{LC}} \quad (150)$$

$$\lambda_p = \frac{v_p}{f} \approx \frac{1}{\frac{\omega}{2\pi} \sqrt{LC}} \left(1 - \frac{1}{8} \left(\frac{R}{\omega L}\right)^2\right) \approx \frac{1}{\frac{\omega}{2\pi} \sqrt{LC}} \quad (151)$$

while the characteristic impedance can only be considered purely real and equivalent to the lossless case for the extended limit $\omega \gg \frac{R}{L}$:

$$\begin{aligned} Z_c &= \sqrt{\frac{R + j\omega L}{j\omega C}} \approx \sqrt{\frac{L}{C} \left(\left(1 + \frac{1}{8} \left(\frac{R}{\omega L}\right)^2\right) - j \frac{1}{2} \frac{R}{\omega L} \left(1 - \frac{1}{8} \left(\frac{R}{\omega L}\right)^2\right) \right)} \\ &\approx \sqrt{\frac{L}{C} \left(1 - \frac{j}{2} \frac{R}{\omega L}\right)} \end{aligned} \quad (152)$$

For a bundle of CNTs the total resistance and total inductance are given by:

$$R_{bdl} = \frac{R_Q}{N_{CNT}} \quad (153)$$

$$L_{bdl} = \frac{L_K}{N_{CNT}} + L_{M,bdl} \quad (154)$$

Hence, the low-loss condition translates into $\omega^2 \gg \left(\frac{R}{L}\right)^2 = \left(\frac{R_Q/N_{CNT}}{L_K/N_{CNT} + L_{M,bdl}}\right)^2$. Because $\left(\frac{R_Q/N_{CNT}}{L_K/N_{CNT} + L_{M,bdl}}\right)^2 \lesssim \left(\frac{R_Q}{L_K}\right)^2 = \left(\frac{1}{\tau}\right)^2$, it is always verified for $\omega^2 \gg \left(\frac{1}{\tau}\right)^2$. There are furthermore two extreme cases: $\omega^2 \gg_{N_{CNT} \ll \frac{L_K}{L_{M,bdl}} \sim 10^4} \left(\frac{1}{\tau}\right)^2$ and $\omega^2 \gg_{N_{CNT} \gg \frac{L_K}{L_{M,bdl}} \sim 10^4} \left(\frac{R_Q}{N_{CNT} L_{M,bdl}}\right)^2 \sim \left(\frac{3690}{N_{CNT} \tau}\right)^2$. This formalizes the intuitive rule that a CNT resonant antenna has a constant lower frequency damping limit due to quantum properties when it is made of a limited number of CNTs but, for large CNT numbers, the CNT bundle becomes similar to a classical metal and can have resonances at lower frequencies.

For the limit case of large CNT numbers, $N_{CNT} = 10^5$, taking $\tau = 3\text{ps}$ as in [10], the low-loss condition becomes $\omega^2 \gg (12.3\text{GHz})^2$ so $f \geq \frac{\sqrt{10}}{2\pi} \times 12.3\text{GHz} = 6.2\text{GHz}$ while for $N_{CNT} = 10^6$ it is $f \geq 620\text{MHz}$.

For all CNT numbers, if we design antennas such that $\omega^2 \gg \left(\frac{1}{\tau}\right)^2$ i.e. with operating frequency $f \geq K F_v$, with $K^2 \gg 1$, the low-loss approximation may be used. For $\tau = 3\text{ps}$, as is used in most of the simulations in the previous section, this condition can be translated as $f \geq \sqrt{10} F_v \approx 168\text{GHz}$ which justifies the approximation for most of the study. For $F_v \approx 53\text{GHz} \leq f < \sqrt{10} F_v \approx 168\text{GHz}$ resonance is possible but resistive losses should not be neglected.

IV.A.2.2.1.1) Rigorous effect of the number of CNTs in the bundle

For $\omega^2 \gg \left(\frac{R}{L}\right)^2$, the propagation velocity along the CNTs can be written:

$$v_{p,bundle} = \frac{1}{\sqrt{LC}} = \frac{1}{\sqrt{\left(\frac{L_K}{N_{CNT}} + L_{M,bdl}\right) C_{bdl}}} \quad (155)$$

The respective influences of the inductances and capacitances is not quite straightforward because they vary differently with N_{CNT} . However the magnetic inductance

and the inverse of the electrostatic capacitance vary logarithmically with the inverse of the radius. Considering these variations as relatively small we proposed a simplified interpretation in the previous section.

We will here calculate rigorously the phase velocity for a bundle of CNTs to gain physical insight on the matter and to be able to implement the formula to design CNT-based antennas.

IV.A.2.2.1.1.1) Derivation of the phase velocity

We start by calculating the total capacitance of the bundle, C_{bdl} , from an electrostatic contribution in the form of $C_{ES,bdl}$ and a quantum capacitance contribution as $C_{Q,bdl} = N_{CNT}C_Q$ for N_{CNT} CNTs in parallel. The inverse of the total capacitance can be expressed as:

$$\begin{aligned} C_{bdl}^{-1} &= C_{ES,bdl}^{-1} + C_{Q,bdl}^{-1} = \Delta C_{ES}^{-1} + C_{ES,CNT}^{-1} + \frac{1}{N_{CNT}} C_Q^{-1} \\ &= C_{CNT}^{-1} + \left(\Delta C_{ES}^{-1} + \left(\frac{1}{N_{CNT}} - 1 \right) C_Q^{-1} \right) \end{aligned} \quad (156)$$

where:

$$\Delta C_{ES}^{-1} \equiv C_{ES,bdl}^{-1} - C_{ES,CNT}^{-1} \quad (157)$$

For a wire parallel to ground disposition (the conclusions are similar for other configurations) this becomes (cf. Table 1 in section I.A.1.1)):

$$\begin{aligned} \Delta C_{ES}^{-1} &= \frac{1}{\pi\epsilon'} \left(\operatorname{arcosh} \left(\frac{h}{a_{bdl}} \right) - \operatorname{arcosh} \left(\frac{h}{a_{CNT}} \right) \right) \\ &\approx \frac{1}{\pi\epsilon'} \left(\ln \left(\frac{h}{a_{bdl}} \right) - \ln \left(\frac{h}{a_{CNT}} \right) \right) \end{aligned} \quad (158)$$

when assuming constant spacing of the wire to the ground. Since the bundle is supposed circular, its radius a_{bdl} and the number of CNTs can be approximately related as:

$$a_{bdl} = a_{CNT} + \sqrt{\frac{N_{CNT} - 1}{\pi}} (a_{CNT} + \Delta r_{CNT}) = a_{CNT} \left(1 + \sqrt{\frac{N_{CNT} - 1}{\pi}} (2k + 1) \right) \quad (159)$$

where $\Delta r_{CNT} = 2ka_{CNT}$, $k > 1$ is the average spacing center-to-center of the CNTs. For $a_{bdl} \gg a_{CNT}$ we thus obtain:

$$a_{bdl} \approx a_{CNT} \sqrt{\frac{N_{CNT}}{\pi}} (2k + 1) \quad (160)$$

Then:

$$\begin{aligned} \Delta C_{ES}^{-1} &= C_{ES,bdl}^{-1} - C_{ES,CNT}^{-1} \approx \frac{1}{\pi\epsilon'} \ln \left(\sqrt{\frac{N_{CNT}}{\pi}} (2k + 1) \right) \\ &= \frac{1}{2\pi\epsilon'} \ln \left(\frac{(2k + 1)^2}{\pi} N_{CNT} \right) \end{aligned} \quad (161)$$

And finally the capacitance of the bundle can be expressed as:

$$\begin{aligned} C_{bdl}^{-1} &= C_{CNT}^{-1} - \left(\frac{1}{2\pi\epsilon'} \ln \left(\frac{(2k + 1)^2}{\pi} N_{CNT} \right) \right) + \left(1 - \frac{1}{N_{CNT}} \right) C_Q^{-1} \\ &\equiv C_{CNT}^{-1} + \Delta C_{bdl-sgl}^{-1} \end{aligned} \quad (162)$$

Where we have defined $\Delta C_{bdl-sgl}^{-1} \equiv C_{bdl}^{-1} - C_{CNT}^{-1}$. Numerically, for $N_{CNT} \in [10, 10^4]$ the term independent of C_Q that varies logarithmically with N_{CNT} is dominant. Similarly for the magnetic inductance we find:

$$\Delta L_M = L_{M,bdl} - L_{M,CNT} \approx \frac{\mu}{2\pi} \ln \left(\frac{(2k + 1)^2}{\pi} N_{CNT} \right) \quad (163)$$

Finally, $\frac{\Delta C_{bdl-sgl}^{-1}}{C_{CNT}^{-1}} \approx \frac{\Delta L_M}{L_{M,CNT}} \approx 0.2 + \ln(N_{CNT})$ which can also be written with a logarithm in base 10 as: $\frac{\Delta C_{bdl-sgl}^{-1}}{C_{CNT}^{-1}} \approx \frac{\Delta L_M}{L_{M,CNT}} \approx 0.2 + \ln(10) \log(N_{CNT}) \approx 0.2 + 2.3 \log(N_{CNT})$.

Finally we find the phase velocity as:

$$v_{p,bundle} = \frac{1}{\sqrt{LC}} = \frac{1}{\sqrt{\left(\frac{L_K}{N_{CNT}} + L_{M,CNT} \left(1 + \frac{\Delta L_M}{L_{M,CNT}} \right) \right) C_{CNT} \left(1 + \frac{\Delta C_{bdl-sgl}^{-1}}{C_{CNT}^{-1}} \right)}}} \quad (164)$$

which is well approximated as:

$$v_{p,bundle} \approx \frac{1}{\sqrt{\left(\frac{L_K}{N_{CNT}(1.2 + 2.3 \log(N_{CNT}))} + L_{M,CNT} \right) C_{ES,CNT}}} \quad (165)$$

where we replaced C_{CNT} by $C_{ES,CNT}$ since for a single CNT, $C_{Q,CNT}^{-1} \sim \frac{1}{20} C_{ES}^{-1}$ (cf. Table 2 in section I.A.1.1)). This original result provides a simple but rigorous form of the phase velocity in a CNT bundle in transmission line configuration (wire over ground) which can specifically be used for the cases of wire monopole and dipole antennas.

IV.A.2.2.1.1.2) Discussion

The expression found for the phase velocity therefore justifies neglecting the quantum capacitance for CNT antennas as has been done in our EM simulations. Furthermore it shows that, for the numbers of CNTs identified as the most interesting for the resonant antenna application considered in this PhD thesis, i.e. $10 \lesssim N_{CNT} \lesssim 1000$, the phase velocity is:

$$v_{p,bundle} \approx X(N_{CNT}) \sqrt{\frac{N_{CNT}}{L_K C_{ES,CNT}}} \gtrsim \sqrt{N_{CNT}} v_{p,CNT} \quad (166)$$

where $v_{p,CNT} \approx \sqrt{\frac{1}{L_K C_{ES,CNT}}}$ is the velocity along a single CNT and:

$$X(N_{CNT}) \equiv \sqrt{\frac{1.2 + 2.3 \log(N_{CNT})}{1 + N_{CNT}(1.2 + 2.3 \log(N_{CNT})) \frac{L_{M,CNT}}{L_K}}} \quad (167)$$

varies between 1.27 for $N_{CNT} = 1000$ and 2.14 for $N_{CNT} = 70$ (1.85 for $N_{CNT} = 10$).

Finally, for large values of N_{CNT} we have the phase velocity of a classical conductor

$$v_{p,bundle} \approx \frac{1}{\sqrt{L_{M,CNT} C_{ES,CNT}}}.$$

Then at fixed CNT length l_{CNT} the resonance frequency is given by:

$$f_{res,bundle} = \frac{v_{p,bundle}}{\lambda_{p,bundle}} \approx \frac{v_{p,bundle}}{4l_{CNT}} \approx X(N_{CNT}) \frac{\sqrt{N_{CNT}}}{l_{CNT}} \frac{1}{4} v_{p,CNT} \quad (168)$$

Note that the resonance frequency is affected by the surrounding medium (typically air-substrate) through the permittivity in the expression of the electrostatic capacitance in the phase velocity and thus, neglecting the quantum capacitance, will vary as the inverse of the effective relative permittivity $\sqrt{\epsilon_{r,meff}}$ like classical antennas.

Reciprocally, for a required $(f_{res,bundle}, Z_{in})$, one can select the appropriate (l_{CNT}, N_{CNT}) . Indeed, for a dipole or a monopole with each arm long of l_{CNT} , neglecting the radiation loss, Z_{in} can be calculated as [16]:

$$Z_{in} = Z_C \coth(\gamma l_{CNT}) \quad (169)$$

which is fully defined by the previous equations. For a monopole over a perfect ground, the propagation constant γ is the same as that of its equivalent dipole while the characteristic impedance is halved. Therefore the final input impedance is half of that of the equivalent dipole. The radiation resistance is halved as well so the efficiency is constant but the lower input impedance could help achieve a better impedance matching while using a moderate number of CNTs.

IV.A.2.2.1.1.3) Input impedance for moderate and low-loss

We note that, for moderate loss, $\omega^2 \gg \left(\frac{R}{L}\right)^2$, the propagation constant is:

$$\gamma = \alpha + j\beta = \omega\sqrt{LC} \left(\frac{R}{2\omega L} + j \right) \quad (170)$$

and for a quarter wavelength:

$$\gamma \frac{\lambda_p}{4} = \frac{1}{4}(\alpha\lambda_p + j2\pi) = \frac{\pi}{2} \left(\frac{R}{2\omega L} + j \right) \quad (171)$$

Extending from [16], the radiation loss could be accounted for by adding a term of the form:

$$Z_{in,r} \approx \frac{-R_{rad}}{\sinh^2(\gamma l_{CNT})} \quad (172)$$

but this should be relatively small unless we are in the low loss regime $\omega \gg \frac{R}{L}$ and therefore, since $\gamma \approx j\beta$:

$$Z_{in} = -jZ_C \cot(\beta l_{CNT}) \quad (173)$$

$$Z_{in,r} = \frac{R_{rad}}{\sin^2(\beta l_{CNT})} \quad (174)$$

IV.A.2.2.1.2) Attenuation

If $\omega^2 \gg \left(\frac{R}{L}\right)^2$, the wave amplitude attenuation over a propagation of a wavelength can be expressed as:

$$A(\lambda_p/4) = e^{-\frac{\pi}{2} \frac{\frac{R}{\omega L}}{1 + \sqrt{1 + \left(\frac{R}{\omega L}\right)^2}}} \sim_{\omega^2 \gg \left(\frac{R}{L}\right)^2} \left(e^{-\frac{\pi R}{4\omega L}} \right) \quad (175)$$

$$A_{dB}(\lambda_p/4) \sim_{\omega^2 \gg \left(\frac{R}{L}\right)^2} \frac{6.8}{\omega\tau \left(1 + N_{CNT} \frac{L_{M,bdl}}{L_K}\right)} \text{ dB} \quad (176)$$

For instance, for $f = \sqrt{10}F_v$, and neglecting $L_{M,bdl}$ which would further decrease losses, the wave retains at least 78% (-2.1dB) of its original amplitude. For even higher frequencies where $\omega \gg \frac{R}{L}$ i.e. $f \geq 10F_v \approx 530\text{GHz}$, it can be further approximated as:

$$A(\lambda_p/4) \sim_{\omega \gg \frac{R}{L}} \left(1 - \frac{\pi R}{4\omega L} \right) \quad (177)$$

Then, for $f = 10F_v$ the wave retains at least 92% (-0.7dB) of its original amplitude after a return trip in the antenna.

IV.A.2.2.2) High-loss regime

The tipping point between under-damped and over-damped dipoles is approximately for $f = F_v$ where the wave is attenuated to 52% of its amplitude (-5.7dB). This confirms the approximate cut-off limit observed in our antenna study. Following usual definitions, the rigorous critical damping should be observed for $Q = \frac{\omega L}{R} = \frac{1}{2}$ so, for a limited N_{CNT} , at $f = \frac{F_v}{2}$.

Finally, in the high-loss limit, $\omega \ll \frac{R}{L}$ – i.e. $f \leq \frac{F_v}{10} \approx 5.3\text{GHz}$ for a limited N_{CNT} and $\tau = 3\text{ps}$ – the wave is asymptotically attenuated to about 21% of its original amplitude:

$$\begin{aligned} A(\lambda_p/4) &= e^{-\frac{\pi}{2} \frac{\frac{R}{\omega L}}{1 + \sqrt{1 + \left(\frac{R}{\omega L}\right)^2}}} \sim_{\omega \ll \frac{R}{L}} e^{-\frac{\pi}{2} \left(1 - \frac{1}{2} \left(\frac{\omega L}{R}\right)^2\right)} \\ &= e^{-\frac{\pi}{2}} e^{\frac{\pi}{4} \left(\frac{\omega L}{R}\right)^2} \sim_{\omega \ll \frac{R}{L}} e^{-\frac{\pi}{2} \left(1 + \frac{\pi}{4} \left(\frac{\omega L}{R}\right)^2\right)} \approx 21\% \end{aligned} \quad (178)$$

This is because the wavelength and the phase velocity decrease proportionally to $\sqrt{\frac{\omega L}{R}} \gtrsim \sqrt{\omega \tau}$ and become small compared to the lossless case:

$$\begin{aligned} f \lambda_p = v_p &\sim_{\omega \ll \frac{R}{L}} \frac{1}{\sqrt{LC}} \sqrt{2 \frac{\omega L}{R} \left(1 - \frac{\omega L}{R}\right)} \sim_{\omega \ll \frac{R}{L}} \frac{1}{\sqrt{LC}} \sqrt{2 \frac{\omega L}{R}} \ll \frac{\sqrt{2}}{\sqrt{LC}} \\ &= \sqrt{2} v_{p,lossless} = \sqrt{2} f \lambda_{p,lossless} \end{aligned} \quad (179)$$

Therefore if a BCNT antenna is designed in the low-loss approximation for a given frequency f_0 with CNT length $l_{CNT} = \frac{\lambda_{p,lossless}(f_0)}{4} = \frac{1}{f_0 \sqrt{LC}}$ and τ is varied in orders of magnitude around $\tau_0 = \frac{1}{2\pi f_0}$ as is the case depending on the quality of CNTs used. Then as τ decreases which is equivalent to R_Q increasing, the wave is attenuated well before reaching the end of the CNT bundle. Finally we can note that the characteristic impedance is large with real and imaginary part of same magnitude:

$$Z_C \approx \sqrt{\frac{L}{C}} \sqrt{\frac{R}{\omega L} \frac{(1-j)}{\sqrt{2}}} \left(1 + \frac{j}{2} \frac{\omega L}{R}\right) \approx \frac{(1-j)}{\sqrt{2}} \sqrt{\frac{L}{C}} \sqrt{\frac{R}{\omega L}} \quad (180)$$

IV.A.2.3) Application to the study of CNT monopoles

This circuit model was implemented in an Excel workbook – the CNT Antenna Designer – to create design charts and allow parametric study of CNT-based monopole and dipole antennas. As reported in [179], we used this to extend the study of section IV.A.1.3) to resonances of bundled carbon nanotubes in the millimeter range and beyond where the previous results hinted for better achievable performance.

We propose to use this approach for the systematic study of bundles because the mostly analytical resolution makes it extremely efficient in terms of computation time – almost instantaneous on a modern laptop for our application. We use the same structure as before. Some geometrical considerations are omitted – the transmission-line model is derived for infinitely long CNTs so edge effects should be accounted for by an effective length while the capacitance for a monopole normal to the ground is slightly different than the approximated wire parallel to ground – but this has been addressed by introducing fitting parameters and setting them according to our previous EM simulations. Remarkably, the presented results are computed using a simple spreadsheet.

We present three typical lengths, the length being a simple parameter to modify in the spreadsheet: 1.25, 5 and 40 micrometer-long CNTs. These lengths can be realized by in-situ growth or even solution techniques for the shorter one – as discussed in section III.D). The resulting antennas resonate in the EHF (millimeter) band and beyond. They could be measured with vector network analyzers (VNAs, DC up to 500GHz), time-domain THz spectroscopy (TDS, from a few hundred GHz) then Fourier-transform infrared (FTIR) spectroscopy.

The results are in accordance with our previous findings in EM simulators. Fig. 59 and Fig. 60 are intended as an abacus for CNT-based monopole design. On Fig. 59 are presented the two main antenna properties, namely resonant frequency and accepted power at 50Ω as a function of its two geometrical parameters: length and number of SWCNTs. Fig. 60 presents the gain in size as compared with a conventional copper antenna, this being the main property that makes a CNT-based antenna more interesting than a metal-based one.

We use these charts and parametric studies as an intermediary step in our design process (cf. Fig. 32). They are adjusted using preliminary full-EM simulation of simple

monopoles and allow a quick parametric extension of these results before proceeding to full-EM simulation of the selected designs for adjustments. The more complex steps of designing the real elements of the antenna – its feed, and optional reflectors or arrays transmission – and studying its radiation properties, possible surrounding elements, transmission configurations can then be led using full-EM simulation.

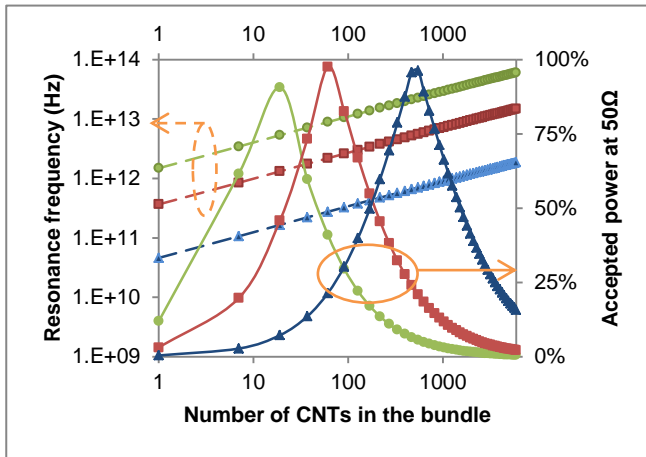


Fig. 61. Resonance frequency (dotted curves) and accepted power at 50Ω (plain curves) as a function of the monopole antenna geometrical parameters: length and number of tubes. $40\mu\text{m}$ (triangles), $5\mu\text{m}$ (squares) and $1.25\mu\text{m}$ (discs)-long CNTs are plotted.

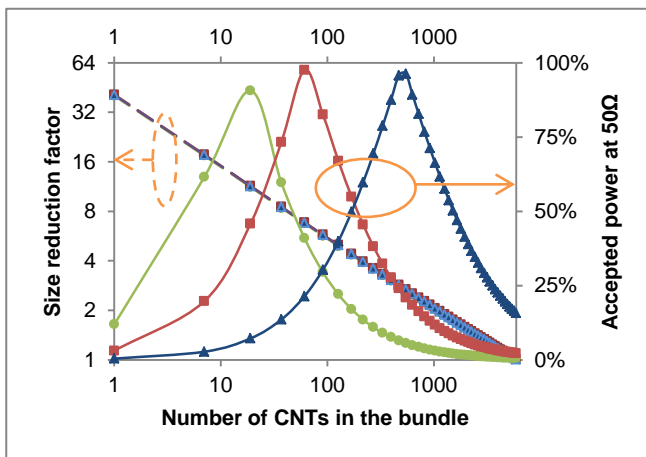


Fig. 62. Size reduction factor (compared to a resonant copper antenna, dotted curves) and accepted power at 50Ω (plain curves) as a function of the antenna geometrical parameters: length and number of tubes. $40\mu\text{m}$ (triangles), $5\mu\text{m}$ (squares) and $1.25\mu\text{m}$ (discs)-long CNTs are plotted. Note the size gain is only dependent on N_{shells} . By operating at higher frequencies or higher impedance, the relative gain in size will be larger for a similar performance.

Although P.J. Burke’s study [16] had already been extended to bundles ([109], [119], [124]), the studies as such did not allow designing real antennas while our approach does by integrating this analytical approach as a design tool in a multi-model design process. We have shown that bundled CNTs allow the conception of tailored antennas for given ranges of frequency and impedance. As exposed in the next sections, our better understanding of the key parameters in this simple configuration in relation with experimental fabrication possibilities allows us to design real sub-wavelength antenna structures.

IV.B) THz characterization and THz FSS

Although the focus of this thesis is on antennas at RF frequencies, the simulation results indicate that CNTs are better adapted to higher frequencies – millimeter-wave, terahertz, infrared and even optical ranges – where most of the trade-offs vanish and common free-space measurement techniques allow experimentation on the material with minimal design. This can be verified with a variety of interesting experimental results, as summarized below. We point out a few interesting directions and draw conclusions useful for the design of electrically-short resonant antennas.

In [180]–[183], [140], G.Y. Slepyan, D. Seliuta, M. V. Shuba and coworkers demonstrate and analyze plasmon antenna resonances in SWCNTs treated in solution then either coated on silica fiber or deposited on silicon substrates. The measurements are made in ranges around 200GHz to 20THz and show a broad length-dependent dipolar resonance frequency. For these short, solution-processed SWCNTs with random orientation, at room temperature, the electron relaxation time is found to be $\tau = 150\text{fs}$ – in the expected range but 20 times lower than the value chosen by Hanson [10] and used in optimistic scenarios for lower frequency antennas in the present work. This corresponds to a lower cut-off frequency $F_v = \frac{1}{2\pi\tau} \approx 1\text{THz}$.

CVD-grown ultra-straight SWCNTs or few-wall CNTs may have a longer mean free path. They also offer the advantage of being scalable to lengths of tens to hundreds of micrometers. These lengths are necessary for antenna applications relying on the CNTs as a plasmon resonating part – while short solution-processed CNTs could be used for antenna loading or in Bucky paper form for conventional antennas.

It would be interesting to measure lattice-aligned SWCNTs or toppled vertically grown CNTs with a known length distribution by time-domain terahertz spectroscopy (TDTS) and Fourier-transform infrared spectroscopy (FTIR) to assess τ for this type of CNTs. Furthermore, engineering the lengths of the CNTs and the way they are connected would allow creating notch-band, narrow-band, multiple-band and broadband terahertz frequency-selective surfaces (THz FSS, see Fig. 63 for fabrication). One additional interest is that these THz FSS would be linear polarizers. Therefore for an incoming linearly polarized THz beam,

the contrast of filtered versus unfiltered frequencies could be adjusted by a simple rotation of the THz FSS.

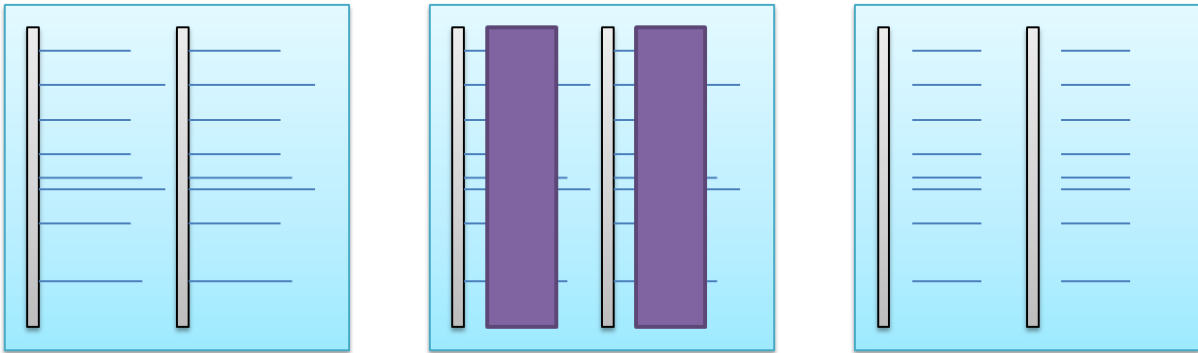


Fig. 63. Proposed fabrication of a THz FSS. 1) Catalyst is patterned on the substrate and CNTs are grown from it by CVD. 2) Masking with thick resist is patterned by photolithography and developed. 3) The unwanted CNTs are dry-etched by O₂ plasma then the resist is removed with acetone, leaving patterned CNTs where desired.

This can be further analyzed with the example of the CNT THz polarizers made from mechanically toppled vertically-grown aligned SWCNTs (C.L. Pint, [184], [185]) demonstrated [134], [186] by L. Ren in J. Kono's group (Rice University). A “non-Drude” resonance was observed at 10THz [187] for 75 μ m-long SWCNTs. A model including ohmic losses and scattering losses was used to explain it which shows a crossover between absorption-dominated losses at lower frequencies and radiation-dominated losses at higher frequencies. This is interesting for antenna applications since it shows that efficient radiation can be achieved at frequencies above 1.8THz in the described experimental case. The choice of a plasmon lifetime of $\tau = 10$ fs in [187] is surprising because it means a linear resistance of the CNTs 15 times higher than usually reported and leads to a lower cut-off frequency of 16THz for plasmon resonances where these may explain the shoulder in the experimental data. It also affects the crossover limit that will be lower for better CNTs.

These toppled CNTs are not suitable for the observation of a slow-wave effect in Drude resonance for two reasons. The first reason is the damping. These 75 μ m-long CNTs at the interface between air and silicon would geometrically resonate around 800GHz – or below if a slow-wave effect could take place. However $\tau = 10 - 150$ fs results in a lower cut-off frequency of 1-16THz. The second reason is the density of this uniform layer which prevents slow-wave effects. Indeed, assuming better quality CNTs and an appropriate cut-off frequency lower than the Drude resonances, these closely packed CNTs would still be coherently excited in at least an area $\sim \lambda^2 \geq (375\mu\text{m})^2$ for 800GHz. Taking 25CNTs/ μ m

laterally by $1\text{CNT}/75\mu\text{m}$ along the CNT direction we find the number of CNTs excited in phase to be $N_{\text{CNT}} \geq 5 \times 10^4$. At these values of N_{CNT} , the magnetic inductance becomes predominant over the kinetic inductance, just as for our dipole antenna model. Hence, the hypothetical resonance would not be shifted to lower frequencies.

Therefore, there appear to be two types of CNTs suitable to realize our experiments. Delimited CNT bundles of arbitrary density could be used as long as the number of CNTs coherently excited remains below 1-2000. Hence the bundles would have to be separated by more than one wavelength. Otherwise the density would need to remain low enough to keep the number of CNTs in λ^2 below 1-2000. Hence, $\lambda = kL_{\text{CNT}}$, $D_{\text{lat,CNT}} \leq \frac{1000}{k\lambda} \sim 1 - 10\mu\text{m}^{-1}$. This makes lattice-aligned CNTs good candidate with their inherent relatively low densities (0.1 to 10CNTs/ μm in general and up to 50CNTs/ μm reported [49], [169], [141], [142], [170], [171], [143]).

IV.C) Prototypes from lattice-aligned metallic SWCNTs on quartz

IV.C.1) Quartz dipole

This antenna design was initially proposed in [188]. Parametric studies and transmission studies were reported in [189], [190] and it was discussed as part of broader scopes in [168], [173]. The simulations are based on metallic SWCNTs using the model developed in section II.B).

IV.C.1.1) Design and experimental realization

The planar dipole antenna design consists of two identical strips of metal aligned longitudinally on the surface of a substrate and separated by a gap, as shown on Fig. 64. An EM field is then applied in the gap through a lumped port. We adapt this simple structure to make a CNT-based electrically-short antenna. The two strips of metal are replaced with aligned SWCNTs of uniform length cut in their middle to constitute the two arms.

This design is compatible with CNTs grown horizontally on a substrate, in particular lattice-aligned CNTs grown on quartz by catalytic chemical vapor deposition (CVD). Indeed, as we explained previously, reported CNT lengths with this technique range up to millimeters while densities range from 0.1 to 50 CNTs/ μm [49], [169], [141], [142], [170], [171], [143].

This is well suited to tailor a strip of aligned CNTs to the desired characteristics (number of CNTs and physical dimensions) for the application considered in this PhD thesis.

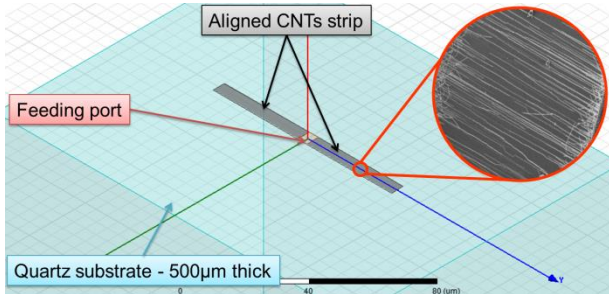


Fig. 64 CNT dipole on quartz substrate that would be realized by lattice-aligned CVD growth then O₂ plasma etching.

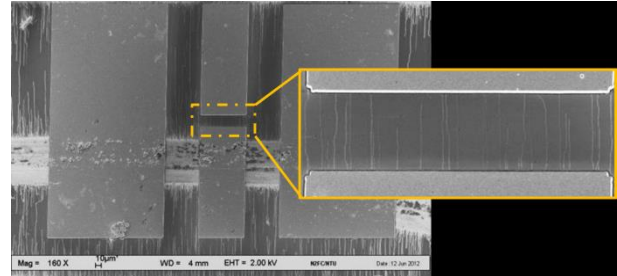


Fig. 65 Demonstration of the fabrication process by the fabrication of Au/Ti CPW gap electrodes over CVD grown CNTs with scratch catalyst.

The planar antenna can be realized in two different ways using lattice-aligned CNTs grown on quartz by TCVD (cf. III.B)). One method is to grow CNTs uniformly on the substrate from parallel catalyst lines then use photolithography to protect the CNTs of the antenna with a mask and proceed to etch the unwanted CNTs by reactive ion etching (RIE) using O₂ plasma. The second method is to pattern the catalyst by photolithography to only grow CNTs where desired. The CNT length and density may be tuned by growth time and catalyst spacing provided the catalyst is of reproducible quality. Using standard photolithography a 2-µm resolution can be achieved and hence, using the appropriate CNT density, the number of CNTs is controlled with a precision ranging from 1 to 100 CNTs – as a trade-off to antenna width.

These monolayer CNTs are extremely flexible and may be transferred to any desired substrate while retaining their alignment and configuration [141], [142]. This offers many possibilities for antenna design. An optional additional step is therefore the transfer of the CNTs to substrates with appropriate permittivity or other interesting properties such as flexibility (e.g. Kapton) that can be used regardless to their resistance to heat. The density may also be increased by multiple transfer steps.

Initial demonstrations of growth of high-purity SWCNTs on quartz in CINTRA and of a full fabrication process of RF-electrode-contacted CNT structures are illustrated by the fabricated CNT characterization structure shown in Fig. 65.

IV.C.1.2) Parametric study

We aim at integrating this antenna in systems which means meeting or formulating resonance frequency, bandwidth and feeding impedance requirements. For instance, to characterize the antenna experimentally with significant signal on a vector network analyzer, impedance matching to 50Ω may be required. The techniques are usually narrow band and correspond to known impedance. A good prior knowledge of the antenna is thus necessary. It can only be achieved through careful theoretical investigation and characterization of the CNTs used for the antenna fabrication.

Many parameters influence the frequency response of this antenna. We divided them as CNT characteristics, antenna geometrical configuration and bundle parameters. Although a circuit interpretation [179] can give some indications on their effect, the non-conventional scales and effects due to the SWCNTs can lead to misinterpretations. On the other hand, full-wave simulation with the technique exposed in II.B) provides a fast and intuitive tool guaranteeing to take all effects into account. It additionally allows for the study of the integration of the antenna with feeding structures, in arrays or in a transmission link as in section IV.C.1.3).

A parametric study of the SWCNT on quartz antenna is thus carried out with EM simulation in HFSS using the SWCNT bulk model presented in section II.B.3).

IV.C.1.2.1) CNT characteristics

The values γ_0 (overlap integral determining the Fermi velocity in CNTs) and τ (plasmon lifetime in CNTs) used in the model are phenomenological constants that depend mainly on the SWCNTs quality and arrangement. Here, we study their effect on the frequency response of a 4-micrometer-wide 160-micrometer-long planar dipole antenna made of two arms of 80 SWCNTs each separated by a 4-micrometer gap. The ranges of values chosen correspond to those found in literature.

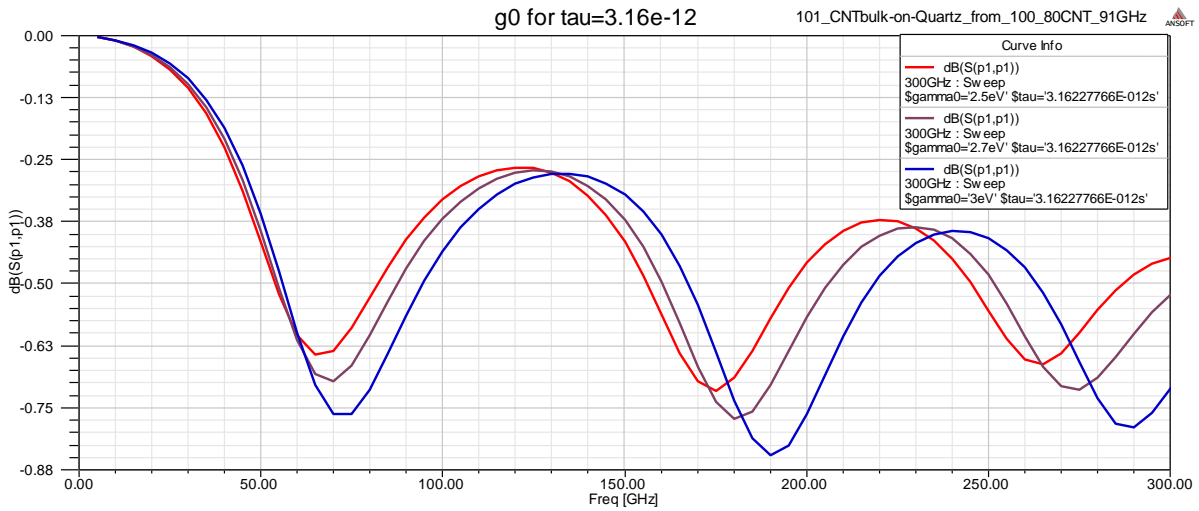


Fig. 66. Effect of γ_0 on the frequency response of a CNT-based antenna. Return loss at 50 Ω plotted from 0 to 300GHz for $\gamma_0 = 2.5, 2.7$ and 3eV. The antenna arms are 78 μm -long by 4 μm -wide, made of 80 aligned CNTs each and separated by a 4 μm gap fed with a 50- Ω lumped port.

On Fig. 66, the return loss of the antenna is plotted against frequency for γ_0 varying in its experimental range. As one would expect, the effect of γ_0 is rather limited as its value only varies by $\pm 10\%$ and only the module of the conductivity is affected, linearly, leaving the relative weight of the imaginary and real part of the conductivity with frequency unchanged.

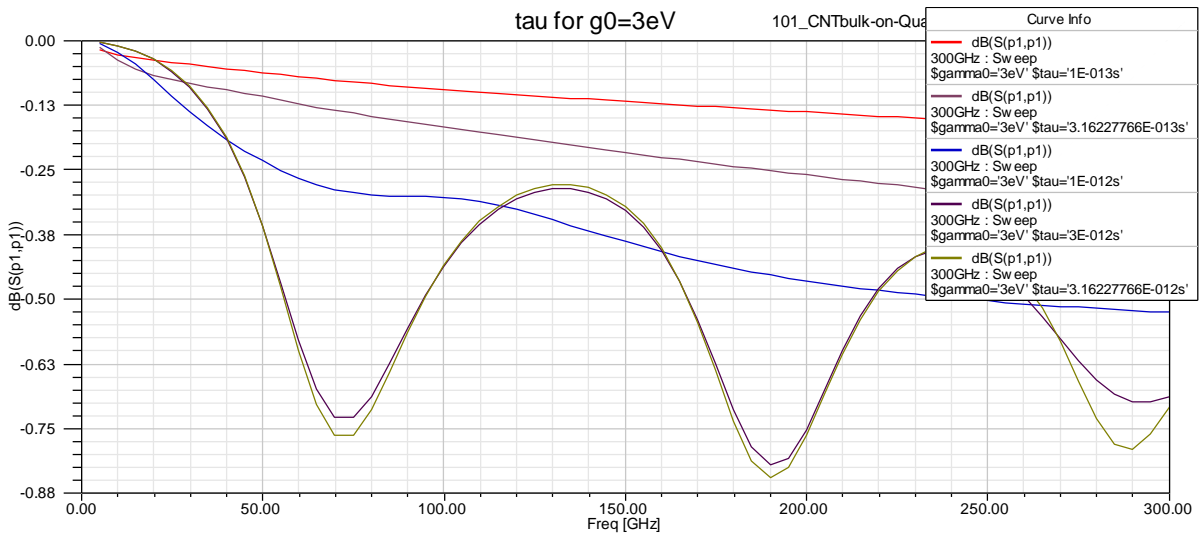


Fig. 67. Effect of τ on the frequency response of a CNT-based antenna. Return loss at 50 Ω plotted from 0 to 300GHz for $\tau = 0.10\text{ps}, 0.32\text{ps}, 1.0\text{ps}, 3.0\text{ps}$ and 3.2ps. The antenna configuration is identical.

On Fig. 67, the return loss of the antenna is plotted against frequency for τ varying in its experimental range. Here, since the range covers an order of magnitude, τ is varied on a logarithmic scale and the effect is very pronounced. As expected, the antenna is over damped when its fundamental resonance frequency is below $F_V(\tau)$ which can vary from 50GHz to

1.5THz. High-quality CNTs are thus a critical element to produce plasmon resonances. Indeed, the presence of impurities and bends in the carbon nanotubes impacts the value of the plasmon lifetime.

IV.C.1.2.2) Antenna geometrical configuration

For the design and experimental realization of the antenna, it is important to understand how topological variations affect its response. We use the same planar dipole antenna design with 78 μm -long 80-SWCNT arms – but we vary the arms width and the gap width to study their influence. We show that these topological variations affect the response of the antenna on a logarithmic scale only.

Because various CNT densities may be achieved experimentally, it is important to consider the effect of density if a fixed number of SWCNTs were to be used. To address this, we simulated the antenna with a logarithmic progression of width from 1 to 32 μm . The return loss at 50 Ω versus frequency is plotted on Fig. 68 and resonances are renormalized at 1 k Ω and compared on Fig. 70 a). As long as the aspect ratio of the antenna arm remains high, the resonance frequency is unchanged. However, when the aspect ratio becomes lower than 10 (here $D_{CNT} \leq 10/\mu\text{m}$), the resonance frequency gradually shifts lower which can be interpreted as increased arm-to-arm capacitance. It is actually a classical result that a dipole resonance shifts lower in frequency and its bandwidth increases with increased width. From 5 to 10 CNTs/ μm the effect is still moderate.

Feeding the dipole with a realistic feed line may require widening its feed gap. Hence, we simulated the antenna with a logarithmic progression of gap width from 4 to 128 μm and the results are presented on Fig. 69 and Fig. 70 b). They show that, if the arm length remains constant, widening the gap should not affect the antenna resonance much. Indeed, most of the effective length seen by the EM wave is due to the CNT arms, which correspond to about 2mm of total equivalent propagation in vacuum at 75GHz. Hence spacing up to 130 μm on quartz (equivalent to 200 μm in vacuum) has little influence on the resonance frequency. The return loss is somewhat degraded with increased width which we interpret as the effect of the lesser confinement of the field in the gap region. Note that, conversely, when the gap is varied at constant dipole length, the frequency shifts upward, accounting for a substantially shorter effective length due to the different propagation speeds in the gap and in the CNTs.

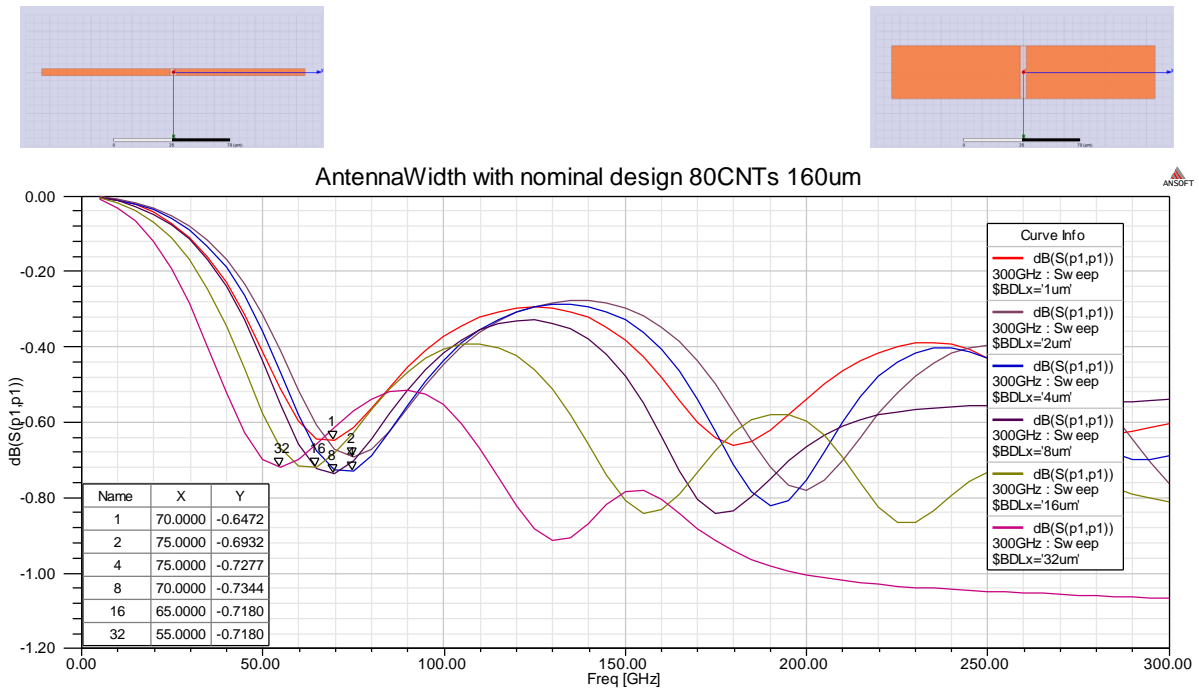


Fig. 68. Effect of antenna width on the frequency response of a CNT-based antenna. Return loss at 50Ω plotted from 0 to 300GHz for $W_A = 1, 2, 4, 8, 16$ and $32\mu\text{m}$.

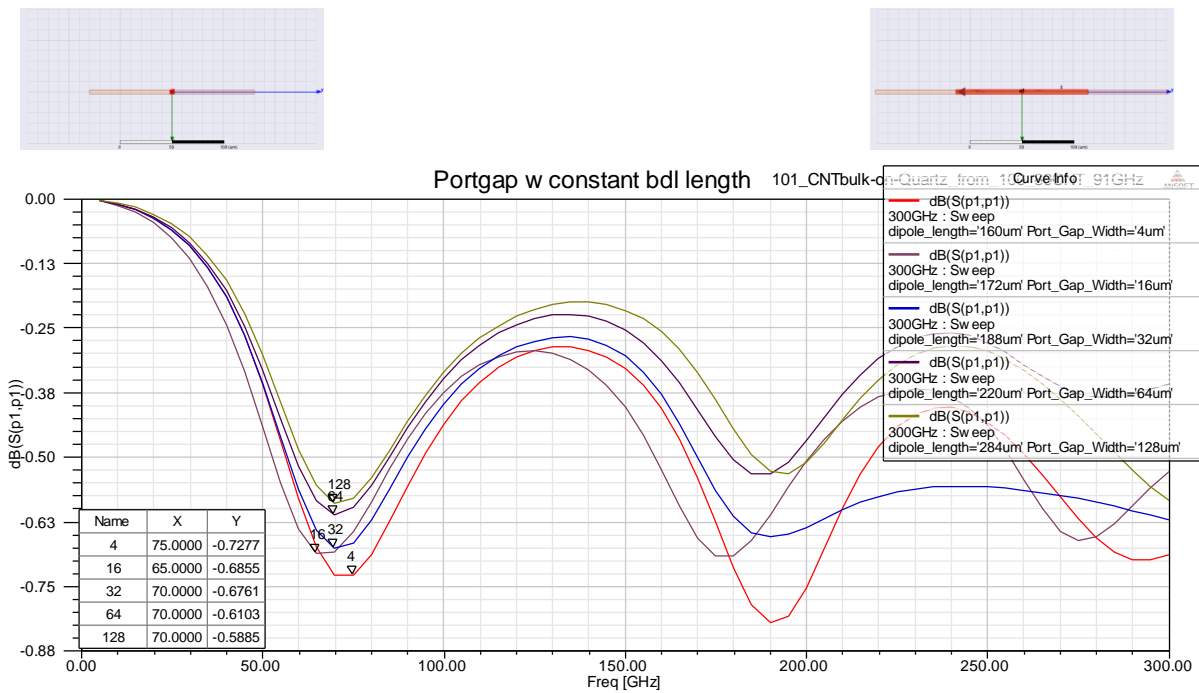


Fig. 69. Effect of feeding port gap width on the frequency response of a CNT-based antenna. Return loss at 50Ω plotted from 0 to 300GHz for $W_{\text{Gap}} = 4, 16, 32, 64$ and $128\mu\text{m}$. The arms are kept $78\mu\text{m}$ -long each.

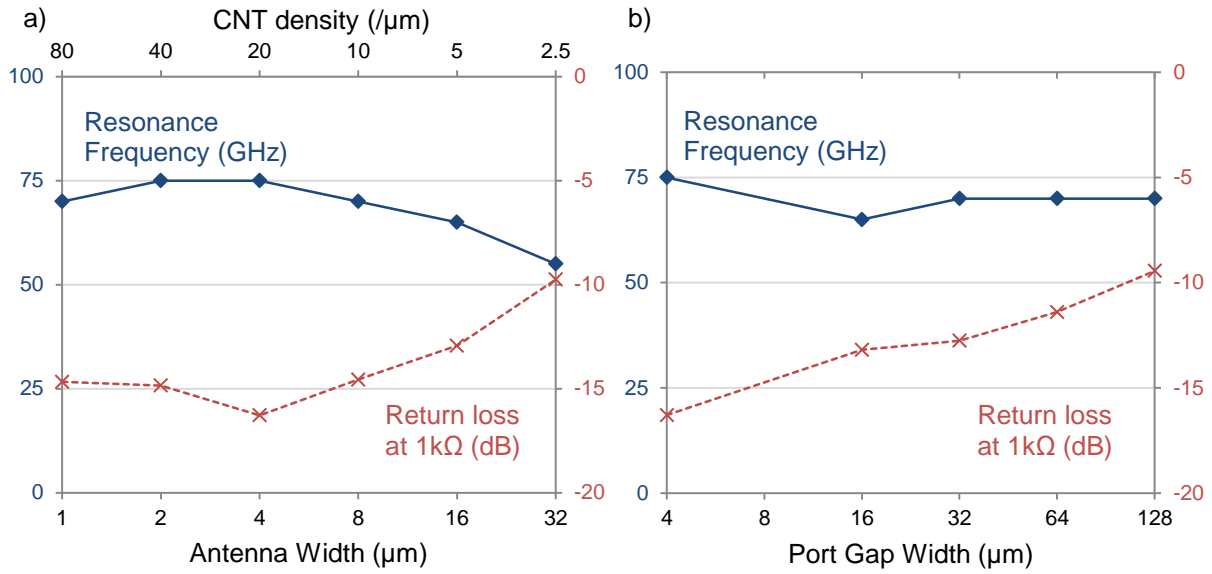


Fig. 70. Summary of the effect on the primary resonance of a CNT-based antenna of a) Antenna width from Fig. 68; note a slight frequency dip for wider values and relatively constant return loss. b) Feeding port gap width, the arms being kept 78- μm -long each, from Fig. 69; note a constant frequency and only slightly increasing mismatch.

IV.C.1.2.3) Bundle parameters and trade-offs

As for the ideal monopole covered in section IV.A), the main design parameters of these electrically-short antennas are the number of CNTs in each arm (N_{CNT}) and their length (l_{CNT}). A number of simulations were run to cover comprehensively the possible designs. Fig. 71 summarizes these many results. It describes the performance of CNT based dipoles on quartz as a function of number of CNTs in each arm (x axis) and length of the CNTs (the different curves). Fig. 71 a) indicates the resonance frequency and input impedance at resonance while b) gives conjugate quantities; size reduction and return loss at 50Ω .

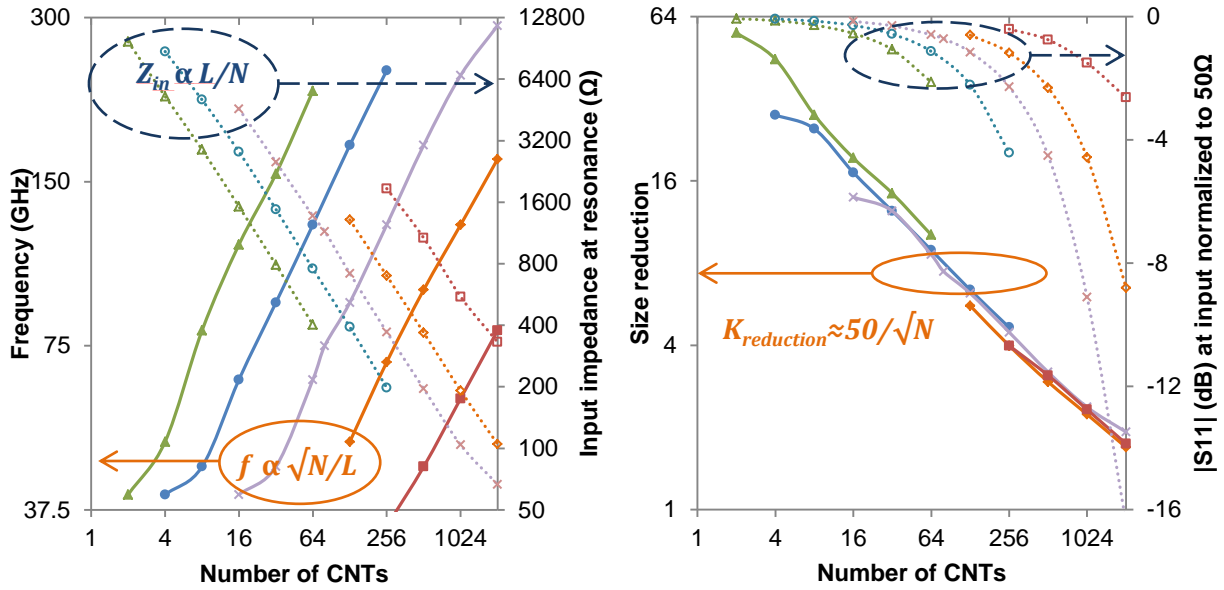


Fig. 71. Characteristics of 50- Ω -fed planar SWCNT-based dipoles as a function of (N_{CNT} , l_{CNT}) a) Resonance frequency and input impedance b) Size reduction and return loss. Dipole lengths are 40 (\blacktriangle), 80 (\bullet), 160 (X), 320 (\blacklozenge), and 640 (\blacksquare) μm with constant 4- μm gap and 4- μm arms width.

As expected, the same trends arise than those observed by EM simulation and explained by circuit analysis for the ideal monopole. By fitting the curves on Fig. 71, we find that the size reduction is only dependent over the N_{CNT} used: $K_{red} \approx \frac{50}{\sqrt{N_{CNT}}}$ while, with minor variations, $f \approx \frac{1600}{l_{CNT}} \sqrt{N_{CNT}}$ and $Z_{in} \approx 400 \frac{l_{CNT}}{N_{CNT}}$ in (μm , GHz, Ω). Here we limited the study to VNA measurable frequencies – up to 300GHz. When limited to these frequencies our charts show that the input impedance necessarily exceeds 200 Ω for configurations of less than 256 CNTs which coincides with a reduction factor $K_{red} \approx 4$. Hence to operate with 50- Ω electronics at technologically relevant frequencies, one should not expect to reduce the size of CNT resonant antennas more than four times with respect to their classical equivalent metallic antennas.

Another, maybe more interesting, application of these antennas is an asymmetric wireless link acting like an impedance transformer between high-impedance nano-components directly connected to/incorporating an impedance-matched CNT antenna and usual microelectronics connected to a classical directive antenna [190].

IV.C.1.3) Transmission

Wireless on-chip communication [12], [191]–[193], [28] could be the ideal application for CNT-based antennas as they save footprint over classical antennas, can operate at higher frequencies and their limited efficiency can be accommodated for short distances. This is a developing field presenting interesting properties such as easier layout and potential higher integration density. Here we investigate the use of CNT-based antennas with high-impedance and 50- Ω components in symmetric and dissymmetric links.

IV.C.1.3.1) Symmetric links

We studied the feasibility and interest of a transmission link using CNT-based electrically-short dipoles. Using 1- μm -long single-SWCNT arms resonant at 1.3THz the resonance peak improved the transmission by 50dB over gold [189]. However due to the limited extent of the antennas and their quasi-isotropic radiation pattern, the transmission was limited to very small range, with values of -11dB at 1 μm spacing if the antennas were excited with a 1150- Ω mode (or -28dB at 50- Ω). The high impedance may be well-suited to nanodevices but is not adapted to common RF electronics while the THz frequency is in a still challenging band.

In an attempt to make longer-range transmission from lower-impedance antennas at currently more sensible frequencies we led a study relying on the structures illustrated Fig. 73. We picked a relevant design in terms of impedance, resonance frequency and size reduction. The planar dipole has 40 μm -long 256-CNT arms, resonates at 217GHz and presents 370-ohm input impedance. This makes it 4 times smaller than its metallic counterpart.

It was studied in symmetric transmission both with antennas side-by-side and antennas disposed on either side of the substrate for 3D electronics integration. For both configurations and for each spacing value the plasmon resonance of the antennas was translated into a transmission improvement over classical metal in the same antenna configuration. The transmission is 5dB better at 10 μm spacing, where coupling plays an important role, and up to 15dB better through a 500 μm substrate [189].

The side-to-side transmission at resonance was reported on Fig. 73 and the detailed results may be found in [189]. However, the transmission level even at tens of micrometers

was too low (cf. Fig. 73; -10dB at 10 μ m, -24dB at 40 μ m) to use as replacement to usual interconnects. It could nevertheless be sufficient to characterize the antennas themselves.

IV.C.1.3.2) Dissymmetric links

If usual transmission is clearly not interesting for CNT antennas, an interesting application would be to communicate with nanodevices. Indeed the intrinsically high impedance of these antennas is better suited to connecting high impedance devices rather than classical 50 Ω ones. Additionally, the CNT antenna dimensions are better matched to nanodevices. Classical electronics could be linked to nanodevices through a dissymmetric antenna link; a conventional full-size antenna collects more of the emitted field from the CNT antenna when further and can be matched to 50 Ω while the CNT antenna is high impedance, thus realizing an interesting impedance conversion. We present two such structures.

IV.C.1.3.2.1) CNT-dipole to conventional dipole

Here, a conventional full-size 50- Ω dipole is placed facing the CNT dipole described earlier. The field and mesh are presented on Fig. 72 to give an appreciation of the scales involved. It can be seen on Fig. 73 that the transmission range is much improved in this dissymmetric case. The transmission levels remain fairly low for conventional communications but allow a communication over a one millimeter range which is sufficiently large for mechanical placement of a probe at the vicinity of the CNT antenna in specific applications.

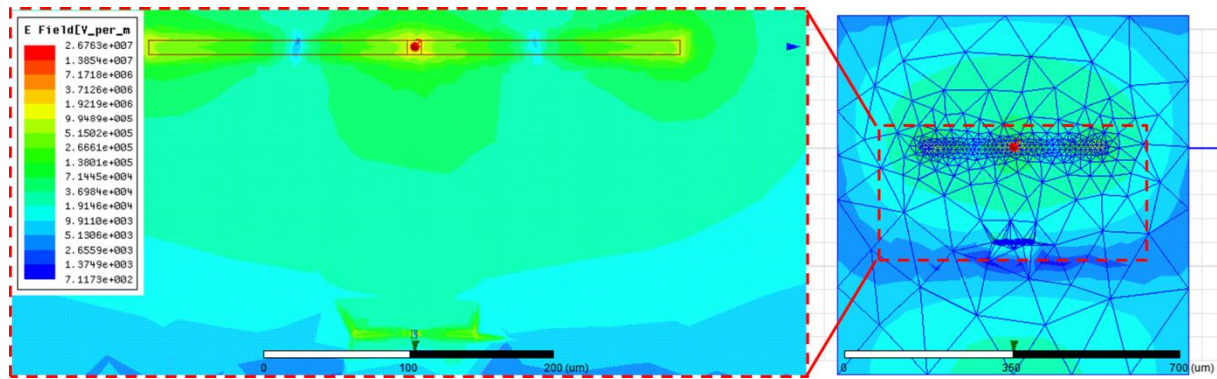


Fig. 72. Left: Plot of the E-field magnitude at the common resonance of a conventional dipole (top) and a CNT dipole (bottom). Right: idem but zoomed-out and showing the FEM mesh.

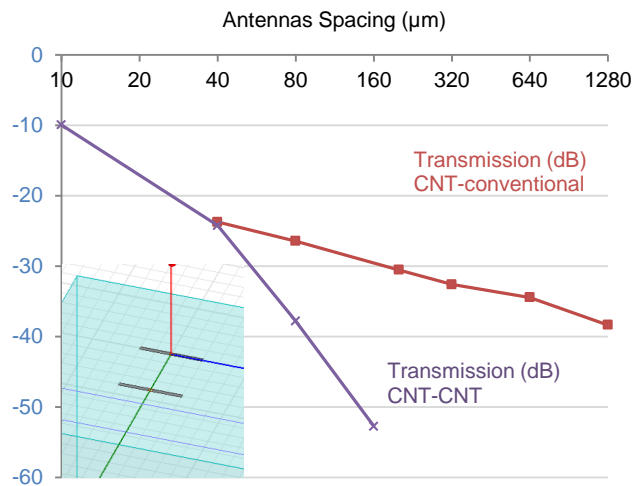


Fig. 73. Dipole-to-dipole transmission. Inset: Two CNT antennas on a quartz substrate side-to-side.

IV.C.1.3.2.2) Contactless read-out of nanodevices

Here, we propose an approach to read information from or communicate information to nanodevices in a more versatile way. Nanodevices would be fabricated with a well-matched high-impedance CNT dipole antenna – here at $300\text{-}370\Omega$ – and arranged on the surface of a chip. The chip would then be scanned by a microantenna – typically a high-frequency horn antenna (cf. Fig. 74). These have the advantage of being directive, broadband and linearly polarized – an ideal match to our tiny, quasi-isotropic, narrow-band, linearly polarized CNT dipoles as we will explain.

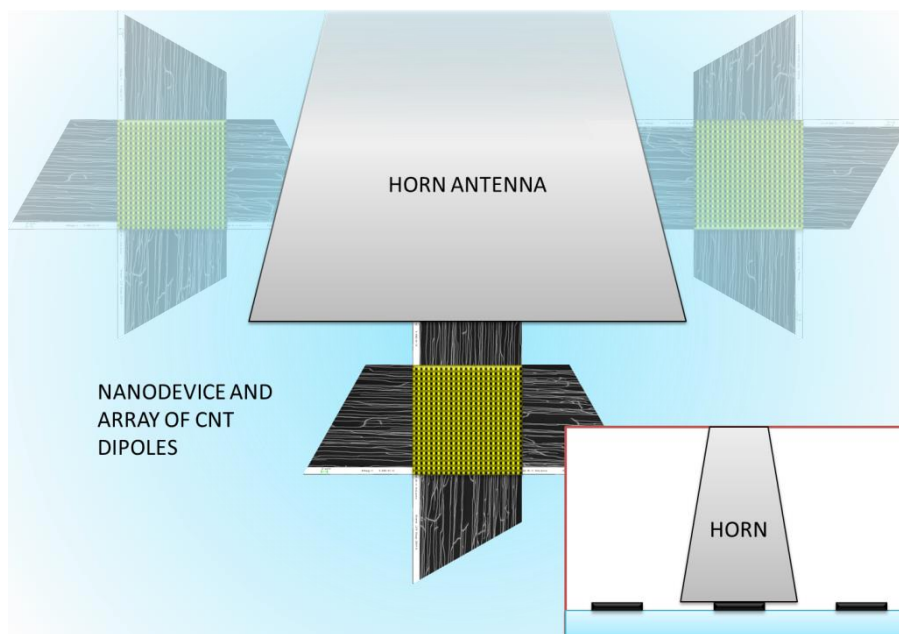


Fig. 74 Scheme of the contactless read-out of nanodevices incorporating CNT dipoles using a horn antenna. The horn is typically one order of magnitude larger than any of the CNT

dipoles. Inset: profile view showing the horn is brought very close to the surface and reads only one zone at a time.

The directivity of the horn and its comparatively large geometrical extent allow a better transmission to and collection from the small CNT dipoles than with a less directive antenna. The quasi isotropic radiation of the CNT dipoles brings robustness against misalignment. Furthermore, in a single read-out zone, several small (narrow band) dipoles of different lengths could be crammed instead of a single classical dipole thus improving the data rate through frequency multiplexing or enabling several different read-outs on a single area through the (broadband) horn antenna. Finally, because both horn antennas and dipoles are linearly polarized, by using dipoles in normal directions one could read only the dipoles in one of the directions then the others by rotating the horn antenna probe by ninety degrees. This would allow stacking up two chips or using the same CNT lengths twice in the same area to double the number of addressable channels.

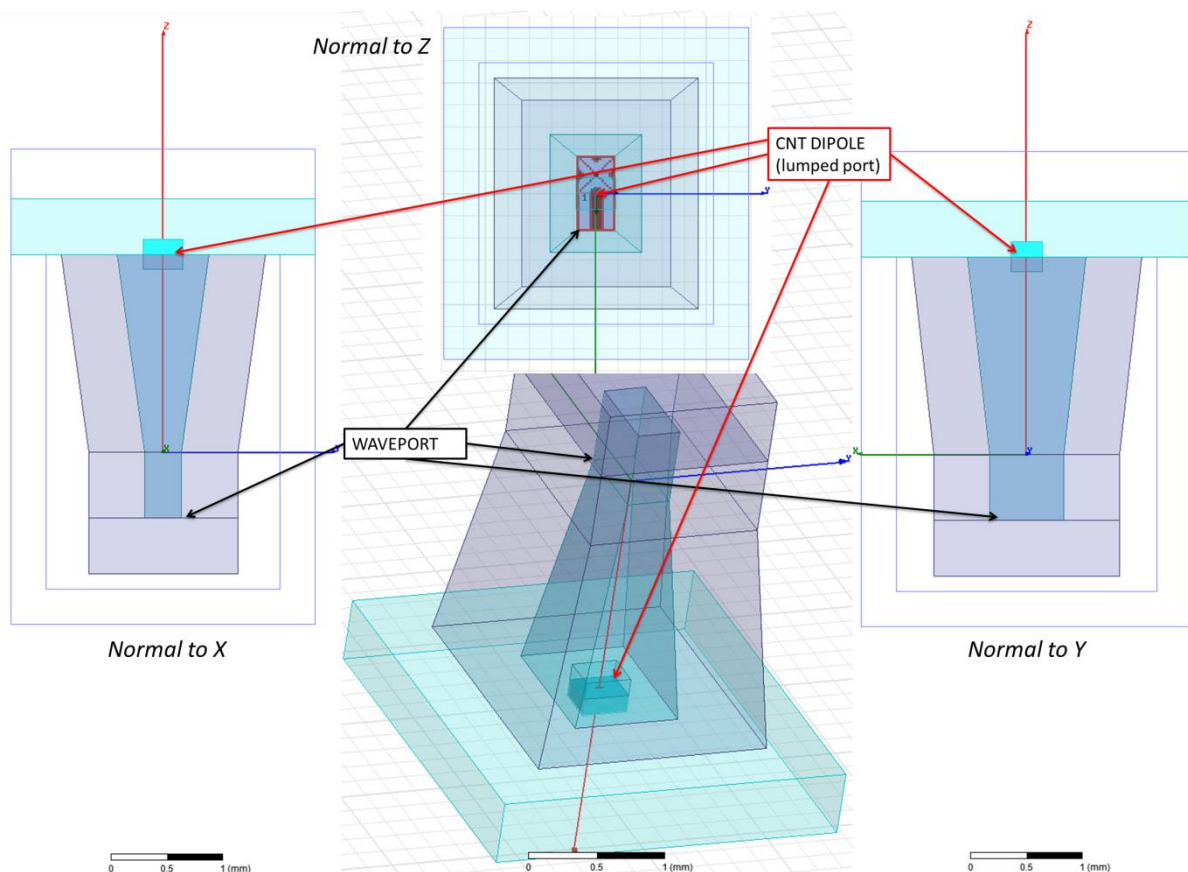


Fig. 75. Horn antenna facing a CNT dipole on quartz. The small boxes are larger than the CNT dipole, that they contain, and smaller than the horn antenna. They do not have any physical impact but help guide the automatic refinement of the mesh in HFSS and keep it progressive.

We have run a few simulations around 220GHz again to support the concept. A dielectric-(quartz)-filled horn-antenna was designed starting from a WR-5 waveguide standard and reducing the dimensions according to the permittivity (cf. Fig. 75). Using a dielectric-filled horn antenna with the filling dielectric matching the nanodevices substrate permittivity is necessary to prevent a high return loss at the horn input due to the reflection of waves at the air-dielectric interface right at the output of the horn antenna. If the CNT antenna is operated sandwiched in the dielectric, its size should be even shorter, by about $K = \sqrt{\frac{\epsilon_r}{\epsilon_{r,eff}}} \approx 1.25$ for quartz and air. In the end we use 29 μ m-long-CNT arms with a 300 Ω input impedance.

The input impedance for the horn and dipole antennas is plotted on the smith chart on Fig. 76. It shows the dipole antenna is relatively well-matched from 190 to 250GHz and the horn antenna is over most of the frequency range studied.

We then vary the spacing of the horn to the dipole with three configurations corresponding to possible applicative cases:

- horn in contact with the substrate – leaving a propagation over $\Delta z = 1.78$ mm from the dipole to the entrance of the waveguide
- edge of the horn 1mm away from the substrate, $\Delta z = 2.82$ mm.
- edge of the horn 5.3mm from the substrate, $\Delta z = 7.09$ mm

The return loss is plotted on Fig. 77 for both antennas in the different configurations. We can observe that the dipole retains a relatively low return loss despite the change in environment and less than 10% shift in frequency. On the other hand the horn is affected by a return loss about 5dB higher in the 170-260GHz range and even more at lower frequencies. Its frequency response becomes mostly flat, remaining in the -6 to -10dB range, when the horn is separated from the substrate. This is due to the dielectric-air interface at its output. This could be reduced by matching the permittivity of the medium between the antennas and that of the substrate and the filling of the horn i.e. read-out in a fluid or use air-cavity or suspended-CNT dipole antenna.

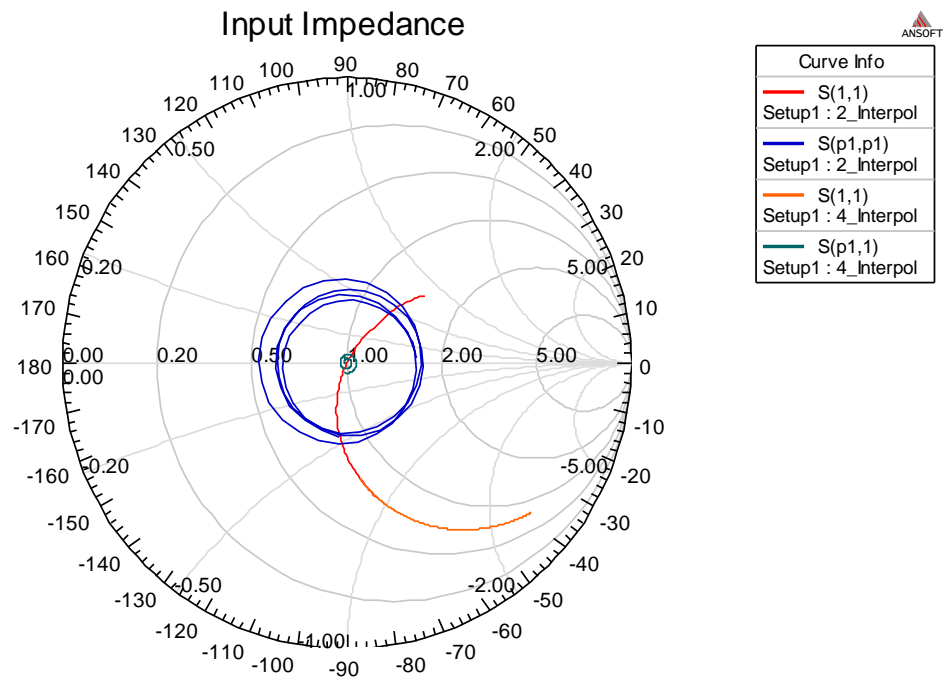


Fig. 76. Smith chart of the horn antenna (blue and green) and dipole antenna (red and orange) for frequencies 170-260GHz and 100-180GHz at nominal spacing i.e. quartz substrate stuck to the horn, 1.78mm to the entrance of the waveguide.

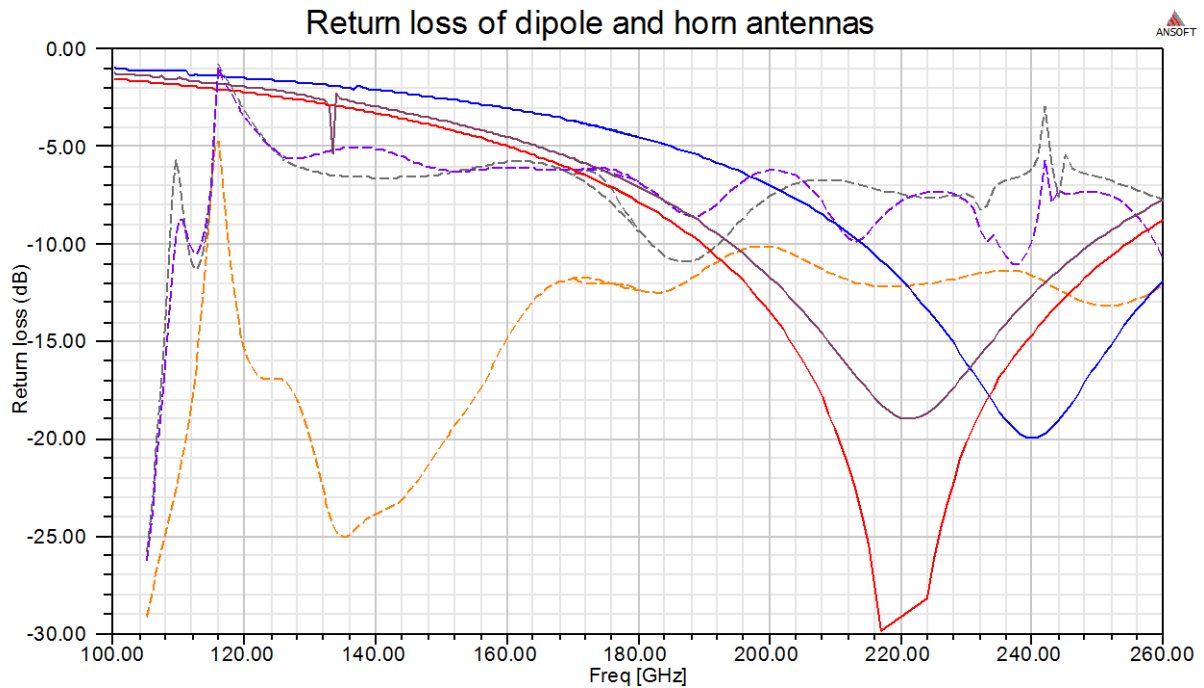


Fig. 77. Return loss of the horn antenna (dash) and dipole antenna (solid) in the range 100-260GHz for different spacing values: : 1.78mm (orange and red), 2.82mm (grey and dark purple), 7.09mm (purple-blue and blue). Values below -30dB were truncated: horn plotted from 105GHz and values around resonance of the dipole at 220GHz in the nominal configuration (-57dB) truncated.

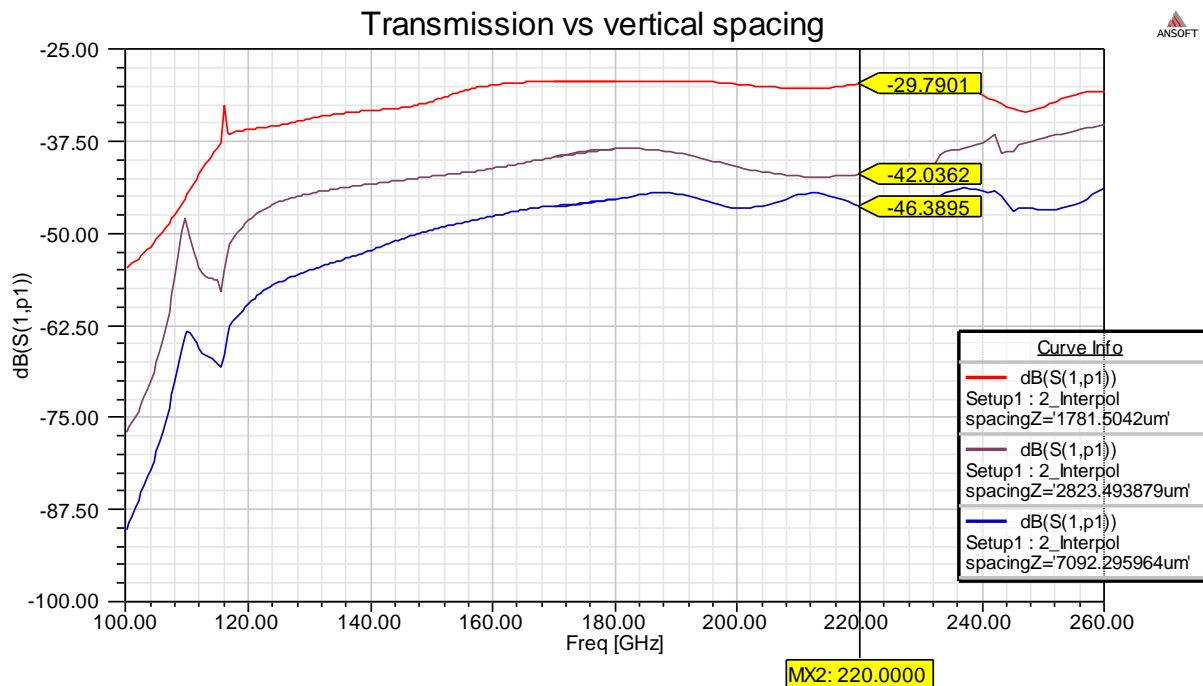


Fig. 78. Transmission between the dipole and the horn antennas at three different spacing values: 1.78mm (contact), 2.82mm (edge of the horn 1mm from the substrate), 7.09mm (edge of the horn 5.3mm from the substrate). The transmission levels are sufficient for the application we describe. Non-contact read-out is possible by hovering a few millimeters over the substrate but reduces the signal by 10 to 20dB.

To conclude, although low, the transmission levels, as plotted on Fig. 78, are sufficient for the read-out application we describe. Non-contact read-out is possible by hovering a few millimeters over the substrate but reduces the signal by 10 to 20dB. There is a step in loss when the horn and substrate are separated because of the reflection at quartz-air interfaces as we analyzed from the return loss. The simulations also show that transmission at contact is -30dB when polarizations are parallel and -54dB when they are crossed, leading to an excellent contrast of 24dB between cross polarizations. Finally lateral misalignments of up to 200μm, more than three times the total length of the dipole and a fairly large mechanical placement error margin, affect the transmission level by less than 1dB.

IV.C.1.4) Conclusion of the planar dipole study

We have developed tools to study the various parameters of an experimentally realizable CNT-based electrically-short antenna. We have also used these tools to study various possibilities of wireless on-chip communication. The transmission remains low. We have shown however that opportunities lie in asymmetric transmission link to bridge micro and nano-electronics.

While the antenna may be directly connected to nano-devices or operated in reflect-array, filter configuration in future applications, the most direct way to characterize its RF response remains to contact it ohmically to metal electrodes. These, in turn, allow reproducible contact to probes or connectors and thus to a vector network analyzer to measure the return loss and transmission in a symmetric or asymmetric link. Let us therefore consider possibilities of experimentally feeding the antenna with a 50Ω probe.

IV.C.2) Coplanar-waveguide-fed dipole and monopole

IV.C.2.1) Coplanar-waveguide-fed dipole

An initial feed design for the quartz dipole was studied and is illustrated on Fig. 79. It is based on a classical coplanar waveguide (CPW) structure that can be directly connected to a vector network analyzer using standard CPW probes. The VNA probe to be used determines the minimum size of the pads ($25 \times 35 \mu\text{m}$ for Infinity probes) and maximum pitch ($100\text{-}150 \mu\text{m}$ usually). The contact pads should have a 50Ω characteristic impedance to guarantee the placement of the probe in this designated area will not affect the measurement. Hence the proportions are set for the contact pads. We use TXline, a free utility from AWR to calculate the CPW line parameters. Additional non- 50Ω sections can be added to realize both dimension and impedance matching to the CNT antenna, as illustrated on Fig. 79. A tapered section or a quarter-wavelength section of specific characteristic impedance are the two most straightforward approaches in our case. The design was successfully simulated, demonstrating good excitation of the classical antenna. For CNT antennas however relative complexity emerges from the disproportionate scales.

An additional challenge – also true for all subsequent designs – lies in the large uncertainty on the actual impedance of the CNT antenna that will be produced experimentally. This is both because of the large variability of CNT properties observed in literature and because of the variability in number of CNTs actually connected. These challenges may be addressed through robust design (broadband impedance matching, match density and resolution limit to limit the uncertainty on the number of CNTs to a negligible fraction of the desired number, etc.) and through refined CNT growth recipes ensuring reproducible densities and uniform CNT quality. Another configuration for a CNT dipole which has similar constraints but – as it is placed as the radiator in a Yagi-Uda configuration

– is more directive can be found in [194]. The reflectors and directors could also be made out of CNTs.

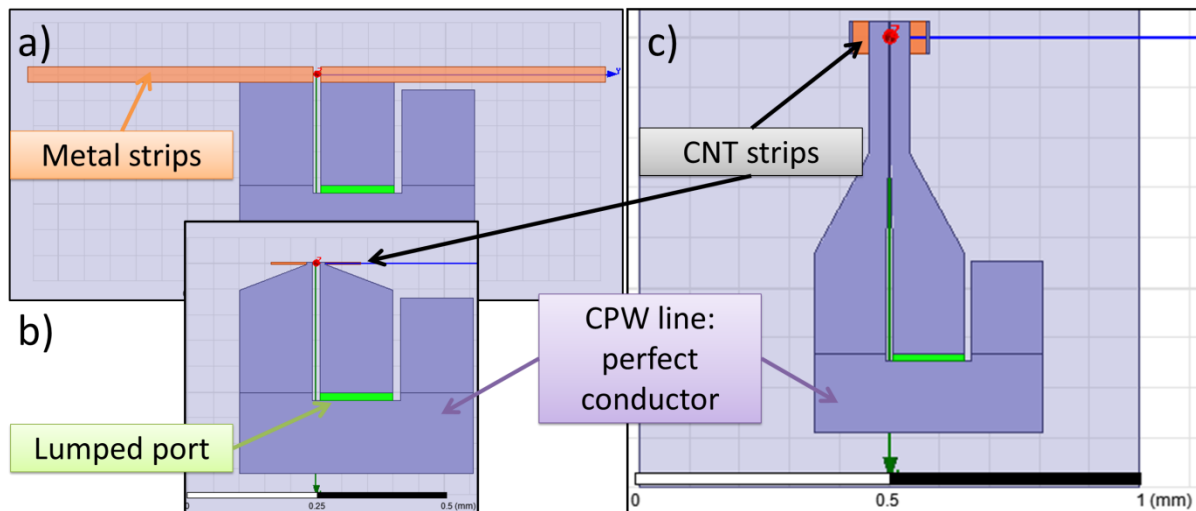


Fig. 79. Tentative coplanar waveguide (CPW) feed designs for planar dipoles. One arm is connected to the ground (G) and one to the signal (S) of this GSG probe. a) Classical dipole; the feed seems to work but may participate in the resonance. b) Ideal CNT dipole (same width-length ratio as classical one); the line is linearly tapered to accommodate the dimensions of the antenna and realize the impedance matching. c) Realistic design for a CNT dipole with two constant-characteristic-impedance lines connected through a taper and CNT density $1/\mu\text{m}$.

IV.C.2.2) Coplanar-waveguide-fed monopole

IV.C.2.2.1) Feed design and general considerations

A second approach we adopted was to simplify the design by transforming the dipole in a monopole. It is also fed by a CPW. This time, however, the CNTs are oriented in the same direction as the propagation of the line. The antenna is simply a CPW line terminated by an open circuit, with the CNTs forming a monopole antenna with the CPW adjacent ground. This also has the advantage of cutting the input impedance of the antenna by two which is non-negligible for these not so dense CNTs and their rather high impedances.

This design also aligns the CNTs with the electric-field lines. Indeed, a CPW is a balanced waveguide that propagates quasi-TEM modes such that the electric-field lines loop from the central conductor (signal) to each of the lateral conductors (ground) [195] – thus circling the slots – while the magnetic field lines loop around the central conductor. Along the line the CNTs should thus be disposed vertically on the conductors or horizontally in the transverse direction in the slots for maximal interaction. At the end of the line, with an open

circuit, the E-field lines close in a pattern similar to the transverse ones as illustrated on Fig. 80. The designs each include 50Ω contact pads, a quarter-wavelength impedance-matching section and a small taper, guaranteeing a smoother transition and easier fabrication by photolithography than a step.

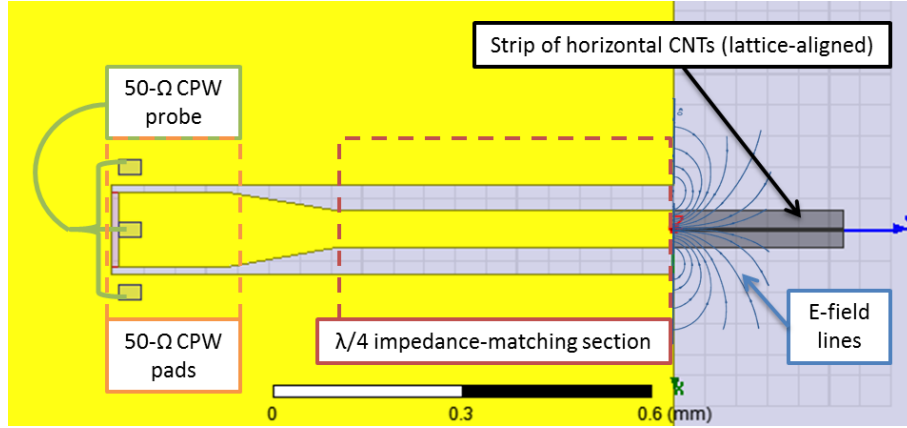


Fig. 80. Illustration of the design of the CPW horizontal-CNT monopole.

The antenna is designed using a quartz substrate for a number of reasons. The first is technological; no transfer step is required when fabricating the antenna from lattice-aligned CVD CNTs which coincidentally are some of the best quality CNTs and most stable processes available. The second is that quartz is an excellent substrate for antennas since it has very low loss and a relatively low permittivity. The low permittivity is especially important in our design because it implies transmission lines will be wider (e.g. than on Si) and thus connect to enough CNTs without an additional widened line section that would complicate both design and interpretation. Additionally, because the antenna is lying flat on the surface of the wafer, at the interface with air, it sees an effective permittivity: $\epsilon_{r,eff} \approx \frac{\epsilon_{r,substrate} + 1}{2}$. Hence if the substrate permittivity is too high the E-field will be confined, limiting the radiation.

IV.C.2.2.2) CNT strip design and improved conductivity

IV.C.2.2.2.1) CNT density and lengths variation

The CNT part was designed to experimentally sweep a large range of CNT densities and lengths. To improve or tune the achievable CNT density, catalyst lines delimiting the antenna are repeated with a given step $\Delta y_{Catalyst}$. As will be described in IV.E), we designed a photolithography mask allowing the fabrication of three different types of CNT antennas based on two types of CPW feed. For each design, the mask design allows the fabrication of 6 identical rows of antennas per sample. We varied the border-to-border catalyst spacing

($\Delta y_{catalyst} - w_{catalyst}$) (where $w_{catalyst} = 6\mu\text{m}$ is the width of one line) for each row on a logarithmic scale and separated the rows in two halves. One half has catalyst lines covering a length of $\sim 150\mu\text{m}$ while they cover $\sim 300\mu\text{m}$ for the other. For the top row there is only one catalyst line which allows fabricating any CNT length by tuning the growth time. Detailed values can be found in section IV.E.2.2).

Finally the number of catalyst designs included in the mask was doubled without increasing the footprint on an already packed mask. Laterally shifted inter-rows were added to the initial ones. The CPW feeds can then be aligned on the original rows or on the inter-rows, the unwanted ones being covered by the CPW ground.

This design allows making the most of the CNTs conductivity while possibly increasing the lengths and densities achievable. Because we use a very thin film of metal ($< 1\text{nm}$) or a solution-prepared catalyst, after annealing, the catalyst lines are not continuous but rather made of small metal droplets with relatively low density which can allow growing CNTs to pass through or – more probably – get entangled with the local root of CNTs, thus creating an initial contact or junction. Furthermore $\Delta y_{catalyst} \geq 20\mu\text{m} > MFP$ for all spacing values so the discontinuities should not induce too much additional resistance.

IV.C.2.2.2.2) Improved effective conductivity with metal inserts

This design also allows an interesting way to improve the effective conductivity of the antenna. Indeed, using the dark-field mask and positive photolithography, a first exposure with the catalyst lines pattern aligned over the initial catalyst spots then a second exposure with the CPW electrodes pattern can be realized before developing, thus opening all these parts before metal deposition. Finally, with only one additional exposure step, the antenna is realized with coplanar access to a CNT strip with regularly spaced metal inserts. This is illustrated on Fig. 81.

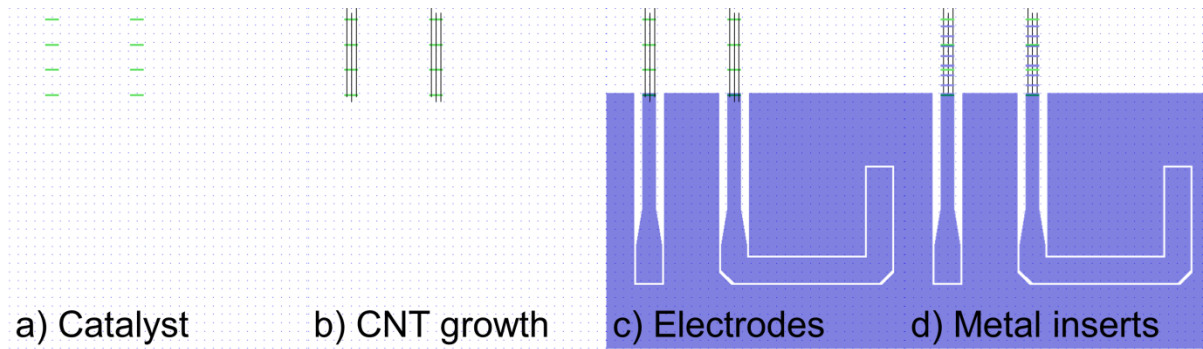


Fig. 81. Steps to fabricate horizontal monopole antennas with CNT strip radiator enhanced with metal inserts. a) Photolithography-defined catalyst lines, b) CNT growth, c) definition of electrodes, d) definition of metal inserts (using the same design as catalyst or denser lines) by second photolithography exposure followed by e-beam deposition of metal and lift-off.

These metal inserts do not shunt the CNTs since they are physically separated but improve the electric connection from one part of the CNT strip to the next. Additionally, since at operating frequency the CNT strip is long of about a quarter-wavelength, the alternated metal-CNT structure is small compared to the wavelength and is seen as an effective medium with a conductivity the sum of the ohmic conductivity (CNTs and interconnections at the catalyst) and of an additional percolation conductivity. CNT decoration with gold nanoparticles, which was demonstrated to help detect CNTs by Surface-Enhanced Raman Spectroscopy [196] may also help in this way.

IV.C.2.2.3) Initial fabrication results on designed CNT strips

Initial growth results for this process, one of the last ones attempted, are reported on Fig. 82. Here we used a thin (<1nm) film of e-beam-deposited iron patterned by standard photolithography into thin strips normal to the lattice/growth direction of the quartz substrate. The growth recipe and run were E0.09 as reported in Appendix 6, the same than for the other horizontal CNT growths reported in section III.B.3). The CNTs and possibly left-over iron seem to form a well-connected structure as there appears to be some dipolar electron absorption-scattering. This could be due to charge absorption when the scanned e-beam first touches the CNTs then increased scattering as the CNTs become saturated in electrons.

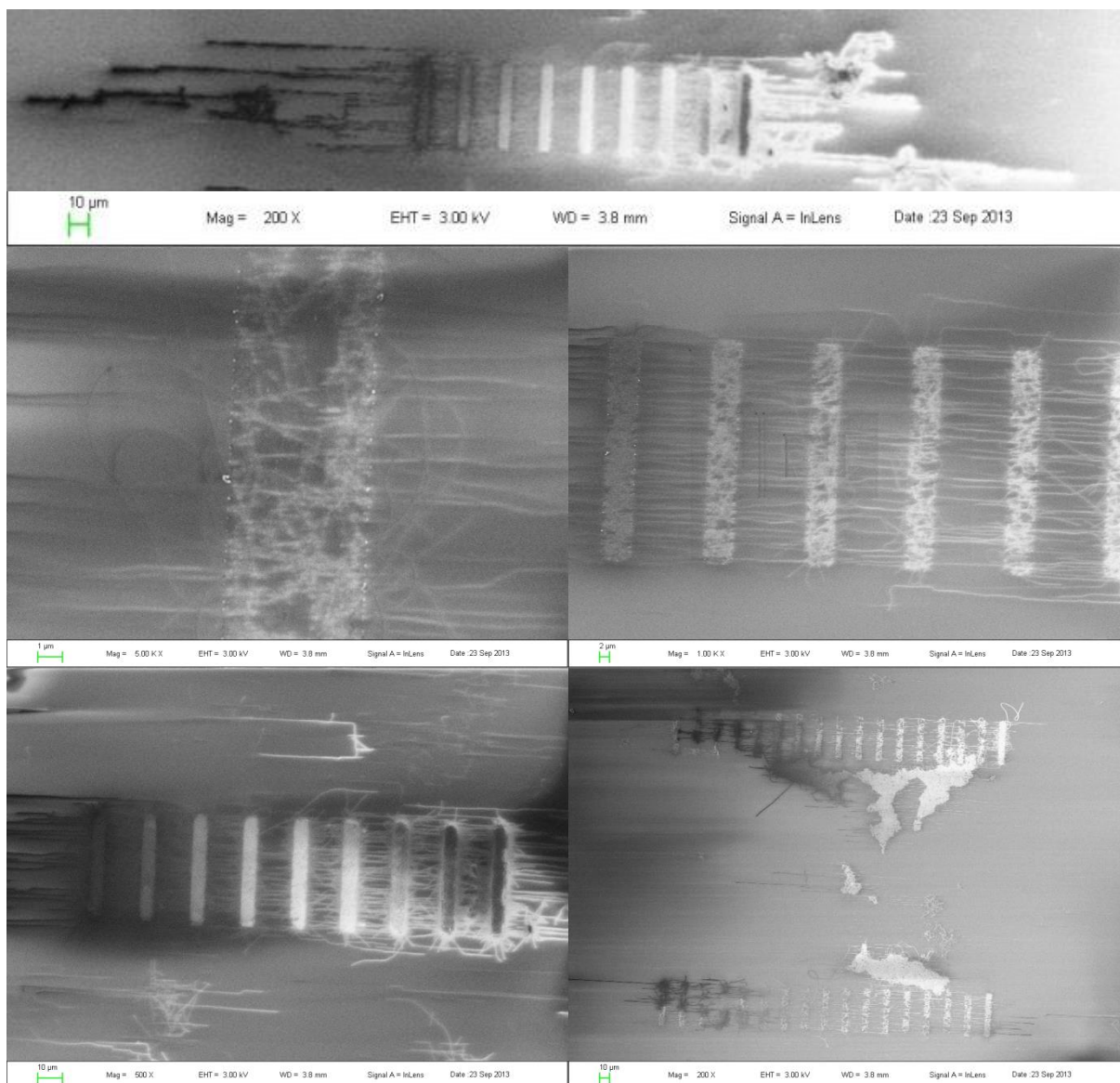


Fig. 82. CVD-grown multi-catalyst-lines CNT strips. The strips may be used as such as dipoles in free space or connected with the CPW feed described in this section to form a monopole. The imperfect patterning is due to small issues in the lift-off process. Dipolar behavior and close-up views confirm the good connection of the multiple parts of each strip – that can still be improved by adding metal over the former catalyst lines.

IV.D) Prototypes from vertically-grown CNTs

As, we have seen in the previous sections, the ideal CNT number in a monopole intended to be an electrically-short resonant antenna is in the 10-1000 range for size reduction factors of ~ 20 to 2. In the case of vertical CNTs it is quite challenging to realize an array with so few CNTs because of the very high areal density they present. It is desirable in applications where they are used as interconnects or absorbers but, in our case, it requires micrometer to sub-micrometer definitions – in the order of magnitude of the optical resolution limit – to

define the CNT array. An additional challenge is the aspect ratio of these arrays. Indeed CNT lengths of tens to hundreds of micrometers are required in the frequency range we are targeting (200-300GHz).

Nevertheless, the expertise of the group of Beng Kang Tay in CINTRA/NTU EEE in vertical CNT array growth probed us into exploring designs relying on these types of CNTs and into finding techniques to work around these limitations and push the experimental boundaries.

We report on the non-trivial feed design for these uncommon antennas and on the techniques and designs developed to address the aspect ratio and robustness issues of the vertical CNT arrays.

IV.D.1) Design

The problematic here was to adapt the ideal case presented in section IV.A) to a feasible experimental antenna including a CPW feed for measurement with a VNA and CPW probes. A vertical monopole is designed but concerns on its robustness lead us to investigate two improvements. The cross-sectional shape of the rod is optimized for improved robustness and preferential toppling directions as the final solution seems to be a vertically-grown toppled monopole.

IV.D.1.1) Vertical monopole

Two KOH-cavity-based monopole designs were elaborated and studied before the much simplified final vertical rod design was adopted. They are exposed for reference in Appendix 8 in their quality of experimentally unimplemented concepts.

The final vertical antenna design stems from designs of classical quarter-wavelength CPW-fed vertical monopoles proposed by Y.K. Yoon and B. Pan in [197]–[200]. The main principle is to use the quasi-infinite ground plane of the CPW line as the ground for the antenna. The ground plane is therefore very close to the rod enabling good coupling and the antenna design is mostly substrate-independent except for the dimensions of the CPW feed. Furthermore, with CNT monopoles, the fabrication process is limited to two steps of lithography and metal deposition – one for the fabrication of a metal plane with the CPW slots and one for the patterned deposition of the catalyst for the growth of the monopole – and one

step of CVD growth. The CPW feed is also well adapted for high frequencies and will allow measurement of the antenna directly with a VNA connected to a probe station. In this design, as for the microstrip feed, the monopole is aligned with the electric-field lines. The general design is shown on Fig. 83 a).

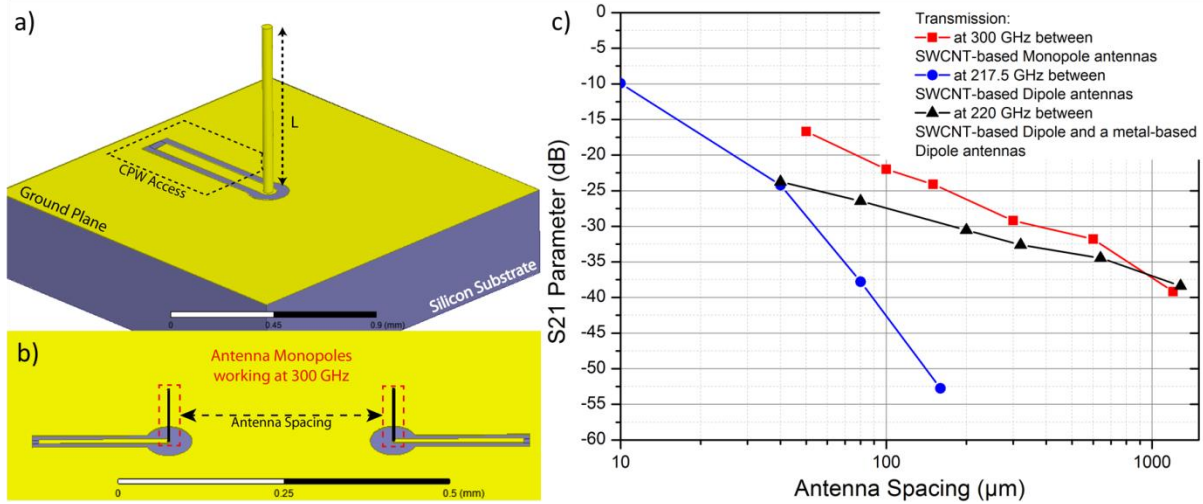


Fig. 83. CPW-fed vertical CNT monopole. a) General design. b) Transmission configuration. c) Transmission level vs. antenna spacing at 300GHz. The results of the horizontal CNT dipoles at 220GHz are also included.

The CNT monopole parameters were determined using the CNT Antenna Designer spreadsheet elaborated in section IV.A.2) and the CPW feed was designed and integrated by Christophe Brun. The design and simulation with CNTs were made possible by using the EM bulk model and simulation methodology I established in [71] as reported in sections II.B) and II.C). Designs at 96, 216 and 300GHz were studied and optimized as reported in [172], [173]. The bundle is made of 1000 CNTs for a radius of $2.2\mu\text{m}$ and lengths of 300, 150 and $100\mu\text{m}$ respectively while classical metallic monopoles in this configuration resonate at these frequencies for lengths of 760, 350 and $250\mu\text{m}$ respectively – about 2.5 times longer. Hence the CNT antennas are slightly above the conventional definition limit of electrically-short antennas. The gain over metal antennas of the same dimensions due to current distribution might be less than 1.6 but the resonance still allows a good impedance matching where the metal rods would not. Even ruling out the size reduction, direct growth of patterned vertical CNTs could be an interesting technological alternative to photopatternable epoxy SU-8 pillars or magnetic lifting [199] to create high-aspect ratio vertically standing structures.

The transmission antenna-to-antenna was studied in facing antennas configuration (Fig. 83 b)). The transmission versus antenna spacing is reported on Fig. 83 c) where we

included some of the horizontal dipole transmission results from IV.C.1.3) as a reference although the differences in operating frequency (220 and 300GHz), structure – and thus effective medium – and size reduction (4 vs. 2.5) do not allow a direct comparison.

This configuration is implemented in the mask described in section IV.E) with various spacing values. The design at 216GHz will be referred to as C with metal below the rod and D with holes in the metal layer corresponding exactly to the shape of the rod for the pattern arrangement V we define then. The design at 300GHz will be referred to as A with metal below the rod and B with holes in the metal layer corresponding exactly to the shape of the rod for the pattern arrangement Y we define then. Finally an additional feed design compatible with 1000-CNT rods resonating between 150 and 350GHz is added, with metal under the rod, and referred to as E.

IV.D.1.2) Aspect ratio issue and monopole cross-sectional shape

On one hand, the standing monopole design requires a low number of CNTs – 1000 or less – resulting in a CNT bundle diameter of 5 μm and below. On the other hand the CNT bundle needs to be sufficiently long for resonance at the desired frequency – 100 μm at 300GHz or 300 μm at 100GHz for a size reduction of ~ 2.5 in air. This leads to the main practical limitation of the design exposed in the previous section: a very high aspect ratio at common CNT densities and measurable frequencies. A rod presenting this kind of aspect ratio is difficult to achieve during the growth and mechanically instable. To reduce the aspect ratio, let us look at the various parameters and see whether we can work our way around the limitation.

Firstly, the necessary length is determined by the frequency (inversely proportional to the length) and the number of tubes (reduction factor). The lowest achievable number of CNTs depends on the density and the lithography resolution. The photolithography limits us to a resolution of 2 μm at best. A lower density would be desirable but cannot be achieved as the vertical growth relies on the Van Der Waals force.

In Fig. 84, we propose rod designs that allow maximizing the footprint while keeping a lower number of CNTs than a circular base rod. They take into account 1.5 μm resolution limits of photolithography. A 3-pointed-star pattern appears to be the optimum. These designs have been included in the monopole mask for mechanical test.

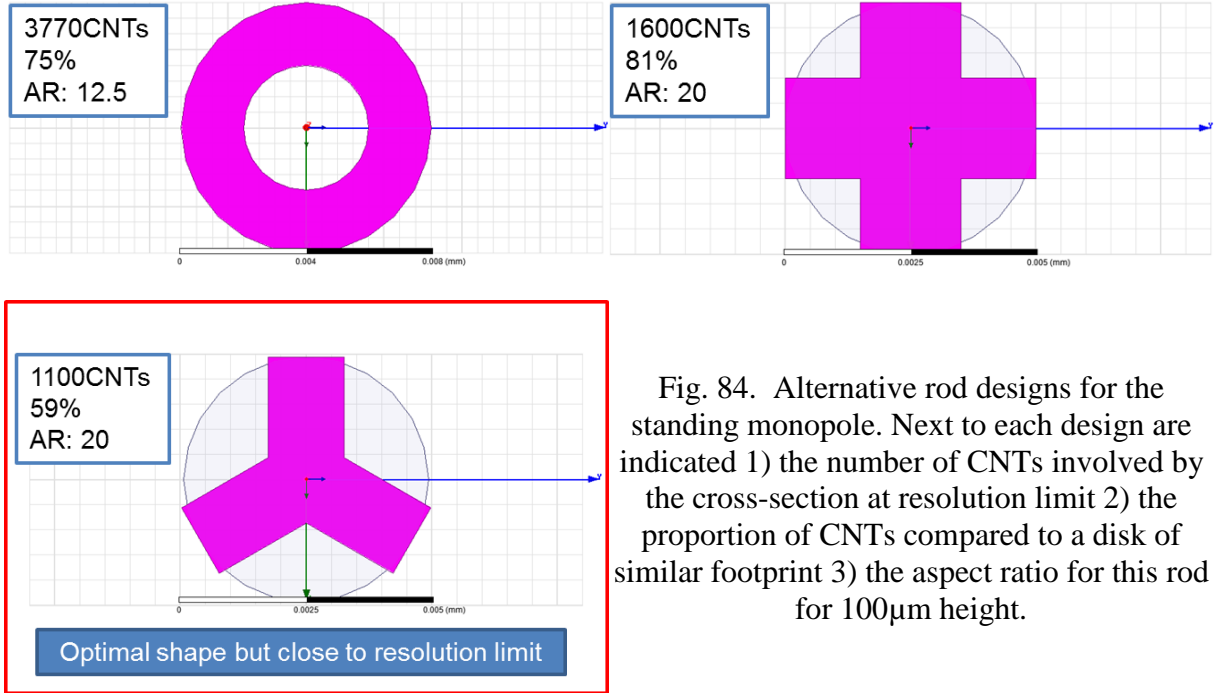


Fig. 84. Alternative rod designs for the standing monopole. Next to each design are indicated 1) the number of CNTs involved by the cross-section at resolution limit 2) the proportion of CNTs compared to a disk of similar footprint 3) the aspect ratio for this rod for 100 μ m height.

We plot the number of CNTs in different shapes of bundles as a function of their effective external radius on Fig. 85. The number of CNTs in the three-pointed star progresses much slower with the increasing dimensions. At resolution limit however the three arms become difficult to define. We derived a modified expression for the calculation of the area covered by a resolution-limited three-pointed-star and thus its number of CNTs:

$$N_{CNT,star} = D_{NT} \left(3 \left(\frac{1}{2} \pi r^2 + (w - 2r)r + w(l - r) \right) + \frac{\sqrt{3}}{4} w^2 + 3 \left(\frac{5\sqrt{3}}{12} - \frac{\pi}{6} \right) r^2 \right) \quad (181)$$

where r is the radius of resolution and w and l are the width and length of the arms of the three-pointed star.

For the mask described in section IV.E), following these observations, we chose to include the six designs listed in Table 5. This way we include designs with minimal number of CNTs ($d_{2,2}$ and $s_{3,3}$ with the star 1.5 times larger but the number of CNTs almost equal), stars with limited number of CNTs (still too many but should be more stable mechanically)

and a relatively large disk as safety net or to compare with the others. On Fig. 86 we show the catalyst patterns as realized by photolithography – after development and before further treatment. The next three pages (Fig. 87) show FE-SEM images of either the tip or the base of a bundle of CNT realized with each pattern, in the same order as in Table 5. This demonstrates the feasibility of such patterned growth at small scales and the fact that the bundle will retain the pattern along its all length (up to 300 μm already fabricated). Furthermore these pictures could serve to analyze the density. The CNTs can be clearly seen at the different zooms.

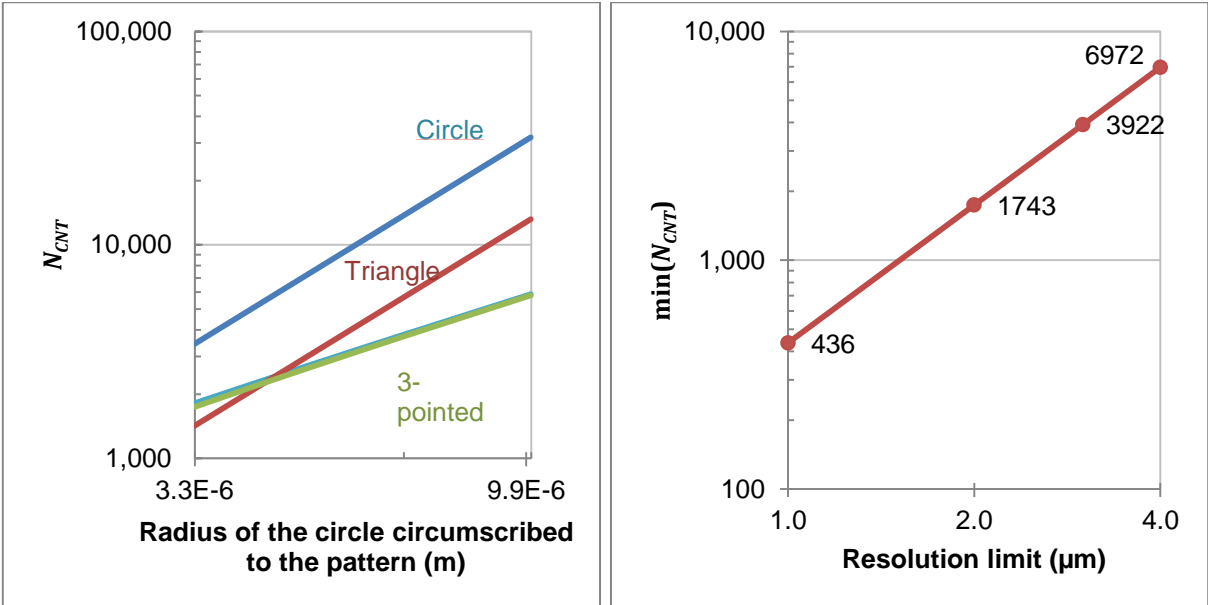


Fig. 85. Effect of the pattern on the number of CNTs. Plots are for a CNT density of 10^{14}m^{-2} . Left: N_{CNT} vs. radius of the pattern shows the advantage of the 3-pointed star vs. disk. Right: $\min(N_{CNT})$ vs. resolution limit for the 3-pointed star

Table 5. Selected patterns for the mask in this order top to bottom. All lengths in μm . The estimated number of CNTs is based on a CNT density of 10^{14}m^{-2} and takes the rounded edges due to diffraction limit into account for the three-pointed-star patterns.

Type	Name	Width of arms	Length of arms	Ext. radius	N_{CNT}
Disk	d ₁₀	-	-	10	31400
Star	s _{5.6}	2	5	5.6	3104
Disk	d _{2.2}	-	-	2.2	1520
Star	s _{3.3}	2	2.7	3.3	1743
Star	s ₄	2	3.5	4	2204
Star	s ₁₀	2	9.5	10	5804

The table is accompanied by a series of microscopic images on the right side, showing the physical catalyst patterns for each row. The patterns are arranged in a grid. The top row shows a large disk pattern. The second row shows a star pattern with 5 arms. The third row shows a small disk pattern. The fourth row shows a star pattern with 3 arms. The fifth row shows a star pattern with 4 arms. The bottom row shows a star pattern with 10 arms. The images are labeled with coordinates at the top and bottom.

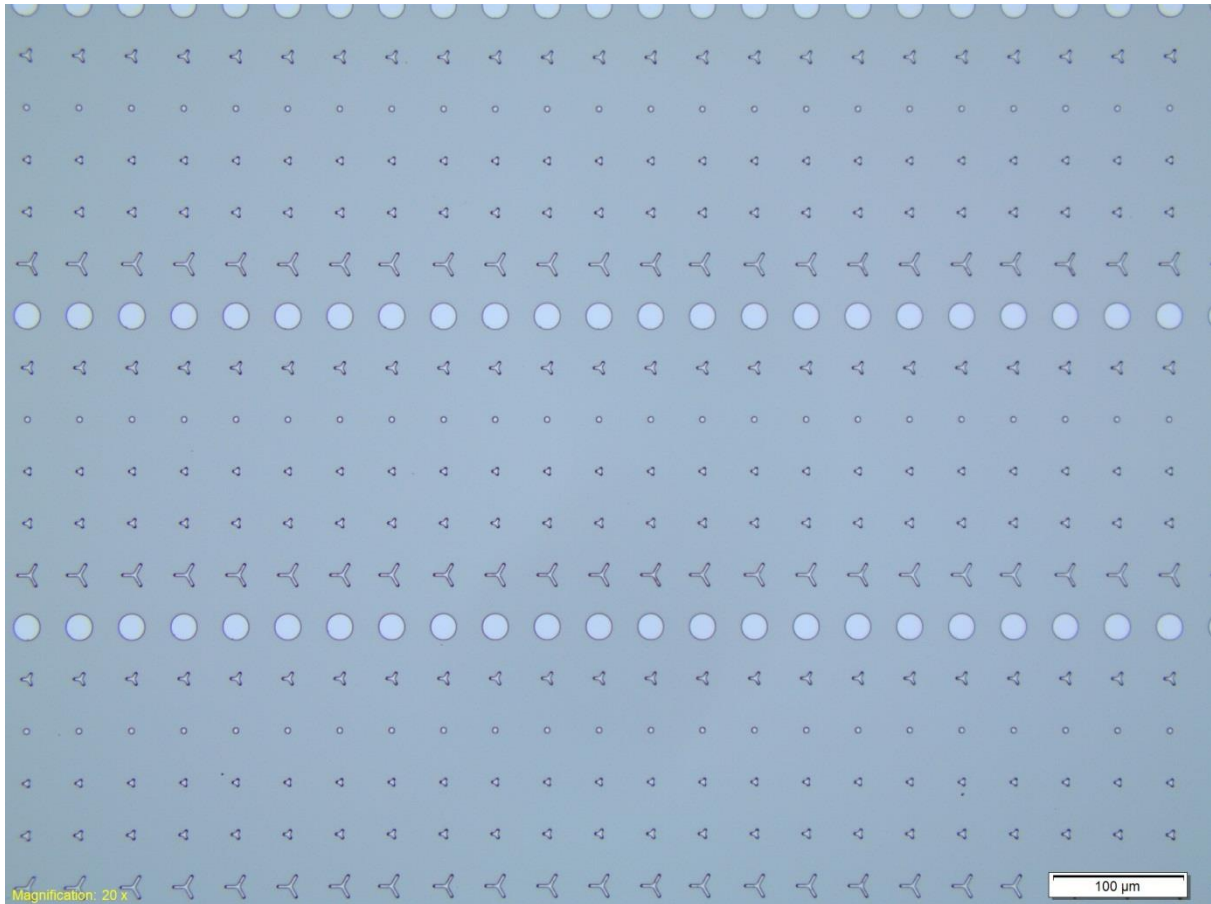
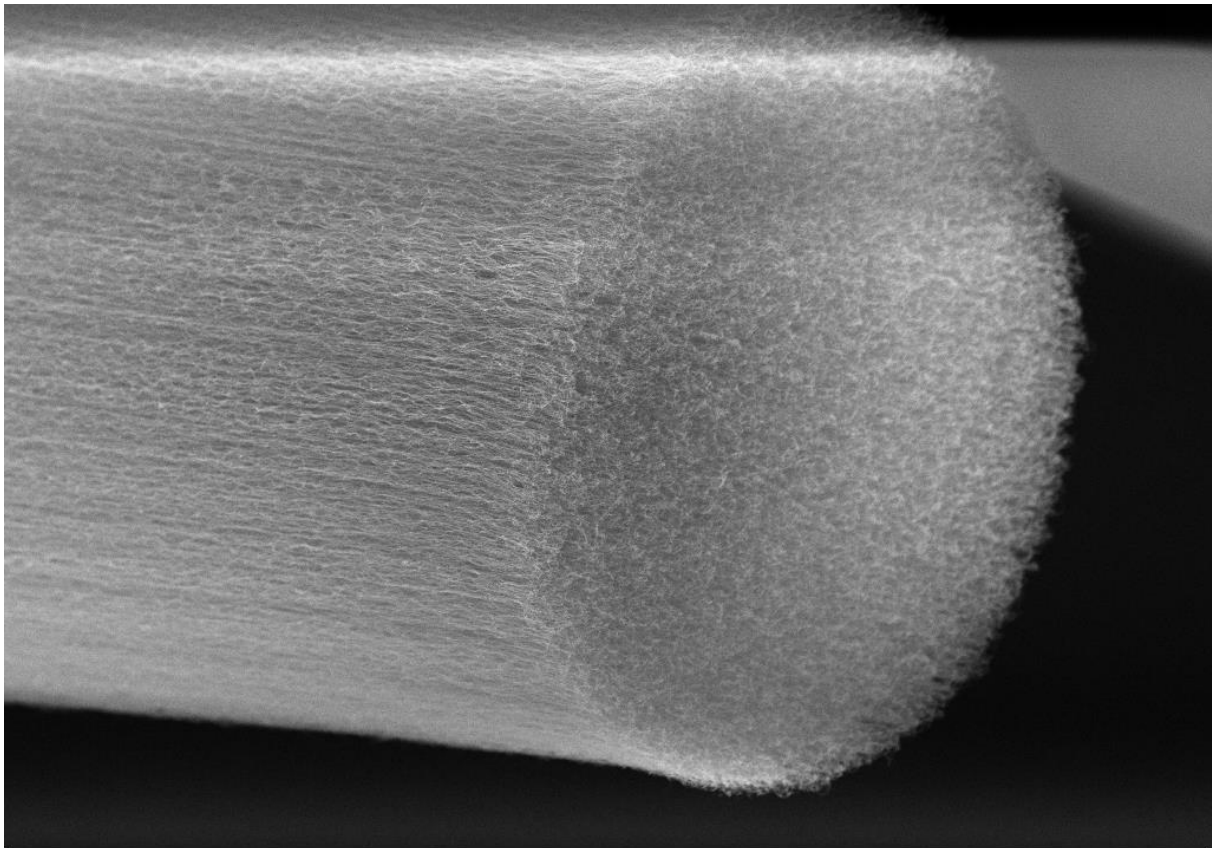
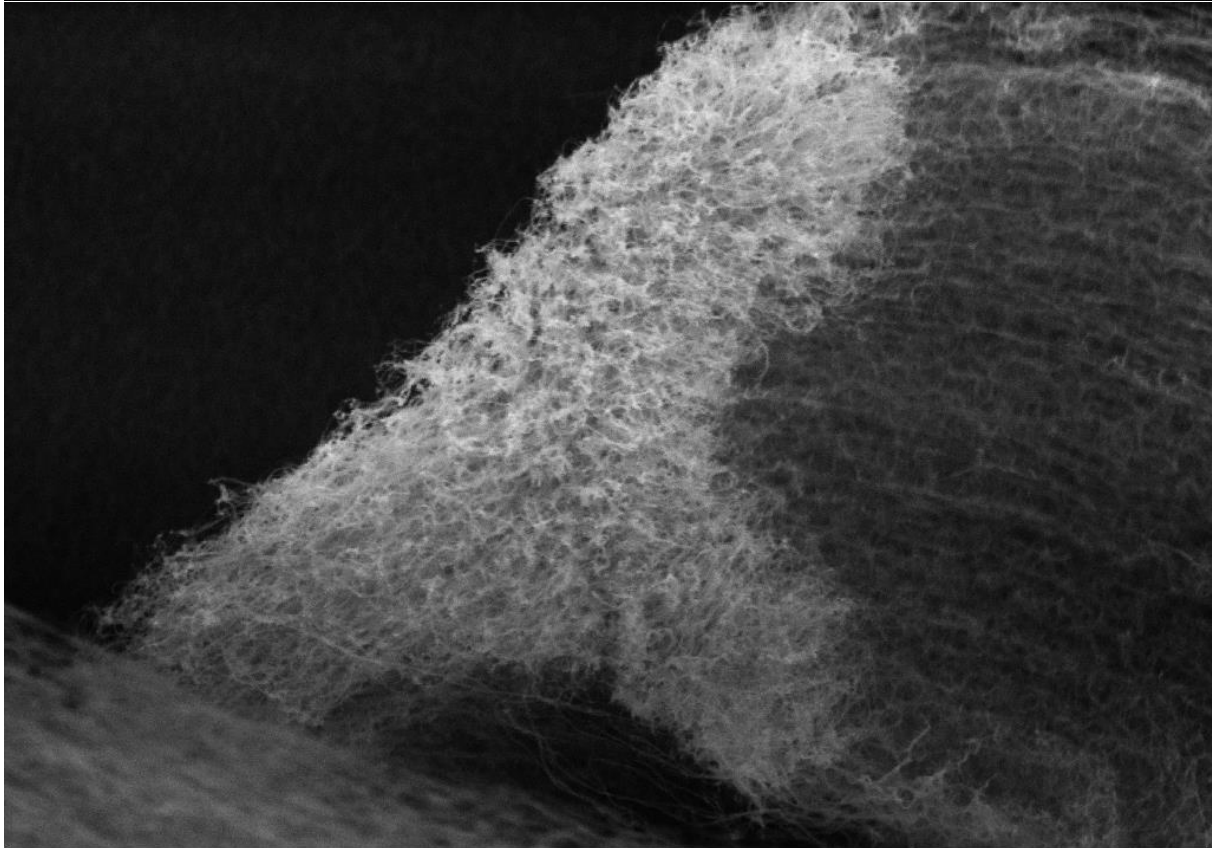


Fig. 86. Catalyst patterns as realized by photolithography (after development and before further treatment).

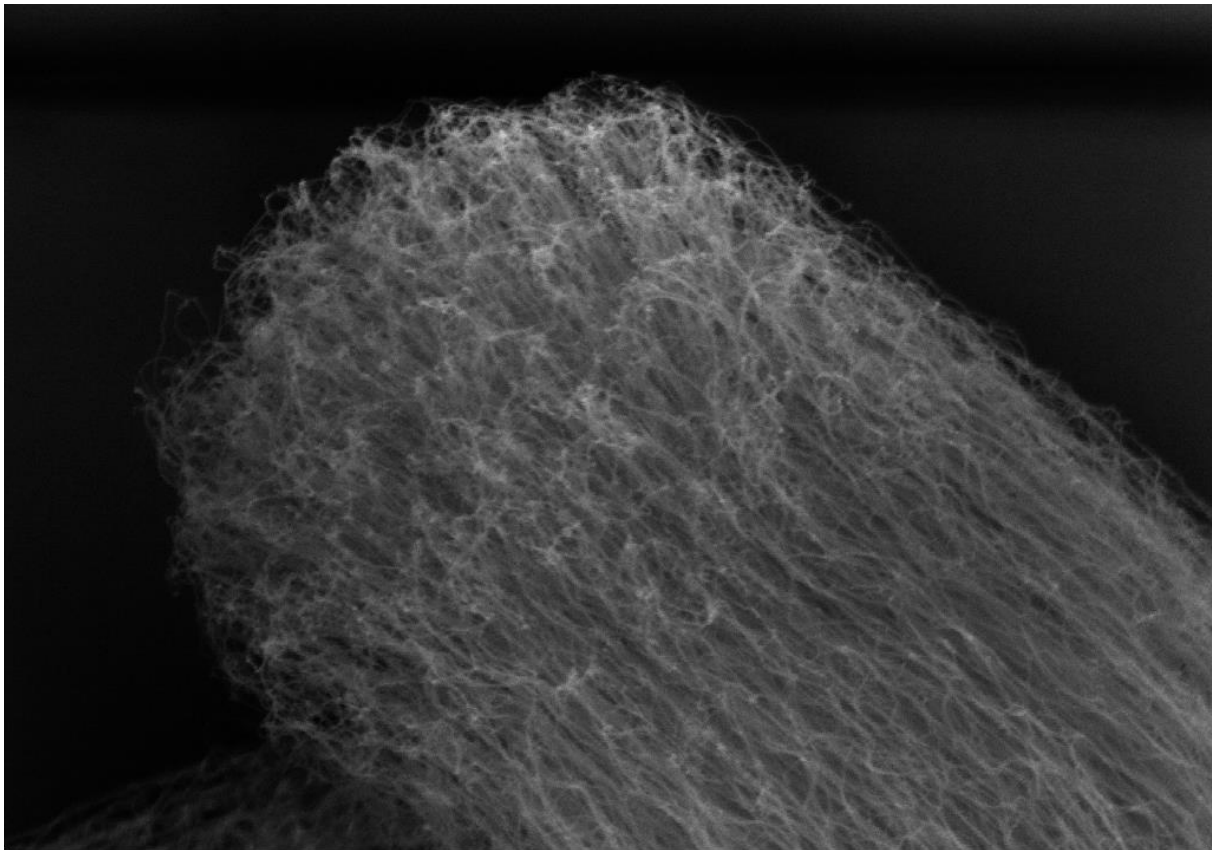
Fig. 87. Below, in this order: bundle tips and bases showing the effect of the catalyst patterns for each $d_{10}(\times 4k)$, $s_{5.6}(\times 13.5k)$, $d_{2.2}(\times 20k)$, $s_{3.3}(\times 20k)$, $s_4(\times 10k)$, $s_{10}(\times 5k)$. The fabrication is demonstrated.



1 μ m
Mag = 4.00 K X EHT = 4.00 kV WD = 8.8 mm Signal A = InLens Date :30 May 2013



200 nm
Mag = 13.50 K X EHT = 4.00 kV WD = 8.9 mm Signal A = InLens Date :30 May 2013



200 nm

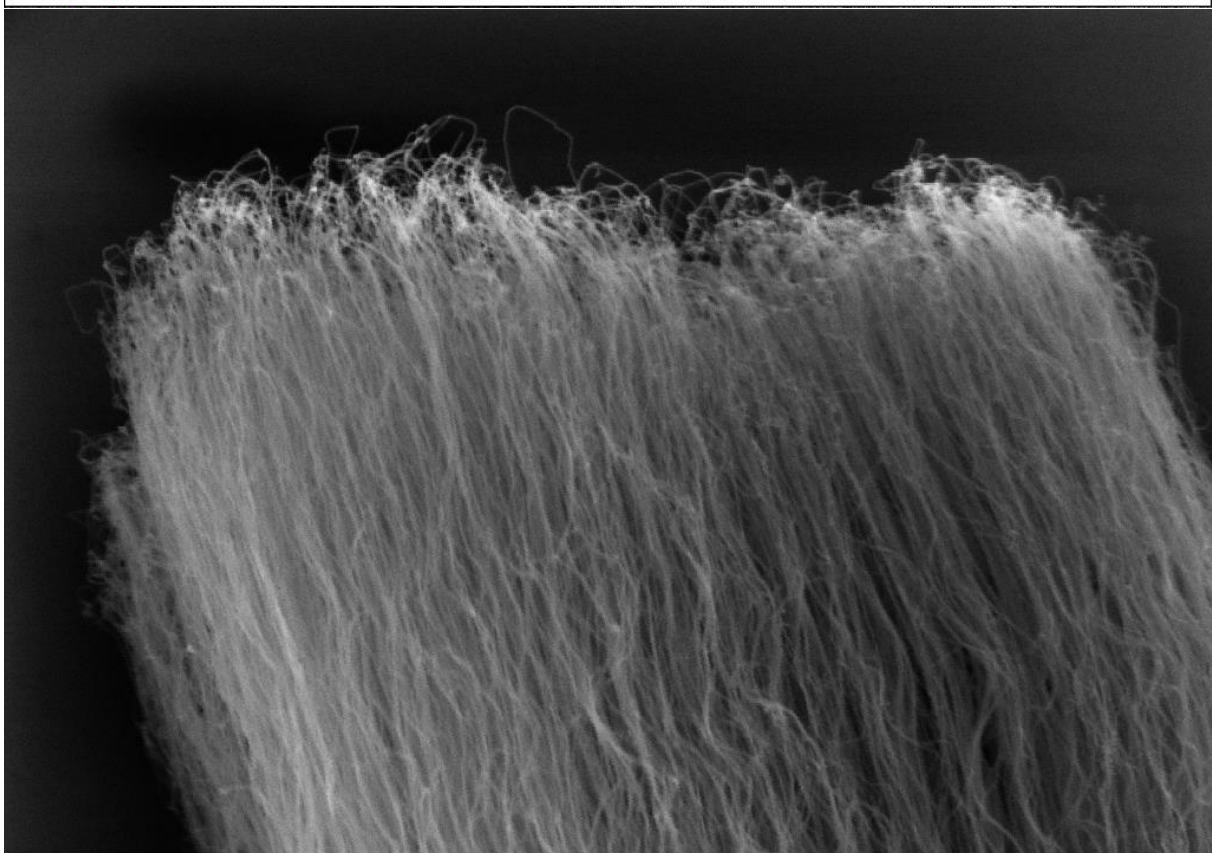
Mag = 20.00 K X

EHT = 4.00 kV

WD = 8.9 mm

Signal A = InLens

Date :30 May 2013



200 nm

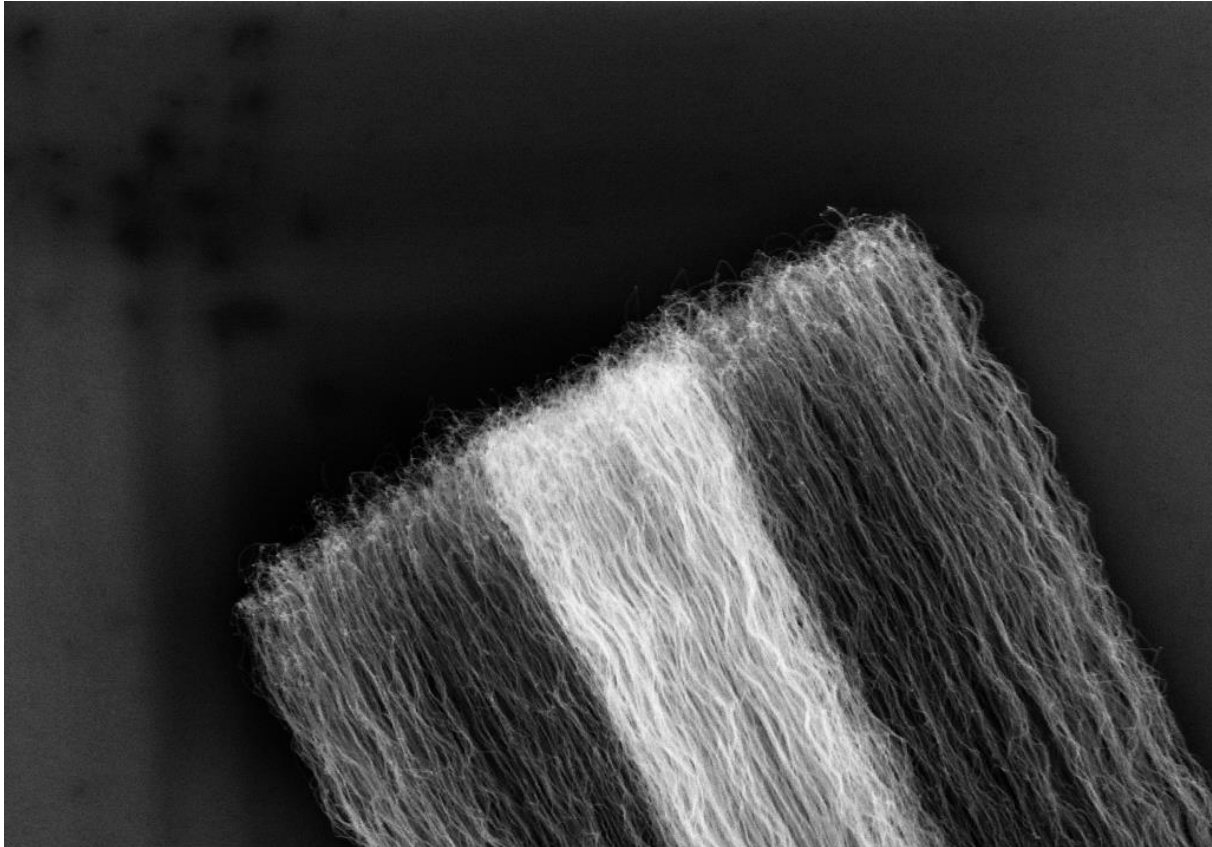
Mag = 20.00 K X

EHT = 4.00 kV

WD = 8.8 mm

Signal A = InLens

Date :30 May 2013



200 nm

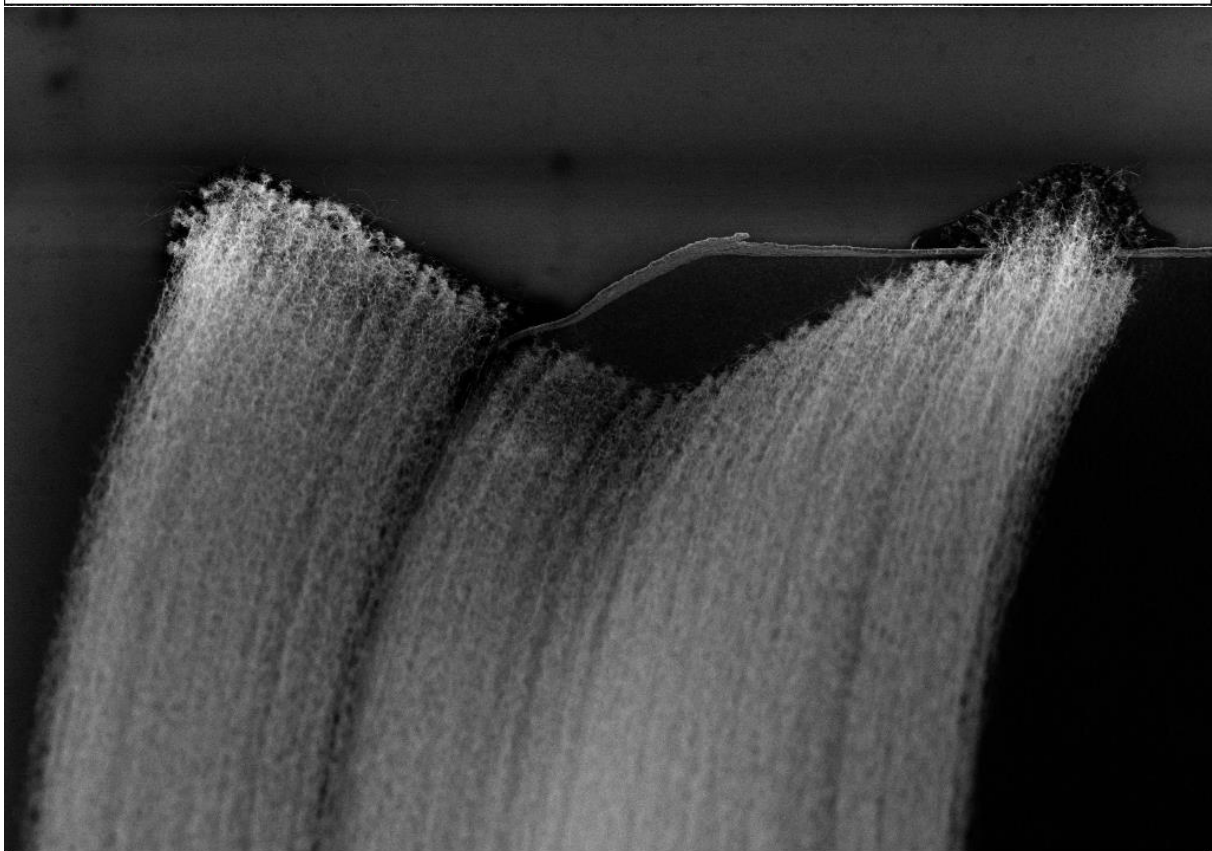

Mag = 10.00 K X

EHT = 4.00 kV

WD = 8.8 mm

Signal A = InLens

Date :30 May 2013



1 μ m


Mag = 5.00 K X

EHT = 4.00 kV

WD = 8.8 mm

Signal A = InLens

Date :30 May 2013

IV.D.1.3) Toppled-CNT horizontal monopole

Admitting the vertical monopole can be grown, there is still concern on its robustness for transport, measurement and integration in planar circuitry. One interesting solution is to design an antenna using a toppled CNT rod. In this case we come back to a horizontal monopole design but with the advantage of using a well-mastered growth technique. A horizontal monopole also requires a lower aspect ratio for the rod to be fabricated as the antenna will be shorter at a given frequency by $\sqrt{\epsilon_{r,eff}}$ (1.55 for quartz and 2.54 for Si). Finally, this antenna design should be robust to misalignment by even 45°: it will affect the capacitive coupling but only on a logarithmic scale.

IV.D.1.3.1) Fabrication

We propose three options to realize toppled vertically-grown CNT bundles. A first option is to fabricate solution-toppled CNT lines and use O₂-plasma etching to define the bundles following the process established by Wai Leong in CINTRA/NTU EEE (cf. Fig. 90 and section II.C.3.3)). This is a wet process which implies condensed CNT bundles and hence rod dimensions (1µm width on 100nm thickness typically) that are challenging to fabricate (below resolution limit of photolithography) and difficult to physically match to the width of usual lines on quartz, typically tens to hundreds of micrometers. Let us look at dry alternatives.

The second, and preferred, option is to grow the CNT rod vertically from patterned catalyst then topple it down with an air/N₂ gun as illustrated on Fig. 88. This is a dry process and requires no further step after toppling the bundle down. A third option is to mechanically roll over the CNT rod to topple it in the way Cary L. Pint reported in [184], [185] over CNT lines (cf. Fig. 89). This may prove cumbersome for a rod that can fall in almost any direction contrary to the lines. Otherwise we can proceed to mechanically topple the lines as in the original papers followed by an O₂ plasma to etch the bundles out with a shadow mask but over 5µm depth and with difficult to obtain 5-10 µm resolution.

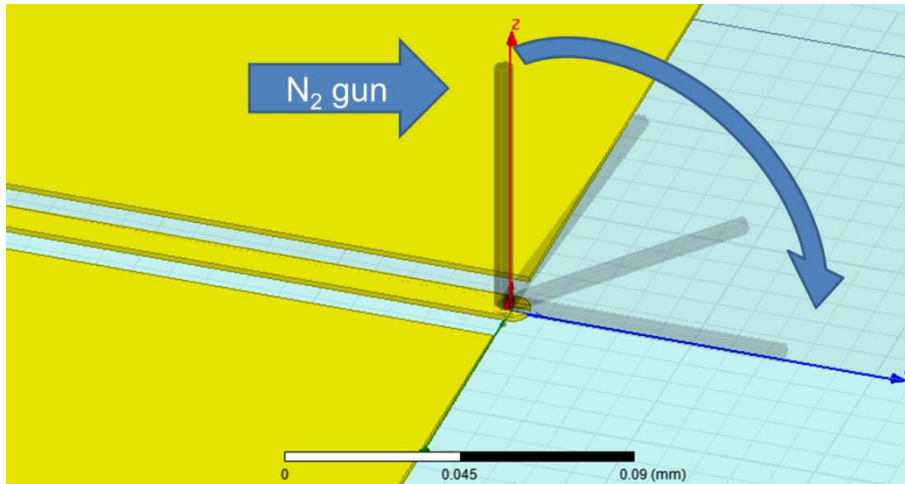


Fig. 88. A CNT rod may be toppled by blowing a gas at it such as N₂.

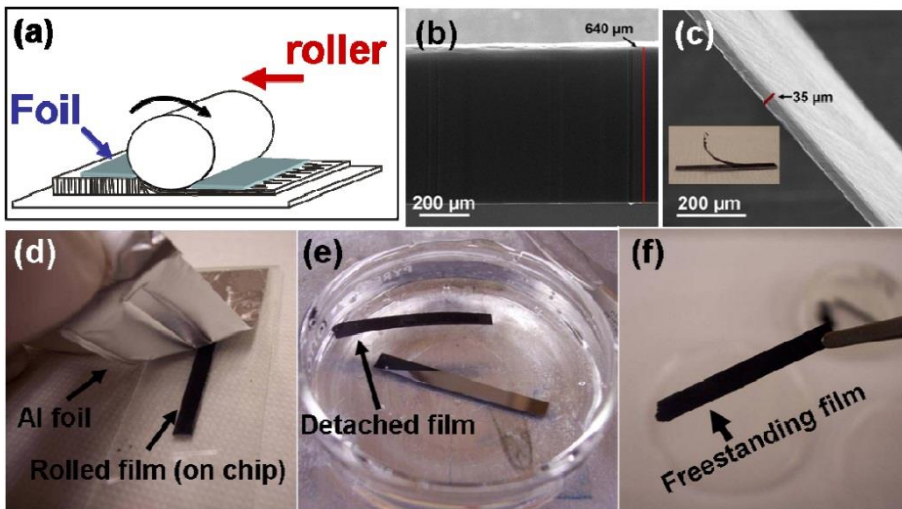


Fig. 89. Mechanical toppling process by Cary L. Pint. Reproduced from the supplementary information of [184].

IV.D.1.3.2) Design and analysis

IV.D.1.3.2.1) Initial study

Before elaborating the final designs we ran a feasibility study on a simple design. Fig. 90 illustrates a 325GHz toppled-CNT-based monopole as simulated in HFSS. A parametric study and performance analysis have been run as reported in the next figures. Fig. 91 and Fig. 92 show the good performance of the antenna for its kind while Fig. 93 and Fig. 94 show that the design is robust in the experimental variability range.

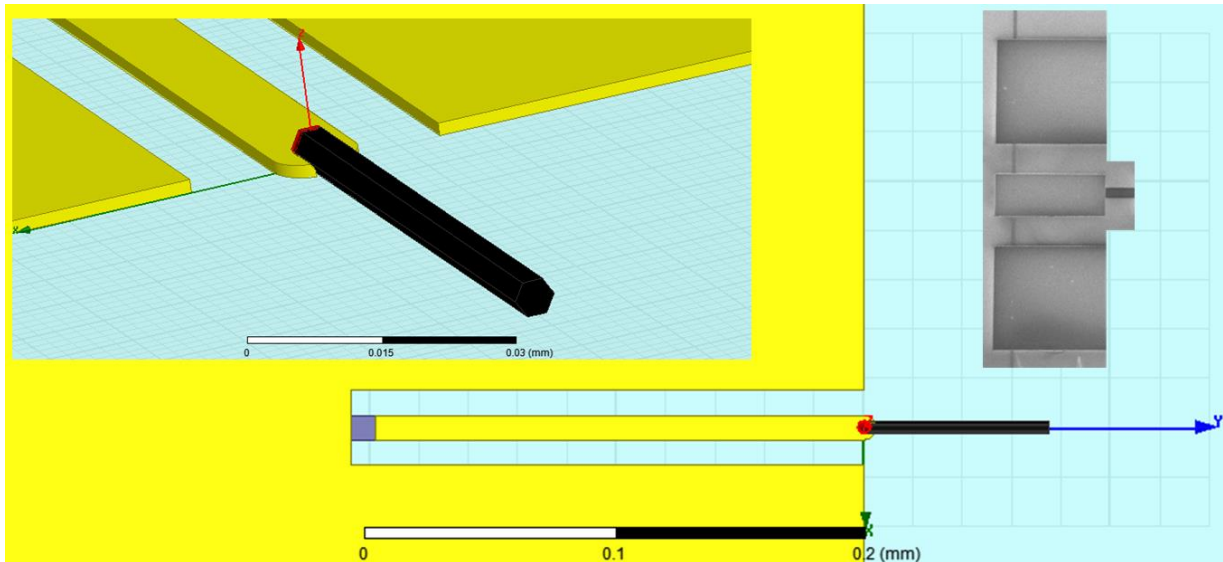


Fig. 90. Horizontal Monopole design in HFSS as simulated and illustration of a possible realization following the process developed by Wai Leong Chow (SEM image of a fabricated gap structure cropped to show how a monopole could be realized with the existing process)

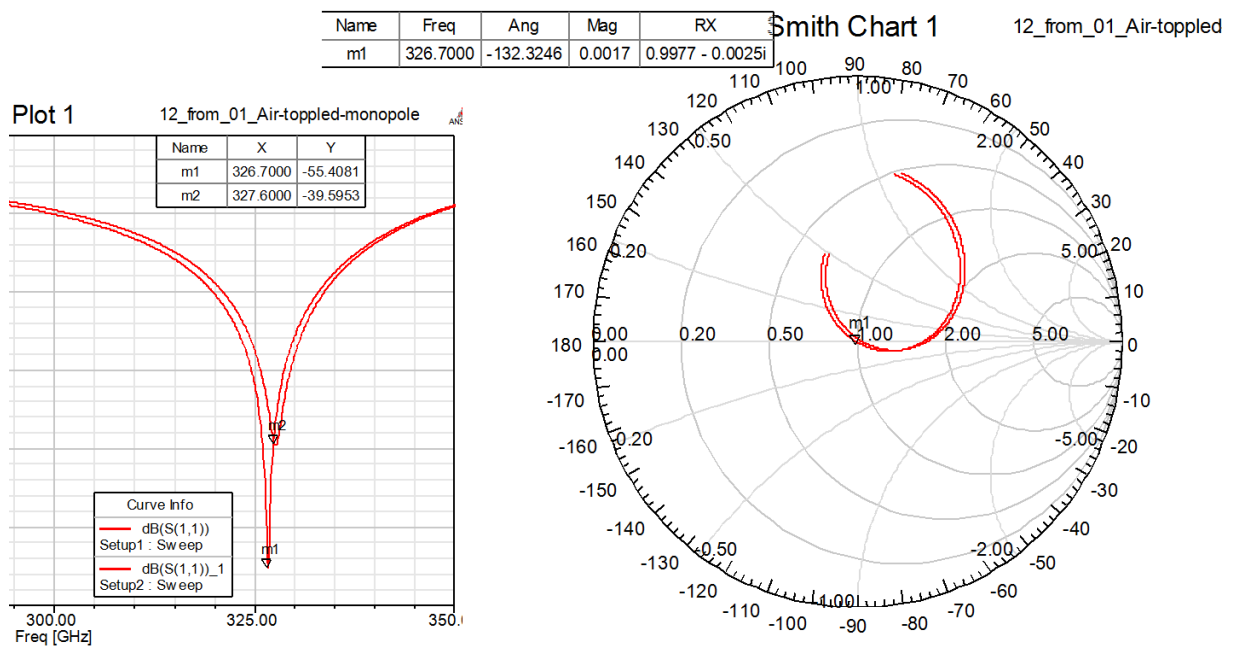


Fig. 91. A sharp resonance in the return loss (left) matched with a normalized complex impedance of almost perfectly 1 on the Smith Chart (right) show an excellent impedance match at 50Ω .

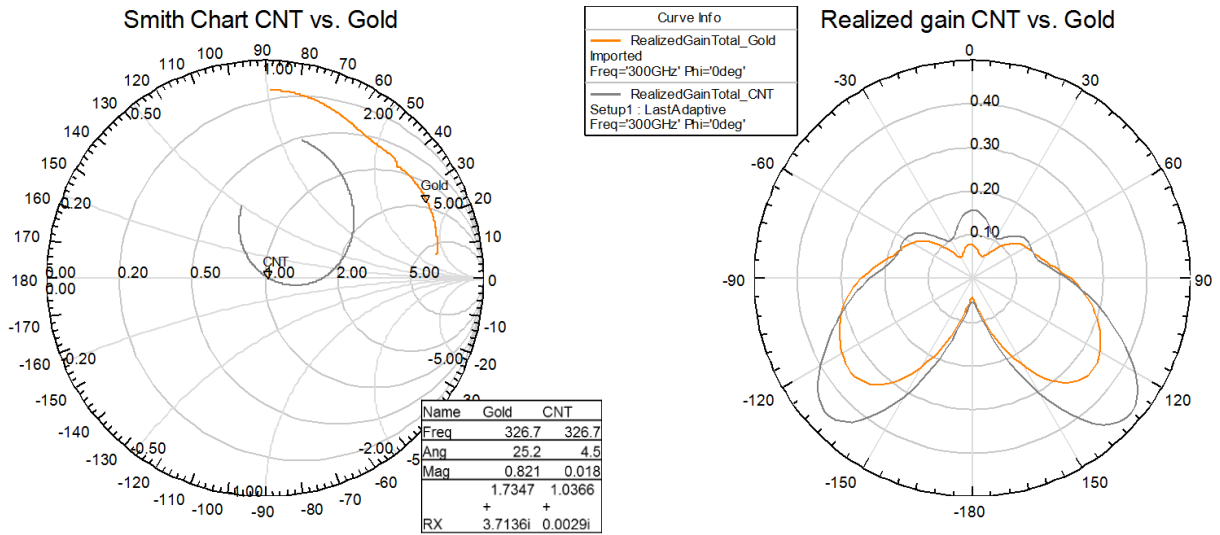


Fig. 92. The fact that the CNT antenna is resonant and impedance-matched to the feed at resonance allows it to have a better realized gain.

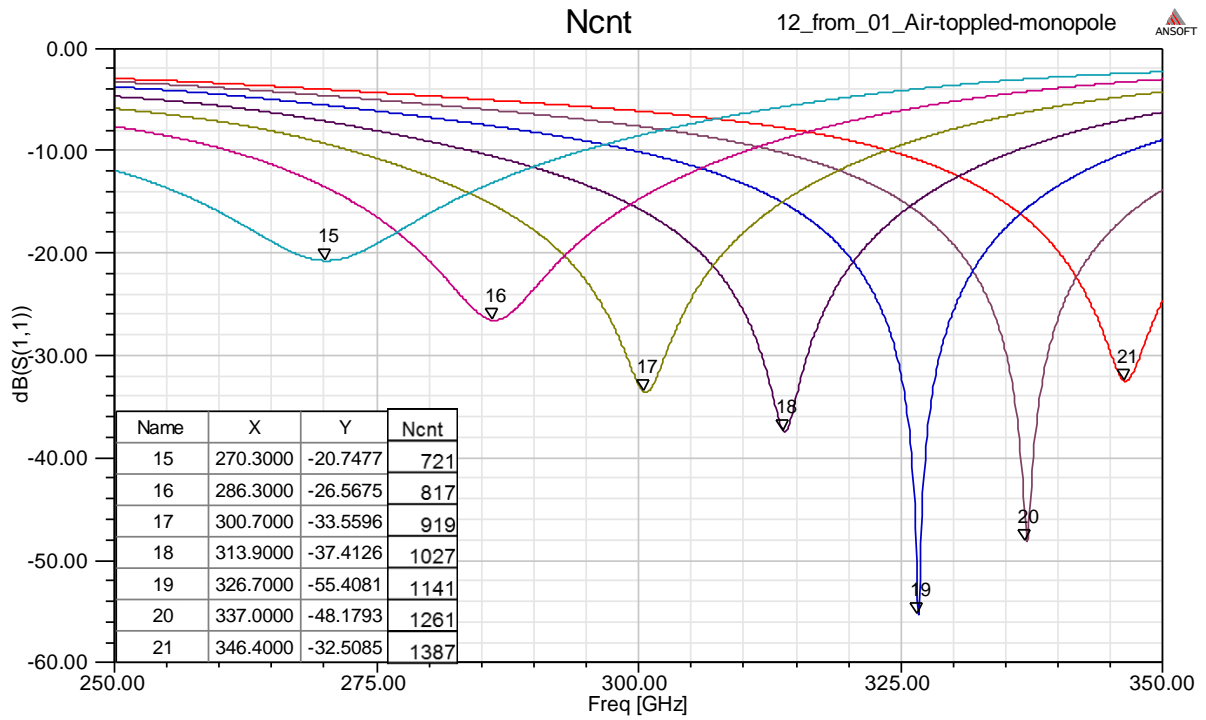


Fig. 93. A parametric analysis on the number of CNTs in the bundle shows that the design works with variable N_{CNT} (ratio of 2 on total number yielding diameters between 3.5 to 5.1 μm)

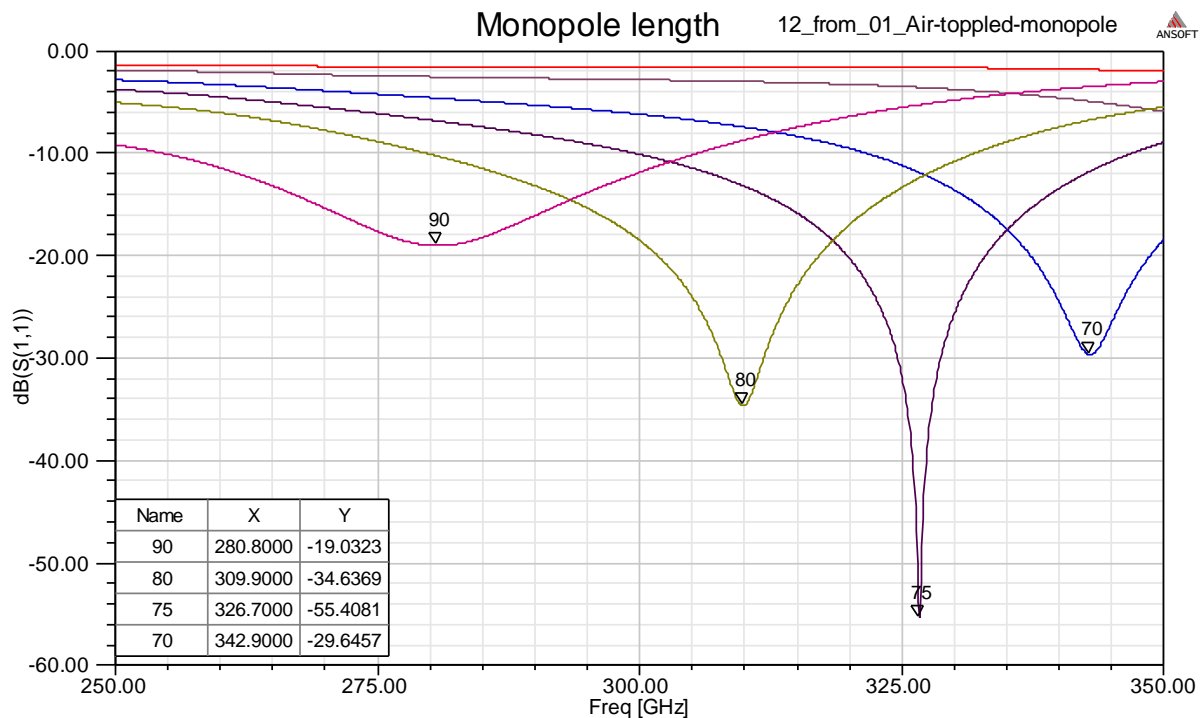


Fig. 94. A parametric analysis on the length of the bundles shows that the resonance frequency scales with length as expected and the design works well with a 5-15 μ m tolerance.

The study is conclusive and shows this type of design is robust and effective in terms of electrically-short antennas while the radiation is indeed mainly from the antenna not from its feed.

IV.D.1.3.2.2) Final designs

We designed four different feeds to address the experimental uncertainties such as the best achievable CNT lengths and aspect ratios on such small catalyst patterns and the actual impedance of the CNTs that would be obtained (we recall that the plasmon lifetime in CNTs can vary by one order of magnitude depending on their quality).

Initially six designs were realized with 50- and 100- μ m minimum pitch for each of the three frequencies corresponding to measurable bands: 90, 200 and 300GHz. The larger pitch is meant to limit failure at the lithography step: at 50- μ m pitch with 25- μ m-wide probe tips, the maximum width for the gaps of a 50- Ω line is around 6 μ m which is relatively small. The three frequencies are both for fabrication and characterization reasons. Lower frequencies require long CNT bundles which had yet to be achieved. Furthermore, the higher the frequency the more likely to observe resonances due to the kinetic inductance of the CNT bundles but the more difficult it gets to find the suitable equipment for measurement.

In Singapore, there are two facilities for measurements up to 300GHz, Virtus in NTU EEE and the A-STAR Institute I2R. Nevertheless the access is difficult and the equipment has never been set up for probe measurement. In France, XLIM has the equipment to measure in the 50-110GHz and 110-170GHz bands with 100- μm pitch probes while IEMN has setups up in the band 140-220GHz with 100- μm pitch probes and in the bands 220-325GHz and 325-500GHz with 50- μm pitch probes. Considering this, the performance of the designs, and the fabrication precision required, four designs were selected. All dimensions are reported in Table 6.

Table 6. Dimensions of the CPW feeds for horizontal monopoles. All lengths are in μm . For all designs, we have $L_3 = 3 \times \max(2\mu\text{m}, |G_2 - G_1|, |W_2 - W_1|)$, $W_2 + 2G_2 = W_1 + 2G_1$, $L_2 \approx \lambda/4$ and $L_1 = 4 \times l_{probe}$.

Design	L_2	G_2	W_2	L_1	G_1	W_1	L_3
1	164	6	54	140	6	54	6
2	250	10	46	140	6	54	24
3	245	20	102	140	12	118	48
4	542	42.5	57	140	12	118	183.5

All designs, include a 50- Ω CPW contact pad of central width W_1 , gaps G_1 and length $L_1 = 140\mu\text{m}$ four times the minimum length recommended for positioning the probes. Hence contact can be made anywhere on the pad without affecting the impedance match and if the pad is damaged the probes can be repositioned.

The next part is a quarter wavelength impedance matching section of central width W_2 , gaps G_2 and length $L_2 = \lambda_0 \epsilon_{r,eff} / 4$ at the nominal frequency. W_2 and G_2 are such that $W_2 + 2G_2 = W_1 + 2G_1$ in order to have straight lines at the ground edges of the gap, easier to fabricate precisely by photolithography. There ratio is defined such that the section has a characteristic impedance $Z_{C2} = \sqrt{50\Omega \times Z_{in,bundle}}$ to allow impedance matching between the CNT monopole and the probes. Additionally, the central conductor is kept wide enough to allow positioning the probes along this section to manually adjust the impedance matching in these exploratory designs.

Finally, a short tapered transition section is inserted between the pad and the impedance matching section. This is both to limit reflection at a discontinuity on the signal line and to make the photolithography process easier because smooth profiles are easier to fabricate than steps. The total width of the sections to connect is equal and so is the total

width of the transition. The taper is symmetric on the signal line. To allow for smooth transition the length is fixed as: $L_3 = 3 \times \max(2\mu\text{m}, |G2 - G1|, |W2 - W1|)$.

This composition is highlighted for designs 3 and 4 on Fig. 97 and Fig. 98.

Designs 1 (Fig. 95) and 2 (Fig. 96) have common 50- Ω CPW contact pad dimensions adapted to probes with pitches of 50 to 150 μm and 50- Ω over a very wideband ($\pm 0.3\%$ between 114-500GHz and less than 1% more down to 43GHz). The antennas were simulated with different contact pad lengths (35 and 140 μm) to check that the pad was indeed 50- Ω and therefore the positioning of the probes would not affect the measurement.

Design 1 has a nominal frequency of 300GHz and is a simple 50- Ω CPW line of the dimensions of the contact pad and of total length equal to the sum of the 140 μm of the pad, 6 μm minimum taper length and a quarter wavelength at 300GHz hence 310 μm . Design 2 has a nominal frequency of 200GHz and a 60- Ω quarter wavelength section. It is 414 μm long in total.

Designs 3 (Fig. 97) and 4 (Fig. 98) have common 50- Ω CPW contact pads adapted to probes with pitches of 100 to 150 μm and 50- Ω over a very wideband (less than 1% more from 500GHz down to 25GHz). Design 3 has a nominal frequency of 200GHz and a 60- Ω quarter wavelength section. It is 433 μm long in total. Design 4 has a nominal frequency of 90GHz and a 87- Ω quarter wavelength section. It is 865.5 μm long in total.

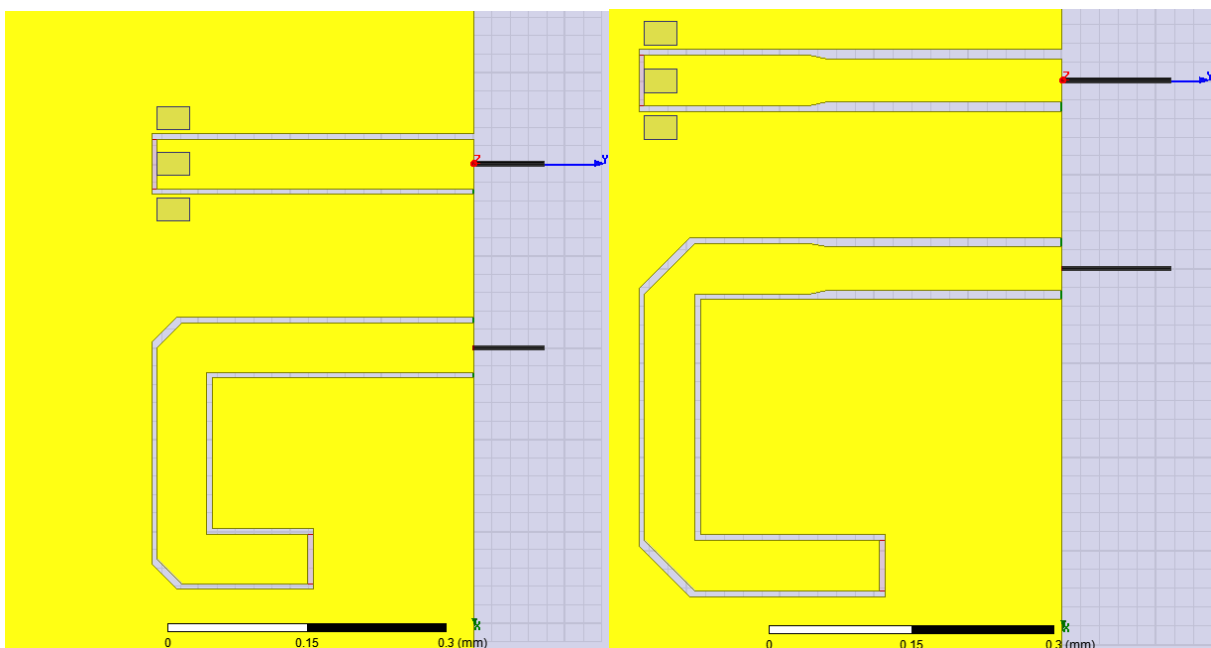


Fig. 95. CPW monopole feed Design 1. Simple I feed and inverted J for transmission. 50- Ω CPW line. Nominal frequency 300GHz. Acceptable probe pitch 50-150 μm .

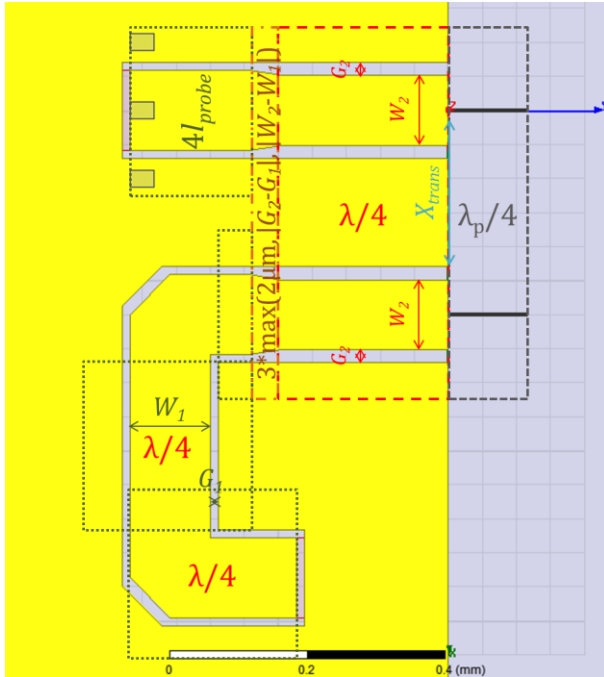


Fig. 96. CPW monopole feed Design 2. Simple I feed and inverted J for transmission. 140 μm 50- Ω pad and $\lambda/4$ 60- Ω CPW line. Nominal frequency 200GHz. Acceptable probe pitch 50-150 μm .

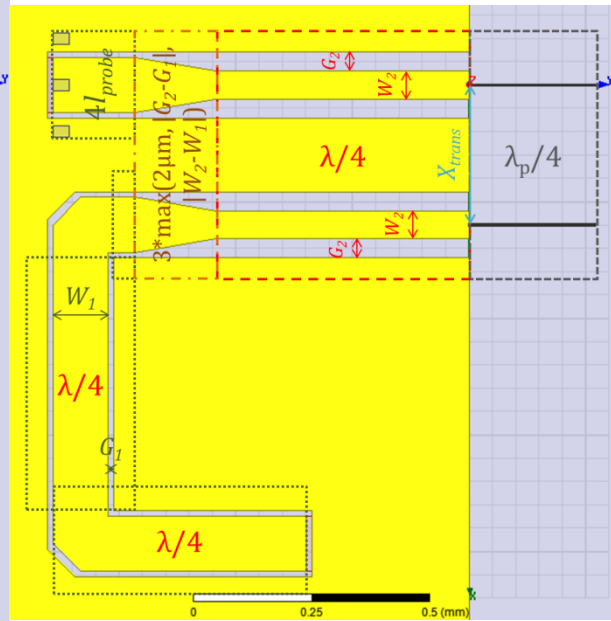


Fig. 97. CPW monopole feed Design 3. Simple I feed and inverted J for transmission. 140 μm 50- Ω pad and $\lambda/4$ 60- Ω CPW line. Nominal frequency 200GHz. Acceptable probe pitch 100-150 μm .

Fig. 98. CPW monopole feed Design 4. Simple I feed and inverted J for transmission. 140 μm 50- Ω pad and $\lambda/4$ 87- Ω CPW line. Nominal frequency 90GHz. Acceptable probe pitch 100-150 μm .

IV.D.1.3.3) Performance

We report some of the simulation results of these designs with 1700 CNTs in the rod and assuming $\tau = 3\text{ps}$. Because of the many experimental uncertainties these are mainly a verification that the design is correct in a particular case and a qualitative indication of what to expect. They will allow a faster fit if positive experimental data is collected. The designs have been simulated in the experimentally relevant frequency band comprising their nominal frequency. The huge contribution to the resonance and radiation pattern can be seen on the following properties.

Return loss

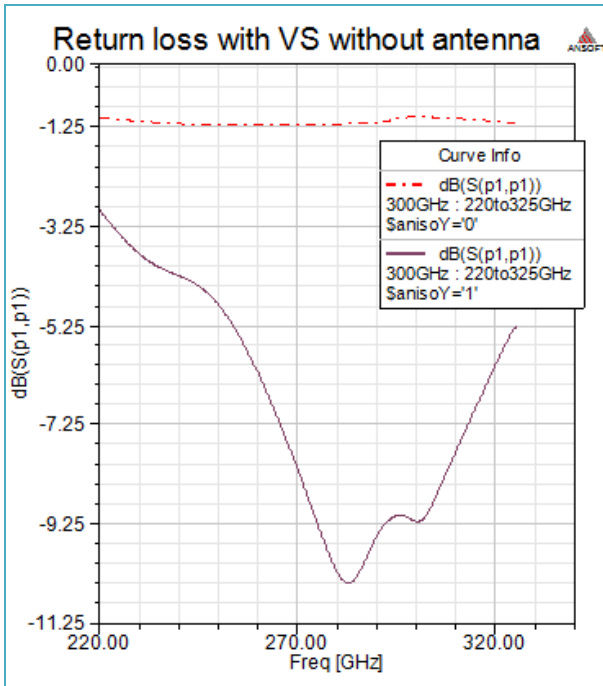


Fig. 99. Magnitude return loss of CPW monopole feed Design 1 with (purple solid) and without (red, dot-dashed) CNT rod.

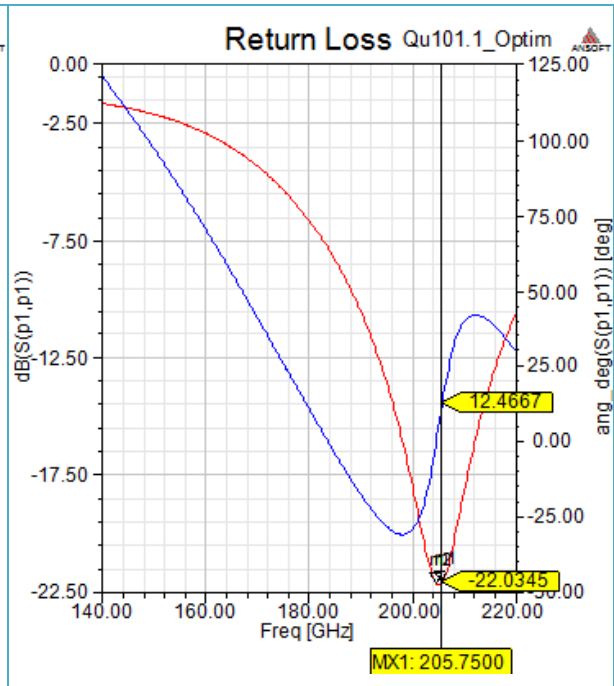


Fig. 100. Return loss of Design 2, magnitude in dB (red) and phase (blue).

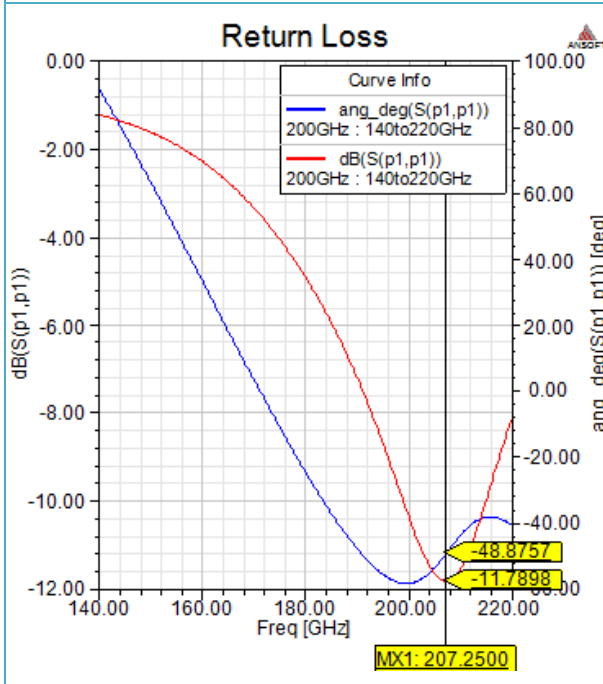


Fig. 101. Return loss of Design 3, magnitude in dB (red) and phase (blue).

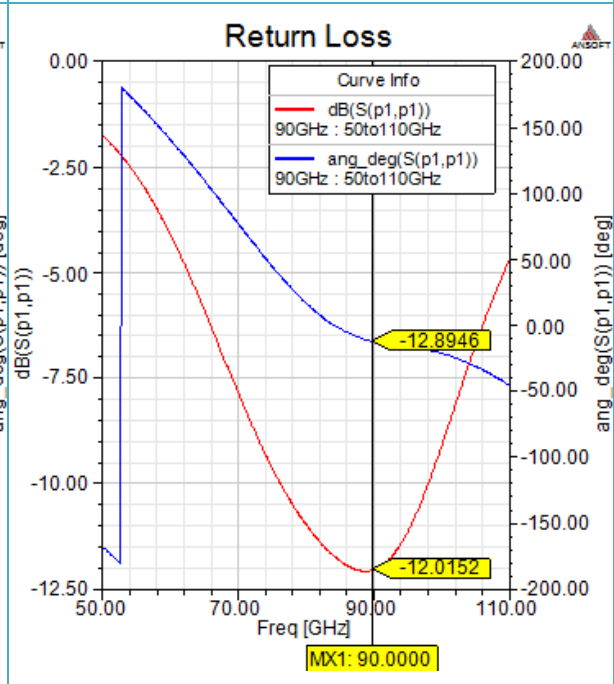


Fig. 102. Return loss of Design 4, magnitude in dB (red) and phase (blue).

Radiation

Radiation patterns are given in Fig. 105, Fig. 106, Fig. 107 and Fig. 108. They use the realized gain i.e. the gain integrating return loss. Design 1 shows that most radiation comes from the CNT rod. The patterns are coherent with an unbalanced monopole behavior.

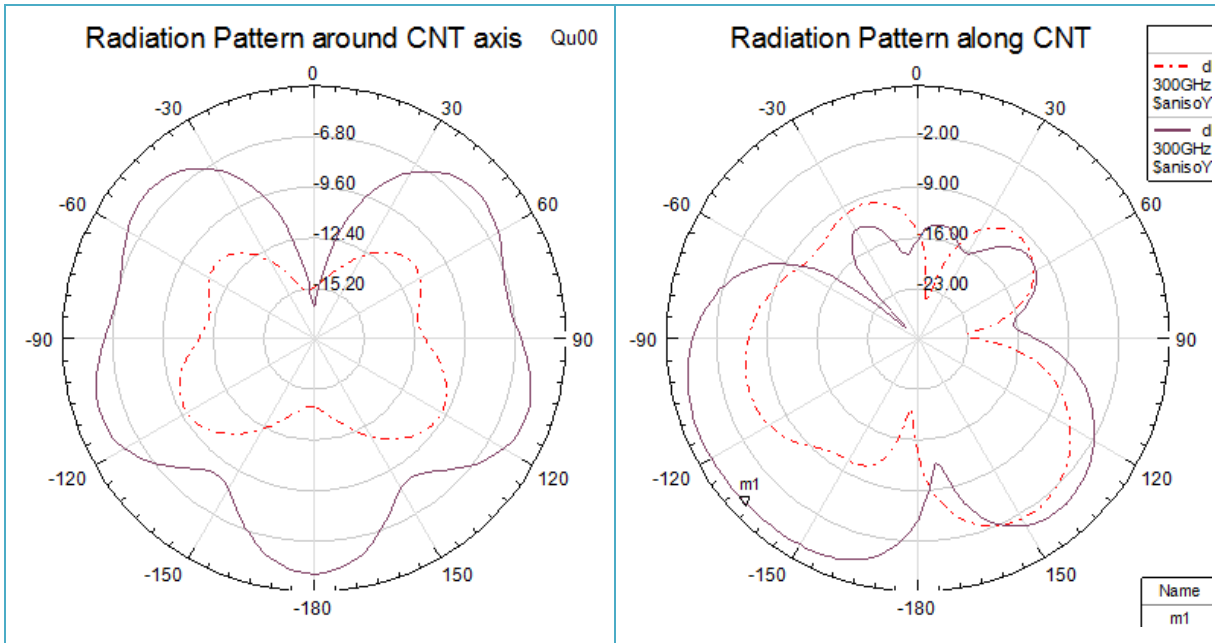


Fig. 103. Realized gain for Design 1. Cut at $\phi=0^\circ$: around the axis of the CNT. With (purple solid) and without (red, dot-dashed) CNT rod.

Fig. 104. Realized gain for Design 1. Cut at $\phi=90^\circ$: along the axis of the CNT. With (purple solid) and without (red, dot-dashed) CNT rod.

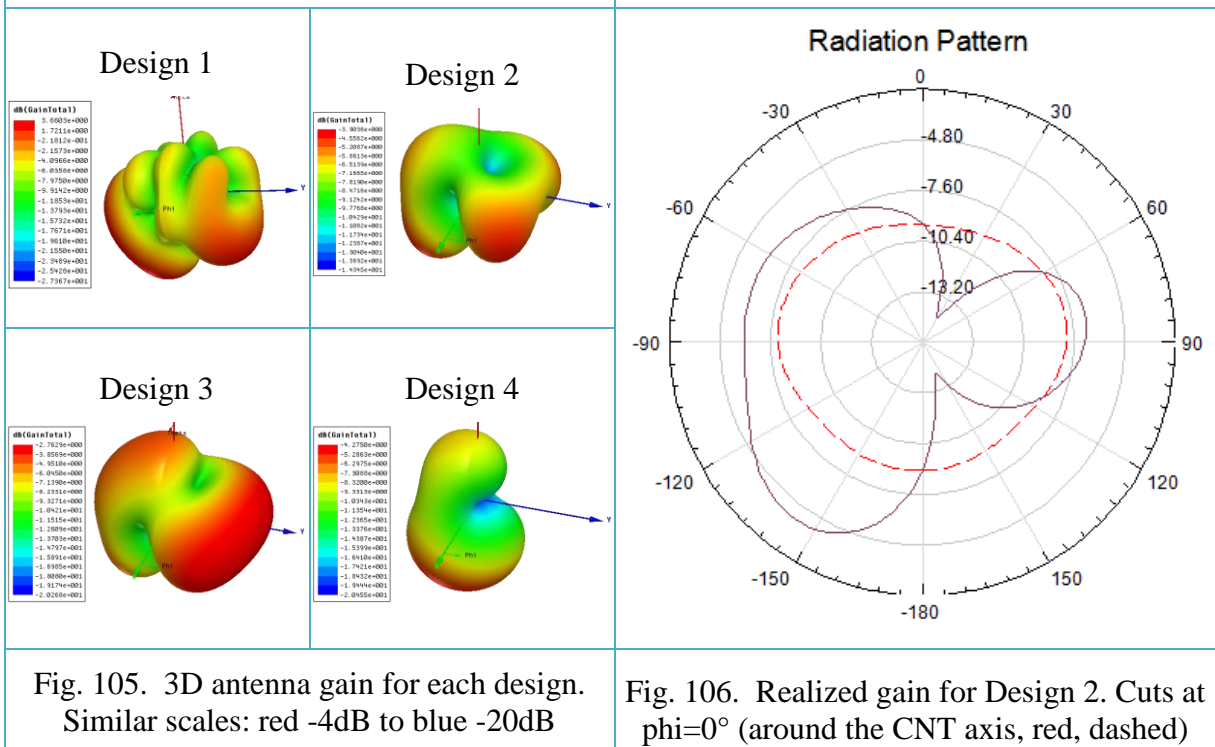
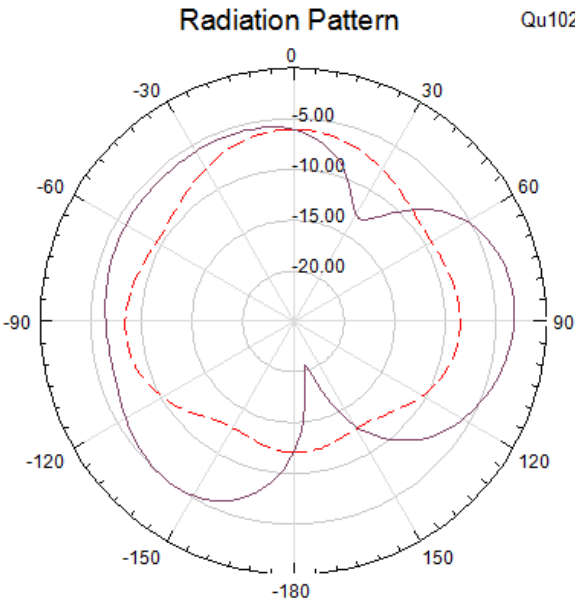
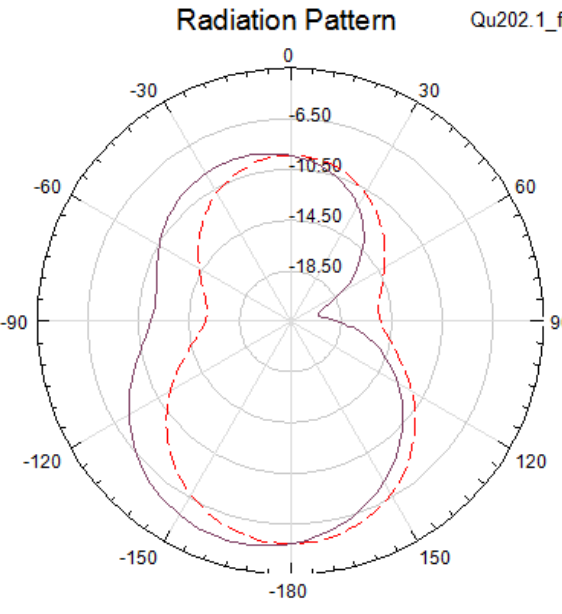


Fig. 105. 3D antenna gain for each design. Similar scales: red -4dB to blue -20dB

Fig. 106. Realized gain for Design 2. Cuts at $\phi=0^\circ$ (around the CNT axis, red, dashed)

	and 90° (along the CNT axis, purple solid).
	
<p>Fig. 107. CPW monopole feed Design 3. Simple I feed and inverted J for transmission. 140μm 50-Ω pad and $\lambda/4$ 60-Ω CPW line. Nominal frequency 200GHz. Acceptable probe pitch 100-150μm.</p>	<p>Fig. 108. CPW monopole feed Design 4. Simple I feed and inverted J for transmission. 140μm 50-Ω pad and $\lambda/4$ 87-Ω CPW line. Nominal frequency 90GHz. Acceptable probe pitch 100-150μm.</p>

IV.D.1.3.4) Transmission

The transmission structure for these toppled-CNT monopoles is simple although not as straightforward as it was for the standing vertical monopoles. Indeed, conventional probe stations use two facing probes – a configuration well adapted to measuring transmission lines. However, the techniques we described to topple CNTs only allow unidirectional CNT toppling and therefore rule out fabricating facing antennas on the same substrate.¹

Given the limited transmission capability of the antennas we need to measure them spaced by distances ranging from 100 μ m to 1mm which excludes fabrication on different substrates. The best way to ensure both antennas in the transmission link are fabricated in the same conditions is to put them side by side. This is what we do and we solve the issue of facing probes by extending the feed of one of the antennas from an I into an inverted J pattern (cf. second antenna on Fig. 95, Fig. 96, Fig. 97 and Fig. 98). The J pattern has the same

¹ Indeed, the only way to do so would be to know the CNT length with an uncertainty of a couple of micrometers in advance and be able to topple the CNTs with a maximum error in direction of 2-3° which is rather unrealistic. Then the tip of the monopoles of the facing antenna would be the base of the bundles and the base the tip. However, even so, ohmic contact with the line would still not be ensured.

dimensions as the I probe pads so that, in a simple one-probe return loss measurement, all the monopoles can be characterized in the exact same way – hence limiting uncertainties due to losses at the turns in the J.

The J pattern requires appropriate design because it is a rather lossy structure. Chamfers have been designed in the corners to reduce the loss and the influence of their dimensions was studied. Furthermore the length of each section of the pattern was set according to the wavelength at resonance. More specifically, the length of the additional line parallel to the original feed is a quarter wavelength (including the corner), and the length of the normal lower section is also set to be a quarter wavelength. This way the total additional length at the antenna operating frequency is a half-wavelength which makes it “transparent” because the fields and currents at both ends of this section are identical.

For design 2 the return loss for both I and inverted J antennas is almost the same although there is less return loss for the inverted J off-resonance (cf. Fig. 110). For the other designs the return loss is low on most of the band with a small dip at the antenna frequency (cf. Fig. 109). Without the antenna, the return loss is low far from the resonance and rather high (minus few dB) around the designed operating frequency (cf. Fig. 109) which shows that the inverted J structure actually fulfills its role properly at this frequency.

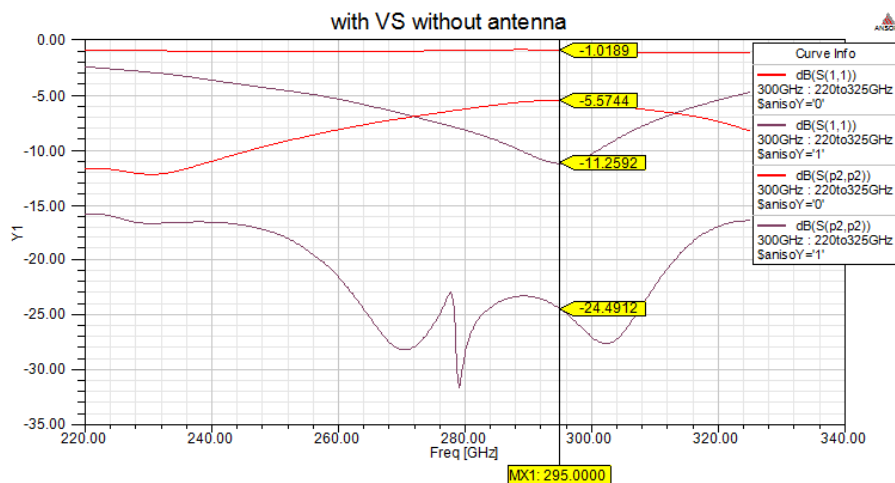


Fig. 109. Design 1. Return loss for the I and J feed with the CNT rod (-11.3dB and -24.5dB) and without a rod (-1.0dB & -5.6dB).

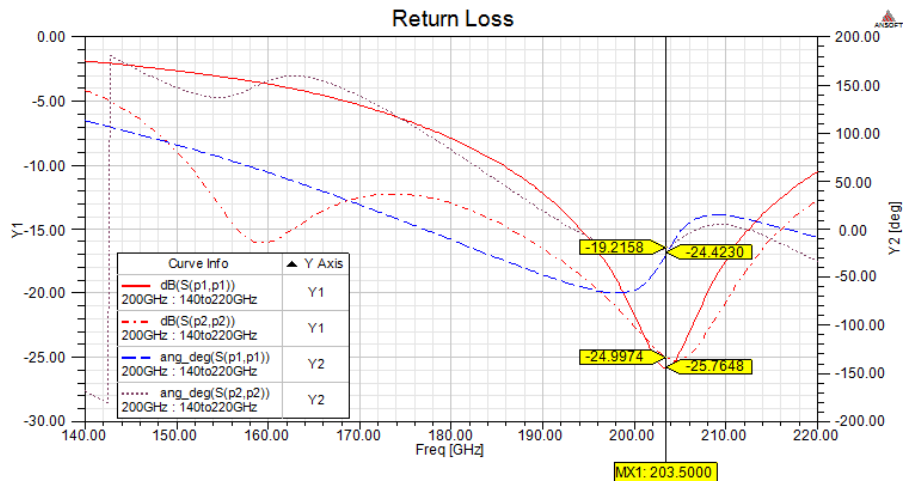


Fig. 110. Design 2. Return loss for the I (Sp1p1) and J (Sp2p2) feeds with the CNT rod, in magnitude (red) and phase (blue).

We also observed that the return loss for both antennas is mostly unaffected by the distance that separates them. On Fig. 111 we present the transmission results for the IJ transmission configuration with the spacing distances included in the photolithography mask and designs 1, 2 and 3 as shown on Fig. 95, Fig. 96 and Fig. 97 respectively. The levels are sufficiently high for measurement and well above transmission without rod up to 0.8mm or above.

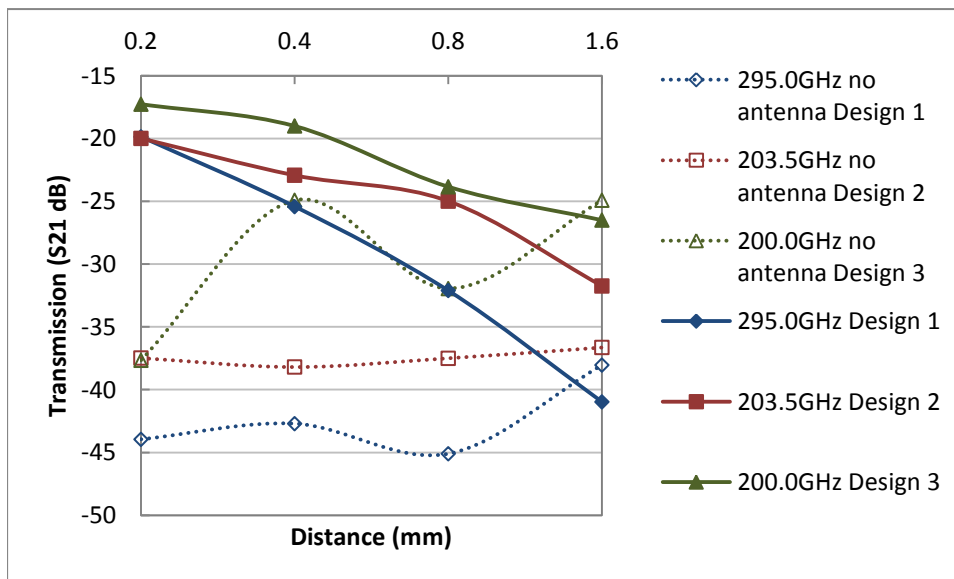


Fig. 111. Transmission at the indicated frequencies between IJ pairs of antennas of the same designs (1, 2 and 3). Transmission levels without the rod are included for comparison. The levels are sufficiently high for measurement.

IV.E) Mask design

Based on designs and variations described in sections IV.C.2) and IV.D.1), we designed a 4-inch photolithography mask that was fabricated in both bright-field and dark-field (cf. Fig. 113) to allow superimposing some patterns (cf. IV.C.2)) or simply using different resist or resist recipes in positive and negative photolithography to attain the

resolution limit of the mask aligner. The layout is presented on Fig. 112. All the contents but the top of zone U (described below) and the title fit in a 3-inch diameter circle.

Horizontal+Vertical CNT Monopole Antennas - CINTRA 2013

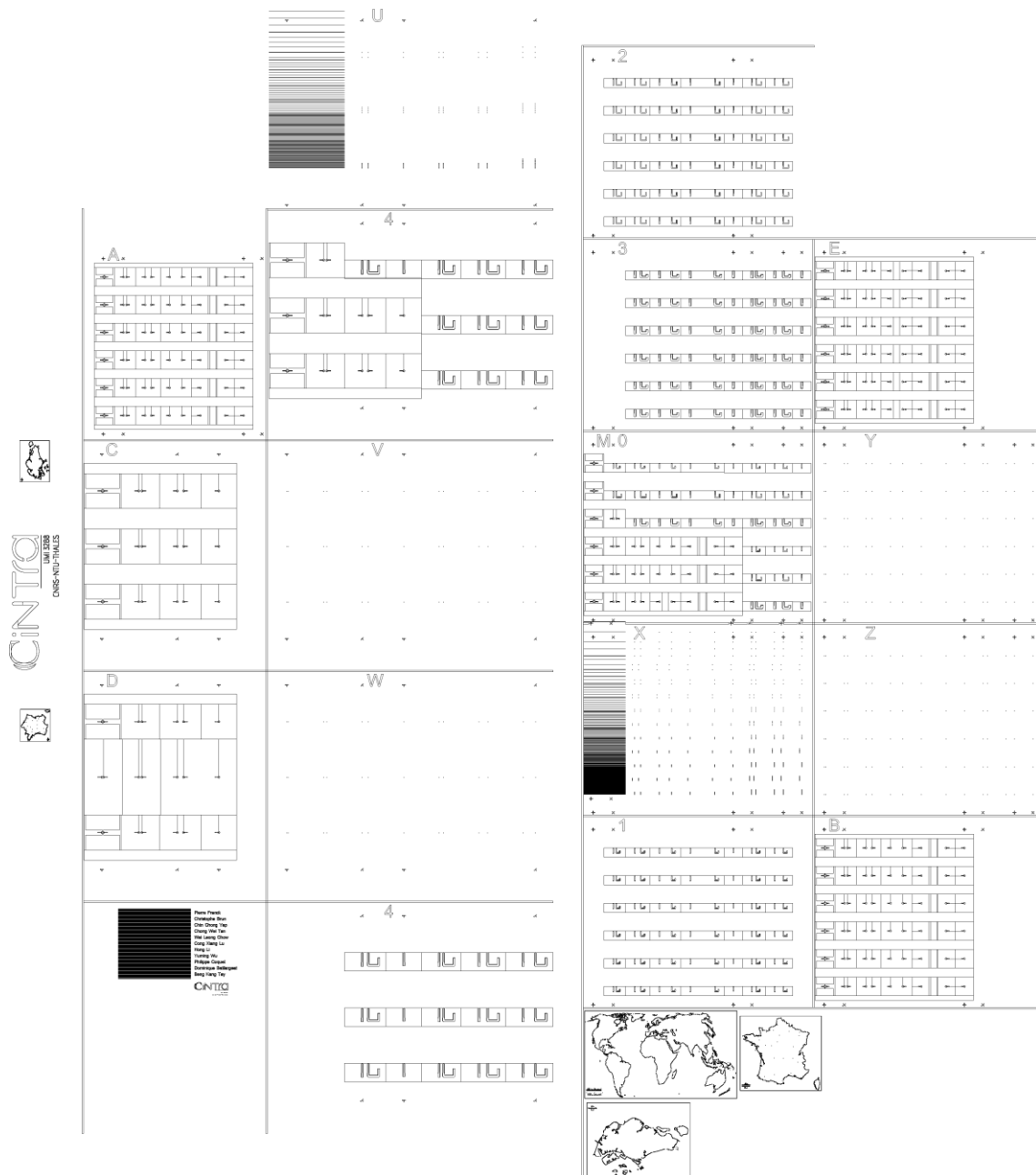


Fig. 112. Global mask layout. The edges representation is chosen to let the patterns appear despite the normally too small patterns.

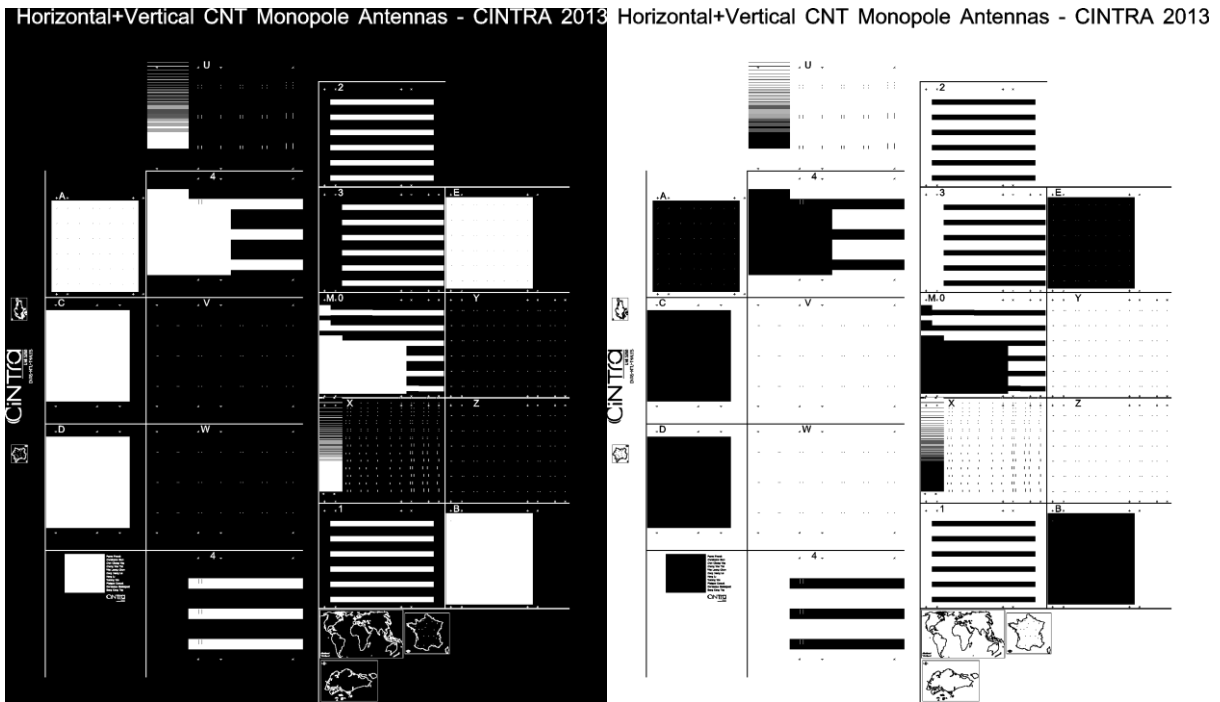


Fig. 113. Effective appearance of the darkfield (left) and brightfield (right) masks.

IV.E.1) Feed designs arrangement

IV.E.1.1) Arrangement of individual designs

The mask includes several regions of 1cmx1cm or 1.5cmx1.5cm the maximum size for optimal hard-contact exposure. These are optimized to reduce footprint on the mask and produce a maximum number of designs in one batch. Two feed zones (M and N) are dedicated to exploration by combining all the smaller designs (1, 2, 3, A, B, E) and all the larger designs (4, C, D) respectively. The other feed zones are dedicated to maximum repetition of a single feed design over the sample.

For the smaller designs, the sample thus contains 6 identic rows. Each row contains 4+2 IJ-pairs of antennas separated by one single antenna for the toppled-CNT designs 1 and 2 (50- μm minimum pitch) – for a total of 13 antennas/row and 78/sample. The distances are a geometric progression of common ratio 2: 200, 400, 800 and 1600 μm on the left and the intermediary $\sqrt{2}$ -common-ratio distances 283 and 566 μm on the right. For design 3 the smallest antenna distance (200 μm) is not compatible due to the larger pads (100- μm minimum pitch) and is replaced by one more single antenna (on the right) – for a total of 12 antennas/row and 72/sample. For the vertical-CNT monopole designs A, B and E, one shorter

distance is added (100 μm , on the left) and the two intermediary distances removed (on the right) – for a total of 11 antennas/row and 66/sample.

Similarly, for the larger designs, the sample contains 3 identic rows. Each row contains 1+3 IJ-pairs of antennas separated by one single antenna for the toppled-CNT design 4 (100- μm minimum pitch) – for a total of 9 antennas/row and 27/sample. The distances are a geometric series of reason $\sqrt{2}$: 400 μm on the left and 283, 566 and 800 μm on the right. For the vertical-CNT monopole designs C and D, two shorter distances are added on the left (100 and 200 μm) and the distances on the right are removed – for a total of 7 antennas/row and 21/sample.

IV.E.1.2) Mixed designs arrangement

Therefore most catalyst patterns are common to all designs. We have arranged them in order to be able to re-use the catalyst patterns and thus save the footprint on the mask while allowing the inclusion of more variations on the catalyst patterns. By appropriately positioning alignment marks one single slightly wider zone than the feed design zone serves as catalyst pattern for all smaller and all larger designs respectively.

This also allows the conception of the zone M (cf. Fig. 114) which is composed of one row of each design in the following order from top to bottom, completed for the incompatible spacing distances by the design in brackets on left or right: (A)1, (B)2, (E)3, A(1), B(2), E(3). Similarly N is made as: (C)4, C(4), D(4).

Coord.	A	B	C	D	E	F	G	H	I	Design
1										(A) 1
2										(B) 2
3										(E) 3
4										A (1)
5										B (2)
6										E (3)
Spacing (μm)	100	200	400	800	1600	0	283	566	0	

Fig. 114. Zone M: illustration of the common spacing distances of the designs (1,2,3, A,B,E).

These zones also allow the simultaneous study of the growth of rods in three conditions: fully on metal, fully on substrate and half-half. Indeed designs A and B and C and D are the same but with or without metal directly under the catalyst pattern. For the toppled-CNT designs the explanation is slightly different.

For these designs, when doing the photolithography for the catalyst dot after fabrication of the electrodes, aligning the small alignment crosses perfectly or tangentially allows to place the catalyst dot in three positions as illustrated on Fig. 116: 50-50 (superposed crosses), on metal (cross on mask 5μm below cross already patterned), on substrate (cross on mask 5μm above cross already patterned). On the M design, since it is an exploration design, these three configurations are simultaneously present, from left to right by simply superposing the crosses. The feed arrangement was indeed modified to allow this as illustrated on Fig. 115.

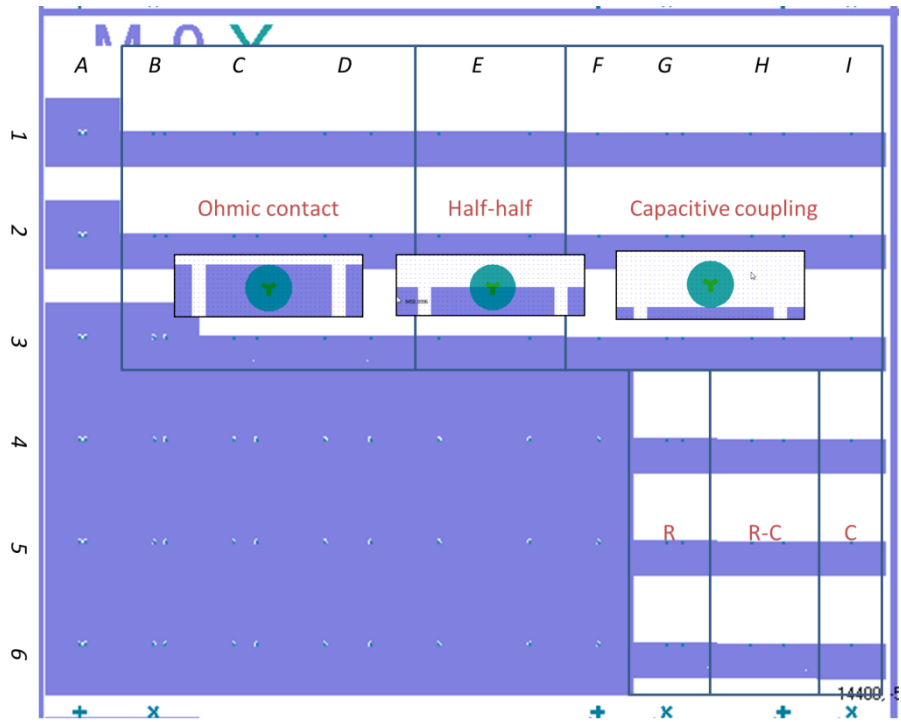
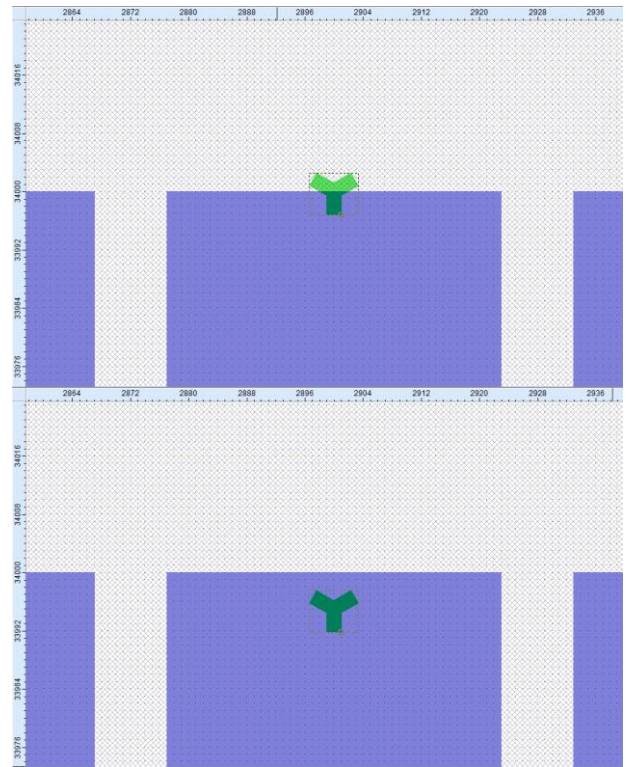
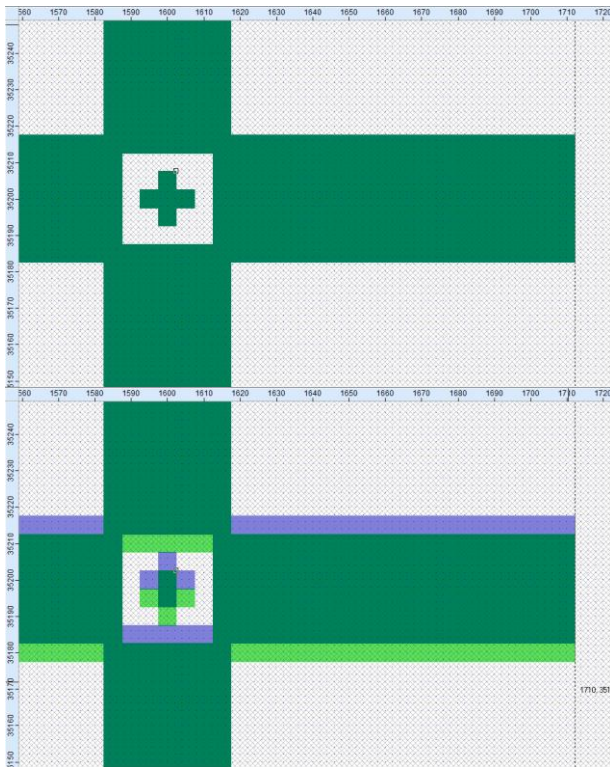


Fig. 115. Zone M: three simultaneous catalyst alignments are present by design.



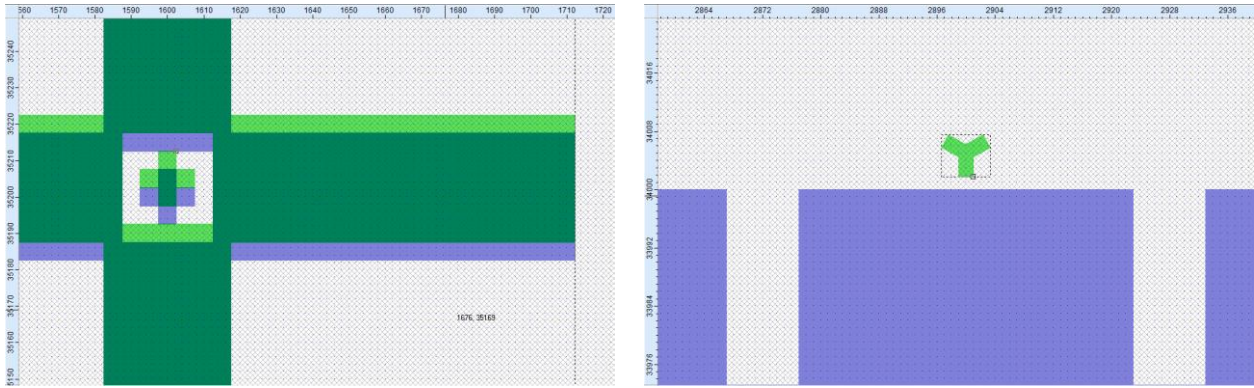


Fig. 116. Usage of the alignment marks to align the catalyst pattern a) half-half on the signal line (easier to topple), b) fully on the signal line (ohmic contact), c) off the edge by ten micrometer for the centre (capacitive excitation, better growth).

IV.E.2) Catalyst patterns arrangement

IV.E.2.1) Vertical CNT rod catalyst patterns

The catalyst zone for designs (1, 2, 3, A, B, E) is made of a repetition of the catalyst pattern along a row such that the 2nd pattern of a pair and the 1st pattern of the next are always equally spaced (1.2mm) and that the pairs along the row have the following distances (in this order, 0 meaning single antenna): 100, 200, 400, 800, 1600, 0, 283, 566, 0. Similarly, the catalyst zone for designs (4, C, D) is made of a repetition of the catalyst pattern along a row such that the 2nd pattern of a pair and the 1st pattern of the next are always equally spaced (2.3mm) and that the pairs along the row have these distances: 100, 200, 400, 800, 1600, 0, 283, 566, 0.

Three catalyst zones have been designed respectively for the smaller and larger designs: X,Y,Z and U,V,W. Each row has the columns that were defined in the previous paragraph.

The rows of zone Y each have a different pattern: the 6 variations chosen for the mask in section IV.D.1.2). The patterns are placed in the order then indicated which is the smallest patterns in the two central rows then a progression to bottom and top edges where the two larger patterns are positioned. Indeed the precision of the contact and thus of the exposition of the pattern in hard-contact photolithography is higher in the center when it is slightly raised by placing a small patch of soft plastic tape below it. This design is meant for exploration as it allows fabricating 11 to 13 antennas from each of the patterns and therefore obtaining small-statistical data on each with a single sample fabrication. V is a similar zone for the larger feed

designs with three patterns only: d_{10} , $s_{3.3}$, $s_{5.6}$ (top to bottom). Therefore W is the same as V with the three other designs: s_4 , $d_{2.2}$, s_{10} .

The rows of zone Z highlight the two estimated higher success rate designs: 3 rows of $s_{3.3}$ then 3 of s_{10} . Indeed the three-pointed star patterns are mechanically stronger for a given N_{CNT} than the disk patterns which makes $s_{3.3}$ the most likely successful design with low CNT number while reciprocally the three-pointed star patterns have less CNTs for a given radius which makes s_{10} quite large but much more interesting for our application than d_{10} .

An additional unnamed zone of 4.6mm by 4.7mm is included in the mask. It is a high-density collection of thousands of equally-spaced repetitions of the six catalyst patterns. The pattern spacing center-to-center in a square lattice is $40\mu\text{m}$ which is large enough to prevent attraction between the CNT arrays. There are 19 rows of each pattern design and 118 patterns/row so a total of 2242 repetitions of each pattern which allows in a single fabrication for each length and with four or five lengths (growth times) to determine the maximum standing aspect ratio for the three-pointed-star- and disk-cross section CNT bundles.

IV.E.2.2) Horizontal CNT strips patterns

Zones X and U are designed for the catalyst of horizontally grown CNTs such as lattice-aligned CNTs on quartz as reported in section IV.C.2) for the design of the corresponding CNT-strip-based monopole antenna. Repeated parallel $6\text{-}\mu\text{m}$ -wide catalyst lines are used to define CNT strips. The lines lengths i.e. CNT strip widths are 46 and $60\mu\text{m}$ for X and U respectively. For X, $46\mu\text{m}$ corresponds to the width of the signal line of the feed design in 2 and is narrower than that of 3 ($102\mu\text{m}$) and that of 1 ($54\mu\text{m}$). Therefore the CNT strips will be fully connected by any of these designs which are each matched to a different impedance. This gives an extra degree of freedom on top of varying the CNT length to hopefully characterize resonant antennas. For U, only design 4 is compatible and $60\mu\text{m}$ corresponds to the signal line width.

On the left half of X, the lengths used to form the strips are in the order of $160\mu\text{m}$ but decreasing with increasing spacing because the CNT density should also decrease and hence the reduction factor increase. On the right half the strips are designed about twice as long. The actual catalyst spacing is the distance between borders of catalyst lines. It will directly affect the CNT density since the number distribution of CNTs can be approximated as inversely

proportional to their length. We therefore vary the actual spacing as a geometric progression of common factor $\sqrt{2}$ for X and $2\sqrt{2}$ for U. The exact parameters are reported in Table 7. For U there are no inter-rows so only three rows.

Table 7. CNT strips length and density variations included in zone X and U.

Row	Interspace (μm, center- to-center)	Actual catalyst spacing (μm)	Number of interspaces (left)	Total length (left, μm)	Number of interspaces (right)	Total length (right, μm)
X$\frac{1}{2}$	646	640	1	646	1	646
X1	454	448	1	454	1	454
X1$\frac{1}{2}$	326	320	1	326	1	326
X2	230	224	1	230	1	230
X2$\frac{1}{2}$	166	160	1	166	1	166
X3	118	112	1	118	2	236
X3$\frac{1}{2}$	86	80	1	86	3	258
X4	62	56	2	124	4	248
X4$\frac{1}{2}$	46	40	3	138	6	276
X5	34	28	4	136	8	272
X5$\frac{1}{2}$	26	20	6	156	11	286
X6	20	14	8	160	16	320
U1	326	320	1	326	2	652
U2	118	112	3	354	5	590
U3	46	40	7	322	13	598

Because this type of growth is incompatible with vertical monopole designs, the corresponding columns have been replaced by continuous catalyst lines, 2.7mm- and 4.9mm-long for X and U respectively. These lines allow an excellent statistical study of the horizontal CNT growth. They are long enough to have a large sample of CNT density for each spacing, especially so because each spacing is repeated over 0.9mm for X and 1.8mm for U. Furthermore, with a 500 aspect ratio in X, the lines should be short enough to be fabricated even as lines rather than slots for one-step fabrication of enriched-resist catalyst lines – which is anyway possible for the much shorter catalyst lines of the strips.

IV.F) Fabrication and characterization

IV.F.1) Design specifications, yield and RF characterization

An initial batch of samples was produced in CINTRA/NTU EEE by Chin Chong (Ray) Yap, Wai Leong Chow, Dunlin Tan and Cong Xiang Lu with coordination by Chong Wei Tan. All are part of Beng Kang Tay's group. Catalyst was from two sources: NTU MAE and Aixtron (Cambridge, UK). CNT growth was performed in NTU EEE and Aixtron with Aixtron BlackMagic PE/T-CVD reactors, following SW and few-wall CNTs recipes. Eleven samples were fabricated, four of which were selected for their successful growth of 100- to 300- μm -long CNT bundles, yielding 69 deemed-measurable pairs of antennas of which:

- 59 with 50- μm minimum pitch
- 10 with 100- μm minimum pitch
- 43 horizontal and 26 vertical
- 37 with 300 μm -long few-wall CNTs (MY2) with resistive (R) and capacitive (C) contacts:
 - Horizontal: 8 R, 6 R-C, 9 C
 - Vertical: 9 R, 5 C
- 32 with 80-100 μm -long CNTs of which 18 SWCNTs and 14 few-wall CNTs

This is an encouraging initial result with longer-than-expected 300- μm -long CNT bundles grown and relatively high yield for horizontal and vertical monopoles. If resonances can be measured the high-number of samples for each antenna design will provide repeatability.

The fabricated design was zone M for the feed designs and zone Y for the catalyst patterns, effectively covering all the variations present on the mask. Pieces of $\sim 475\text{-}\mu\text{m}$ -thick high-resistivity silicon wafers were used as substrates to start validating the fabrication process while sourcing quartz wafers was underway. Therefore, for designs 1, 2, 3, the horizontal monopoles access pads that were designed to be 50-ohm on quartz are 35-ohm on silicon. Measurements can still be made and analyzed if the probes are systematically placed at the same longitudinal position on the pads and the position is reported. Measurement on a VNA up to 170GHz was performed in XLIM by Damien Passerieux. No specific issue were recorded except careful lateral positioning of the probes is necessary for the vertical

monopoles access pads since they are 25- μm -wide, same as the probe width, while the gaps are 5- μm -wide. However, as could be expected, the measurements did not return any positive result. Measurements up to 220GHz for all samples and 325GHz (maybe 500GHz) for the 59 accepting 50- μm -pitch probes are to be made by the end of 2013 at IEMN (Institut d'Electronique de Microelectronique et de Nanotechnologie, UMR CNRS 8520, Lille, France).

IV.F.2) Fabrication of the vertical and toppled monopoles

A high resistivity silicon wafer of $> 10 \text{ k}\Omega$ coated with 655 nm thermal oxide was used as substrate. A first photolithography process was used to define the CPW access feeds fabricated with 500nm Pt on top of 100nm Ti adhesion layer by electron beam deposition. Pt was used instead of Au here despite its lower conductivity because it presents better surface quality after deposition and when exposed to the high temperatures of the growth process which allows a better CNT growth. A second photolithography step then allowed the definition of the CNT rod catalyst patterns. A 10nm Al_2O_3 barrier layer was deposited followed by 1nm Fe catalyst. The growth of the vertically aligned CNTs was carried out using the AIXTRON Black Magic II PECVD system at growth temperature of 625 °C with 150sccm of C_2H_2 as carbon feedstock and under a low vacuum pressure of 10 mbar. A vertical CNT monopole successfully fabricated during the first batch is illustrated on Fig. 117.

The intended toppling processes and quartz substrate for the toppled monopole, as described in section IV.D.1.3) have yet to be undertaken. However, liquid toppling of CNT rods has been experimented along with the toppled CNT lines fabricated by Wai Leong Chow and they mostly follow the liquid flow.

Furthermore, during the vertical and toppled monopoles fabrication process, most small cross-section bundles spontaneously topple, as expected, and thanks to the specifically designed arrangement they often directly topple in the right direction. Thanks to this many antennas were successfully fabricated in the first batch without further processing with many much less probable antenna pairs, as illustrated on Fig. 118 and Fig. 119.

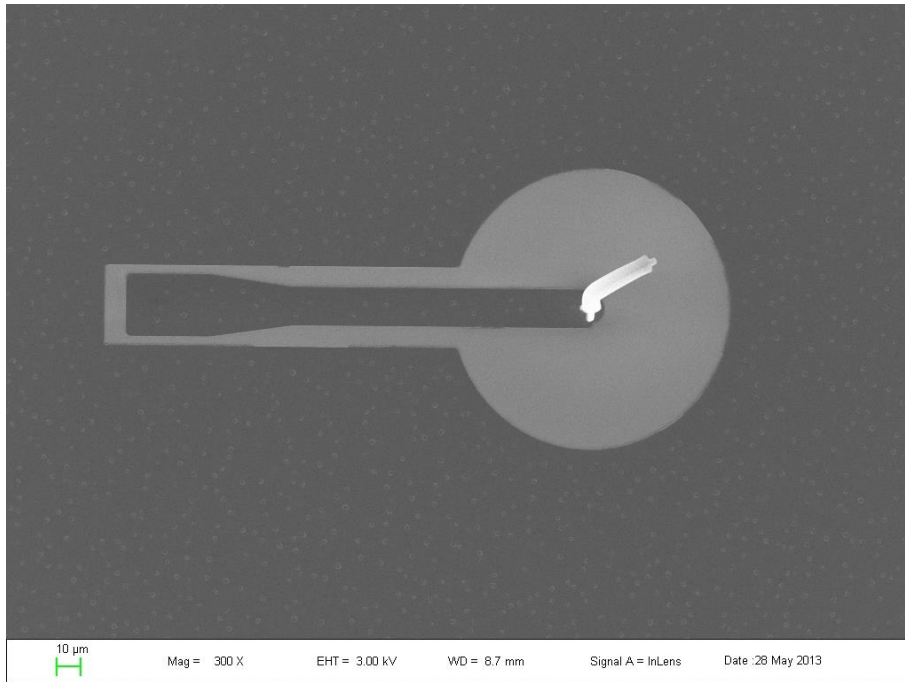


Fig. 117. Vertical CNT monopole successfully fabricated with three-pointed star pattern.

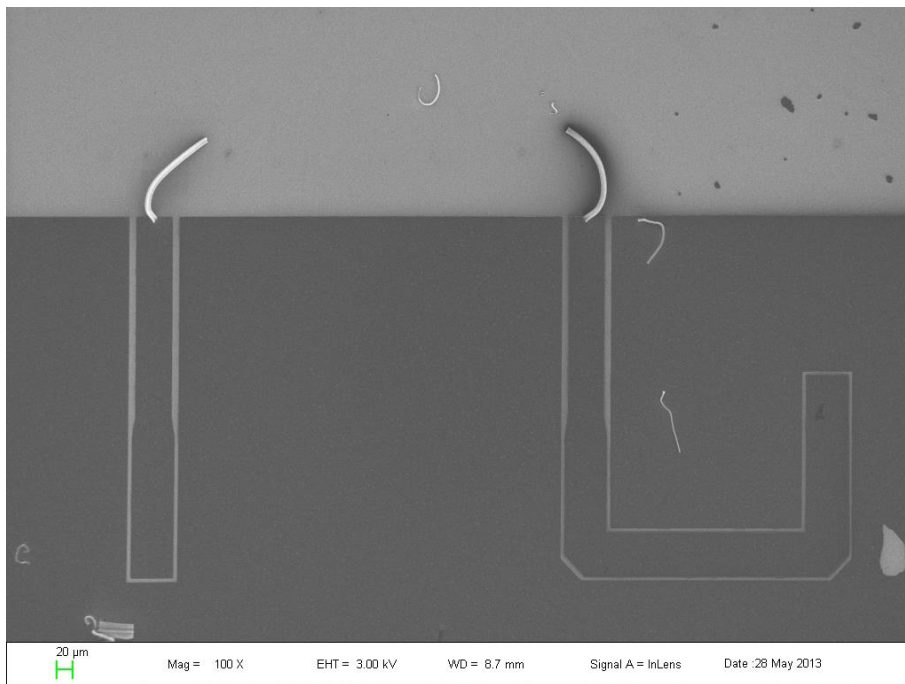


Fig. 118. Pair of self-toppled CNT monopoles successfully fabricated with three-pointed star pattern preferentially toppling in the correct direction (1/3 but even more if the pattern is tangent or half-way over the edge of the metallization).

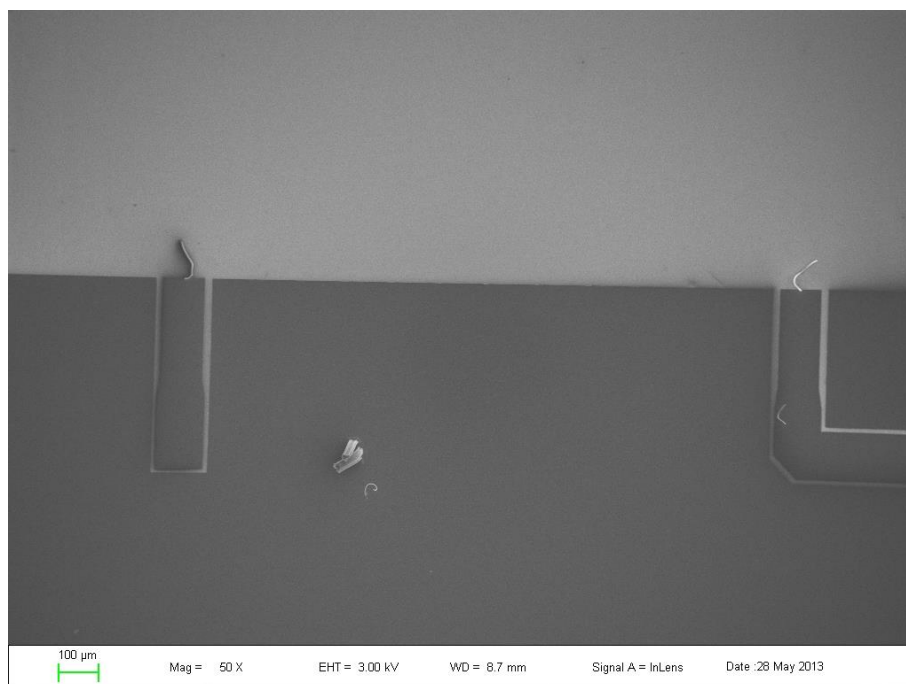


Fig. 119. Another pair of self-topped CNT monopole antennas.

IV.F.3) Visual inspection and material characterization

Raman spectroscopy was performed by Wai Leong Chow to verify that the nature of the CNTs grown from SWCNT and few-wall-CNT recipes was consistent with the recipe used.

With the help of Chin Chong (Ray) Yap, all designs were carefully studied with scanning electron microscopy (SEM) using the LEO FE-SEM in NTU EEE N2FC Cleanroom 1 and an additional optical microscopy inspection was carried out. Indeed, the height of the fabricated CNT bundles is such that the base and the tip are usually not in optical focus at the same time. This therefore allows determining if a bent bundle is touching an electrode, which – despite the higher resolution – is difficult to do rigorously with the SEM since it has a much longer depth of focus. This illustrated on Fig. 120.

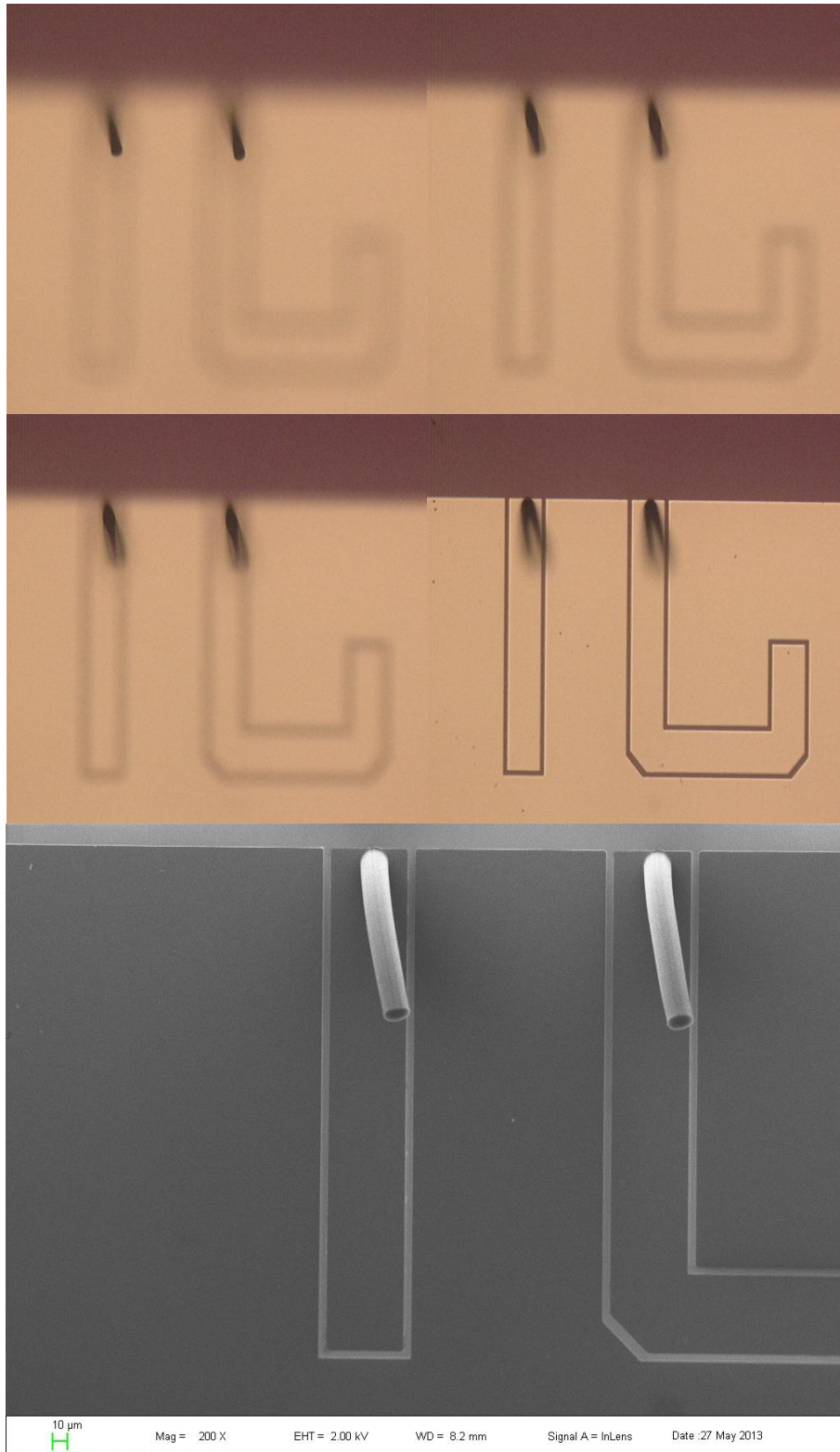


Fig. 120. Optical microscope images of a pair of monopole antennas at different focus and FE-SEM image of the same pair. This shows how both techniques can complement each other to allow a good global view and shallow-depth slice-like observation. Here the rods are seen standing which is not the original nature of the design but still provides a working configuration. They could later be toppled to resonate at lower frequencies with the same length as the effective permittivity would be raised by the substrate influence.

IV.F.4) Second batch

A second much more ambitious batch is underway with the experiment plan exposed in Appendix 9. The fabrication is undertaken at CINTRA/NTU EEE and Aixtron by Chin Chong (Ray) Yap, Wai Leong Chow, Dunlin Tan and Cong Xiang Lu with coordination by Chong Wei Tan. All are part of Beng Kang Tay's group. If fabricated in time this batch could be measured in IEMN together with the initial batch.

IV.G) Conclusion on CNT-based antenna design

To conclude we have developed a full set of tools for the modeling, design, understanding and realization of CNT-based electrically-short antennas. These tools include an original effective bulk model for CNT arrays, formulas for characteristic impedance and phase velocity in CNT bundles from transmission-line analysis in arbitrary loss conditions and design charts and spreadsheets from EM and circuit analysis. They are not limited to this case and their use may be extended to other fields of CNT-based electronics and electromagnetics.

Extensive analysis has been carried out to draw design rules on aspects such as loss regimes, size reduction scaling with the number of CNTs and interrelated impedance and frequency ranges. Based on these and the developed tools, the design and fabrication of three different types of antennas was undertaken and successfully completed and RF characterization initiated. A photolithography mask was realized which includes several variations to realize an extensive experimental study of all the parameters that can influence the RF response, transmission or mechanical properties of these antennas. Based on the expected characteristics, some applications in wireless on-chip communication and microelectronicsto nanodevices link have been suggested and studied.

The RF characterization of the fabricated CNT monopole antennas is ongoing. Initial measurements up to 170GHz in XLIM by Damien Passerieux reported no resonance – as expected. Measurement is planned at IEMN for higher frequencies, up to 325GHz soon and normally 500GHz later on. Once the single radiators will be fully validated, CNT array antennas could be the next logical step. Another aspect of this PhD project was to assess the feasibility of optically controlled antenna arrays. In the next chapter, we expose the fabrication and photocurrent characterization of initial CNT-based structures.

Chapter V) Initial characterization towards optical control

Another aspect of the project was the optical switch or modulation of the properties of a single antenna radiator to allow optical actuation of phased-array antennas. In this case, the antenna can either be an electrically-short CNT antenna like the monopoles described earlier or a conventional one. In any case, semi-conducting CNTs will be needed if we are aiming for photocurrent. However, there is also a significant competing photothermoelectric current that arises in metallic CNTs.

For this part we changed tactics. As we have seen, the properties of carbon nanotubes and their composites vary a lot depending on their nature and chirality often is not controlled which makes it complicated to analytically evaluate the photocurrent response expected; quite a few experimental studies have been led and report an effect of light on a type of CNT but this does not allow us to predict the photoresponse quantitatively. Instead, we prepared samples with many of the techniques introduced in Chapter III) to assess the photoresponse based on our fabrication capabilities. Part of this work has been presented in ICMAT [201].

V.A) Photocurrent samples: sorting metallic and semi-conducting CNTs

As explained in section I.A), single-wall carbon nanotubes can be seen as rolled-up graphene and depending on the roll-up axis (chirality) they can be either metallic or semi-conducting. Assuming all chiral number pairs have the same probability of occurring at growth, as-grown SWCNTs are $1/3$ metallic and $2/3$ semiconducting. MWCNTs are predominantly metallic because their shells are in parallel and larger would-be semiconducting shells actually have a bandgap so small that they become metallic at room temperature (cf. modeling in sections II.A.4.2) and II.B.3.3)).

For a photoelectronic switch, metallic CNTs are undesirable because they will allow current through without any light hitting them and will thus dramatically decrease the ON-OFF ratio of the switch. The switch can be seen as a series resistance with a photodiode (the semiconducting SWCNTs) in parallel with a shunt resistance (the metallic CNTs). Therefore the primary aim is to produce samples where semiconducting SWCNTs are the predominant if not only species. There are, to date, a few methods to achieve this, none of which was

originally in use in CINTRA. We review the options in the following subsections and present the samples fabricated after careful consideration.

An additional parameter that should be accounted for is the diameter of the semiconducting SWCNTs. Indeed their bandgap – and thus the illumination wavelength that can be used to excite them – is inversely proportional to their diameter. Therefore a narrow diameter distribution is preferable to excite all the CNTs with a monochromatic light source such as a continuous laser. Lasers offer more versatility for optical actuation, using MEMS actuated mirrors for instance, higher achievable local intensities and do not require bulky optics compared to other common light sources and would thus be a preferred option. Pulsed lasers present a frequency/wavelength spectrum width inversely proportional to the temporal width of their pulses which could be well suited for relatively narrow CNT diameter distributions.

For completeness we shall note that, as will be treated in more details in section V.C), metallic CNTs may still be used for photomodulation of the electronic response of devices. Indeed they can be used as simple metals for their difference in Seebeck (thermoelectric) coefficients with other materials to create a photothermoelectric current [202]–[205]. This phenomenon is far less wavelength-dependent than the photocurrent and its effect may be measured predominantly if the wavelength of the light source is not matched to the bandgap of the semiconducting CNTs.

V.A.1) Selective growth

Chirality control during growth would be the ideal solution. However it is arduous to achieve and is still a current topic of research. Changing the carbon precursor is often seen to lead to some selectivity as in [206] where bimetallic Co-Mo catalyst is used with four different gas precursors or in [146] where growth of well aligned CNTs on quartz is reported to present a semiconducting CNT ratio varying in accordance to the ratio of methanol to ethanol used as liquid carbon feedstock through a bubbler and up to 95% semiconducting CNTs are claimed. More recently, using Fe catalyst and isopropyl alcohol (IPA) as carbon feedstock in the same process was reported to yield 97.6% sc for only 52.4% with ethanol in the same conditions [207].

In our case, we would retain the two latter solutions as they are a simple adjustment to the fabrication technique highlighted for horizontal monopoles and should return high-quality CNTs thanks to lattice-aligned growth on quartz. However, before the recipe could be tuned reproducible catalyst was needed for which we only recently developed the techniques.

Introducing water in the growth process has also been demonstrated to preferentially etch metallic CNTs [208]. A last interesting, yet difficult to apply to devices, method is to use a graphite substrate to deviate CNTs during growth according to their chirality [209].

V.A.2) Sort in solution

Sorting semiconducting and metallic CNTs is usually done in solution. In one of the most advanced processes, M.C. Hersam's group has developed structure-discriminating surfactants to engineer differences in the buoyant densities of CNTs of different diameters [210]. Using density-gradient ultracentrifugation, they can isolate narrow distributions of SWCNTs in which >97% are within a 0.02-nm-diameter range. Earlier methods had been devised as can be seen from the prior art related in the paper. Coating with surfactants may be detrimental for electronic properties and some solution-based techniques have been proposed to avoid using them [211].

However, solution processing involves breaking down the CNTs at lengths of around 1 μ m and below. Indeed the CNTs are dispersed using sonication – mechanical agitation at ultrasonic frequencies, 20kHz and above. This breaks long CNTs into shorter segments. As explained in sections III.A.1.2.1) and III.A.2.4), long CNTs cannot be maintained homogeneous in a solution as they would get entangled. Often to obtain a stable suspension extra chemical cutting of CNTs by acid attack is undertaken.

A recently reported technique could allow combining the refined sorting methods developed for CNTs in solution with the advantages of long aligned CNTs produced by CVD. In [212], J. Liu and co-workers (the same who reported on IPA as feedstock for CVD growth) demonstrate the growth of CNTs which retain the chirality of short CNT segments used as seeds. They use vapor-phase epitaxy and solution-purified CNTs as seeds and no metal catalyst is needed. Work with similar goals has been ongoing for a few years as referred to in [213].

We have not developed solutions to sort CNTs in solution but solution-sorted CNTs are available commercially from NanoIntegris (co-founded by M.C. Hersam) or Sigma-Aldrich (CoMoCAT, [214]) for instance.

V.A.3) Imperfection-immune design

A very interesting option is to use designs that actually accommodate metallic CNTs by statistically filtering them out of the final device response. Robust designs were originally proposed in [215], [216] then successfully implemented for very-large-scale-integration-(VLSI-) compatible transistor fabrication [217]–[219] up to the recent first carbon nanotube computer [3] as highlighted in editorial of *Nature* [220].

V.A.3.1) Concept

The main idea is to connect in series short fractions of parallel CNTs in a sufficient number to ensure that there is at least one semiconducting CNT portion. Then, assuming the CNTs have constant chirality over their length, the same chain is reproduced multiple times along the length of the CNTs and connected in parallel. This way high ON-OFF ratios and high through currents can be obtained at the same time. Although the technique was used for FETs there is no fundamental difference that would prevent its use for photocurrent. The main drawback of the technique would be the relatively large footprint of the transistors thus fabricated compared to prevailing standards in silicon technology and the subsequent low cut-off frequency. In our case the footprint is not an issue as the radiator part will be orders of magnitude larger.

V.A.3.2) CPW gap samples

The difficulty resides in obtaining a reproducible growth of aligned horizontal CNTs to adapt the spacing of the connecting pads. Although we are now close to this, as reported in section III.B), at the time these experiments were made, we only mastered CVD growth of aligned horizontal CNTs using rather variable hand-held scratch catalyst.

Therefore, samples were fabricated from these. CPW gold electrodes of central conductor width of 80 μm , signal-ground gap width of 60 μm , ground width of 200 μm and total length of 400 μm were fabricated with a gap in the middle of the signal line of 5, 10, 20 and 50 μm . Density being non-uniform over the sample, the number of CNTs connected varies

from 1 to few tens with random distribution of chirality. This can be seen on Fig. 121 and Fig. 122 where the two samples of this type that underwent photocurrent measurement are presented. Many additional devices were fabricated a selection of which can be found in Appendix 7.

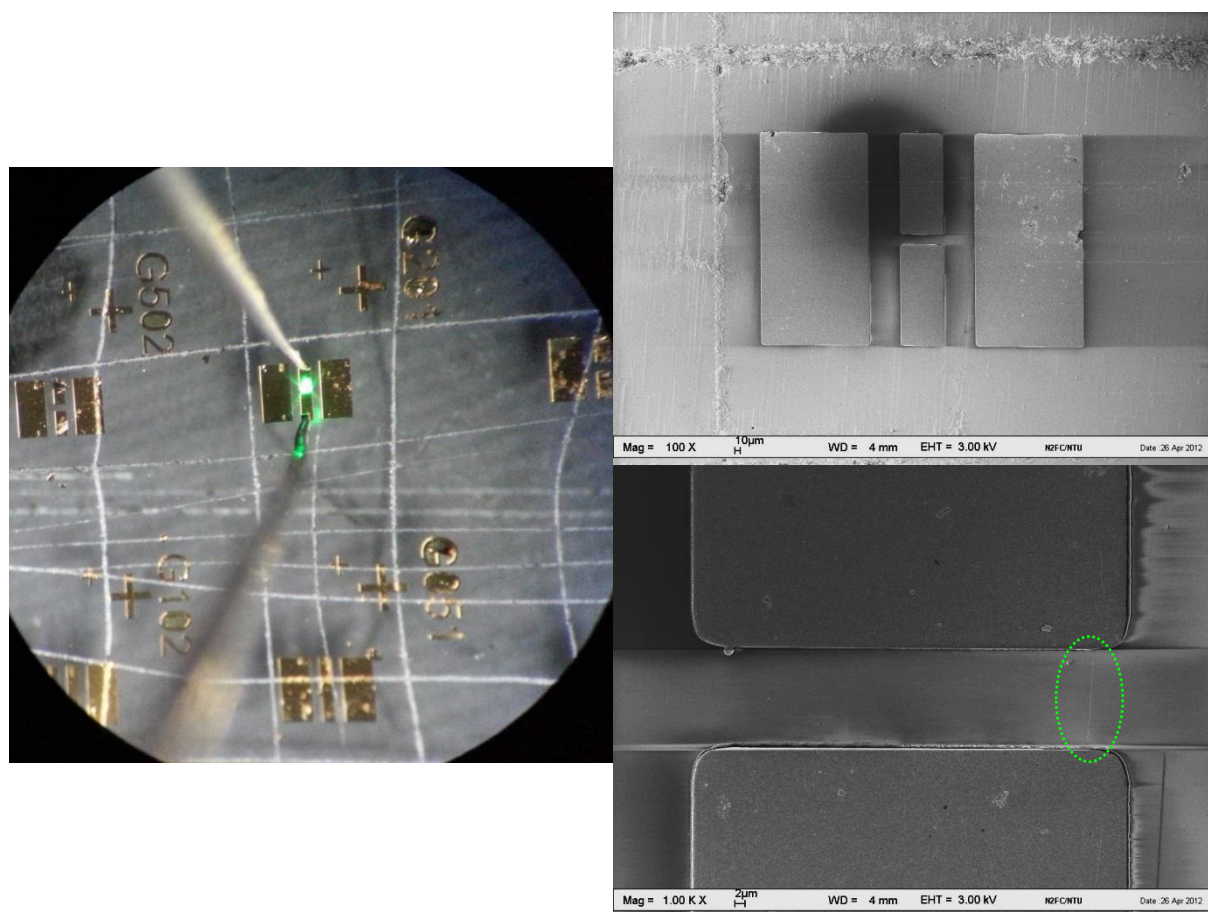


Fig. 121. Gold CPW gap electrodes fabricated on lattice-aligned CNTs grown by ethanol CVD from scratch catalyst on quartz (E0.03). Left: 4 sizes of gap are fabricated (5, 10, 20, 50 μm) and repeated thrice each; G201 (1st 20- μm gap) is probed under illumination. Right: SEM images of G201 reveal the CNTs around G201; because the gap is placed quite far from the catalyst line, a single CNT bridges the signal electrodes. Because it is a semiconducting SWCNT it appears faintly contrasted with the dielectric substrate.

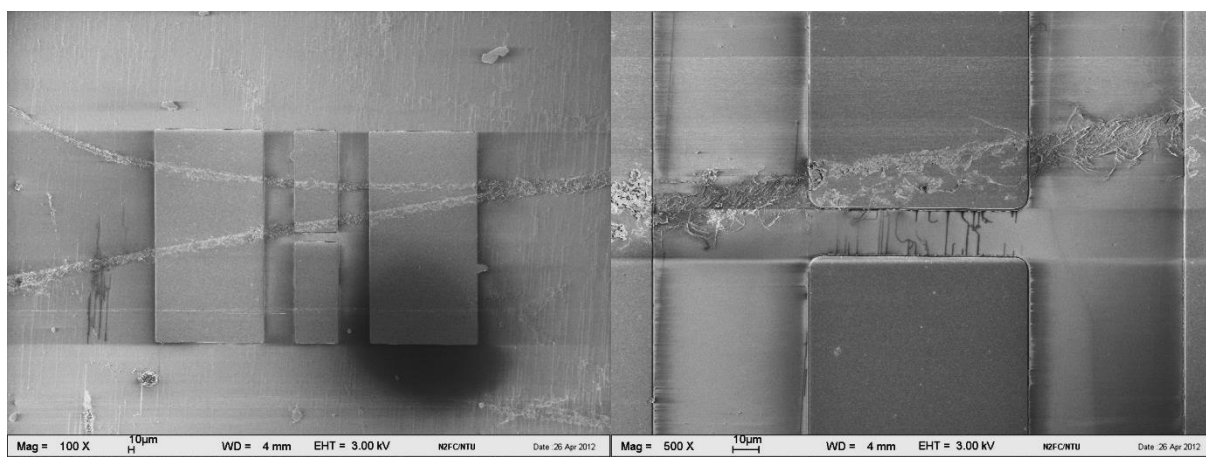


Fig. 122. G202 is a device on the same sample (E0.03) as G201 on Fig. 121. The gap is aligned next to the scratch and the number of CNTs is thus much higher.

With our recent progress in fabrication, metallic-CNT-tolerant design may be used as the base of future largely repeatable samples with characteristics optimized from the measurements on our first exploratory batch. We should therefore be able to scale the single radiator unit to a full array without dead cell like the CNT computer is a demonstration of scaling from single transistors to numerous ones with a defect rate low enough to prevent including a single defective transistor.

V.A.3.3) Sprayed-CNT samples with interdigitated electrodes

A similar concept can be applied to CNT films, and does not need a very particular topology, as pointed out by P. Bondavalli et al. [144], [221]. Unsorted SWCNTs contain about twice as many semiconducting CNTs as metallic CNTs. When lengths of film used between electrodes are several times longer than the CNTs in the film, then the electric paths run through several short CNTs and the longer the path relatively to the CNTs length the lower the probability that there will not be a single semiconducting CNT in it. The transmission is mostly through percolation and by fine-tuning the CNT density, the percolation threshold can be exceeded for semiconducting CNTs only since their density is twice superior than that of metallic CNTs. This probed us into fabricating samples from sprayed CNT films.

As reported in section III.C.2), CNTs were sprayed over square glass microscope cover slips and kapton sheets. Electrodes were fabricated by photolithography based on an interdigitated electrode design provided by Xin Yu Chin, a PhD student at NTU SPMS in

Cesare Soci's group, who normally uses it for characterization of conductive polymers. The interdigitated design allows increasing greatly the width of material used for transmission across a given gap and thus the overall conductivity across the gap while keeping a limited footprint. Some of the realized samples can be seen on Fig. 123, Fig. 124 and Fig. 125. Fully printed samples were also characterized but an inadequate curing resulted in the silver electrodes to fuse under electrical current or high laser illumination.

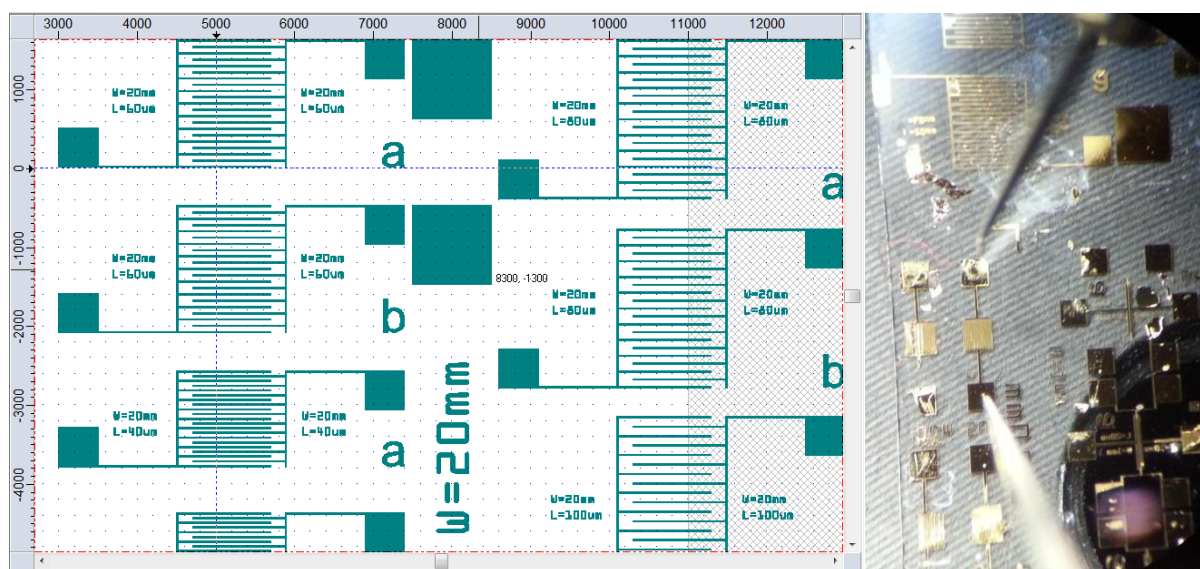


Fig. 123. A few of the interdigitated electrode design variations that were fabricated. Left: mask layout. Right: actual sample.

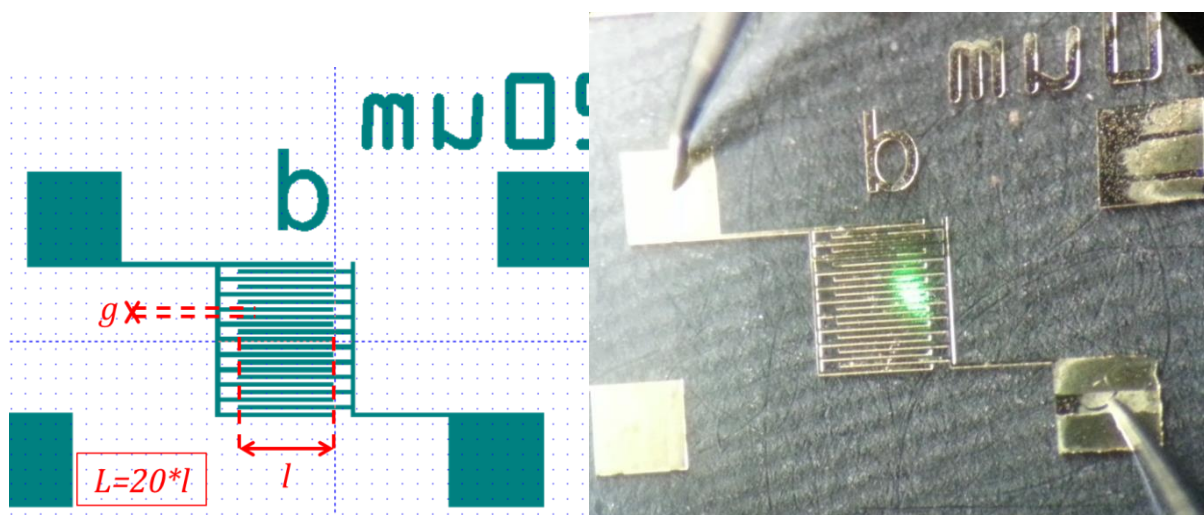


Fig. 124. 20- μm -gap (g) interdigitated electrode design, d (inverted). Left: mask layout; the effective connecting width is $L=20 \cdot l=20\text{mm}$. Right: actual sample with laser spot; note the CNTs are completely invisible.

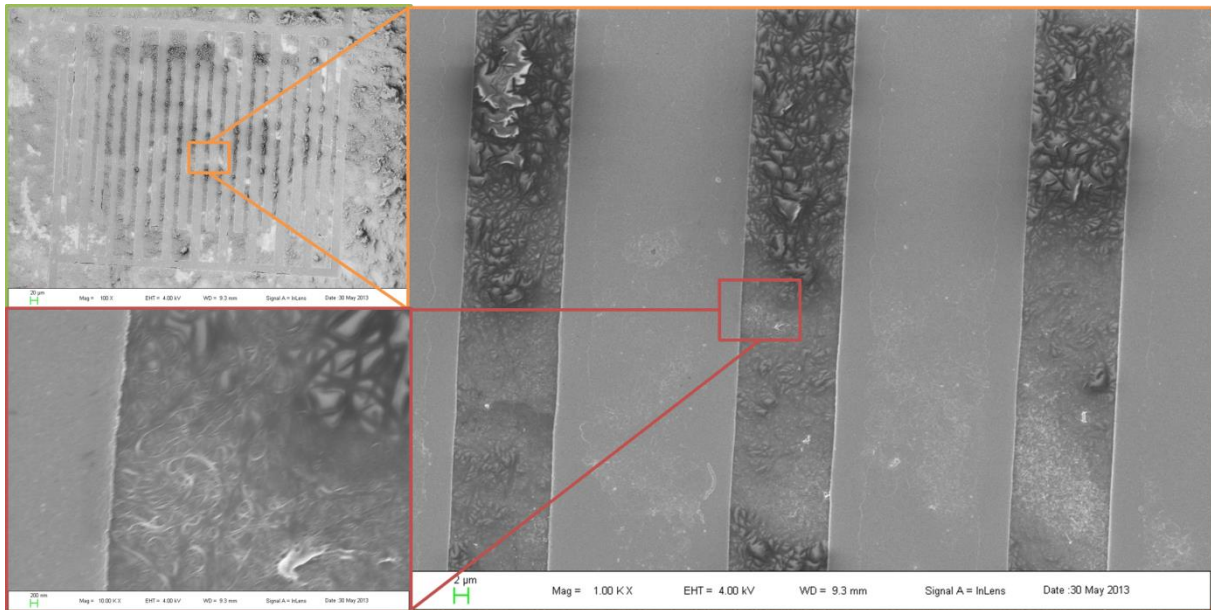


Fig. 125. 20- μ m-gap interdigitated electrode design, d (inverted), SEM images.

The properties of the 99% sc-SWCNTs deposited on our samples, as provided by NanoIntegris, are as follow: produced by arc discharge, high quality (from provided Raman spectrum), average length of 1 μ m within a 100nm-4 μ m range and average diameter of 1.4nm within a 1.2-1.7nm range. Catalyst and carbonaceous impurities are estimated to be respectively 1 and 5% by mass. Finally the absorption spectrum is as reproduced on Fig. 126. It matches a few usual continuous-wave-laser wavelengths but not all. A green 532nm laser may be used and is preferable to red to infrared lasers which are poorly absorbed but blue and near-infrared lasers around 1 μ m may produce better results. This is because, for the given CNT diameter, the primary bandgaps correspond to wavelengths close to 1 μ m and the secondary bandgaps to wavelengths around 500nm.

IsoNanotubes-S

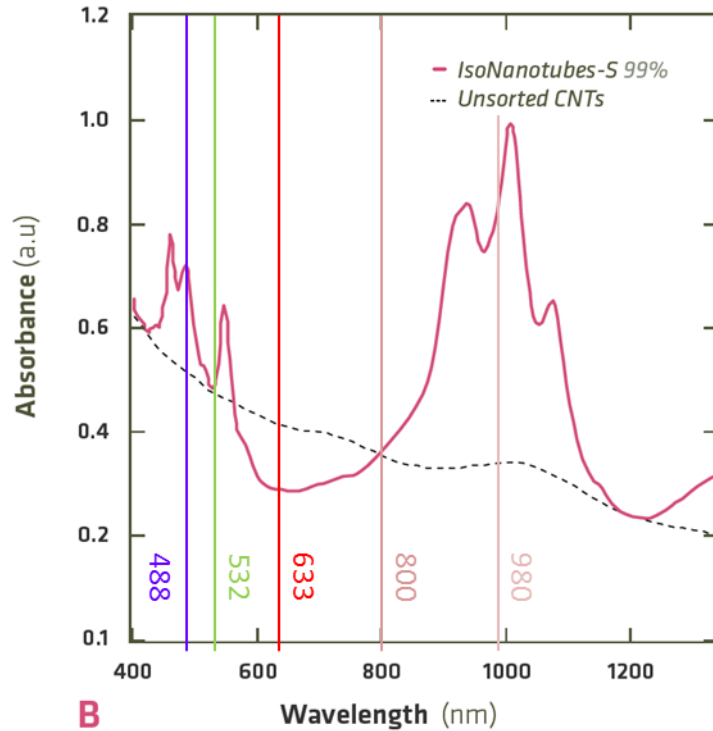


Fig. 126. Optical absorption spectrum of sc-SWCNTs IsoNanotubes-S 99% from NanoIntegris (source: datasheet) fitted with some of the usual continuous-wave-laser wavelengths. A green 532nm laser may be used and is preferable to red lasers but blue and near-infrared lasers around 1 μm may produce better results.

V.A.4) Post-processing

A straightforward method to selectively remove metallic CNTs in ohmically connected CNT bundles and films was devised by P.G. Collins and P. Avouris (IBM, T.J. Watson Research Center). They use electrical breakdown [222], [223]. A high current is passed through the CNTs in air. Since only metallic CNTs let the current through, they heat up by joule heating until thermal damage occurs while semiconducting CNTs are left untouched if they are not in extremely close vicinity. The metallic CNTs are mostly degraded as amorphous carbon that can deposit around the failure. The technique is thus better adapted to moderate density arrays or bundles than to CNT ropes. It has later been extended into a remote technique by simply placing the samples in a microwave oven at full power [224] and monitoring the outcome by transmission and reflection terahertz time-domain spectroscopy (THz TDS). This extension is key to large scale application of the method as individual connection to each bundle would not be scalable.

In the case of our samples, electrical breakdown could be attempted to keep only semiconducting CNTs since the spacing between CNTs is sufficient to prevent collateral damage. We did not apply it at first to the CPW gap samples but did a try on spray-deposited CNT films. One of the samples can be seen on Fig. 127. NanoIntegris 99%-semiconducting SWCNTs were sprayed over the whole surface of a glass microscope cover slip. Silver-ink pads were then manually defined in a corner. The response to high biases and successive electrical breakdowns is reported on Fig. 128. At the first electrical breakdown, at 110V bias i.e. 150V/mm, the resistance is multiplied by 100. At second electrical breakdown, at 230V bias i.e. 310V/mm it is multiplied by 10000. This indicates that the current takes longer and longer paths in the CNT film. However, only small fluctuations in an otherwise mostly ohmic IV curve could be observed even after electrical breakdown. This could be because the gap is much larger than the laser spot here (cf. Fig. 127).

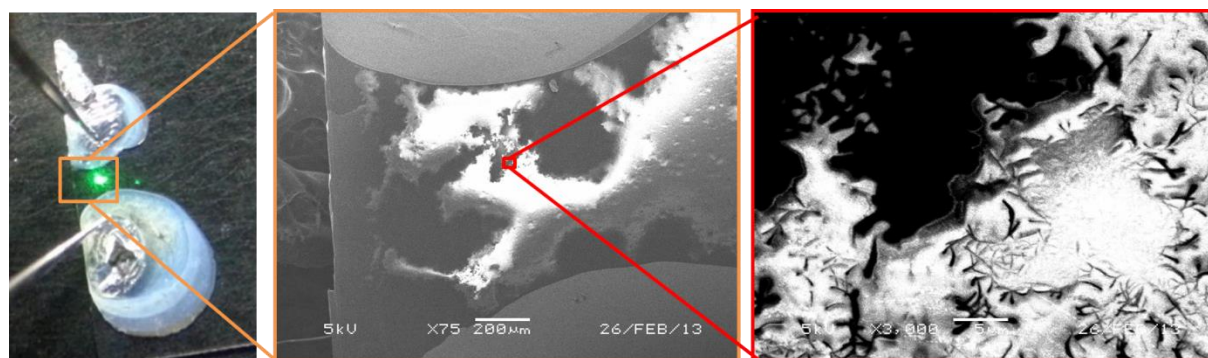


Fig. 127. Silver-ink pads deposited on sprayed CNTs on glass. From left to right: optical image and SEM images after electrical breakdown. The CNTs used should be 99% semiconducting but high-scattering regions are observed indicating some metallic content. However the shorter metallic paths linking the two electrodes seem to be cut. The gap is about 740- μm -wide.

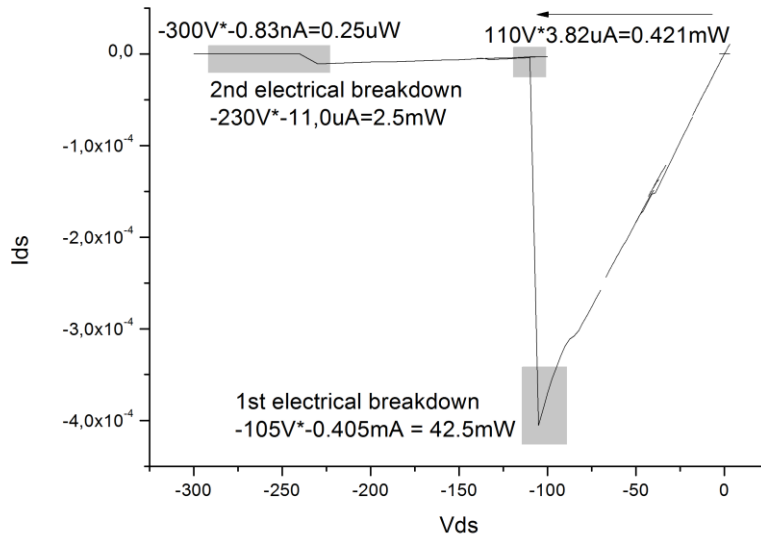


Fig. 128. Observation of two irreversible electrical breakdown steps while measuring the I-V curve of the CNT film. A voltage source was used as no current source was available.

V.B) Measurement and characterization

V.B.1) Physical characterization

V.B.1.1) Raman spectroscopy

Raman spectroscopy was used to check the nature and quality of the CNTs in the fabricated samples.

Raman spectroscopy is a characterization method for crystalline and amorphous materials. It is based on the acousto-optical Raman effect, an inelastic photon scattering. An impeding photon will be scattered with an optical frequency shift corresponding to the vibration frequency of resonant phonons in the crystal lattice or in gas molecules. The majority of the photons is actually scattered elastically so the fundamental frequency needs to be filtered out. The remaining spectrum is measured in a grating-based high-sensitivity spectrometer – a grating disperses polychromatic light just like a prism does but can be engineered to meet the application needs. For a very regular crystal the inelastic scattering produces sharp peaks in the spectrum characteristic of the lattice while for amorphous materials, the broad distribution in lattice will produce a broad spectral shape. The spectrum is usually expressed in terms of Raman shift in cm^{-1} which corresponds to wave vectors (photon/phonon) that can be summed directly.

The main Raman characteristics of SWCNTs are [225] two first order Raman features and a second order one. First, the G band is similar to the first-order graphene lattice peak, at circa 1580cm^{-1} , but actually made of several peaks, the two main being G+ (vibrations along the CNT axis) and G- (vibrations around the circumference of the CNT) at around 1590 and 1570cm^{-1} respectively. A large G+ G- splitting indicates small diameter SWCNTs while MWCNTs usually have a single G peak. The other first-order feature, characteristic of CNTs, is the existence of radial breathing modes (RBM) between 100 and 500cm^{-1} . Using several laser lines RBM frequencies actually allow characterizing the ratio of metallic to semiconducting CNTs in a sample [225]. From the RBM frequency which is inversely proportional to the diameter of the tube d_t (for example $\omega_{\text{RBM}} = 248 / d_t \text{ cm}^{-1}$), we can estimate the diameter d_t for SWCNTs. MWCNTs, unless they have a very small inner radius, normally do not exhibit RBM. A second order feature is the D band (disorder-induced feature), around 1350cm^{-1} , indicating defects and multiwall CNTs. Sample purity can be investigated using the D/G band intensity ratio for SWNTs [225]. Here we verify the general appearance of the Raman spectrum according to these criteria to check that we produce high-purity/quality SWCNTs. Analyzing the type of CNT and diameter is interesting if done on fabricated devices to match this and the electrical measurement. Full coverage of the theory can be found in [225], [226].

We used the WITec confocal Raman spectrometry system in Nanoelectronics laboratory 1, School of EEE, NTU (Fig. 129). It can be used with three different continuous-wave laser sources, blue, green and red. We only used the green 532nm laser as it gave sufficient performance in our case. However not all CNTs respond properly to Raman spectroscopy with a given wavelength [196]. The system is comprised of the laser source, an optical microscope switchable from bright-field(observation) to confocal mode (spectrum acquisition), and a grating-based spectrometer which CCD is operated cooled down to -60°C to prevent thermal noise. Shot noise is prevented by averaging over multiple samples (long integration or repeated acquisitions). There are two gratings allowing to choose between larger spectrum or higher spectral finesse.

The sample support is piezo-activated in XYZ and allows scanning predefined zones automatically to record an XY map of Raman spectra – which can be referred to as Raman mapping.



Fig. 129. WITec confocal Raman spectrometry system in Nanoelectronics laboratory 1, School of EEE, NTU.

V.B.1.1.1) Sprayed CNT films

The Raman spectrum measured on the sprayed CNT films (Fig. 130) corroborates the information from NanoIntegris and verifies that the CNTs were not degraded in the process.

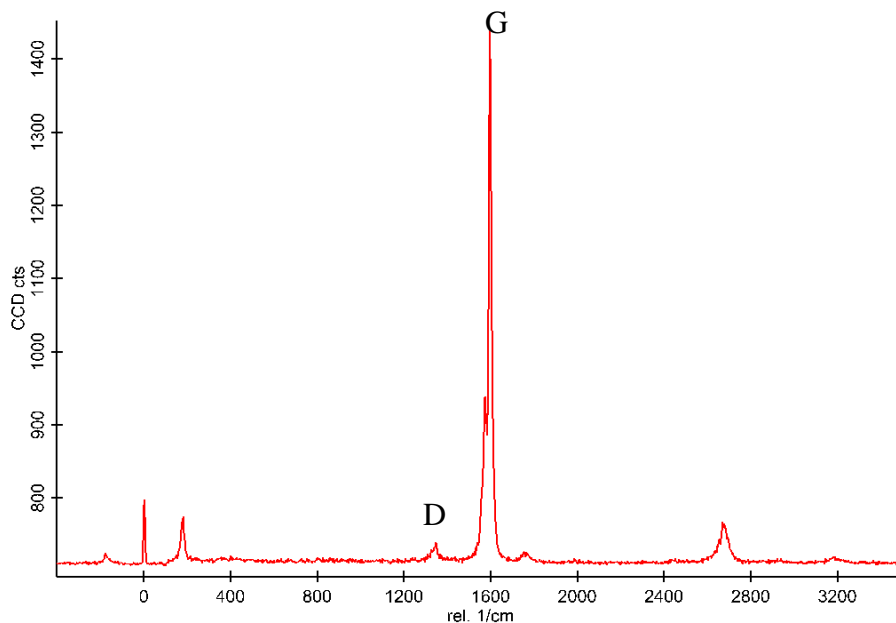


Fig. 130. Raman spectrum measured on the sprayed CNT film over glass of the interdigitated sample. $I_D/I_G=45\%$.

V.B.1.1.2) CVD-CNT-bridged CPW gaps

For the 20- μm -gap device E0.03 G201 presented section V.A.3.2), Raman mapping was attempted to locate the single CNT without success. For E0.03 G202 (Fig. 131), on the same substrate, Raman mapping was successful enough to find the CNTs and show they are high quality SWCNTs. Raman spectra on darker parts of the sample likely the most defective, with amorphous carbon and MWCNTs reveal a moderate defect peak Fig. 132. These are nevertheless rare regions on the sample and the rest displays either only the substrate response or the response of high-quality SWCNTs.

The nature and quality of the SWCNTs produced is reproducible as presented with Raman mappings and spectra on two zones of another sample produced in a repetition of the growth process, E0.04. These measurements are presented on Fig. 133, Fig. 134 and Fig. 135 and the geometrical correspondence between the CNTs observed under SEM and those detected by Raman mapping is demonstrated on both picked areas.

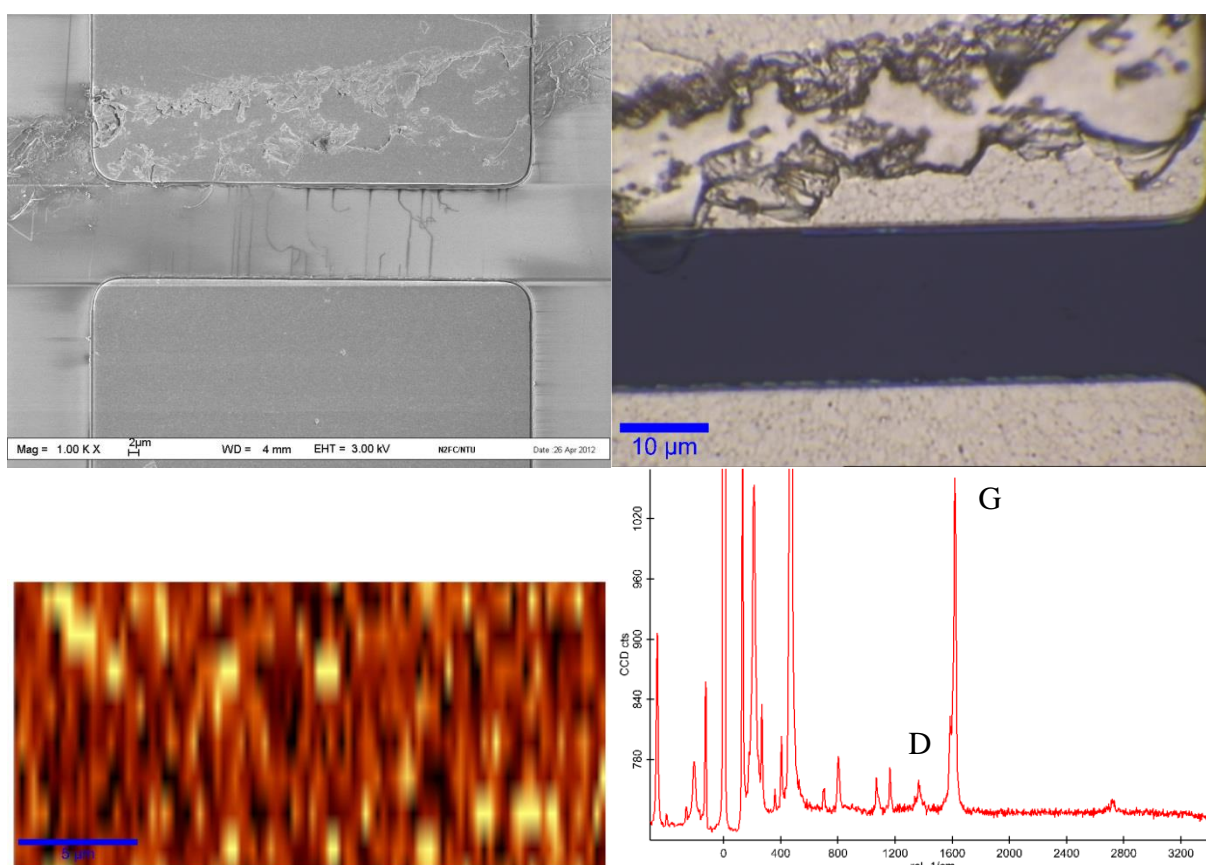


Fig. 131. Device G202 on sample E0.03. Left to right, top to bottom: SEM image, optical microscope image, Raman map (sum of the signal over the $1550\text{-}1630\text{cm}^{-1}$ band for each

position (x,y) to find regions with a high G peak) and representative Raman spectrum for the area.

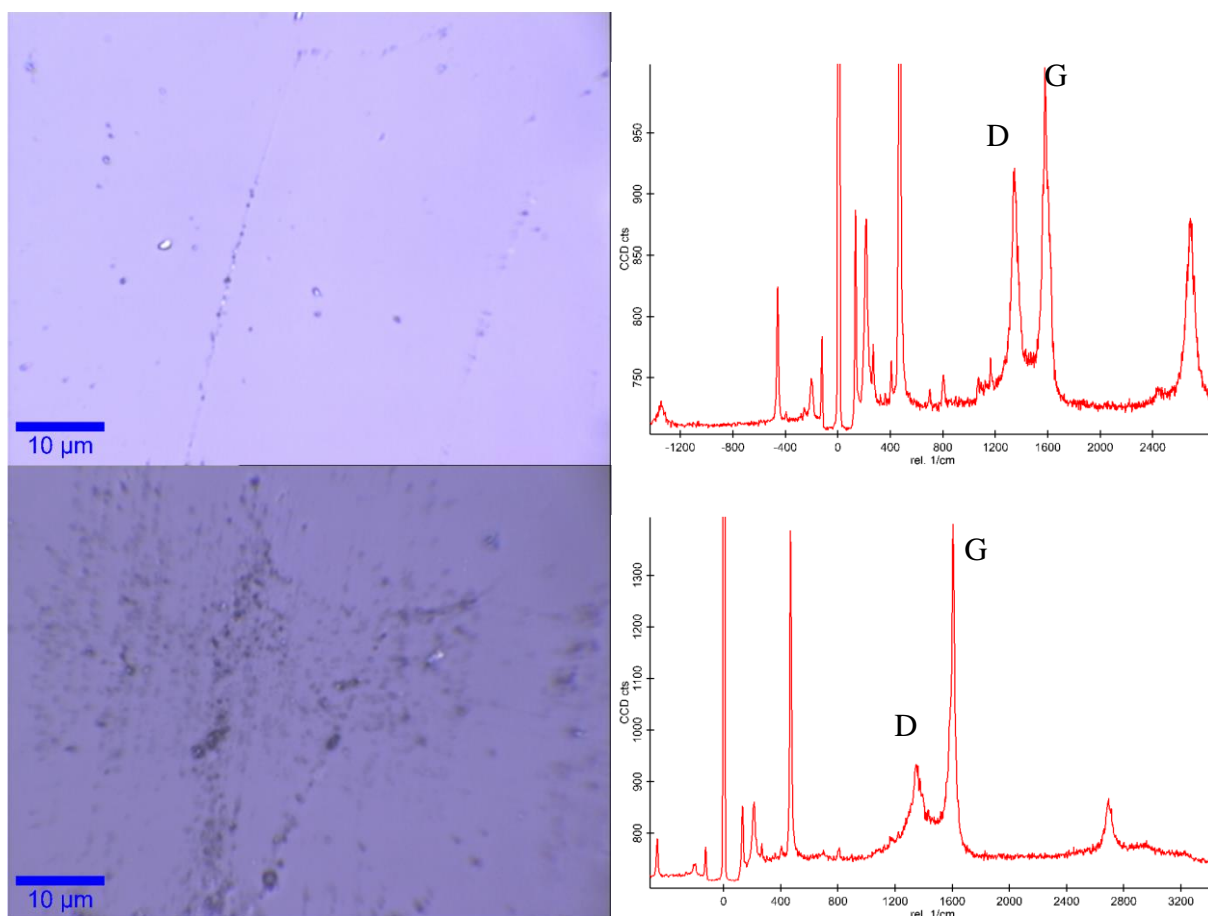


Fig. 132. Optically visible wires and dark regions reveal a CNT spectrum as well but with some more defects and possibly MWCNTs.

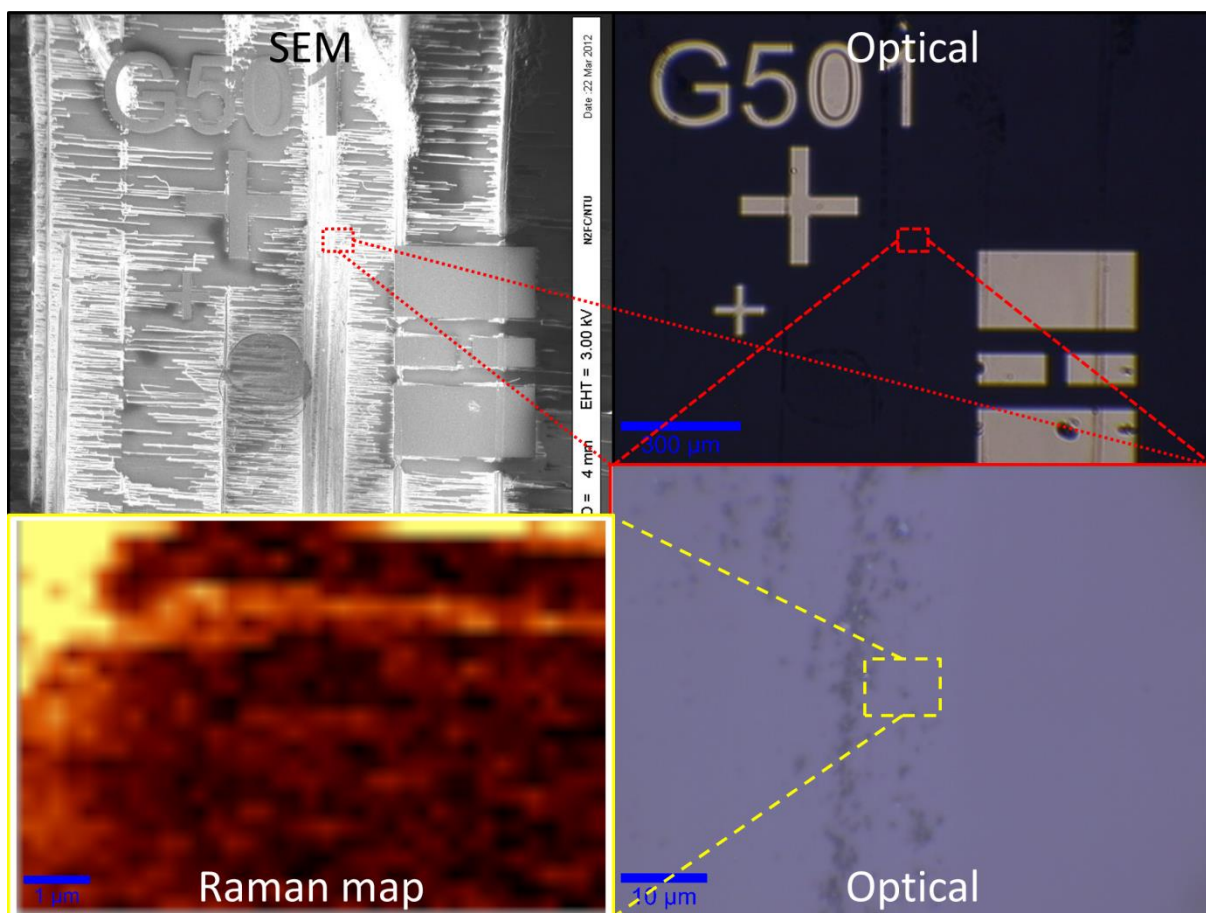


Fig. 133. Raman mapping of the $1580\text{-}1630\text{cm}^{-1}$ shifts matches the position of the CNTs growing out of a catalyst line by device G501 on sample E0.04. The CNTs are invisible to simple optical microscopy but can be detected and identified through SEM or Raman spectroscopy.

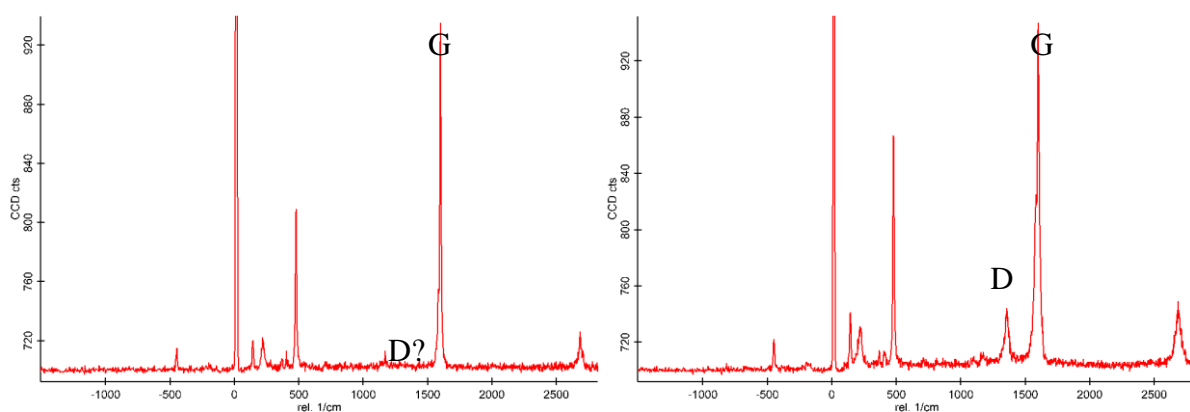


Fig. 134. Full Raman spectra acquired on the CNTs characterized on Fig. 133; from I_D/I_G we see that very high quality SWCNTs are obtained.

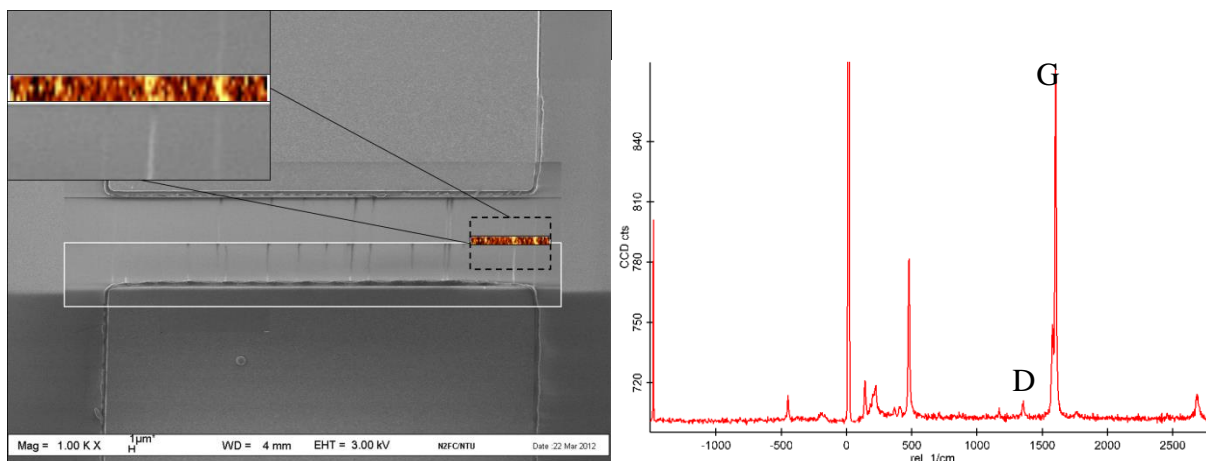


Fig. 135. Left: Raman mapping of the $1580\text{-}1630\text{cm}^{-1}$ shifts (brown color scale) matches the SEM-recorded position of the CNTs in the gap of device G201 on sample E0.04. Right: full Raman spectrum acquired on one of the CNTs (similar for the others in the mapping; very high quality SWCNTs are obtained).

V.B.1.2) Atomic Force Microscopy

Atomic Force Microscopy (AFM) is a physical characterization technique with many variations but the core principle is to use an atomically-thin tip and piezo actuators to physically scan the surface of a sample. This gives access to resolutions down to 1nm.

AFM is often used to characterize horizontal growth of CNTs or CNT catalyst. We used it to characterize the surface of spray coated samples and shall use it on the CPW gap samples as a final characterization step to determine the exact number and diameters of the CNTs bridging the gaps. However this was not undertaken yet due to the risk of damage (section) of the CNTs by this technique which would destroy the sample in our case. All optoelectrical characterization should thus be achieved before proceeding to AFM characterization. AFM measurement on CNTs grown by techniques and recipes similar to the ones we follow indicate that the CNTs should have an average diameter between 1.1-1.2nm [142], [143] and 1.8nm [158].

V.B.2) Photocurrent characterization

V.B.2.1) Photocurrent setup

The setup we use to measure photocurrent is part of the facilities in Cesare Soci's laboratory in NTU SPMS. Wang Zilong, one of his PhD students, conceived and set up the bench. It is based on homodyne detection. The principle is to modulate the signal to detect by a given frequency. This modulation frequency, the synchronization signal, is passed onto a

lock-in amplifier receiving the signal. The lock-in amplifier then averages through time the product of the signal it receives (signal to detect and noise) and the synchronization signal. Over a long enough integration time only the component of the received signal modulated at the synchronization will have a non-null average. This technique has two advantages: it effectively reduces the noise – but at the cost of integration time – and, being phase-sensitive, it allows reading a signal without ambiguity. The noise filtering can be further enhanced by preliminary filters, taking good care not to cut the modulating frequency.

In our case the signal to detect is the photocurrent. Therefore the light used to illuminate the sample is modulated using a chopper. A lock-in amplifier is synchronized with the chopper driver. The electrodes at both ends of the CNT are connected as the signal. The device is connected as a current source. To add extra frequency filters the device can be plugged through an intermediary pre-amplifier which itself will need to be connected as voltage source. The setup and its different aspects are illustrated on Fig. 136, Fig. 138 and Fig. 137. For the measurements we present in the next section, the light source used was a 532nm CW laser.

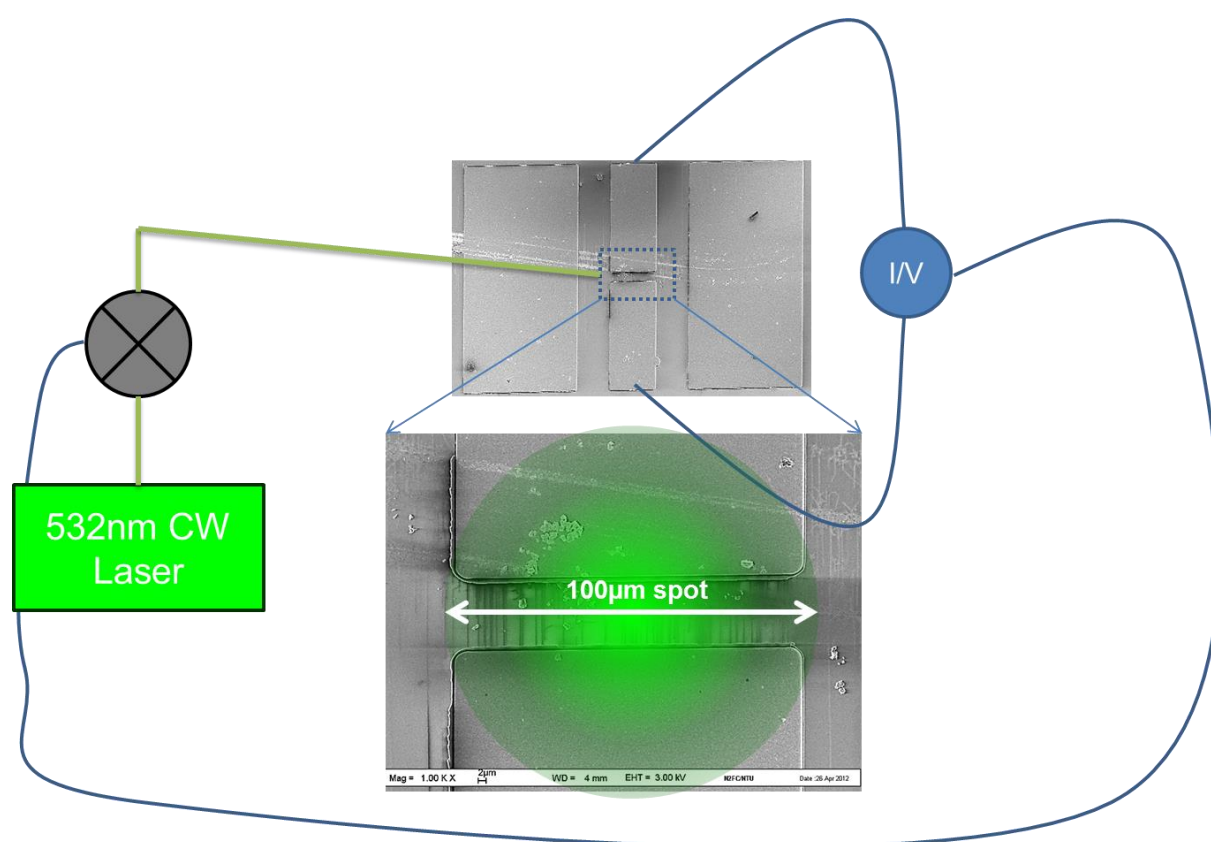


Fig. 136. Schematic illustration of the characterization on a CPW gap sample. The laser is chopped before being propagated to the gap where its 100-µm-diameter spot covers the gap.

The chopper frequency is fed to the lock-in amplifier connected to the electrodes of the sample.

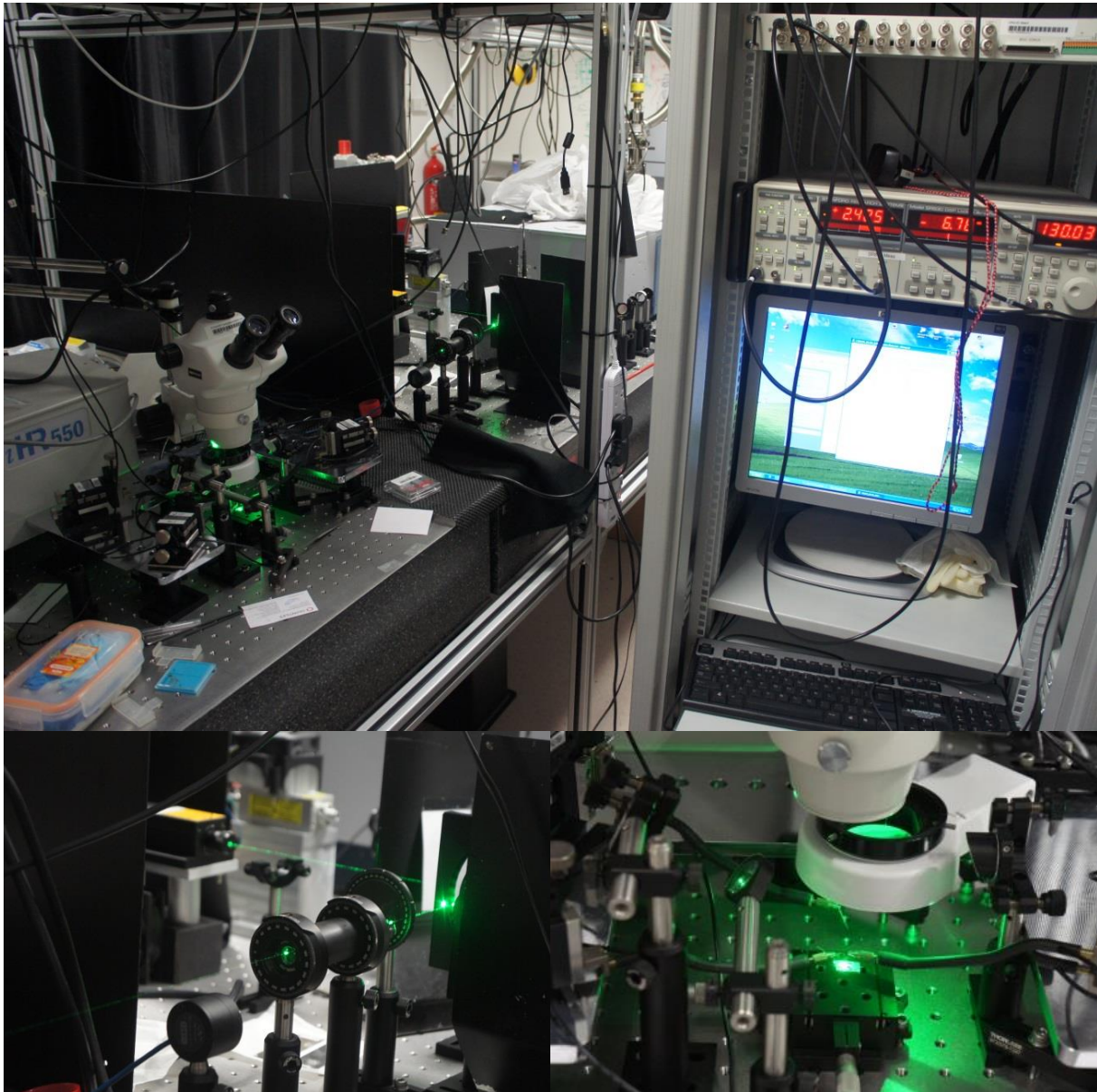


Fig. 137. Experimental photocurrent lock-in amplifier setup using a 532nm CW laser. Top right: lock-in amplifier, top left optical table with freespace laser propagation. Bottom left: going upstream on the optical path, quarter wavelength plate, polarizer, variable density, chopper, laser. Bottom right: Mirror and focusing lens bring the laser to the quartz substrate under the probes.

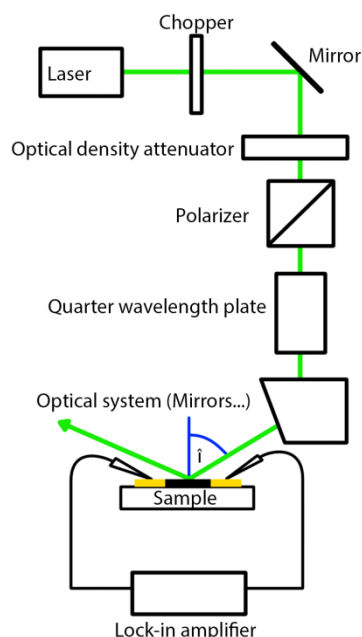


Fig. 138. Principle of the experimental setup. \hat{i} is the incidence angle of the laser on the sample.

V.B.2.2) Characterization range

We mostly tried to remain conservative in the ranges of values used to prevent irreversible damage to the samples before completing the characterization.

For optical power, since laser ablation of CNTs is a known and used technique, we may check the range. In [227], an optical parametric oscillator (OPO) producing 10ps-long $24\mu\text{J}$ pulses separated by 10ns and by bursts of $1\mu\text{s}$ at 25Hz for an average power of 60mW is focused on a $100\mu\text{m}$ -diameter spot. The peak intensity threshold of ablation of CNTs aligned along light polarization is found to be $13\text{MW}/\text{mm}^2$. The ablation is believed to be of thermal nature. The CNTs are estimated to be heated up to temperatures in excess of 500°C . Depending on the thermal dissipation rate, the intensity to take into account might be lower than the peak pulse intensity. The burst average intensity can give a lower limit approximation of the actual value and is found to be $13\text{kW}/\text{mm}^2$ since CNTs are a good thermal dissipater and the substrate used (quartz) is transparent, the average intensity in this case, $325\text{mW}/\text{mm}^2$ is clearly an underestimate. In our case, we used a very similar case of CNTs on a quartz substrate, with a spot diameter of about $100\mu\text{m}$ as well but a continuous 532nm-wavelength laser up to 140mW power. Hence the intensity was well below damage threshold to CNTs even at maximum power where it is around $18\text{W}/\text{mm}^2$.

However when electrical current is flowed through the CNTs at the same time, additional heating of the CNTs occurs from Joule heating. This should be taken into account to prevent damaging the CNTs. It also provides an interesting differentiation technique that could be used to selectively remove metallic CNTs. Indeed laser ablation was shown to be orientation selective but, as expected because of its thermal nature, insensitive to chirality. On another hand we explained how selective metallic CNT removal was achieved using electrical breakdown [222], [223]. Because the number of conduction channels depends on a number of conditions such as source-drain and gate bias some semi-conducting CNTs may be damaged in the process. A semi-conducting to metallic voltage threshold at 3kV/cm (60mV bias across a 20 μ m wide gap) in CNT films has been measured experimentally and reported in [228]. The current and therefore voltage threshold for joule-heating-induced damage could be lowered by combining electrical breakdown to laser heating below damage threshold. However temperature dependence of the conduction of semiconducting SWCNTs would also have to be taken into account.

V.B.2.3) Measurement results

All measurements were made at a chopper frequency of 130Hz unless stated otherwise. This is rather slow so should not filter too much of the signal out if the response is not fast (cf. section V.B.2.3.2), Fig. 157 in particular). It is suited to the filters on the lock-in amplifier and not a multiple of 50 and 60Hz, the mains modulation frequencies which need to be filtered out using notch filters.

V.B.2.3.1) CVD-CNT-bridged CPW gaps

V.B.2.3.1.1) Gap bridged by 13 to 16 CNTs of mixed chirality

The first device we present, E0.03 G202, comprises a mix of metallic and semiconducting CNTs. This leads to a relatively large ohmic current. The IV curve, Fig. 139, shows a mostly-ohmic response with apparent current saturation above 1-1.5V. At 1V the total resistance is 133k Ω and over a 20- μ m-long gap this means a linear resistivity of 6.67k Ω/μ m which is compatible with 1 to 10CNTS conducting. In the zone where current would normally saturate, the effect of illumination at 245 μ W (red) and 2mW (green) seems to allow additional conduction with some remanence as the curves after illumination (blue) remain higher than the original one (black-greys).

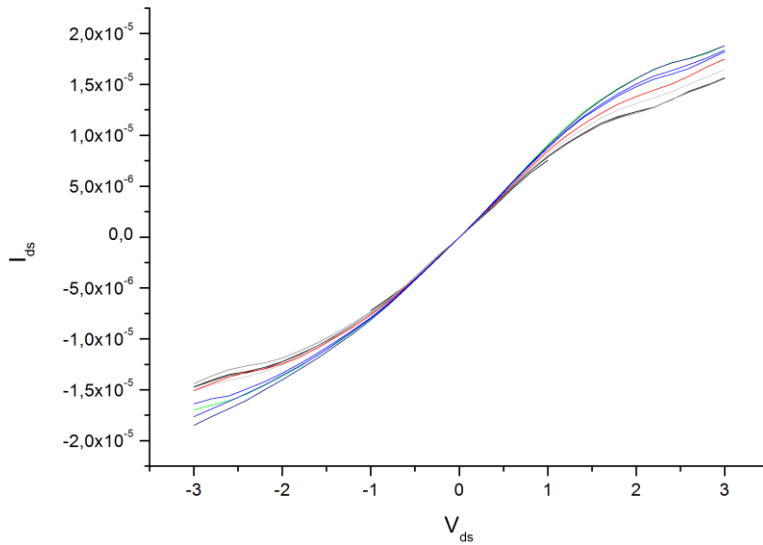


Fig. 139. IV curve shows a mostly-ohmic response with apparent current saturation above 1-1.5V.

The photocurrent, Fig. 140, seems to scale with optical power and displays an exponential increase with bias before saturation. The saturation threshold shifts higher in bias as the laser power decreases. It must be limited by the total amount of power that can flow through the CNTs as was previously seen on saturation of the ohmic regime on Fig. 139.

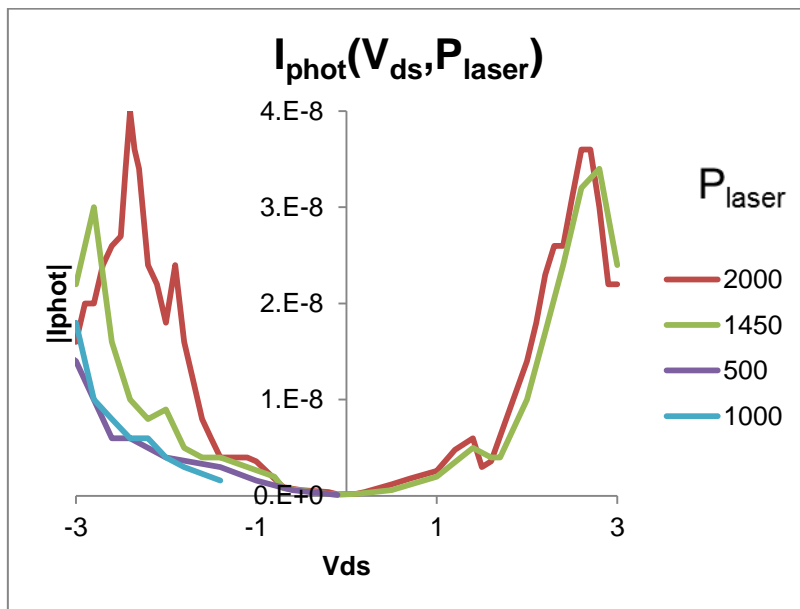


Fig. 140. Photocurrent (module) as a function of bias (V_{ds}). There is actually a sign change between negative and positive bias. For lower powers measurements were only recorded with negative bias because of the relative symmetry of the curve.

However, characterization of the many other devices we fabricated would be necessary to extract statistical data on these mixed CNT samples. The next device we report on provides a shortcut to some valuable information.

V.B.2.3.1.2) Gap bridged by a single semiconducting-SWCNT

The device E0.03 G201 gives us more insight on the photocurrent in sc-SWCNTs as we will experimentally characterize a single CNT only with repeatable electrical contact, well defined alignment and exposed length.

First observation, as reported Fig. 141, the photocurrent is dependent on the position of the incident beam on the device. Because of the small dimensions of the device, the position is varied arbitrarily and assigned a pseudoposition number respecting the spatial order of the successive beam positions. If the beam is scanned from left to right on the figure (direction normal to the CNT), the photocurrent profile seems to follow the incident beam profile, radially decreasing. This is actually expected, provided that the photocurrent scales with the light intensity: it is then somewhat equivalent to convoluting the beam profile with a Dirac. If the laser beam is scanning from top to bottom (along the CNT axis), the current is minimum at the center and maximum at the extremities of the electrodes. This can be understood as the necessity to create asymmetries in the structure to induce preferential differentiation of the photocurrent carriers. CNT-metal contact could also be an explanation [202].

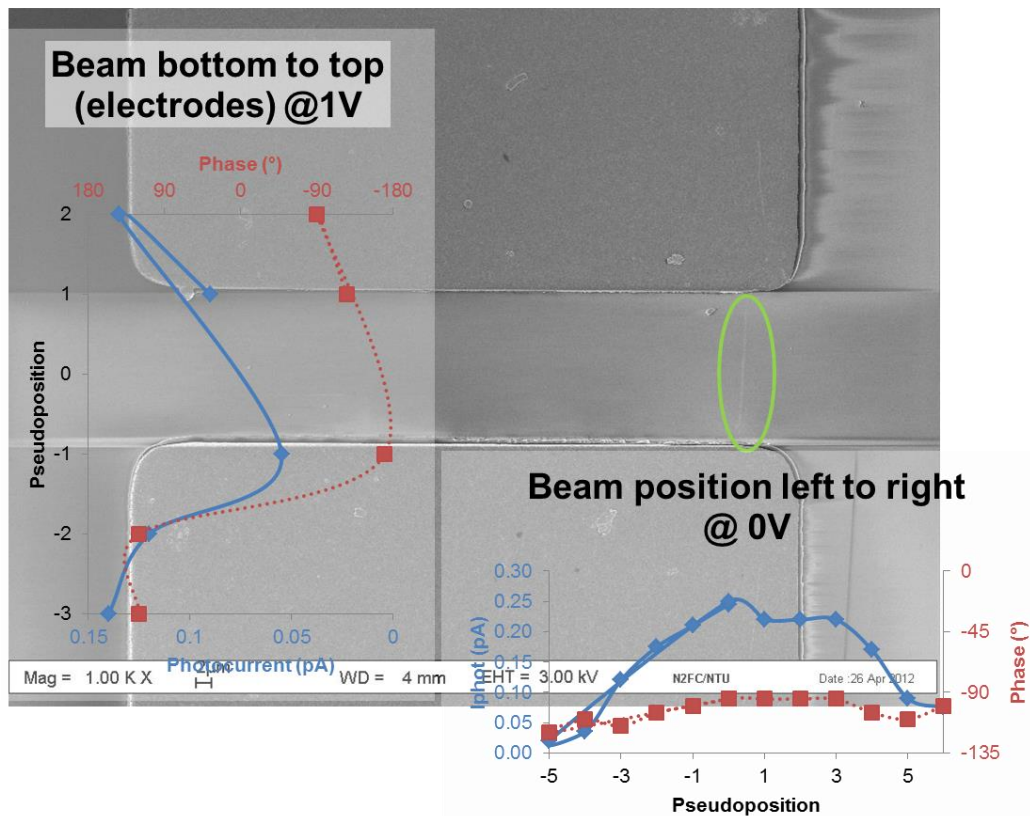


Fig. 141. The photocurrent is dependent on the position of the incident beam on the device. Because of the small dimensions of the device, the position is varied arbitrarily and assigned a pseudoposition number respecting the spatial order.

The next observation is that the photocurrent in a sc-SWCNT is independent of bias, at least moderate, as checked up to 1V i.e. an electric field of 50V/mm on Fig. 144. On this same figure the photocurrent appears to scale with the incoming laser power. On Fig. 145 we show that there exists a linear relation between photocurrent and laser power, as expected.

On Fig. 142 and Fig. 143 we show two relative orientations of the CNT and incoming light. The initial measurements were made with the CNT parallel to the incoming polarization but normal to the incidence plane. However it is clear that the transfer of momentum will be much more efficient if the CNT is aligned with the plane of incidence, especially with a 45-50° incidence angle that is very similar to the angles used to excite plasmons at the surface of metals. On Fig. 146 we verify that the photocurrent generated in the optimal configuration is five times stronger for the same illumination. What is less clear a priori is how the crossed configurations compare – CNT normal to the plane of incidence but parallel to polarization and CNT in the plane of incidence but normal to polarization. Using a quarter-wavelength plate to rotate the polarization we investigated incidence parallel and normal to the CNT with all linear polarizations. The results are presented on Fig. 147.

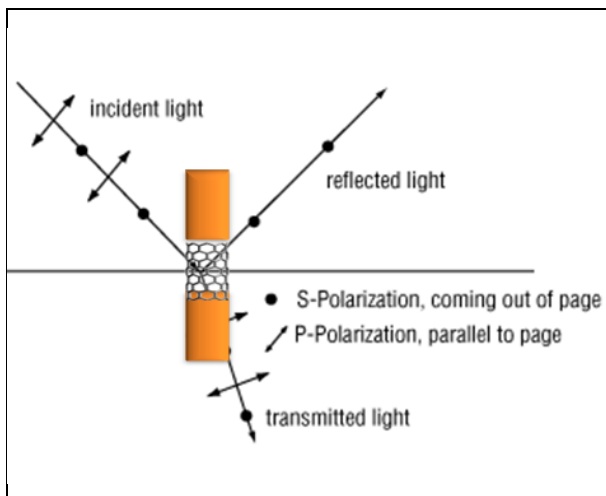


Fig. 142. CNT normal to the plane of incidence, s-polarization parallel to CNT.

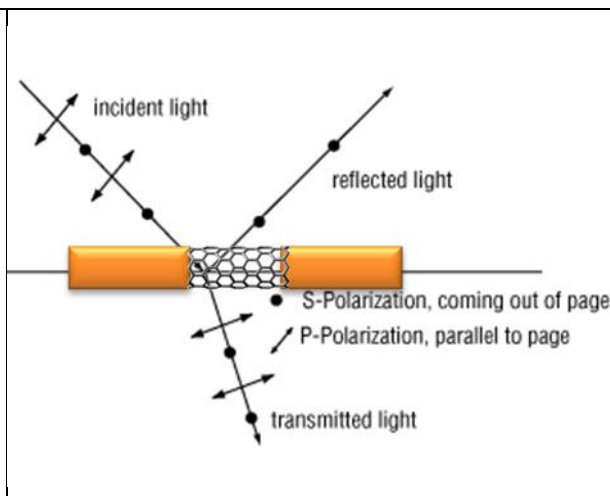


Fig. 143. CNT in the plane of incidence, p-polarization parallel to CNT.

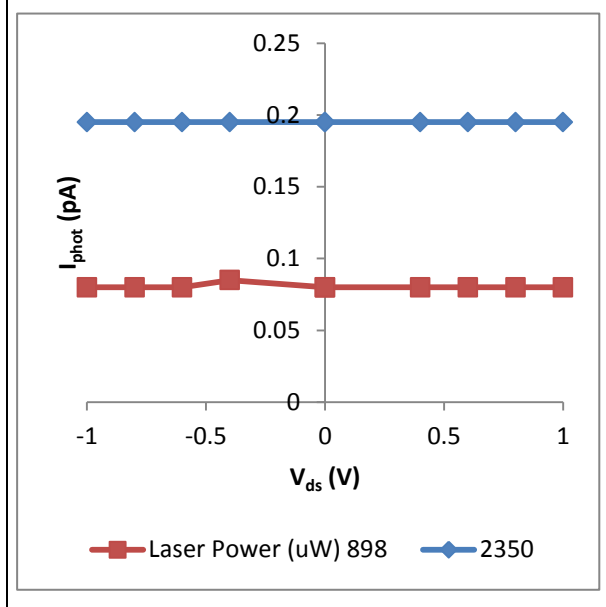


Fig. 144. Photocurrent independent of $V_{ds} < 1V$ (measured with CNT normal to the plane of incidence and s-polarization)

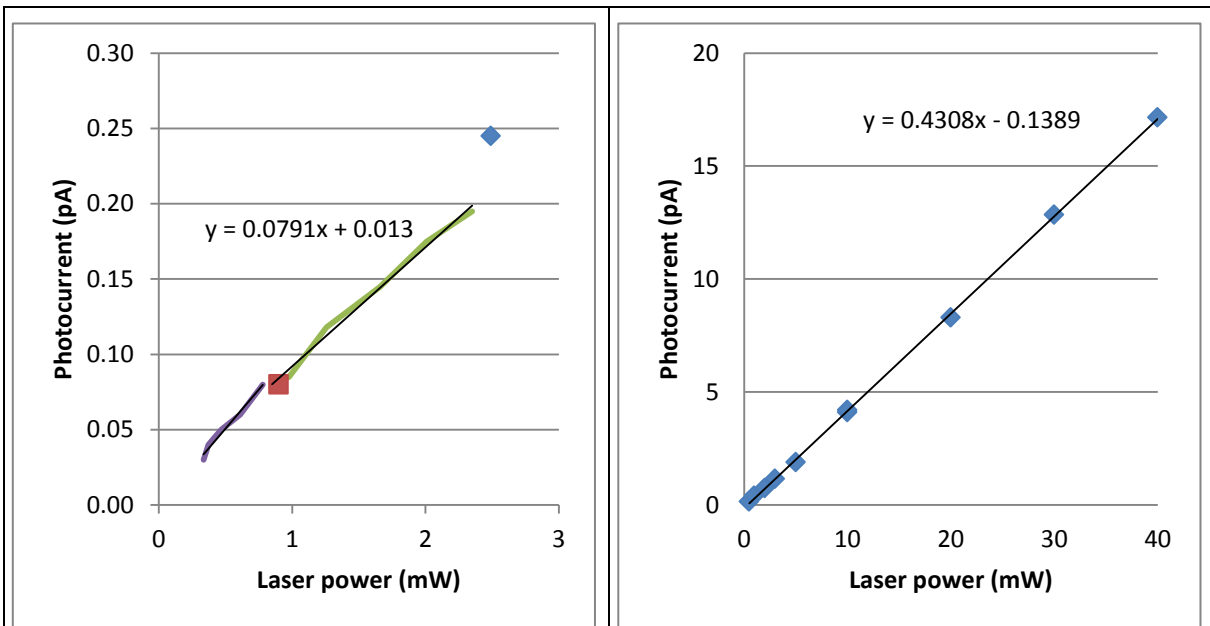


Fig. 145. Laser power dependence of photocurrent for CNT normal to the plane of incidence and s-polarization (thus parallel to CNT). Different colors correspond to measurement taken at different times thus validating the reproducibility of the measure.

Fig. 146. Laser power dependence of photocurrent for CNT in the plane of incidence and p-polarization (thus parallel to CNT).

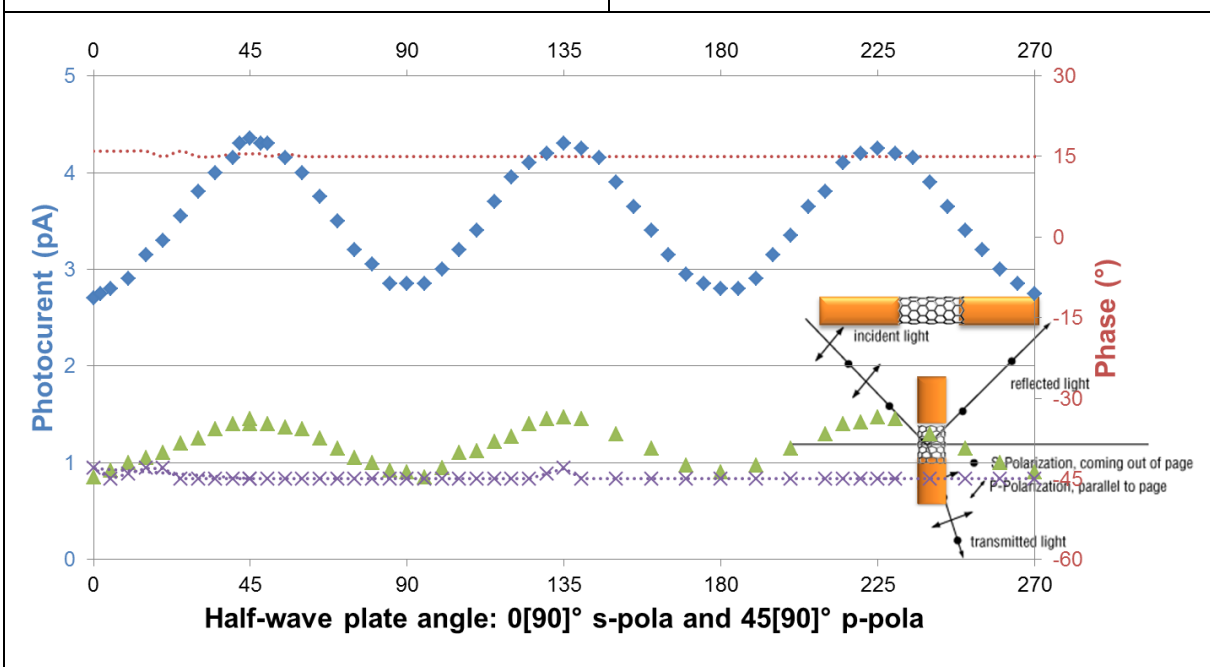


Fig. 147. CVD single SWCNT polarization and incidence. Laser power: 10mW, chopped.

For an incidence parallel to the CNT, as expected, the efficiency is maximum when the polarization is aligned with the CNT and penetrating the substrate (p) while it is minimum when the polarization is normal to the CNT and almost fully reflected at the surface of the substrate (s) – because we work close to the Brewster angle for quartz. However the other

results are not as straightforward. Firstly, whatever the polarization, incidence parallel to the CNT is at least twice as efficient as normal incidence. Secondly, for normal incidence, p-polarization is 1.7 times more efficient than s-polarization which is parallel to the CNT. This may be due to the better penetration through the substrate or minor misalignments that make the projection of the p-polarization along the CNT non-null.

As a conclusion we have determined the optimal illumination parameters for aligned pure sc-SWCNTs and verified a linear relation between light intensity and photocurrent while limited bias was shown not to affect the response.

V.B.2.3.2) Sprayed-CNT films

A scalable way to produce good semiconducting films from CNTs is spray gun. By concentrating on DC response for now we can use interdigitated designs to improve dramatically the currents thanks to a much longer connection.

We shall now experimentally investigate their properties. On Fig. 148 we observe that the response to laser power or more precisely the resulting light intensity is linear like before but with 33 times more photocurrent. This time however, bias plays an important role because the CNT film is not fully semiconductor and, although the gap is not longer, the electrodes are further apart. The response to tension is quasi-linear which we can also express through a photoimpedance (Fig. 149). The beam is much smaller than the exposable area this time (100- μ m-diameter for more than 1mmx1mm for the patterned area), and the response is variable from 0 to 300 pA depending on the exposed area. Tuning the position of the beam is therefore needed at the current fabrication stage. We also study beam incidence influence like we have done in the previous section. Fig. 150 and Fig. 151 illustrate the incidences parallel and normal to propagation between the gaps. Fig. 152 and Fig. 153 show that, again, p-polarization is the most effective with any incidence. We show on Fig. 155 that the photocurrent response is the same for the two orthogonal incidence directions chosen if the polarization is the same and the spot used is the same; Fig. 154 illustrates one of the optimal spots found that was used for these measurements by rotating the sample then reoptimizing the response through beam methodic sweeping.

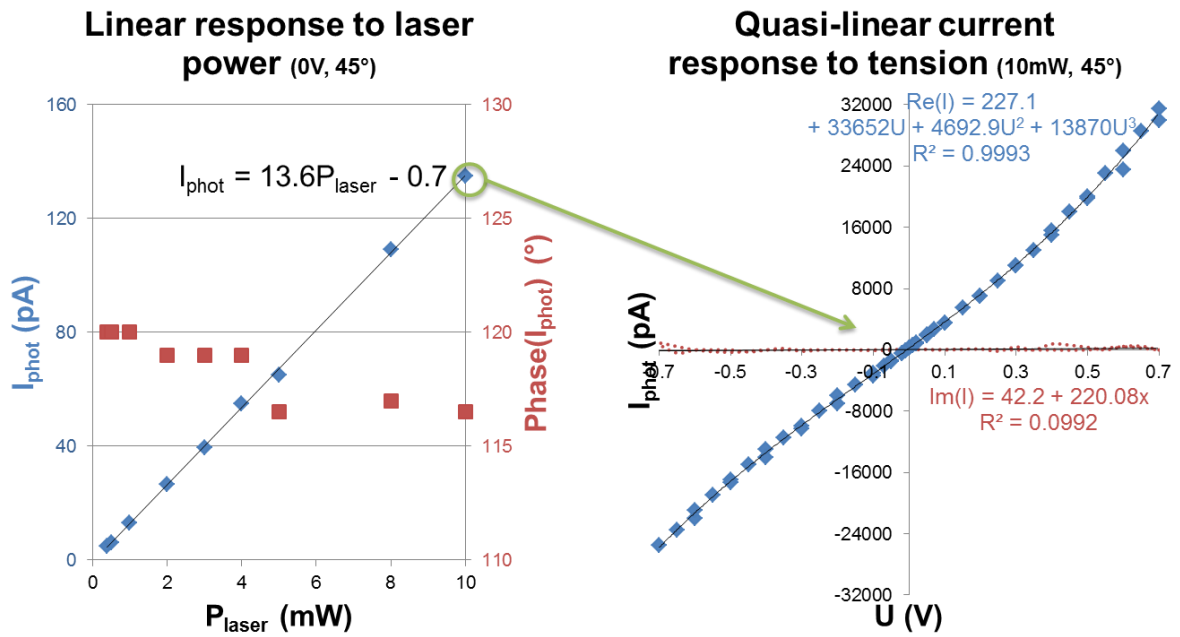


Fig. 148. Photocurrent response of randomly oriented sc-SWCNT films to light intensity at 0V bias (left) and bias at 10mW laser power (right).

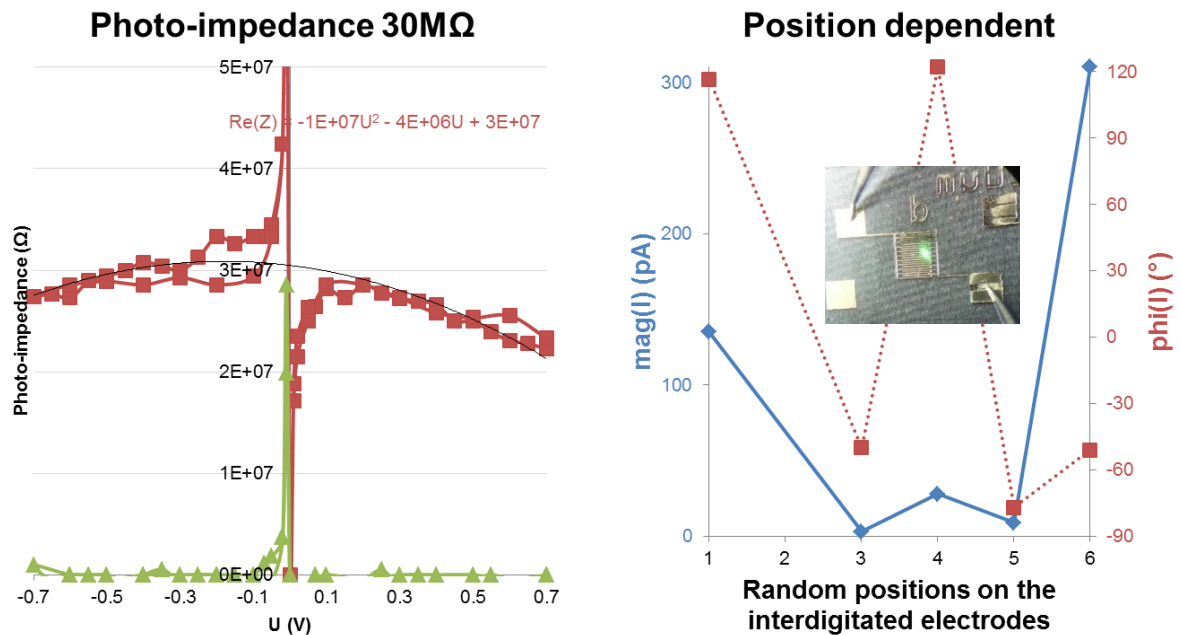


Fig. 149. Very high photo-impedance of the film (left) as calculated from the data reported on Fig. 148 and dependence of the photocurrent over the position of the beam illustrated (right) by a sample of positions over the grid (as shown on the inset) and the measured current.

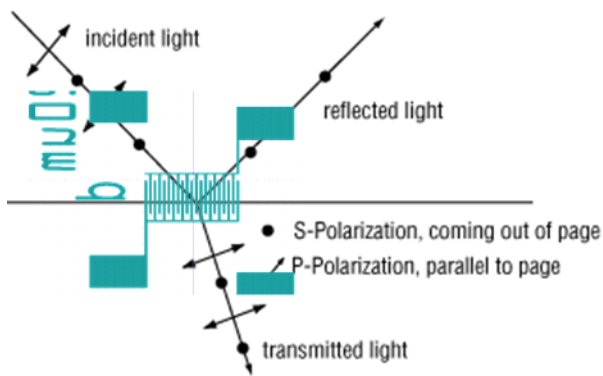


Fig. 150. Incidence parallel to propagation in the gaps.

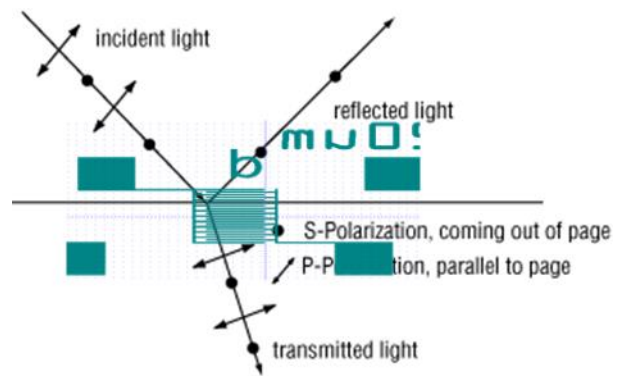


Fig. 151. Incidence normal to propagation in the gaps.

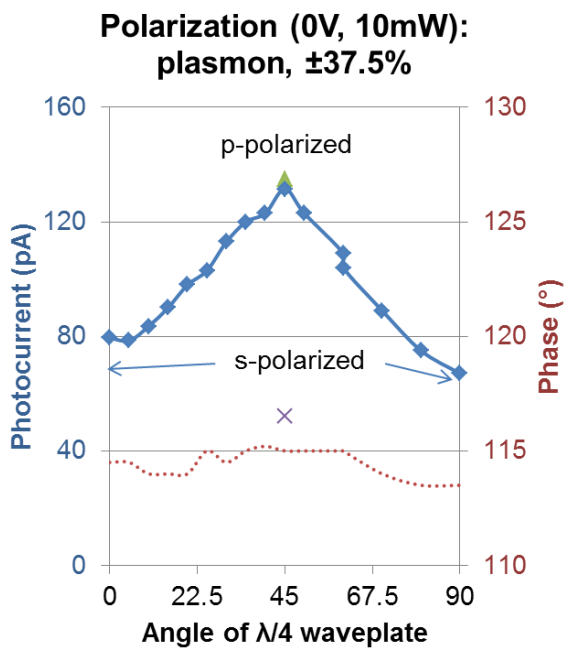


Fig. 152. Photocurrent dependence in polarization at incidence parallel to the gap propagation, 0V and 10mW.

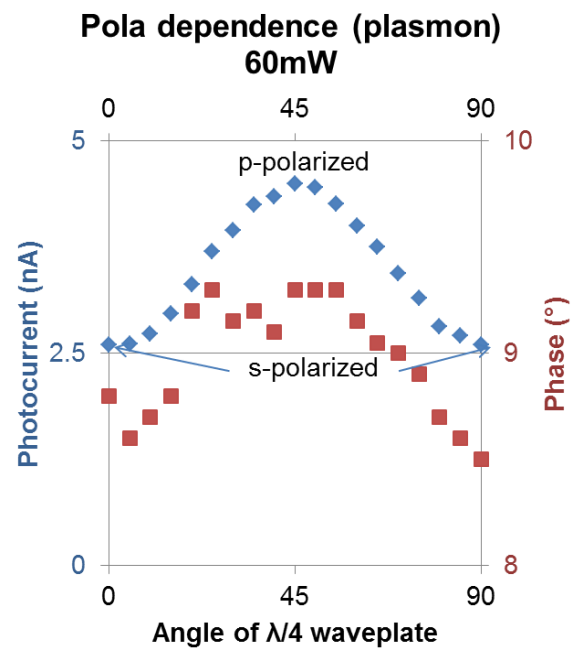


Fig. 153. Photocurrent dependence in polarization at incidence normal to the gap propagation, 0V and 60mW.

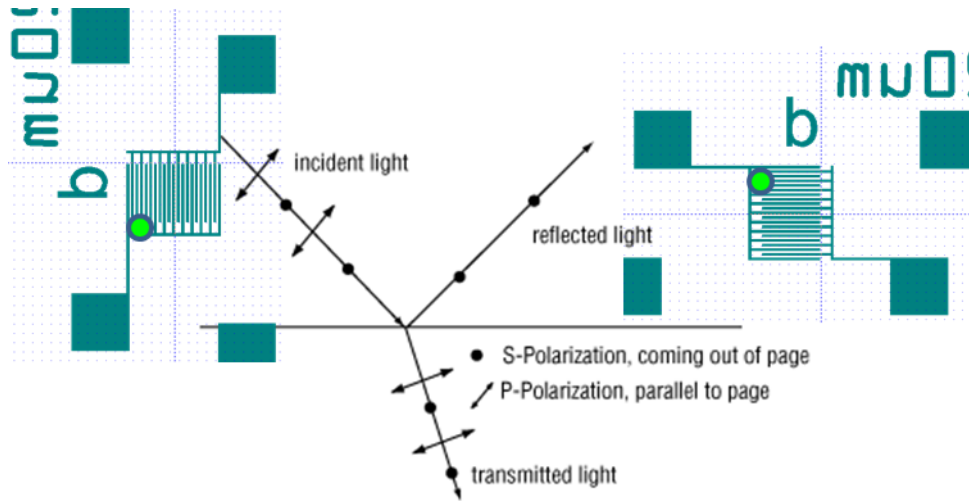


Fig. 154. Schema of same spot used in incidence both parallel and normal to the gaps.

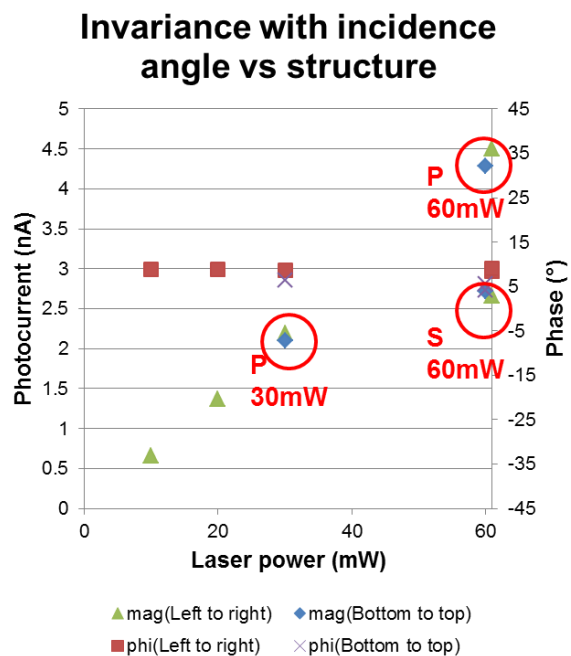


Fig. 155. Using the exact same spot be it with incidence plane parallel (bottom to top) or normal (left to right) to the gap the response is the same. However p-polarization is systematically more efficient than s.

In a second time we study the low frequency/DC dynamics of the photocurrent response. By manually chopping the beam at $\sim 2\text{Hz}$ we see the photocurrent ON-OFF ratio is very good: 850pA vs. 300pA at 0 bias and 64mW impeding green laser power (cf. Fig. 156). However the ratio is limited by a slow time response. At 130Hz, the modulation is already limited. We quantified the decrease in photocurrent for frequency modulation from 85Hz through to 4kHz. The result of these measurements is reported on Fig. 157.

Finally we evaluate the scalability of our fabrication technique by comparing the photocurrent performance of three similar devices fabricated on the same glass cover slip. The response, reported on Fig. 158, shows similar but far from identic performances, indicating that homogenizing the coating would be required for potential large scale applications.

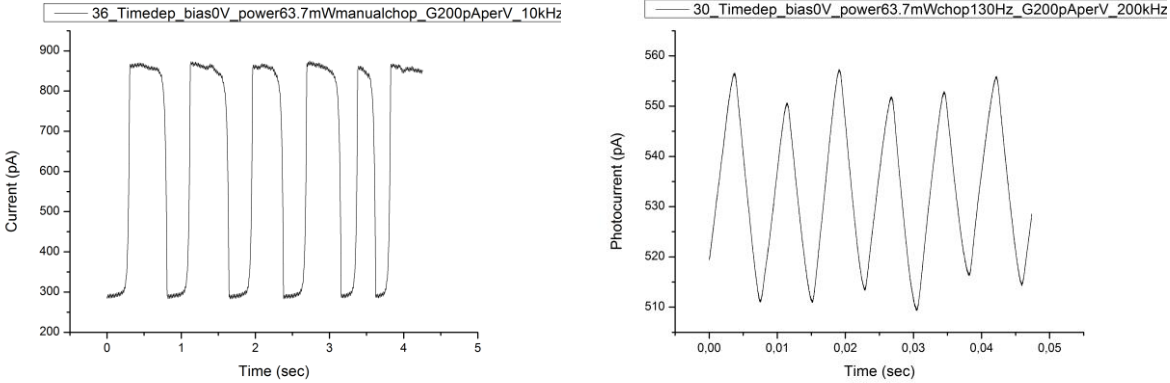


Fig. 156. Direct current measurement shows a clear ΔI but a slow response; at 130Hz the modulation is limited by the time response and only varies by 10% instead of +200% at 63.7mW and 0V bias.

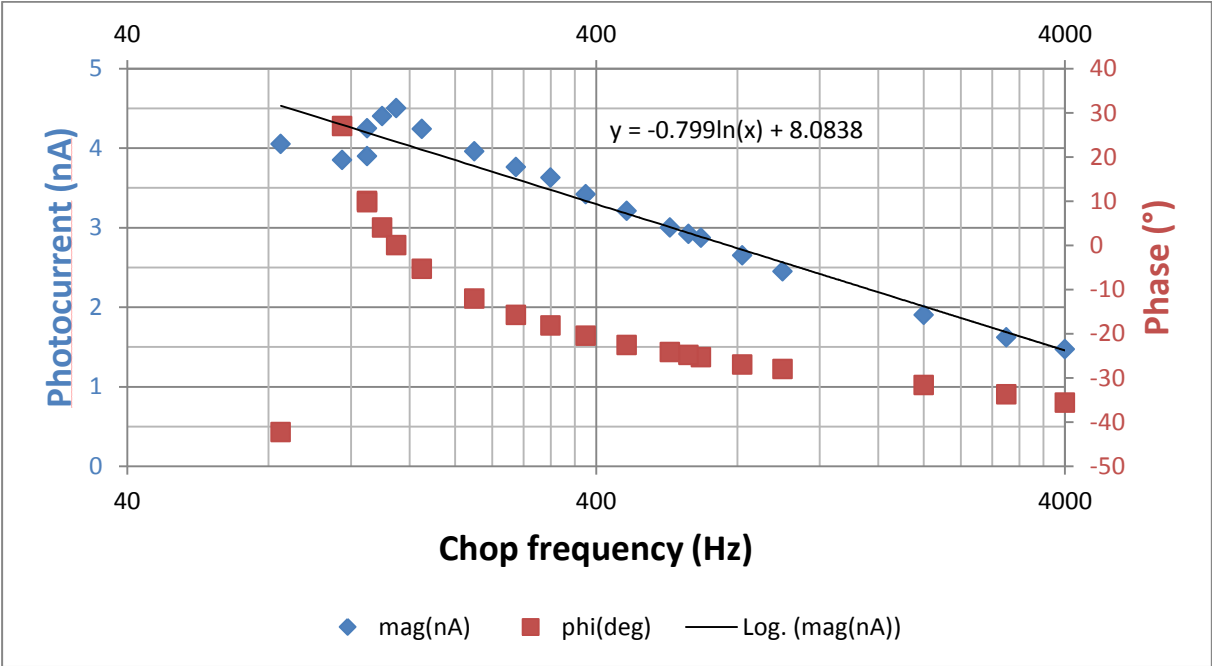


Fig. 157. Signal dependence on chop frequency. If the signal is modulated too fast the modulation amplitude decreases because the current does not rise or fall fast enough to reach its minimum and maximum values.

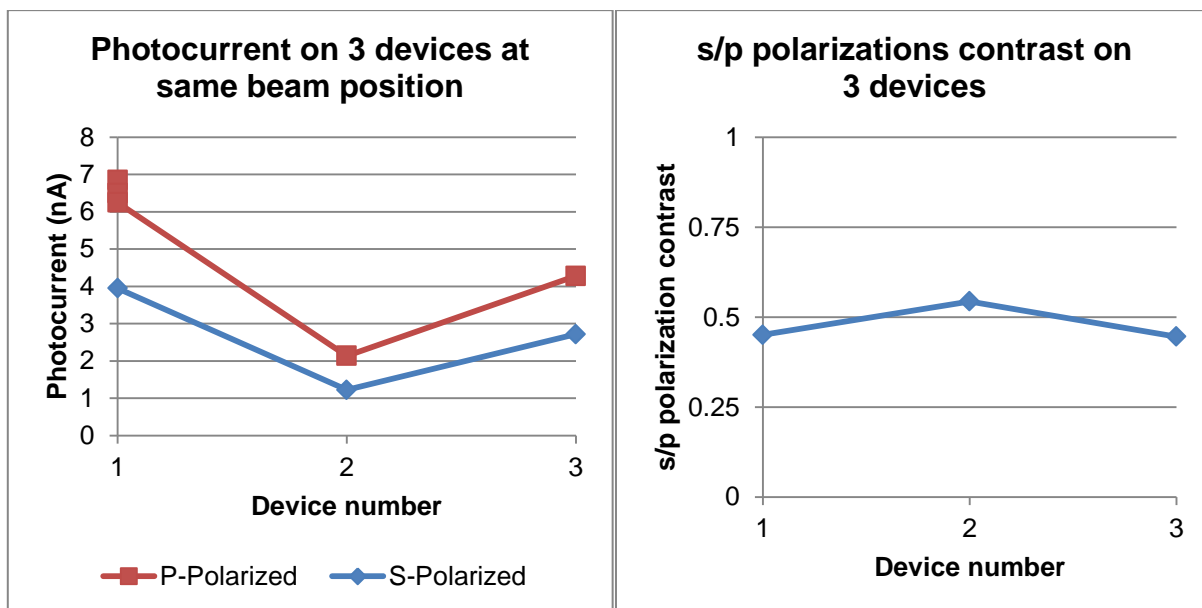


Fig. 158. Improve uniformity of coating: 3 devices have quite similar but still different performance.

As a conclusion we have determined the optimal illumination parameters for randomly-oriented SWCNTs with small metallic content. The incidence plane has been shown to be indifferent but p-polarization is consistently more effective than s-polarization which is expected since p-polarization will penetrate the substrate better close to Brewster angle. We have verified a linear relation between light intensity and photocurrent with a small threshold (for one of the measured position, 13.6pA/mW -0.7pA for another 67pA/mW) and a quasi-linear relation with bias indicating that at 10mW optical power the impedance added in parallel is 30M Ω at this position. Hence photomodulation will be difficult to achieve as such. But since only a small part of the design is illuminated this could be improved. Furthermore the large position dependence indicates there are better photocurrent generating sites. At slow modulation the current is seen to vary very widely (almost +200%) against only 10% modulation at 130Hz. Hence for slow modulation optical control could be possible.

V.C) Clues for analysis and design

The full analysis of the photocurrent could not be carried out due to limited time. Although we expect the trends outlined here will be maintained, additional experimental parameters should be tested in particular using better suited laser wavelengths to improve the absolute value of the photocurrent, measuring the high-frequency response and depositing a gate over compatible samples to tune the CNTs bandgap. Temperature-dependent response would be interesting too, not for our final application, but it could help distinguish

contributions. Below we report a few directions that could be investigated to understand the physics of photocurrent response in CNTs and improve it and antenna designs that may be actuated optically. Again, due to limited time, this material is incomplete but provided as such here because it may help for future interpretation, analysis and design.

V.C.1) Photovoltaic current vs. Photothermoelectric current

There are competing sources in the photocurrent we observe. Interesting reviews can be found in [229] and [230], [231].

For semiconducting CNTs, distance from the charge separation position to the two electrodes may be sufficient to create a net current. A better response can be engineered by introducing asymmetric electrodes. A difference in workfunction can be used by contacting CNTs with two different metals such as titanium and palladium [232] or aluminum and palladium [233]. p-n junctions with CNTs as the hole acceptor and Si [30] or CdSe [234] as electron donor were also reported.

The photothermoelectric current observable in metallic CNTs is a rather fast process and the current generation is due to a difference in Seebeck (thermoelectric) coefficients between the CNTs and the metal of the electrodes. Scanning photocurrent microscopy shows clear maximums at the CNT-metal junctions with a current reversal in the middle of the gap [229], [202]–[205]. The response is polarization sensitive as also modeled in [205] and quite a fast process as the author claim no sign of cut-off seen up to 6 kHz using a lock-in amplifier.

Finally potential improvement of light sensitivity could be obtained by CNT decoration with gold nanoparticles [196] which has proved to enhance Raman response by large factors.

V.C.2) Antenna designs

These are a few ideas of planar agile antenna designs that may be fabricated with CNTs using the processes we established. They have not been simulated yet and the change in conductivity from the CNTs necessary to their operation needs to be assessed.

V.C.2.1) Tunable PIFA

A fully monolayer planar inverted-F antenna could be realized using the process for the CPW gaps with the shorting loop to the ground made of lattice-aligned CNTs or the fabrication process of the interdigitated samples with solution-deposited CNTs.

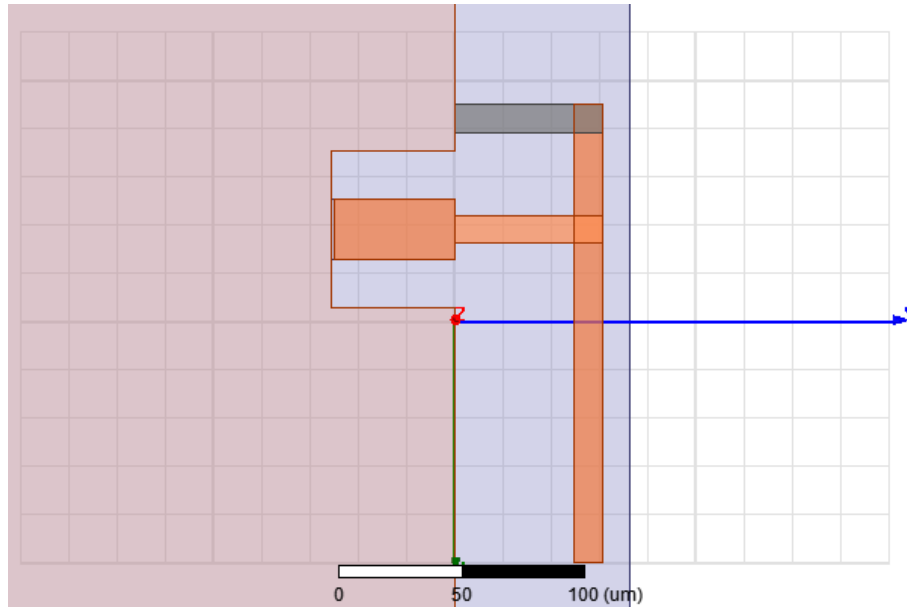


Fig. 159. Concept of a CPW-fed PIFA antenna with a horizontal CNT shorting loop realized by lattice-aligned CVD grown CNTs or spray-coated/inkjet-printed CNTs.

V.C.2.2) Rejection-band antenna

A trapezoidal monopole realizes an ultra-wide-band (UWB) antenna. By carving a slot in the monopole (cf. Fig. 160), an antiresonance peak can be created forming a notch rejection band in the otherwise UWB antenna. By covering this slot with a photoswitchable material, the rejection band could be activated or deactivated at will by optical control.

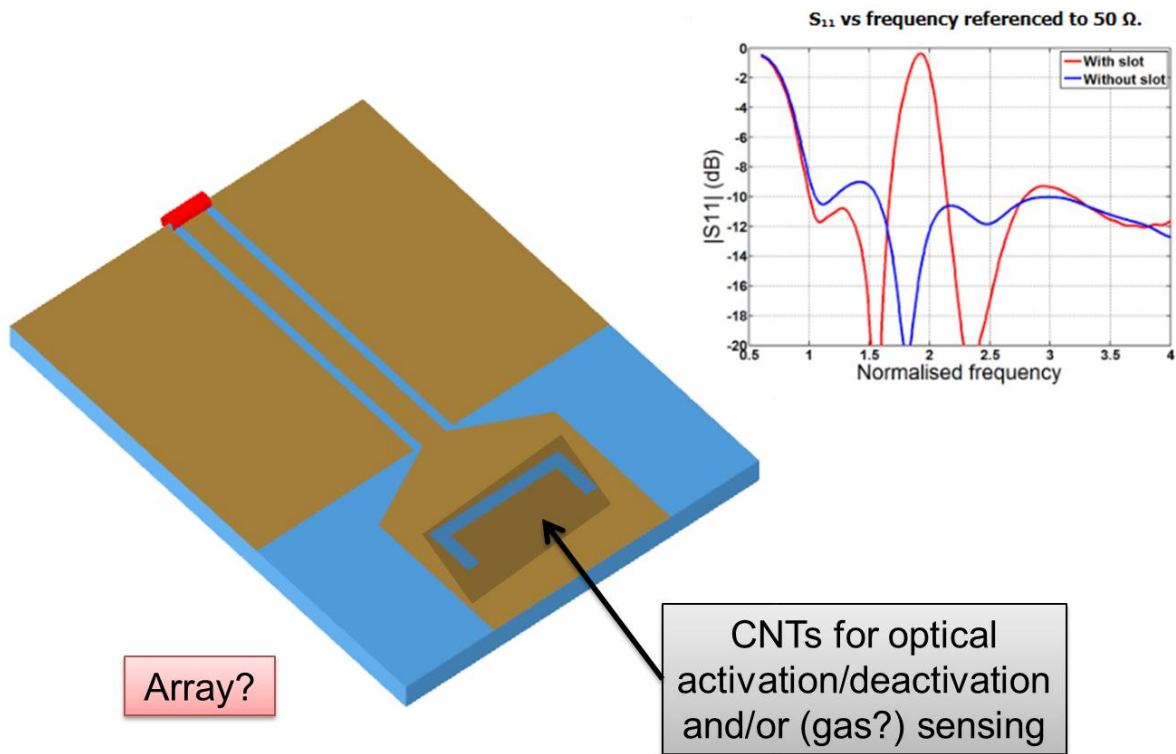


Fig. 160. Sprayed CNTs in the slot of a notched trapezoidal monopole (adapted from Antenna Magus online repository). The CNTs could allow switching on and off the notch filter.

V.C.2.3) Low profile corrugated antennas

Holographic antennas and bull's eye antennas are low profile corrugated antennas that allow well directed radiation from a planar geometry. By locally changing the conductivity of the groves one could imagine realizing beam-shifting without the need for an antenna array. This could be realized with spray-coated CNT groves if the photoresponse is sufficiently pronounced.

Chapter VI) Conclusion and outlook

VI.A) Summary of the main achievements

In this PhD project we set the ambitious goal of investigating the use of CNTs to design and fabricate short resonant antennas and optically-controlled antennas, starting only from models for a single metallic SWCNT and unperfected growth of vertical CNT arrays in a then one-year-old joint Singaporean-French laboratory on the campus of the still relatively young, but quickly evolving, dynamic and state-of-the-art-equipped Nanyang Technological University.

Significant progress has been made in the course of these three years. At start, simulation and fabrication capabilities dealt with almost unrelated cases – on one hand a single to a few metallic SWCNTs excited with a lumped port but not even connecting electrodes and, on the other hand, CNT ropes, unpatterned or large CNT arrays with hundreds to billions of CNTs that need to be contacted through micrometer-scale electrodes. We have now bridged the gap between modeling and fabrication techniques to an extent such that we could simulate and fabricate first measurable antenna prototypes.

This was possible in part thanks to the close collaboration with and training received from research students and staff in NTU specialized in CNT growth and microelectronics fabrication techniques. Knowing and practicing the existing fabrication processes allowed conceiving designs based on them while, as one of the main contributions of this PhD work, the mesoscopic model approach allowed modeling the numerous CNTs in fabricated structures while highlighting the only important local physical parameter: the average CNT density. Inhomogeneity at a scale below operating wavelength can be averaged and above this can be implemented as position dependent density. Therefore simulation requires infinitely less input than when CNTs were described singularly with their diameter and position.

If the initial move was to adapt the CNT model to the existing fabrication and characterization techniques, simulation of CNT-based antennas eventually pointed to fabrication requisites. A second major contribution of this PhD work was the development of latticed-aligned horizontal CNT growth on quartz substrate a technique that was not mastered or even in use in the laboratory. This was accompanied by a parametric study on catalyst

deposition methods to remedy to the issues the rest of the group faced with scarcely available e-beam-deposited iron catalyst of variable quality. State-of-the-art results have been obtained although additional refinement should be carried out.

A third achievement, building upon the two first ones, is the elaboration of a complete engineering toolbox for CNT-based resonant antenna design and the realization of first prototypes from design and simulation to fabrication and characterization.

Finally, characterization methods, physical models and antenna designs were identified for the development of CNT-based optically controlled agile antennas while optimal illumination parameters were determined experimentally. In the subsections below, we draw the main conclusions on each of these achievements and indicate possible perspectives.

VI.A.1) Modeling

We developed and adapted all necessary models for advanced engineering, design and simulation from the peculiar properties of carbon nanotubes and nanowires. Metallic SWCNTs were the focus of our work for the relative simplicity they provide compared to MWCNTs in terms of predictive design but models for semiconducting SWCNTs and MWCNTs have been established as well. Similarly the approach adopted for deriving the CNT model is fairly general and can be applied to many types of nanostructures. Although we lacked the time to explore this much, combined to the suited fabrication processes, it could help assess the interest of certain nanostructures as metamaterials. A few structures that could be modeled and on which experimental collaboration in Singapore is possible include: the SiNW-CNT hybrids we have developed, 3D graphene [235] as developed by Xiehong Cao et al. in NTU or suspended graphene on CNT scaffolds as developed by Sharon Xiaodai Lim [236] in NUS.

In the case of materials without a full theoretical model but correctly characterized our approach could help establish phenomenological models to then predict the effect of tuning densities, lengths and orientations in the nanostructure.

The CNT model could also benefit from a direct relation between remote material characterization such as Raman and the phenomenological constants of the model (plasmon

lifetime) to make quantitative assessment of CNTs rather than qualitative before or without the need for the fabrication of electrical contacts for direct measurement.

VI.A.2) Fabrication

We identified and developed a stable and repeatable growth technique for high quality horizontally aligned CNTs. We also demonstrated the use of varied sources of metal catalyst such as scratching, e-beam deposition and solution-based techniques. The process could benefit from some extra fine-tuning in particular to regulate the metallic to semiconducting CNT ratio. Spray-coating of solution-sorted CNTs was successfully implemented and would provide a scalable fabrication technique for photosensitive devices using shadow masks or photolithography to pattern the CNTs and metallic parts. Indeed the steps in the photolithography process were shown not to remove CNTs on the surface of the substrate.

VI.A.3) Design

Tools, rules and charts were established for electrically-short resonant CNT antennas. Some of the main rules follow. For a given plasmon lifetime τ , dependent on the CNT quality i.e. on the absence of defects and bends, $F_v = \frac{1}{2\pi\tau}$ is the minimum operating frequency to observe a size reduction and, for a limited number of CNTs, the losses become negligible for $f \geq \sqrt{10}F_v$. For $\tau = 3\text{ps}$, these limits are 53GHz and 168GHz. Common CVD CNTs may have τ three to ten times smaller and thus $F_v \sim 160 - 530\text{GHz}$ which highlights the necessity for very high quality CNTs unless prepared to work at THz frequencies which is coincidentally the domain where most CNT resonance studies have been reported in simulation and experiments and, with the reduction factor the plasmon wavelength conveniently corresponds to the lengths of solution-processed CNTs. As a rule of thumb, the size reduction only depends on the number of SWCNTs in the bundle and is about $50/\sqrt{N_{CNT}}$ while the resonance frequency varies as the inverse of CNT length and the square root of the number of CNTs i.e. $f_{res,bundle} \propto \frac{\sqrt{N_{CNT}}}{l_{CNT}}$ (the precise formula is slightly different cf. equation (168)), the input impedance varies as $Z_{in} \propto \frac{l_{CNT}}{N_{CNT}}$. With these tendencies it is clear that for a fixed size reduction and thus number of CNTs lower input impedances can be achieved at higher frequency.

Beyond this specific application, the tools we developed allow us to study varied structures of which the follow-up project initiated by Philippe Coquet, Philippe Ferrari, Florence Podevin and Dominique Baillargeat that should be investigated by Mathieu Cometto who is starting his PhD in CINTRA. The model is in use in CINTRA and XLIM as an assessment tool for various CNT-based structures [72].

VI.A.4) Optical control

The ideal illumination configuration has been determined as being an incident angle close to the Brewster angle and p-polarization to favor the penetration of light. If the CNTs are preferentially aligned along a direction then the light effect is polarization sensitive and, still hitting at Brewster angle and p-polarisation the incidence plane should be aligned with the CNT for maximum efficiency. Different fabrication techniques were analyzed, and a scalable spray-gun fabrication technique identified. Further investigation will need to be carried out on light wavelength dependence – 488nm and 1 μ m lasers should yield better efficiency than the 532nm CW laser used as the only available source then – and on RF and time-dependent photocurrent. Depending on their photosensitivity CNTs could be used either as photoactivable cells or as loading of classical metallic radiators and in this second case the response could be enhanced through multimaterial junctions that are better suited for photocurrent generation.

VI.B) Conclusions on CNT-based antennas

Electrically-short resonant CNT antennas do provide a gain in performance for niche applications where the size reduction is necessary despite already physically small antennas at operating frequencies above 100GHz. The gain in radiation over classical electrically-short CNT antennas is only 1.6 (+2dB) but the fact that these antennas are resonant and thus have a real input impedance at resonance allows designing impedance-matched feeds which is difficult to attain for conventional electrically-short dipoles. Therefore the realized gain (power radiated/power at the terminal) can be quite well improved.

They are also an interesting solution for wireless connection of nano-elements and nanodevices to classical microelectronics where ohmic contact is not appropriated and realize an interesting impedance transformation through free-space transmission. They could be directly fabricated as part of the nanodevice. In this case, as we have proposed, arrays of

remotely-interrogated nanosensors could be fabricated for biological sampling for instance then scanned by a tiny hovering horn antenna or similar. High-density on chip communication could also be an application [191], [192].

The design of these resonant antennas is however challenging in terms of both modeling and fabrication considerations. This led us to develop advanced tools and know-hows on nanostructures EM and circuit modeling, CNT growth and CNT-based fabrication processes – a toolbox that can now be applied to a broad range of applications.

Future work on electrically-short CNT antennas should be focused on integrating the antennas with suitable nanodevices on one hand and designing more advanced structures such as potentially super-resolved array antennas on the other hand. Future work on optical control will include the realization of classical antennas and array antennas with a photosensitive area using low-cost flexible substrates such as Kapton and low-cost scalable processes such as spray-coating with shadow masks and inkjet printing. An exciting perspective lies in the fabrication of antennas using CNT arrays as a substrate for miniaturization relying only on the metallic nature of the CNTs and their anisotropy. Departing from the initial antenna applications, there is huge potential for CNTs in RF and THz electromagnetics or even optics using their specific anisotropy in aligned arrays and the dependence of their electrical and optical properties on their number of walls, density and chirality – when these can be controlled.

VI.C) Outlook on related slow-wave technologies

VI.C.1) Metamaterial substrate

In electrically-short resonant CNT antennas we were using the increased inductance from the kinetic inductance to decrease the propagation speed along a transmission line i.e., recalling equation (144):

$$v_p = \frac{\omega}{\beta} = \frac{1}{\sqrt{LC}} \sqrt{\frac{2}{1 + \sqrt{1 + \left(\frac{R}{\omega L}\right)^2}}} \approx \left(\frac{R}{\omega L}\right)^2 \ll 1 \frac{1}{\sqrt{LC}} \quad (182)$$

Reducing the phase velocity allows reducing the size of components. In the low-loss approximation the expression of v_p is symmetric in L and C . Hence artificially increasing C or L by manipulating the substrate properties would have the same slow-wave effect.

VI.C.2) Graphene and hybrid structures

Graphene shares the slow-wave propagation property of CNTs and has certain advantages over them in particular the better contact for planar electronics and its sheet like configuration that makes it preferable to aligned CNT strips in certain configurations as the CNTs density may vary. It is investigated for THz antennas and arrays in a few groups [66], [68], [69], [83], [193], [237]–[239]. Hybrid structures like graphene suspended on CNT pillars [236] could also be an interesting path.

Bibliography

Personal publications (17)

First author of 12 publications:

Two journal papers:

[71] P. Franck, D. Baillargeat, and B. K. Tay, "Mesoscopic Model for the Electromagnetic Properties of Arrays of Nanotubes and Nanowires: A Bulk Equivalent Approach," *IEEE Trans. Nanotechnol.*, vol. 11, no. 5, pp. 964–974, Sep. 2012.

[168] P. Franck, D. Baillargeat, and B. K. Tay, "Carbon-nanotube-based electrically-short resonant antennas," *Int. J. Microw. Wirel. Technol.*, in press, 2013.

Six publications in international symposia with online proceedings (IEEE and SPIE):

[88] P. Franck, C. Brun, C. C. Yap, D. Tan, E. H. T. Teo, S. Bila, D. Baillargeat, et B. K. Tay, « Plasmon Resonances of Carbon-nanotube-based Dipole Antennas for Nano-Interconnects », in *Electronics Packaging Technology Conference, 2011. EPTC 2011.*, Singapore, 2011, p. 242-245.

[89] P. Franck, D. Baillargeat, and B. K. Tay, "Trade-offs in Designing Antennas from Bundled Carbon Nanotubes," in *Microwave Symposium Digest (MTT), 2012 IEEE MTT-S International*, Montréal, Canada, 2012.

[179] P. Franck, D. Baillargeat, et B. K. Tay, « Designing carbon-nanotube-based millimeter to sub-millimeter antennas », in *IEEE International Topical Symposium on RF Nanotechnology 2012*, Singapore, 2012.

[189] P. Franck, D. Baillargeat, and B. K. Tay, "Performance assessment of optimized carbon-nanotube-based wireless on-chip communication," in *SPIE Optics and Photonics 2012: Nanoscience and Engineering*, San Diego, USA, 2012, vol. 8462.

[190] P. Franck, D. Baillargeat, and B. K. Tay, "Design and Assessment of Carbon-nanotube-based Remote Links to Nanodevices," in *Microwave Symposium Digest (MTT), 2013 IEEE MTT-S International*, Seattle, USA, 2013.

[240] P. Franck, C. C. Yap, C. Brun, S. Pacchini, W. L. Chow, H. Li, D. Baillargeat, and B. K. Tay, “Carbon-nanotube-based RF components with multiple applications,” in *Wireless Symposium Digest (MTT), 2013 IEEE MTT-S International*, Beijing, China, 2013.

of which two invited [179], [240], three accepted as oral [88], [89], [189] and one accepted as poster [190]. Presented [88], [89], [179], [189] in Singapore, Montreal and San Diego.

Three communications in international symposia (MRS):

[188] P. Franck, D. Baillargeat, and B. K. Tay, “Parametric Study of Realistic Carbon-nanotube-based Electrically-short Resonant Antennas,” in *International Conference of Young Researchers on Advanced Materials, IUMRS-ICYRAM 2012*, Singapore, 2012.

[201] P. Franck, Z. Wang, D. Baillargeat, C. Soci, and B. K. Tay, “Photocurrent Study of Locally Grown and Solution-deposited Carbon Nanotubes,” in *International Conference on Materials for Advanced Technologies, MRS, ICMAT 2013*, Singapore, 2013, vol. Symposium G: Carbon Nanotubes and Graphene: Synthesis, Functionalisation and Applications, p. ICMAT13–A–2309.

[72] P. Franck, C. Brun, W. Chow, C. X. Lu, D. Tan, H. Li, D. Baillargeat, and B. K. Tay, “Applications of a Mesoscopic Electromagnetic Model for Carbon Nanotubes Arrays,” in *International Conference on Materials for Advanced Technologies, MRS, ICMAT 2013*, Singapore, 2013, vol. Symposium G: Carbon Nanotubes and Graphene: Synthesis, Functionalisation and Applications, p. ICMAT13–A–2338.

of which two presented as orals [72], [201] and one as poster [188].

One publication in national symposium (JNM) with proceedings:

[167] P. Franck, D. Baillargeat, and B. K. Tay, “Antennes électriquement courtes à base de nanotubes de carbone,” in *18èmes Journées Nationales Microondes*, Paris, 2013.

Second author of 4 publications:

Three publications in international symposiums with proceedings (IEEE):

[110] C. Brun, P. Franck, C. C. Yap, D. Tan, E. H. T. Teo, S. Bila, D. Baillargeat, and B. K. Tay, “Hybrid EM/Circuit Modeling for Carbon Nanotubes based Interconnects,” in *Electronics Packaging Technology Conference, 2011. EPTC 2011.*, Singapore, 2011.

[172] C. Brun, P. Franck, P. Coquet, D. Baillargeat, and B. K. Tay, “Monopole Antenna based on Carbon Nanotubes,” in *Microwave Symposium Digest (MTT), 2013 IEEE MTT-S International*, Seattle, USA, 2013.

[173] C. Brun, P. Franck, P. Coquet, D. Baillargeat, and B. K. Tay, “Horizontal and vertical carbon-nanotube-array-based antenna designs,” in *Microwave Conference, 2013. European*, Nuremberg, Germany, 2013.

of which one invited [173].

One publication in national symposium (JNM) with proceedings:

[241] C. Brun, P. Franck, P. Coquet, D. Baillargeat, and B. K. Tay, “Antennes Monopoles à base de Nanotubes de Carbone,” in *18èmes Journées Nationales Microondes*, 2013.

Co-author of 1 invited publication:

[242] C. C. Yap, D. Tan, C. Brun, P. Franck, H. Li, E. H. T. Teo, D. Baillargeat, and B. K. Tay, “Carbon Based Nanotechnologies Dedicated to High Frequency Applications,” in *IEEE 4th International Nanoelectronics Conference (INEC), 2011*, Chang Gung University, Tao-Yuan, Taiwan, 2011.

Bibliography

- [1] A. D. Franklin, M. Luisier, S.-J. Han, G. Tulevski, C. M. Breslin, L. Gignac, M. S. Lundstrom, et W. Haensch, « Sub-10 nm Carbon Nanotube Transistor », *Nano Lett.*, vol. 12, n° 2, p. 758-762, 2012.
- [2] F. Kreupl, « Electronics: Carbon nanotubes finally deliver », *Nature*, vol. 484, n° 7394, p. 321-322, avr. 2012.
- [3] M. M. Shulaker, G. Hills, N. Patil, H. Wei, H.-Y. Chen, H.-S. P. Wong, et S. Mitra, « Carbon nanotube computer », *Nature*, vol. 501, n° 7468, p. 526-530, sept. 2013.
- [4] S. Bae, H. Kim, Y. Lee, X. Xu, J.-S. Park, Y. Zheng, J. Balakrishnan, T. Lei, H. Ri Kim, Y. I. Song, Y.-J. Kim, K. S. Kim, B. Özyilmaz, J.-H. Ahn, B. H. Hong, et S. Iijima, « Roll-to-roll production of 30-inch graphene films for transparent electrodes », *Nat. Nanotechnol.*, vol. 5, n° 8, p. 574-578, août 2010.
- [5] T. Kobayashi, M. Bando, N. Kimura, K. Shimizu, K. Kadono, N. Umezū, K. Miyahara, S. Hayazaki, S. Nagai, Y. Mizuguchi, Y. Murakami, et D. Hōbara, « Production of a 100-m-long high-quality graphene transparent conductive film by roll-to-roll chemical vapor deposition and transfer process », *Appl. Phys. Lett.*, vol. 102, n° 2, p. 023112, janv. 2013.
- [6] P. Pasanen, M. Voutilainen, M. Helle, X. Song, et P. J. Hakonen, « Graphene for future electronics », *Phys. Scr.*, vol. 2012, n° T146, p. 014025, janv. 2012.
- [7] G. Y. Slepyan, S. A. Maksimenko, A. Lakhtakia, O. Yevtushenko, et A. V. Gusakov, « Electrodynamics of carbon nanotubes: Dynamic conductivity, impedance boundary conditions, and surface wave propagation », *Phys. Rev. B*, vol. 60, n° 24, p. 17136, déc. 1999.
- [8] P. J. Burke, « Luttinger liquid theory as a model of the gigahertz electrical properties of carbon nanotubes », *IEEE Trans. Nanotechnol.*, vol. 1, n° 3, p. 129-144, sept. 2002.
- [9] L. Nougaret, G. Dambrine, S. Lepilliet, H. Happy, N. Chimot, V. Derycke, et J.-P. Bourgoin, « Gigahertz characterization of a single carbon nanotube », *Appl. Phys. Lett.*, vol. 96, n° 4, p. 042109, 2010.

- [10] G. W. Hanson, « Fundamental transmitting properties of carbon nanotube antennas », *IEEE Trans. Antennas Propag.*, vol. 53, n° 11, p. 3426- 3435, nov. 2005.
- [11] C. Lan, P. Srisungsitthisunti, P. B. Amama, T. S. Fisher, X. Xu, et R. G. Reifenberger, « Measurement of metal/carbon nanotube contact resistance by adjusting contact length using laser ablation », *Nanotechnology*, vol. 19, p. 125703, mars 2008.
- [12] H. Yordanov et P. Russer, « Wireless inter-chip and intra-chip communication », in *Microwave Conference, 2009. EuMC 2009. European*, 2009, p. 145–148.
- [13] I. A. Levitsky et W. B. Euler, « Photoconductivity of single-wall carbon nanotubes under continuous-wave near-infrared illumination », *Appl. Phys. Lett.*, vol. 83, n° 9, p. 1857-1859, sept. 2003.
- [14] D.-H. Lien, W.-K. Hsu, H.-W. Zan, N.-H. Tai, et C.-H. Tsai, « Photocurrent Amplification at Carbon Nanotube–Metal Contacts », *Adv. Mater.*, vol. 18, n° 1, p. 98–103, 2006.
- [15] Y. Liu, S. Lu, et B. Panchapakesan, « Alignment enhanced photoconductivity in single wall carbon nanotube films », *Nanotechnology*, vol. 20, n° 3, p. 035203, janv. 2009.
- [16] P. J. Burke, Shengdong Li, et Zhen Yu, « Quantitative theory of nanowire and nanotube antenna performance », *IEEE Trans. Nanotechnol.*, vol. 5, n° 4, p. 314-334, juill. 2006.
- [17] J. Hao et G. W. Hanson, « Electromagnetic scattering from finite-length metallic carbon nanotubes in the lower IR bands », *Phys. Rev. B*, vol. 74, n° 3, p. 035119, juill. 2006.
- [18] G. Y. Slepian, M. V. Shuba, S. A. Maksimenko, et A. Lakhtakia, « Theory of optical scattering by achiral carbon nanotubes and their potential as optical nanoantennas », *Phys. Rev. B*, vol. 73, n° 19, p. 195416, mai 2006.
- [19] M. V. Shuba, S. A. Maksimenko, et A. Lakhtakia, « Electromagnetic wave propagation in an almost circular bundle of closely packed metallic carbon nanotubes », *Phys. Rev. B*, vol. 76, n° 15, p. 155407, oct. 2007.
- [20] M. V. Shuba, G. Y. Slepian, S. A. Maksimenko, C. Thomsen, et A. Lakhtakia, « Theory of multiwall carbon nanotubes as waveguides and antennas in the infrared and the visible regimes », *Phys. Rev. B*, vol. 79, n° 15, p. 155403, avr. 2009.
- [21] J. Werth et S. O'Donnell, « Carbon Nanotubes for Small Antennas », 2007. [En ligne]. Disponible sur: <http://www.mitre.org/news/events/tech07/2666.pdf>. [Consulté le: 07-mars-2013].
- [22] J. Werth, S. O'Donnell, D. Lamensdorf, J. Marshall, et L. Teig, « Carbon nanotube-based electronic devices », US8013247 B206-sept-2011.
- [23] S. Demoustier, E. Minoux, M. Le Baillif, M. Charles, et A. Ziaei, « Review of two microwave applications of carbon nanotubes: nano-antennas and nano-switches 10.1016/j.crhy.2008.01.001 : Comptes Rendus Physique | ScienceDirect.com », *Comptes Rendus Phys.*, vol. 9, n° 1, p. 53-66, janv. 2008.
- [24] J. Chazelas, D. Decoster, M. Zegaoui, E. H. Dogheche, C. Canseliet, et J. Martinaud, « Electronic scanning antenna composed of a network of two-dimensional radiating nano elements », EP234157907-juin-2011.
- [25] P. J. Burke et C. Rutherglen, « CARBON NANOTUBE BASED VARIABLE FREQUENCY PATCH-ANTENNA », 17-sept-2009.
- [26] A. S. Biris, H. M. Al-Rizzo, T. Elwi, et D. Rucker, « Nano and micro based antennas and sensors and methods of making same », *Pat. Appl.*, n° 20100097273, avr. 2010.
- [27] M. Voutilainen, E. T. Seppala, P. Pasanen, et M. Oksanen, « Graphene and Carbon Nanotube Applications in Mobile Devices », *IEEE Trans. Electron Devices*, vol. 59, n° 11, p. 2876-2887, 2012.
- [28] « Samsung funds graphene antenna project for wireless, ultra-fast intra-chip links | ExtremeTech », *ExtremeTech*. [En ligne]. Disponible sur: <http://www.extremetech.com/extreme/149172-samsung-funds-graphene-antenna-project-for-wireless-ultra-fast-intra-chip-links>. [Consulté le: 24-juill-2013].
- [29] S. Iijima, « Helical microtubules of graphitic carbon », *Nature*, vol. 354, n° 6348, p. 56-58, nov. 1991.
- [30] J. Wei, Y. Jia, Q. Shu, Z. Gu, K. Wang, D. Zhuang, G. Zhang, Z. Wang, J. Luo, A. Cao, et D. Wu, « Double-Walled Carbon Nanotube Solar Cells », *Nano Lett.*, vol. 7, n° 8, p. 2317-2321, 2007.
- [31] I. Robel, B. A. Bunker, et P. V. Kamat, « Single-Walled Carbon Nanotube–CdS Nanocomposites as Light-Harvesting Assemblies: Photoinduced Charge-Transfer Interactions », *Adv. Mater.*, vol. 17, n° 20, p. 2458-2463, oct. 2005.
- [32] W. B. Choi, D. S. Chung, J. H. Kang, H. Y. Kim, Y. W. Jin, I. T. Han, Y. H. Lee, J. E. Jung, N. S. Lee, G. S. Park, et J. M. Kim, « Fully sealed, high-brightness carbon-nanotube field-emission display », *Appl. Phys. Lett.*, vol. 75, n° 20, p. 3129-3131, 1999.
- [33] A. Bianco, K. Kostarelos, et M. Prato, « Applications of carbon nanotubes in drug delivery », *Curr. Opin. Chem. Biol.*, vol. 9, n° 6, p. 674-679, déc. 2005.
- [34] C. Rutherglen, D. Jain, et P. Burke, « Nanotube electronics for radiofrequency applications », *Nat Nano*, vol. 4, n° 12, p. 811-819, déc. 2009.

- [35] J.-O. J. Wesström, « Signal propagation in electron waveguides: Transmission-line analogies », *Phys. Rev. B*, vol. 54, n° 16, p. 11484-11491, oct. 1996.
- [36] R. Zhang, Y. Zhang, Q. Zhang, H. Xie, W. Qian, et F. Wei, « Growth of Half-Meter Long Carbon Nanotubes Based on Schulz–Flory Distribution », *ACS Nano*, juin 2013.
- [37] S. A. Getty, M. Li, L. Hess, N. Costen, T. T. King, P. A. Roman, W. B. Brinckerhoff, et P. R. Mahaffy, « Integration of a carbon nanotube field emission electron gun for a miniaturized time-of-flight mass spectrometer », 2009, p. 731816-731816-14.
- [38] N. G. Shang, Y. Y. Tan, V. Stolojan, P. Papakonstantinou, et S. R. P. Silva, « High-rate low-temperature growth of vertically aligned carbon nanotubes », *Nanotechnology*, vol. 21, n° 50, p. 505604, déc. 2010.
- [39] G. Y. Chen, B. Jensen, V. Stolojan, et S. R. P. Silva, « Growth of carbon nanotubes at temperatures compatible with integrated circuit technologies », *Carbon*, vol. 49, n° 1, p. 280-285, janv. 2011.
- [40] J. J. Butler, G. T. Georgiev, J. L. Tveekrem, M. Quijada, S. Getty, et J. G. Hagopian, « Initial studies of the bidirectional reflectance distribution function of carbon nanotube structures for stray light control applications », in *Proceedings of SPIE*, 2010, p. 78620D-78620D-16.
- [41] J. G. Hagopian, S. A. Getty, M. Quijada, J. Tveekrem, R. Shiri, P. Roman, J. Butler, G. Georgiev, J. Livas, C. Hunt, A. Maldonado, S. Talapatra, X. Zhang, S. J. Papadakis, A. H. Monica, et D. Deglau, « Multiwalled carbon nanotubes for stray light suppression in space flight instruments », in *Proceedings of SPIE*, 2010, p. 77610F-77610F-10.
- [42] M. A. Quijada, J. G. Hagopian, S. Getty, R. E. Kinzer, Jr., et E. J. Wollack, « Hemispherical reflectance and emittance properties of carbon nanotubes coatings at infrared wavelengths », in *Proceedings of SPIE*, 2011, p. 815002-815002-11.
- [43] S. M. Bachilo, M. S. Strano, C. Kittrell, R. H. Hauge, R. E. Smalley, et R. B. Weisman, « Structure-Assigned Optical Spectra of Single-Walled Carbon Nanotubes », *Science*, vol. 298, n° 5602, p. 2361-2366, déc. 2002.
- [44] R. B. Weisman et S. M. Bachilo, « Dependence of Optical Transition Energies on Structure for Single-Walled Carbon Nanotubes in Aqueous Suspension: An Empirical Kataura Plot », *Nano Lett.*, vol. 3, n° 9, p. 1235-1238, sept. 2003.
- [45] J. Lefebvre, S. Maruyama, et P. Finnie, « Photoluminescence: Science and Applications », in *Carbon Nanotubes*, Springer Berlin Heidelberg, 2008, p. 287-319.
- [46] Q. Cao, S. Han, G. S. Tulevski, Y. Zhu, D. D. Lu, et W. Haensch, « Arrays of single-walled carbon nanotubes with full surface coverage for high-performance electronics », *Nat. Nanotechnol.*, vol. 8, n° 3, p. 180-186, janv. 2013.
- [47] C. Rutherglen et P. Burke, « Carbon Nanotube Radio », *Nano Lett.*, vol. 7, p. 3296-3299, nov. 2007.
- [48] K. Jensen, J. Weldon, H. Garcia, et A. Zettl, « Nanotube Radio », *Nano Lett.*, vol. 7, n° 11, p. 3508-3511, nov. 2007.
- [49] C. Kocabas, H. Kim, T. Banks, J. A. Rogers, A. A. Pesetski, J. E. Baumgardner, S. V. Krishnaswamy, et H. Zhang, « Radio frequency analog electronics based on carbon nanotube transistors », *Proc. Natl. Acad. Sci.*, vol. 105, n° 5, p. 1405-1409, févr. 2008.
- [50] Yijun Zhou, Y. Bayram, Feng Du, Liming Dai, et J. L. Volakis, « Polymer-Carbon Nanotube Sheets for Conformal Load Bearing Antennas », *IEEE Trans. Antennas Propag.*, vol. 58, n° 7, p. 2169-2175, juill. 2010.
- [51] T. A. Elwi, H. M. Al-Rizzo, D. G. Rucker, E. Dervishi, Z. Li, et A. S. Biris, « Multi-walled carbon nanotube-based RF antennas », *Nanotechnology*, vol. 21, p. 045301, janv. 2010.
- [52] A. Mehdipour, I. D. Rosca, A.-R. Sebak, C. W. Trueman, et S. V. Hoa, « Full-Composite Fractal Antenna Using Carbon Nanotubes for Multiband Wireless Applications », *IEEE Antennas Wirel. Propag. Lett.*, vol. 9, p. 891-894, 2010.
- [53] A. Mehdipour, I. D. Rosca, A.-R. Sebak, C. W. Trueman, et S. V. Hoa, « Carbon nanotube composites for wideband millimeter-wave antenna applications », *Antennas Propag. IEEE Trans. On*, vol. 59, n° 10, p. 3572-3578, 2011.
- [54] L. Yang, R. Zhang, D. Staiculescu, C. P. Wong, et M. M. Tentzeris, « A Novel Conformal RFID-Enabled Module Utilizing Inkjet-Printed Antennas and Carbon Nanotubes for Gas-Detection Applications », *IEEE Antennas Wirel. Propag. Lett.*, vol. 8, p. 653-656, 2009.
- [55] S. Li, Q. Zhu, et H. Xin, « Experimental research on the microwave properties of carbon nanotube array », in *2012 IEEE International Workshop on Antenna Technology (iWAT)*, 2012, p. 331-334.
- [56] Y. Wang, K. Kempa, B. Kimball, J. B. Carlson, G. Benham, W. Z. Li, T. Kempa, J. Rybczynski, A. Herczynski, et Z. F. Ren, « Receiving and transmitting light-like radio waves: Antenna effect in arrays of aligned carbon nanotubes », *Appl. Phys. Lett.*, vol. 85, n° 13, p. 2607, 2004.

- [57] K. Kempa, J. Rybczynski, Z. Huang, K. Gregorczyk, A. Vidan, B. Kimball, J. Carlson, G. Benham, Y. Wang, A. Herczynski, et Z. F. Ren, « Carbon Nanotubes as Optical Antennae », *Adv. Mater.*, vol. 19, n° 3, p. 421-426, févr. 2007.
- [58] M. F. Becker, A. B. Buckman, R. M. Walser, T. Lépine, P. Georges, et A. Brun, « Femtosecond laser excitation dynamics of the semiconductor-metal phase transition in VO₂ », *J. Appl. Phys.*, vol. 79, n° 5, p. 2404-2408, 1996.
- [59] M. Rini, A. Cavalleri, R. W. Schoenlein, R. López, L. C. Feldman, R. F. Haglund Jr, L. A. Boatner, et T. E. Haynes, « Photoinduced phase transition in VO₂ nanocrystals: ultrafast control of surface-plasmon resonance », *Opt. Lett.*, vol. 30, n° 5, p. 558-560, 2005.
- [60] S. B. Choi, J. S. Kyoung, H. S. Kim, H. R. Park, D. J. Park, B.-J. Kim, Y. H. Ahn, F. Rotermund, H.-T. Kim, K. J. Ahn, et D. S. Kim, « Nanopattern enabled terahertz all-optical switching on vanadium dioxide thin film », *Appl. Phys. Lett.*, vol. 98, n° 7, p. 071105, 2011.
- [61] M. Liu, H. Y. Hwang, H. Tao, A. C. Strikwerda, K. Fan, G. R. Keiser, A. J. Sternbach, K. G. West, S. Kittiwatanakul, J. Lu, S. A. Wolf, F. G. Omenetto, X. Zhang, K. A. Nelson, et R. D. Averitt, « Terahertz-field-induced insulator-to-metal transition in vanadium dioxide metamaterial », *Nature*, vol. 487, n° 7407, p. 345-348, juill. 2012.
- [62] C. Tripon-Canseliet, S. Faci, D. Decoster, A. Pagies, S. F. Yoon, K. L. Pey, et J. Chazelas, « Nano photoconductive switches for microwave applications », p. 863117-863117, févr. 2013.
- [63] J. Borghetti, V. Derycke, S. Lenfant, P. Chenevier, A. Filoramo, M. Goffman, D. Vuillaume, et J.-P. Bourgoin, « Optoelectronic Switch and Memory Devices Based on Polymer-Functionalized Carbon Nanotube Transistors », *Adv. Mater.*, vol. 18, n° 19, p. 2535-2540, 2006.
- [64] A. Georgiadis, A. Collado, et J. Perruisseau-Carrier, « Patents on reconfigurable reflectarray antennas », *Recent Pat. Electr. Eng.*, vol. 2, n° 1, 2009.
- [65] S. V. Hum et J. Perruisseau-Carrier, « Reconfigurable Reflectarrays and Array Lenses for Dynamic Antenna Beam Control: A Review », *IEEE Trans. Antennas Propag.*, vol. 62, n° 1, p. 183-198, janv. 2014.
- [66] Y. Huang, Lin-Sheng Wu, Min Tang, et Junfa Mao, « Design of a Beam Reconfigurable THz Antenna With Graphene-Based Switchable High-Impedance Surface », *IEEE Trans. Nanotechnol.*, vol. 11, n° 4, p. 836-842, juill. 2012.
- [67] M. Esquiús-Morote, J. S. Gomez-Diaz, et J. Perruisseau-Carrier, « Sinusoidally Modulated Graphene Leaky-Wave Antenna for Electronic Beamscanning at THz », *IEEE Trans. Terahertz Sci. Technol.*, vol. 4, n° 1, p. 116-122, 2014.
- [68] E. Carrasco, M. Tamagnone, et J. Perruisseau-Carrier, « Tunable graphene reflective cells for THz reflectarrays and generalized law of reflection », *Appl. Phys. Lett.*, vol. 102, n° 10, p. 104103, mars 2013.
- [69] E. Carrasco et J. Perruisseau-Carrier, « Reflectarray Antenna at Terahertz Using Graphene », *IEEE Antennas Wirel. Propag. Lett.*, vol. 12, p. 253-256, 2013.
- [70] L. Pierantoni, « RF Nanotechnology-Concept, Birth, Mission, and Perspectives [Member Benefits] », *IEEE Microw. Mag.*, vol. 11, n° 4, p. 130-137, 2010.
- [71] P. Franck, D. Baillargeat, et B. K. Tay, « Mesoscopic Model for the Electromagnetic Properties of Arrays of Nanotubes and Nanowires: A Bulk Equivalent Approach », *IEEE Trans. Nanotechnol.*, vol. 11, n° 5, p. 964-974, sept. 2012.
- [72] P. Franck, C. Brun, W. Chow, C. X. Lu, D. Tan, H. Li, D. Baillargeat, et B. K. Tay, « Applications of a Mesoscopic Electromagnetic Model for Carbon Nanotubes Arrays », in *International Conference on Materials for Advanced Technologies, MRS, ICMAT 2013*, Singapore, 2013, vol. Symposium G: Carbon Nanotubes and Graphene: Synthesis, Functionalisation and Applications, p. ICMAT13-A-2338.
- [73] J. M. Soler, E. Artacho, J. D. Gale, A. García, J. Junquera, P. Ordejón, et D. Sánchez-Portal, « The SIESTA method for ab initio order-N materials simulation », *J. Phys. Condens. Matter*, vol. 14, n° 11, p. 2745, mars 2002.
- [74] S. Uck et Y. Kawazoe, « Nanodesign and Simulation Toward Nanoelectronic Devices », in *Carbon Nanotubes Applications on Electron Devices*, J. M. Marulanda, Éd. InTech, 2011.
- [75] K. Stokbro, J. Taylor, M. Brandbyge, et P. Ordejón, « TranSIESTA: A Spice for Molecular Electronics », *Ann. N. Y. Acad. Sci.*, vol. 1006, n° 1, p. 212-226, 2003.
- [76] M. Gajdoš, K. Hummer, G. Kresse, J. Furthmüller, et F. Bechstedt, « Linear optical properties in the projector-augmented wave methodology », *Phys. Rev. B*, vol. 73, n° 4, p. 045112, janv. 2006.
- [77] E. Runge et E. K. U. Gross, « Density-Functional Theory for Time-Dependent Systems », *Phys. Rev. Lett.*, vol. 52, n° 12, p. 997-1000, mars 1984.
- [78] L. Pierantoni, D. Mencarelli, et T. Rozzi, « A New 3-D Transmission Line Matrix Scheme for the Combined Schrödinger-Maxwell Problem in the Electronic/Electromagnetic Characterization of Nanodevices », *IEEE Trans. Microw. Theory Tech.*, vol. 56, n° 3, p. 654-662, mars 2008.

- [79] L. Pierantoni, D. Mencarelli, et T. Rozzi, « Boundary Immittance Operators for the Schrödinger–Maxwell Problem of Carrier Dynamics in Nanodevices », *IEEE Trans. Microw. Theory Tech.*, vol. 57, n° 5, p. 1147-1155, mai 2009.
- [80] W. Sui, J. Yang, X. H. Yun, et C. Wang, « Including Quantum Effects in Electromagnetic System—An FDTD Solution to Maxwell-Schrödinger Equations », in *Microwave Symposium, 2007. IEEE/MTT-S International*, 2007, p. 1979-1982.
- [81] I. Ahmed, E. H. Khoo, E. Li, et R. Mittra, « A Hybrid Approach for Solving Coupled Maxwell and Schrödinger Equations Arising in the Simulation of Nano-Devices », *IEEE Antennas Wirel. Propag. Lett.*, vol. 9, p. 914-917, 2010.
- [82] T. Takeuchi, S. Ohnuki, T. Sako, Y. Ashizawa, K. Nakagawa, et M. Tanaka, « Efficient Hybrid Simulation for Maxwell-Schrödinger Problems », in *Electromagnetic Theory (EMTS), Proceedings of 2013 URSI International Symposium on*, 2013, p. 1058-1060.
- [83] L. Pierantoni, D. Mencarelli, et F. Coccetti, « Graphene-based wireless communications systems: Analysis of the EM-quantum transport of coupled nano-patch antennas », in *2013 IEEE Wireless Power Transfer (WPT)*, 2013, p. 66-68.
- [84] S. M. Mikki et A. A. Kishk, « Mean-Field Electrodynamics Theory of Aligned Carbon Nanotube Composites », *IEEE Trans. Antennas Propag.*, vol. 57, n° 5, p. 1412-1419, mai 2009.
- [85] I. S. Nefedov et S. A. Tretyakov, « Effective medium model for two-dimensional periodic arrays of carbon nanotubes », *Photonics Nanostructures - Fundam. Appl.*, vol. 9, n° 4, p. 374-380, oct. 2011.
- [86] J. W. G. Wilder, L. C. Venema, A. G. Rinzler, R. E. Smalley, et C. Dekker, « Electronic structure of atomically resolved carbon nanotubes », *Nature*, vol. 391, n° 6662, p. 59-62, janv. 1998.
- [87] G. W. Hanson, « A Common Electromagnetic Framework for Carbon Nanotubes and Solid Nanowires—Spatially Dispersive Conductivity, Generalized Ohm’s Law, Distributed Impedance, and Transmission Line Model », *IEEE Trans. Microw. Theory Tech.*, vol. 59, n° 1, p. 9-20, janv. 2011.
- [88] P. Franck, C. Brun, C. C. Yap, D. Tan, E. Teo, S. Bila, D. Baillargeat, et B. K. Tay, « Plasmon Resonances of Carbon-nanotube-based Dipole Antennas for Nano-Interconnects », in *Electronics Packaging Technology Conference, 2011. EPTC 2011. Singapore*, 2011, p. 242-245.
- [89] P. Franck, D. Baillargeat, et B. K. Tay, « Trade-offs in Designing Antennas from Bundled Carbon Nanotubes », in *Microwave Symposium Digest (MTT), 2012 IEEE MTT-S International*, Montréal, Canada, 2012.
- [90] « ANSYS HFSS ». [En ligne]. Disponible sur: <http://www.ansoft.com/products/hf/hfss/>. [Consulté le: 19-oct-2011].
- [91] M. P. A. Fisher et L. I. Glazman, « Transport in a One-Dimensional Luttinger Liquid », in *Mesoscopic Electron Transport*, L. L. Sohn, L. P. Kouwenhoven, et G. Schön, Éd. Springer Netherlands, 1997, p. 331-373.
- [92] M. Buttiker et T. Christen, « Admittance and nonlinear transport in quantum wires, point contacts, and resonant tunneling barriers », in *Mesoscopic Electron Transport*, vol. 345, 1997, p. 259-289.
- [93] M. Bockrath, D. H. Cobden, J. Lu, A. G. Rinzler, R. E. Smalley, L. Balents, et P. L. McEuen, « Luttinger-liquid behaviour in carbon nanotubes », *Nature*, vol. 397, n° 6720, p. 598-601, févr. 1999.
- [94] M. W. Bockrath, « Carbon nanotubes: electrons in one dimension », University of California, 1999.
- [95] P. J. Burke, « Corrections to “Luttinger Liquid Theory as a Model of the Gigahertz Electrical Properties of Carbon Nanotubes” », *IEEE Trans. Nanotechnol.*, vol. 3, n° 2, p. 331-331, juin 2004.
- [96] A. Naeemi et J. D. Meindl, « Design and Performance Modeling for Single-Walled Carbon Nanotubes as Local, Semiglobal, and Global Interconnects in Gigascale Integrated Systems », *IEEE Trans. Electron Devices*, vol. 54, n° 1, p. 26-37, janv. 2007.
- [97] S. Haruehanroengra et Wei Wang, « Analyzing Conductance of Mixed Carbon-Nanotube Bundles for Interconnect Applications », *IEEE Electron Device Lett.*, vol. 28, n° 8, p. 756-759, août 2007.
- [98] M. S. Sarto, A. Tamburrano, et M. D’Amore, « New Electron-Waveguide-Based Modeling for Carbon Nanotube Interconnects », *IEEE Trans. Nanotechnol.*, vol. 8, n° 2, p. 214-225, mars 2009.
- [99] D. M. Pozar, « Microwave engineering », 3rd ed., Hoboken, NJ: J. Wiley, 2005.
- [100] « Advanced Design System (ADS) | Agilent ». [En ligne]. Disponible sur: <http://www.home.agilent.com/en/pc-1297113/advanced-design-system-ads?nid=-34346.0&cc=SG&lc=eng>. [Consulté le: 11-sept-2013].
- [101] S. Salahuddin, M. Lundstrom, et S. Datta, « Transport Effects on Signal Propagation in Quantum Wires », *IEEE Trans. Electron Devices*, vol. 52, n° 8, p. 1734-1742, août 2005.
- [102] Y. Matsuda, W.-Q. Deng, et W. A. Goddard, « Contact Resistance Properties between Nanotubes and Various Metals from Quantum Mechanics », *J. Phys. Chem. C*, vol. 111, n° 29, p. 11113-11116, juill. 2007.

- [103] Y. Matsuda, W.-Q. Deng, et W. A. Goddard, « Contact Resistance for “End-Contacted” Metal–Graphene and Metal–Nanotube Interfaces from Quantum Mechanics », *J. Phys. Chem. C*, vol. 114, n° 41, p. 17845 -17850, oct. 2010.
- [104] Y. Woo, G. S. Duesberg, et S. Roth, « Reduced contact resistance between an individual single-walled carbon nanotube and a metal electrode by a local point annealing », *Nanotechnology*, vol. 18, p. 095203, mars 2007.
- [105] Y. Chai, A. Hazeghi, K. Takei, H.-Y. Chen, P. C. H. Chan, A. Javey, et H.-S. P. Wong, « Low-Resistance Electrical Contact to Carbon Nanotubes With Graphitic Interfacial Layer », *IEEE Trans. Electron Devices*, vol. 59, n° 1, p. 12 -19, janv. 2012.
- [106] « TX-LINE: Transmission Line Calculator ». [En ligne]. Disponible sur: <http://www.awrcorp.com/products/optional-products/tx-line-transmission-line-calculator>. [Consulté le: 19-sept-2013].
- [107] H. Li, W.-Y. Yin, K. Banerjee, et J.-F. Mao, « Circuit Modeling and Performance Analysis of Multi-Walled Carbon Nanotube Interconnects », *IEEE Trans. Electron Devices*, vol. 55, n° 6, p. 1328-1337, 2008.
- [108] A. Naeemi et J. D. Meindl, « Compact physical models for multiwall carbon-nanotube interconnects », *IEEE Electron Device Lett.*, vol. 27, n° 5, p. 338-340, 2006.
- [109] Yue Wang, Yu Ming Wu, Lei Lei Zhuang, Shao Qing Zhang, Le Wei Li, et Qun Wu, « Electromagnetic performance of single walled carbon nanotube bundles », in *Microwave Conference, 2009. APMC 2009. Asia Pacific*, 2009, p. 190-193.
- [110] C. Brun, P. Franck, C. C. Yap, D. Tan, E. H. T. Teo, S. Bila, D. Baillargeat, et B. K. Tay, « Hybrid EM/Circuit Modeling for Carbon Nanotubes based Interconnects », in *Electronics Packaging Technology Conference, 2011. EPTC 2011.*, Singapore, 2011.
- [111] S. Tanachutiwat, « Carbon Nanotubes Interconnect Analyzer (CNIA) », 2009.
- [112] C. Rutherglen, D. Jain, et P. Burke, « rf resistance and inductance of massively parallel single walled carbon nanotubes: Direct, broadband measurements and near perfect 50 Ω impedance matching », *Appl. Phys. Lett.*, vol. 93, n° 8, p. 083119, 2008.
- [113] H. Li, C. Xu, N. Srivastava, et K. Banerjee, « Carbon Nanomaterials for Next-Generation Interconnects and Passives: Physics, Status, and Prospects », *IEEE Trans. Electron Devices*, vol. 56, p. 1799-1821, sept. 2009.
- [114] M. Zhang, X. Huo, P. C. H. Chan, Q. Liang, et Z. K. Tang, « Radio-frequency characterization for the single-walled carbon nanotubes », *Appl. Phys. Lett.*, vol. 88, n° 16, p. 163109, 2006.
- [115] J. J. Plombon, K. P. O'Brien, F. Gstrein, V. M. Dubin, et Y. Jiao, « High-frequency electrical properties of individual and bundled carbon nanotubes », *Appl. Phys. Lett.*, vol. 90, n° 6, p. 063106, 2007.
- [116] A. Tselev, M. Woodson, C. Qian, et J. Liu, « Microwave Impedance Spectroscopy of Dense Carbon Nanotube Bundles », *Nano Lett*, vol. 8, n° 1, p. 152-156, 2007.
- [117] Y. A. Kim, T. Hayashi, M. Endo, Y. Gotoh, N. Wada, et J. Seiyama, « Fabrication of aligned carbon nanotube-filled rubber composite », *Scr. Mater.*, vol. 54, n° 1, p. 31-35, janv. 2006.
- [118] V. Parkash et A. K. Goel, « Electrostatic capacitances for carbon nanotube interconnects », *Microw. Opt. Technol. Lett.*, vol. 51, n° 10, p. 2374-2378, oct. 2009.
- [119] Y. Huang, Wen-Yan Yin, et Qing Huo Liu, « Performance Prediction of Carbon Nanotube Bundle Dipole Antennas », *IEEE Trans. Nanotechnol.*, vol. 7, n° 3, p. 331-337, mai 2008.
- [120] I. Nefedov, « Electromagnetic waves propagating in a periodic array of parallel metallic carbon nanotubes », *Phys. Rev. B*, vol. 82, n° 15, p. 155423, oct. 2010.
- [121] G. Miano et F. Villone, « An Integral Formulation for the Electrodynamics of Metallic Carbon Nanotubes Based on a Fluid Model », *IEEE Trans. Antennas Propag.*, vol. 54, n° 10, p. 2713-2724, oct. 2006.
- [122] Y. Yang, C. Y. Tan, W. Q. Sun, W. Li, C. K. Ong, Y. Liu, Y. Li, et S. Y. Xu, « High frequency resistance of single-walled and multiwalled carbon nanotubes », *Appl. Phys. Lett.*, vol. 98, p. 093107, 2011.
- [123] Q. Zhu, W. Liu, H. Zhang, et H. Xin, « Experimental study of microwave radiation of carbon nanotube arrays », *Appl. Phys. Lett.*, vol. 95, p. 083119, 2009.
- [124] S. Choi et K. Sarabandi, « Performance Assessment of Bundled Carbon Nanotube for Antenna Applications at Terahertz Frequencies and Higher », *IEEE Trans. Antennas Propag.*, vol. 59, n° 3, p. 802 -809, mars 2011.
- [125] W. S. Weighofer, A. Lakhtakia, et B. Michel, « Maxwell Garnett and Bruggeman formalisms for a particulate composite with bianisotropic host medium », *Microw. Opt. Technol. Lett.*, vol. 15, n° 4, p. 263-266, juill. 1997.

- [126] R. Landauer, « Electrical conductivity in inhomogeneous media », *AIP Conf. Proc.*, vol. 40, n° 1, p. 2-45, avr. 1978.
- [127] J. A. Reynolds et J. M. Hough, « Formulae for Dielectric Constant of Mixtures », *Proc. Phys. Soc. Sect. B*, vol. 70, p. 769-775, août 1957.
- [128] F. J. García-Vidal, J. M. Pitarke, et J. B. Pendry, « Effective Medium Theory of the Optical Properties of Aligned Carbon Nanotubes », *Phys. Rev. Lett.*, vol. 78, n° 22, p. 4289, juin 1997.
- [129] Z. Han, D. Li, X. W. Wang, et Z. D. Zhang, « Microwave response of FeCo/carbon nanotubes composites », *J. Appl. Phys.*, vol. 109, p. 07A301, 2011.
- [130] Q. Zhang, S. Rastogi, D. Chen, D. Lippits, et P. J. Lemstra, « Low percolation threshold in single-walled carbon nanotube/high density polyethylene composites prepared by melt processing technique », *Carbon*, vol. 44, n° 4, p. 778-785, avr. 2006.
- [131] C. Geuzaine et J. Remacle, « Gmsh: A 3-D finite element mesh generator with built-in pre- and post-processing facilities », *Int. J. Numer. Methods Eng.*, vol. 79, n° 11, p. 1309-1331, sept. 2009.
- [132] C. A. Santini, A. Volodin, C. Van Haesendonck, S. De Gendt, G. Groeseneken, et P. M. Vereecken, « Carbon nanotube-carbon nanotube contacts as an alternative towards low resistance horizontal interconnects », *Carbon*, vol. 49, n° 12, p. 4004-4012, oct. 2011.
- [133] J.-O. Lee, C. Park, J.-J. Kim, J. Kim, J. W. Park, et K.-H. Yoo, « Formation of low-resistance ohmic contacts between carbon nanotube and metal electrodes by a rapid thermal annealing method », *J. Phys. Appl. Phys.*, vol. 33, p. 1953-1956, août 2000.
- [134] L. Ren, C. L. Pint, L. G. Booshehri, W. D. Rice, X. Wang, D. J. Hilton, K. Takeya, I. Kawayama, M. Tonouchi, R. H. Hauge, et J. Kono, « Carbon Nanotube Terahertz Polarizer », *Nano Lett.*, vol. 9, n° 7, p. 2610-2613, juill. 2009.
- [135] X. Lim, H. W. G. Foo, G. H. Chia, et C.-H. Sow, « Capillarity-Assisted Assembly of Carbon Nanotube Microstructures with Organized Initiations », *ACS Nano*, vol. 4, n° 2, p. 1067-1075, 2010.
- [136] R. Vyas, V. Lakafosis, A. Rida, N. Chaisilwattana, S. Travis, J. Pan, et M. M. Tentzeris, « Paper-Based RFID-Enabled Wireless Platforms for Sensing Applications », *IEEE Trans. Microw. Theory Tech.*, vol. 57, n° 5, p. 1370-1382, mai 2009.
- [137] A. Rida, L. Yang, R. Vyas, et M. M. Tentzeris, « Conductive Inkjet-Printed Antennas on Flexible Low-Cost Paper-Based Substrates for RFID and WSN Applications », *IEEE Antennas Propag. Mag.*, vol. 51, n° 3, p. 13-23, juin 2009.
- [138] H. Subbaraman, R. T. Hen, X. Lu, et M. Y. Chen, « Fully Printed, Flexible, Phased Array Antenna for Lunar Surface Communication », *NASA Tech Briefs July 2013*, juill. 2013.
- [139] K. Byun, H. Subbaraman, X. Lin, X. Xu, et R. T. Chen, « A 3µm channel, ink-jet printed CNT-TFT for phased array antenna applications », in *2013 Texas Symposium on Wireless and Microwave Circuits and Systems (WMCS)*, 2013, p. 1-3.
- [140] M. V. Shuba, A. G. Paddubskaya, P. P. Kuzhir, S. A. Maksimenko, V. K. Ksenevich, G. Niaura, D. Seliuta, I. Kasalynas, et G. Valusis, « Soft cutting of single-wall carbon nanotubes by low temperature ultrasonication in a mixture of sulfuric and nitric acids », *Nanotechnology*, vol. 23, n° 49, p. 495714, déc. 2012.
- [141] S. J. Kang, C. Kocabas, H.-S. Kim, Q. Cao, M. A. Meitl, D.-Y. Khang, et J. A. Rogers, « Printed Multilayer Superstructures of Aligned Single-Walled Carbon Nanotubes for Electronic Applications », *Nano Lett.*, vol. 7, n° 11, p. 3343-3348, 2007.
- [142] N. Patil, A. Lin, E. R. Myers, K. Ryu, A. Badmaev, C. Zhou, H.-S. P. Wong, et S. Mitra, « Wafer-Scale Growth and Transfer of Aligned Single-Walled Carbon Nanotubes », *Nanotechnol. IEEE Trans. On*, vol. 8, n° 4, p. 498-504, juill. 2009.
- [143] W. Zhou, C. Rutherglen, et P. J. Burke, « Wafer scale synthesis of dense aligned arrays of single-walled carbon nanotubes », *Nano Res.*, vol. 1, n° 2, p. 158-165, juill. 2008.
- [144] P. Bondavalli, P. Legagneux, D. Pribat, A. Balan, et S. Nazeer, « Gas fingerprinting using carbon nanotubes transistor arrays », *J. Exp. Nanosci.*, vol. 3, n° 4, p. 347-356, 2008.
- [145] P. Bondavalli, L. Gorintin, P. Legagneux, et P. Ponard, « Method for depositing nanoparticles on a surface and corresponding nanoparticle depositing appliance », 21-févr-2013.
- [146] L. Ding, A. Tselev, J. Wang, D. Yuan, H. Chu, T. P. McNicholas, Y. Li, et J. Liu, « Selective Growth of Well-Aligned Semiconducting Single-Walled Carbon Nanotubes », *Nano Lett.*, vol. 9, n° 2, p. 800-805, févr. 2009.
- [147] T. Altalhi, T. Kumeria, A. Santos, et D. Losic, « Synthesis of well-organised carbon nanotube membranes from non-degradable plastic bags with tuneable molecular transport: Towards nanotechnological recycling », *Carbon*, vol. 63, p. 423-433, nov. 2013.

- [148] L. Cao, D. N. Barsic, A. R. Guichard, et M. L. Brongersma, « Plasmon-Assisted Local Temperature Control to Pattern Individual Semiconductor Nanowires and Carbon Nanotubes », *Nano Lett.*, vol. 7, n° 11, p. 3523-3527, nov. 2007.
- [149] Y. F. Lu, Y. S. Zhou, W. Xiong, M. Mahjouri-Samani, Y. Gao, et M. Mitchell, « Optically-Controlled Growth of Carbon Nanotubes », in *Femtosecond Laser Microfabrication (2009)*, paper LMTuD2, 2009.
- [150] W. Xiong, Y. S. Zhou, M. Mahjouri-Samani, W. Q. Yang, K. J. Yi, X. N. He, S. H. Liou, et Y. F. Lu, « Self-aligned growth of single-walled carbon nanotubes using optical near-field effects », *Nanotechnology*, vol. 20, n° 2, p. 025601, janv. 2009.
- [151] Y. S. Zhou, W. Xiong, Y. Gao, M. Mahjouri-Samani, M. Mitchell, L. Jiang, et Y. F. Lu, « Towards carbon-nanotube integrated devices: optically controlled parallel integration of single-walled carbon nanotubes », *Nanotechnology*, vol. 21, n° 31, p. 315601, août 2010.
- [152] M. Mahjouri-Samani, Y. S. Zhou, X. N. He, W. Xiong, P. Hilger, et Y. F. Lu, « Plasmonic-enhanced carbon nanotube infrared bolometers », *Nanotechnology*, vol. 24, n° 3, p. 035502, janv. 2013.
- [153] A. Moysala, A. G. Nasibulin, et E. I. Kauppinen, « The role of metal nanoparticles in the catalytic production of single-walled carbon nanotubes—a review », *J. Phys. Condens. Matter*, vol. 15, p. S3011, 2003.
- [154] S. Huang, Q. Fu, L. An, et J. Liu, « Growth of aligned SWNT arrays from water-soluble molecular clusters for nanotube device fabrication », *Phys. Chem. Chem. Phys.*, vol. 6, p. 1077, 2004.
- [155] A.-C. Dupuis, « The catalyst in the CCVD of carbon nanotubes—a review », *Prog. Mater. Sci.*, vol. 50, n° 8, p. 929-961, nov. 2005.
- [156] L. Ding, W. Zhou, H. Chu, Z. Jin, Y. Zhang, et Y. Li, « Direct Preparation and Patterning of Iron Oxide Nanoparticles via Microcontact Printing on Silicon Wafers for the Growth of Single-Walled Carbon Nanotubes », *Chem. Mater.*, vol. 18, n° 17, p. 4109-4114, août 2006.
- [157] D. Yuan, L. Ding, H. Chu, Y. Feng, T. P. McNicholas, et J. Liu, « Horizontally Aligned Single-Walled Carbon Nanotube on Quartz from a Large Variety of Metal Catalysts », *Nano Lett.*, vol. 8, n° 8, p. 2576-2579, août 2008.
- [158] B. Li, X. Cao, X. Huang, G. Lu, Y. Huang, C. F. Goh, F. Y. C. Boey, et H. Zhang, « Facile “Needle-Scratching” Method for Fast Catalyst Patterns Used for Large-Scale Growth of Densely Aligned Single-Walled Carbon-Nanotube Arrays », *Small*, vol. 5, n° 18, p. 2061-2065, sept. 2009.
- [159] X. Cao, B. Li, Y. Huang, F. Boey, T. Yu, Z. Shen, et H. Zhang, « Facile “Scratching” Method with Common Metal Objects To Generate Large-Scale Catalyst Patterns Used for Growth of Single-Walled Carbon Nanotubes », *ACS Appl Mater Interfaces*, vol. 1, n° 9, p. 1873-1877, 2009.
- [160] Y. Liu, C. Lor, Q. Fu, D. Pan, L. Ding, J. Liu, et J. Lu, « Synthesis of Copper Nanocatalysts with Tunable Size Using Diblock Copolymer Solution Micelles », *J Phys Chem C*, vol. 114, n° 13, p. 5767-5772, 2010.
- [161] Y. Homma, S. Chiashi, et Y. Kobayashi, « Suspended single-wall carbon nanotubes: synthesis and optical properties », *Rep. Prog. Phys.*, vol. 72, n° 6, p. 066502, juin 2009.
- [162] Y. Cao, J.-H. He, J.-L. Zhu, et J.-L. Sun, « Fabrication of carbon nanotube/silicon nanowire array heterojunctions and their silicon nanowire length dependent photoresponses », *Chem. Phys. Lett.*, vol. 501, n° 4-6, p. 461-465, janv. 2011.
- [163] P. Castrucci, C. Scilletta, S. D. Gobbo, M. Scarselli, L. Camilli, M. Simeoni, B. Delley, A. Continenza, et M. D. Crescenzi, « Light harvesting with multiwall carbon nanotube/silicon heterojunctions », *Nanotechnology*, vol. 22, n° 11, p. 115701, mars 2011.
- [164] S. Blatt, F. Hennrich, H. v. Löhneysen, M. M. Kappes, A. Vijayaraghavan, et R. Krupke, « Influence of Structural and Dielectric Anisotropy on the Dielectrophoresis of Single-Walled Carbon Nanotubes », *Nano Lett.*, vol. 7, n° 7, p. 1960-1966, juill. 2007.
- [165] A. Vijayaraghavan, S. Blatt, D. Weissenberger, M. Oron-Carl, F. Hennrich, D. Gerthsen, H. Hahn, et R. Krupke, « Ultra-Large-Scale Directed Assembly of Single-Walled Carbon Nanotube Devices », *Nano Lett.*, vol. 7, n° 6, p. 1556-1560, juin 2007.
- [166] S. Blatt, « Dielectrophoresis of Single-Walled Carbon Nanotubes », 2008.
- [167] P. Franck, D. Baillargeat, et B. K. Tay, « Antennes électriquement courtes à base de nanotubes de carbone », in *18èmes Journées Nationales Microondes*, Paris, 2013.
- [168] P. Franck, D. Baillargeat, et B. K. Tay, « Carbon-nanotube-based electrically-short resonant antennas », *Int. J. Microw. Wirel. Technol.*, vol. in press, 2013.
- [169] C. Kocabas, M. Shim, et J. A. Rogers, « Spatially Selective Guided Growth of High-Coverage Arrays and Random Networks of Single-Walled Carbon Nanotubes and Their Integration into Electronic Devices », *J. Am. Chem. Soc.*, vol. 128, n° 14, p. 4540-4541, avr. 2006.
- [170] L. Ding, D. Yuan, et J. Liu, « Growth of High-Density Parallel Arrays of Long Single-Walled Carbon Nanotubes on Quartz Substrates », *J Am Chem Soc*, vol. 130, n° 16, p. 5428-5429, 2008.

- [171] S. J. Kang, C. Kocabas, T. Ozel, M. Shim, N. Pimparkar, M. A. Alam, S. V. Rotkin, et J. A. Rogers, « High-performance electronics using dense, perfectly aligned arrays of single-walled carbon nanotubes », *Nat Nano*, vol. 2, n° 4, p. 230-236, avr. 2007.
- [172] C. Brun, P. Franck, P. Coquet, D. Baillargeat, et B. K. Tay, « Monopole Antenna based on Carbon Nanotubes », in *Microwave Symposium Digest (MTT), 2013 IEEE MTT-S International*, Seattle, USA, 2013.
- [173] C. Brun, P. Franck, P. Coquet, D. Baillargeat, et B. K. Tay, « Horizontal and vertical carbon-nanotube-array-based antenna designs », in *Microwave Conference, 2013. European*, Nuremberg, Germany, 2013.
- [174] J. D. Kraus et R. J. Marhefka, *Antennas for all applications*. McGraw-Hill, 2002.
- [175] G. Hanson, « Radiation efficiency of nano-radius dipole antennas in the microwave and far-infrared regimes », *Antennas Propag. Mag. IEEE*, vol. 50, n° 3, p. 66-77, 2008.
- [176] P. Legagneux, S. Xavier, E. Minoux, et J. Schnell, « Method for manufacturing carbon nanotubes with metal cores », EP193280604-juill-2010.
- [177] P. Franck, C. Brun, Y. C. Chong, D. Tan, E. T. H. Tong, S. Bila, D. Baillargeat, et B. K. Tay, « Plasmon resonances of carbon-nanotube-based dipole antennas for nano-interconnects », in *Electronics Packaging Technology Conference (EPTC), 2011 IEEE 13th*, 2011, p. 167 -170.
- [178] M. F. Pantoja, A. R. Bretones, D. H. Werner, P. L. Werner, S. G. Garcia, et R. G. Martin, « On the performance of bundles of CNT-dipoles in the terahertz regime », in *Proceedings of the 5th European Conference on Antennas and Propagation (EUCAP)*, 2011, p. 448-451.
- [179] P. Franck, D. Baillargeat, et B. K. Tay, « Designing carbon-nanotube-based millimeter to sub-millimeter antennas », in *IEEE International Topical Symposium on RF Nanotechnology 2012*, Singapore, 2012.
- [180] G. Y. Slepyan, M. V. Shuba, S. A. Maksimenko, C. Thomsen, et A. Lakhtakia, « Terahertz conductivity peak in composite materials containing carbon nanotubes: Theory and interpretation of experiment », *Phys. Rev. B*, vol. 81, n° 20, p. 205423, mai 2010.
- [181] D. Seliuta, I. Kašalynas, J. Macutkevicius, G. Valušis, M. V. Shuba, P. P. Kuzhir, G. Y. Slepyan, S. A. Maksimenko, V. K. Ksenevich, V. Samuilov, et Q. Lu, « Terahertz sensing with carbon nanotube layers coated on silica fibers: Carrier transport versus nanoantenna effects », *Appl. Phys. Lett.*, vol. 97, n° 7, p. 073116, 2010.
- [182] M. V. Shuba, A. G. Paddubskaya, A. O. Plyushch, P. P. Kuzhir, G. Y. Slepyan, S. A. Maksimenko, V. K. Ksenevich, P. Buka, D. Seliuta, I. Kasalynas, J. Macutkevicius, G. Valusis, C. Thomsen, et A. Lakhtakia, « Experimental evidence of localized plasmon resonance in composite materials containing single-wall carbon nanotubes », *Phys. Rev. B*, vol. 85, n° 16, p. 165435, avr. 2012.
- [183] M. V. Shuba, D. Seliuta, P. P. Kuzhir, S. A. Maksimenko, V. K. Ksenevich, I. Kašalynas, J. Macutkevicius, et G. Valušis, « Antenna resonances in terahertz photoconductivity of single wall carbon nanotube fibers », *Diam. Relat. Mater.*, vol. 27-28, n° 0, p. 36-39, juill. 2012.
- [184] C. L. Pint, Y.-Q. Xu, M. Pasquali, et R. H. Hauge, « Formation of Highly Dense Aligned Ribbons and Transparent Films of Single-Walled Carbon Nanotubes Directly from Carpets », *ACS Nano*, vol. 2, n° 9, p. 1871-1878, sept. 2008.
- [185] C. L. Pint, Y.-Q. Xu, S. Moghazy, T. Cherukuri, N. T. Alvarez, E. H. Haroz, S. Mahzooni, S. K. Doorn, J. Kono, M. Pasquali, et R. H. Hauge, « Dry Contact Transfer Printing of Aligned Carbon Nanotube Patterns and Characterization of Their Optical Properties for Diameter Distribution and Alignment », *ACS Nano*, vol. 4, n° 2, p. 1131-1145, févr. 2010.
- [186] L. Ren, C. L. Pint, T. Arikawa, K. Takeya, I. Kawayama, M. Tonouchi, R. H. Hauge, et J. Kono, « Broadband Terahertz Polarizers with Ideal Performance Based on Aligned Carbon Nanotube Stacks », *Nano Lett.*, vol. 12, n° 2, p. 787-790, févr. 2012.
- [187] L. Ren, Q. Zhang, C. L. Pint, A. K. Wójcik, M. Bunney, T. Arikawa, I. Kawayama, M. Tonouchi, R. H. Hauge, A. A. Belyanin, et J. Kono, « Collective antenna effects in the terahertz and infrared response of highly aligned carbon nanotube arrays », *Phys. Rev. B*, vol. 87, n° 16, avr. 2013.
- [188] P. Franck, D. Baillargeat, et B. K. Tay, « Parametric Study of Realistic Carbon-nanotube-based Electrically-short Resonant Antennas », in *International Conference of Young Researchers on Advanced Materials, IUMRS-ICYRAM 2012*, Singapore, 2012.
- [189] P. Franck, D. Baillargeat, et B. K. Tay, « Performance assessment of optimized carbon-nanotube-based wireless on-chip communication », in *SPIE Optics and Photonics 2012: Nanoscience and Engineering*, San Diego, USA, 2012, vol. 8462.
- [190] P. Franck, D. Baillargeat, et B. K. Tay, « Design and Assessment of Carbon-nanotube-based Remote Links to Nanodevices », in *Microwave Symposium Digest (MTT), 2013 IEEE MTT-S International*, Seattle, USA, 2013.
- [191] H. Yordanov, « Wired and Wireless Inter-Chip and Intra-Chip Communications », 2010.

- [192] B. Atakan et O. B. Akan, « Carbon nanotube-based nanoscale ad hoc networks », *IEEE Commun. Mag.*, vol. 48, n° 6, p. 129-135, 2010.
- [193] I. Llatser, C. Kremers, A. Cabellos-Aparicio, J. M. Jornet, E. Alarcón, et D. N. Chigrin, « Graphene-based nano-patch antenna for terahertz radiation », *Photonics Nanostructures - Fundam. Appl.*, vol. 10, n° 4, p. 353-358, oct. 2012.
- [194] M. Sun et Y. P. Zhang, « 100-GHz quasi-Yagi antenna in silicon technology », *Electron Device Lett. IEEE*, vol. 28, n° 5, p. 455-457, 2007.
- [195] R. N. S. Simons, « Conventional Coplanar Waveguide », in *Coplanar Waveguide Circuits, Components, and Systems*, John Wiley & Sons, Inc., 2002, p. 11-86.
- [196] H. Chu, J. Wang, L. Ding, D. Yuan, Y. Zhang, J. Liu, et Y. Li, « Decoration of Gold Nanoparticles on Surface-Grown Single-Walled Carbon Nanotubes for Detection of Every Nanotube by Surface-Enhanced Raman Spectroscopy », *J. Am. Chem. Soc.*, vol. 131, n° 40, p. 14310-14316, oct. 2009.
- [197] Y.-K. Yoon, B. Pan, P. Kirby, J. Papapolymerou, M. Tentzeris, et M. G. Allen, « Surface micromachined electromagnetically radiating RF MEMS », in *Digest of Solid-State Sensor, Actuator, and Microsystems Workshop*, 2004, p. 328-331.
- [198] B. Pan, Y. K. Yoon, P. Kirby, J. Papapolymerou, M. M. Tenzeris, et M. Allen, « A W-band surface micromachined monopole for low-cost wireless communication systems », in *Microwave Symposium Digest, 2004 IEEE MTT-S International*, 2004, vol. 3, p. 1935-1938.
- [199] Y.-K. Yoon, B. Pan, J. Papapolymerou, M. Tentzeris, et M. G. Allen, « Surface-micromachined millimeter-wave antennas », in *The 13th International Conference on Solid-State Sensors, Actuators and Microsystems, 2005. Digest of Technical Papers. TRANSDUCERS '05*, 2005, vol. 2, p. 1986-1989 Vol. 2.
- [200] B. Pan, G. DeJean, J. Papapolymerou, M. M. Tentzeris, Y. Yoon, et M. G. Allen, « High performance system-on-package integrated Yagi-Uda antennas for W-band applications and mm-wave ultra-wideband data links », in *Electronic Components and Technology Conference, 2006. Proceedings. 56th*, 2006, p. 6-pp.
- [201] P. Franck, Z. Wang, D. Baillargeat, C. Soci, et B. K. Tay, « Photocurrent Study of Locally Grown and Solution-deposited Carbon Nanotubes », in *International Conference on Materials for Advanced Technologies, MRS, ICMAT 2013*, Singapore, 2013, vol. Symposium G: Carbon Nanotubes and Graphene: Synthesis, Functionalisation and Applications, p. ICMAT13-A-2309.
- [202] B. C. St-Antoine, D. Ménard, et R. Martel, « Position Sensitive Photothermoelectric Effect in Suspended Single-Walled Carbon Nanotube Films », *Nano Lett.*, vol. 9, n° 10, p. 3503-3508, oct. 2009.
- [203] B. C. St-Antoine, D. Ménard, et R. Martel, « Single-Walled Carbon Nanotube Thermopile For Broadband Light Detection », *Nano Lett.*, vol. 11, n° 2, p. 609-613, févr. 2011.
- [204] B. St-Antoine, D. Ménard, et R. Martel, « Photothermoelectric effects in single-walled carbon nanotube films: Reinterpreting scanning photocurrent experiments », *Nano Res.*, vol. 5, n° 2, p. 73-81, 2012.
- [205] S. Nanot, A. W. Cummings, C. L. Pint, A. Ikeuchi, T. Akiho, K. Sueoka, R. H. Hauge, F. Léonard, et J. Kono, « Broadband, Polarization-Sensitive Photodetector Based on Optically-Thick Films of Macroscopically Long, Dense, and Aligned Carbon Nanotubes », *Sci. Rep.*, vol. 3, févr. 2013.
- [206] B. Wang, « Chirality selective growth of single-walled carbon nanotube in chemical vapor deposition. », Thesis, 2009.
- [207] Y. Che, C. Wang, J. Liu, B. Liu, X. Lin, J. Parker, C. Beasley, H.-S. P. Wong, et C. Zhou, « Selective Synthesis and Device Applications of Semiconducting Single-Walled Carbon Nanotubes Using Isopropyl Alcohol as Feedstock », *ACS Nano*, vol. 6, n° 8, p. 7454-7462, août 2012.
- [208] W. Zhou, S. Zhan, L. Ding, et J. Liu, « General Rules for Selective Growth of Enriched Semiconducting Single Walled Carbon Nanotubes with Water Vapor as in Situ Etchant », *J. Am. Chem. Soc.*, vol. 134, n° 34, p. 14019-14026, août 2012.
- [209] Y. Chen, Z. Shen, Z. Xu, Y. Hu, H. Xu, S. Wang, X. Guo, Y. Zhang, L. Peng, F. Ding, Z. Liu, et J. Zhang, « Helicity-dependent single-walled carbon nanotube alignment on graphite for helical angle and handedness recognition », *Nat. Commun.*, vol. 4, juill. 2013.
- [210] M. S. Arnold, A. A. Green, J. F. Hulvat, S. I. Stupp, et M. C. Hersam, « Sorting carbon nanotubes by electronic structure using density differentiation », *Nat. Nanotechnol.*, vol. 1, n° 1, p. 60-65, 2006.
- [211] S. H. Jin, S. N. Dunham, J. Song, X. Xie, J. Kim, C. Lu, A. Islam, F. Du, J. Kim, J. Felts, Y. Li, F. Xiong, M. A. Wahab, M. Menon, E. Cho, K. L. Grosse, D. J. Lee, H. U. Chung, E. Pop, M. A. Alam, W. P. King, Y. Huang, et J. A. Rogers, « Using nanoscale thermocapillary flows to create arrays of purely semiconducting single-walled carbon nanotubes », *Nat. Nanotechnol.*, vol. 8, n° 5, p. 347-355, avr. 2013.
- [212] J. Liu, C. Wang, X. Tu, B. Liu, L. Chen, M. Zheng, et C. Zhou, « Chirality-controlled synthesis of single-wall carbon nanotubes using vapour-phase epitaxy », *Nat. Commun.*, vol. 3, p. 1199, nov. 2012.
- [213] Z. Ren, « Nanotube synthesis: Cloning carbon », *Nat. Nanotechnol.*, vol. 2, n° 1, p. 17-18, 2007.

- [214] « CoMoCAT® Carbon Nanotubes », *Sigma-Aldrich*. [En ligne]. Disponible sur: <http://www.sigmaaldrich.com/materials-science/nanomaterials/comocat-carbon-nanotubes.html#ref>. [Consulté le: 18-mars-2013].
- [215] A. Lin, N. Patil, H. Wei, S. Mitra, et H.-S. P. Wong, « A metallic-CNT-tolerant carbon nanotube technology using Asymmetrically-Correlated CNTs (ACCNT) », in *2009 Symposium on VLSI Technology*, 2009, p. 182 -183.
- [216] A. Lin, J. Zhang, N. Patil, H. Wei, S. Mitra, et H.-S. P. Wong, « ACCNT: A Metallic-CNT-Tolerant Design Methodology for Carbon Nanotube VLSI: Analyses and Design Guidelines », *IEEE Trans. Electron Devices*, vol. 57, n° 9, p. 2284 -2295, sept. 2010.
- [217] N. Patil, A. Lin, J. Zhang, H. Wei, K. Anderson, H.-S. P. Wong, et S. Mitra, « Scalable Carbon Nanotube Computational and Storage Circuits Immune to Metallic and Mispositioned Carbon Nanotubes », *IEEE Trans. Nanotechnol.*, vol. 10, n° 4, p. 744 -750, juill. 2011.
- [218] J. Zhang, N. P. Patil, A. Hazeghi, H.-S. P. Wong, et S. Mitra, « Characterization and Design of Logic Circuits in the Presence of Carbon Nanotube Density Variations », *IEEE Trans. Comput.-Aided Des. Integr. Circuits Syst.*, vol. 30, n° 8, p. 1103 -1113, août 2011.
- [219] J. Zhang, A. Lin, N. Patil, H. Wei, L. Wei, H.-S. P. Wong, et S. Mitra, « Carbon Nanotube Robust Digital VLSI », *IEEE Trans. Comput.-Aided Des. Integr. Circuits Syst.*, vol. 31, n° 4, p. 453 -471, avr. 2012.
- [220] F. Kreupl, « Electronics: The carbon-nanotube computer has arrived », *Nature*, vol. 501, n° 7468, p. 495-496, sept. 2013.
- [221] L. Gorintin, P. Bondavalli, P. Legagneux, et D. Pribat, « High performances CNTFETs achieved using CNT networks for selective gas sensing », in *Proceedings of SPIE*, 2009, vol. 7399, p. 739909.
- [222] P. G. Collins, M. S. Arnold, et P. Avouris, « Engineering carbon nanotubes and nanotube circuits using electrical breakdown », *Science*, vol. 292, n° 5517, p. 706-709, 2001.
- [223] P. Avouris, P. G. Collins, et R. Martel, « Methodology for electrically induced selective breakdown of nanotubes », 642358323-juill-2002.
- [224] Z. Wu, L. Wang, I. Zimmerman, et Hao Xin, « Microwave to terahertz characterization of carbon nanotube materials », in *2011 IEEE 11th Topical Meeting on Silicon Monolithic Integrated Circuits in RF Systems (SiRF)*, 2011, p. 181-184.
- [225] M. S. Dresselhaus, G. Dresselhaus, R. Saito, et A. Jorio, « Raman spectroscopy of carbon nanotubes », *Phys. Rep.*, 2004.
- [226] R. Saito, M. Hofmann, G. Dresselhaus, A. Jorio, et M. S. Dresselhaus, « Raman spectroscopy of graphene and carbon nanotubes », *Adv. Phys.*, vol. 60, n° 3, p. 413-550, 2011.
- [227] C. Kocabas, M. A. Meitl, A. Gaur, M. Shim, et J. A. Rogers, « Aligned Arrays of Single-Walled Carbon Nanotubes Generated from Random Networks by Orientationally Selective Laser Ablation », *Nano Lett.*, vol. 4, n° 12, p. 2421-2426, déc. 2004.
- [228] D. Seliuta, L. Subačius, I. Kašalynas, M. Shuba, A. Paddubskaya, V. Ksenevich, P. Kuzhir, S. Maksimenko, et G. Valušis, « Electrical conductivity of single-wall carbon nanotube films in strong electric field », *J. Appl. Phys.*, vol. 113, n° 18, p. 183719-183719-6, mai 2013.
- [229] S. Nanot, E. H. Hároz, J.-H. Kim, R. H. Hauge, et J. Kono, « Optoelectronic Properties of Single-Wall Carbon Nanotubes », *Adv. Mater.*, vol. 24, n° 36, p. 4977-4994, 2012.
- [230] P. Avouris, M. Freitag, et V. Perebeinos, « Carbon-nanotube photonics and optoelectronics », *Nat. Photonics*, vol. 2, n° 6, p. 341-350, 2008.
- [231] P. Avouris et R. Martel, « Progress in carbon nanotube electronics and photonics », *MRS Bull.*, vol. 35, n° 04, p. 306-313, 2010.
- [232] C. Chen, Y. Lu, E. S. Kong, Y. Zhang, et S.-T. Lee, « Nanowelded Carbon-Nanotube-Based Solar Microcells », *Small*, vol. 4, n° 9, p. 1313-1318, sept. 2008.
- [233] M. Engel, M. Steiner, R. S. Sundaram, R. Krupke, A. A. Green, M. C. Hersam, et P. Avouris, « Spatially Resolved Electrostatic Potential and Photocurrent Generation in Carbon Nanotube Array Devices », *ACS Nano*, vol. 6, n° 8, p. 7303-7310, août 2012.
- [234] E. Shi, J. Nie, X. Qin, Z. Li, L. Zhang, Z. Li, P. Li, Y. Jia, C. Ji, J. Wei, K. Wang, H. Zhu, D. Wu, Y. Li, Y. Fang, W. Qian, F. Wei, et A. Cao, « Nanobelt-carbon nanotube cross-junction solar cells », *Energy Environ. Sci.*, vol. 5, n° 3, p. 6119-6125, mars 2012.
- [235] X. Cao, Y. Shi, W. Shi, G. Lu, X. Huang, Q. Yan, Q. Zhang, et H. Zhang, « Preparation of Novel 3D Graphene Networks for Supercapacitor Applications », *Small*, vol. 7, n° 22, p. 3163-3168, 2011.
- [236] S. X. Lim, G. K. W. Koon, D. Zhan, Z. Shen, B. Özyilmaz, et C. Sow, « Assembly of suspended graphene on carbon nanotube scaffolds with improved functionalities », *Nano Res.*, vol. 5, n° 11, p. 783-795, oct. 2012.

- [237] J. S. Gómez-Díaz et J. Perruisseau-Carrier, « Graphene-based plasmonic switches at near infrared frequencies », *Opt. Express*, vol. 21, n° 13, p. 15490, juin 2013.
- [238] O. V. Shapoval, J. S. Gomez-Diaz, J. Perruisseau-Carrier, J. R. Mosig, et A. I. Nosich, « Integral Equation Analysis of Plane Wave Scattering by Coplanar Graphene-Strip Gratings in the THz Range », *IEEE Trans. Terahertz Sci. Technol.*, vol. 3, n° 5, p. 666-674, sept. 2013.
- [239] I. Llatser, C. Kremers, D. N. Chigrin, J. M. Jornet, M. C. Lemme, A. Cabellos-Aparicio, et E. Alarcón, « Characterization of graphene-based nano-antennas in the terahertz band », in *Antennas and Propagation (EUCAP), 2012 6th European Conference on*, 2012, p. 194-198.
- [240] P. Franck, C. C. Yap, C. Brun, S. Pacchini, W. L. Chow, H. Li, D. Baillargeat, et B. K. Tay, « Carbon-nanotube-based RF components with multiple applications », in *Wireless Symposium Digest (MTT), 2013 IEEE MTT-S International*, Beijing, China, 2013.
- [241] C. Brun, P. Franck, P. Coquet, D. Baillargeat, et B. K. Tay, « Antennes Monopoles à base de Nanotubes de Carbone », in *18èmes Journées Nationales Microondes*, 2013.
- [242] C. C. Yap, D. Tan, C. Brun, P. Franck, H. Li, E. H. T. Teo, D. Baillargeat, et B. K. Tay, « Carbon Based Nanotechnologies Dedicated to High Frequency Applications », in *IEEE 4th International Nanoelectronics Conference (INEC), 2011*, Chang Gung University, Tao-Yuan, Taiwan, 2011.
- [243] C. A. Balanis, *Antenna theory: analysis and design*, 3rd ed. Hoboken, NJ: John Wiley, 2005.
- [244] « KOH Etching of Silicon wafers, Silicon Dioxide (SiO₂) and Silicon Nitride (SiN) ». [En ligne]. Disponible sur: <http://www.cleanroom.byu.edu/KOH.phtml>. [Consulté le: 30-nov-2011].
- [245] H. A. Wheeler, « Transmission-Line Properties of a Strip on a Dielectric Sheet on a Plane », *IEEE Trans. Microw. Theory Tech.*, vol. 25, n° 8, p. 631-647, 1977.
- [246] C. Brun, « Carbon nanotubes based nanopackaging dedicated to innovative high frequency interconnections », 2013.
- [247] « Nanotube Modeler (Nanocones, Bucky-Ball, Fullerenes, Simulation Software) ». [En ligne]. Disponible sur: <http://www.jcrystal.com/products/wincnt/>. [Consulté le: 11-sept-2013].

Appendices

Appendix 1 – Effective circuit diagram for an SWCNT

Here, following [8], [94], we show how the representation of four spinless interacting modes of a SWCNT as parallel transmission lines reported in section I.A.1.1) is correctly simplified to a single effective transmission line.

The electrons in the four channels interact, which is encompassed by a distributed electrostatic capacitance, C_{ES} . A length independent C_{ES} is effectively defined for CNTs longer than the Debye length or close enough to another conductor [94]. Thus, writing a generalized $Q=CV$ [8]:

$$\begin{pmatrix} V_{a\uparrow} \\ V_{a\downarrow} \\ V_{b\uparrow} \\ V_{b\downarrow} \end{pmatrix} = \begin{pmatrix} C_{Q1}^{-1} + C_{ES}^{-1} & C_{ES}^{-1} & C_{ES}^{-1} & C_{ES}^{-1} \\ C_{ES}^{-1} & C_{Q1}^{-1} + C_{ES}^{-1} & C_{ES}^{-1} & C_{ES}^{-1} \\ C_{ES}^{-1} & C_{ES}^{-1} & C_{Q1}^{-1} + C_{ES}^{-1} & C_{ES}^{-1} \\ C_{ES}^{-1} & C_{ES}^{-1} & C_{ES}^{-1} & C_{Q1}^{-1} + C_{ES}^{-1} \end{pmatrix} \begin{pmatrix} \rho_{a\uparrow} \\ \rho_{a\downarrow} \\ \rho_{b\uparrow} \\ \rho_{b\downarrow} \end{pmatrix} \quad (183)$$

Or in vector notation:

$$\mathbf{v} = \mathbf{C}^{-1}\boldsymbol{\rho} \quad (184)$$

where (a,b) are the two sublattice channels and (\uparrow,\downarrow) the two spin states and $V_{x\uparrow}$ is the potential for the $x\uparrow$ mode. Let us demonstrate that by choosing ingeniously the base we can obtain four independent modes – and hence extract the net current and the characteristics of the CNT TL.

\mathbf{C}^{-1} is a real symmetric matrix hence it can be diagonalized by an orthogonal matrix \mathbf{M} (i.e. such that $\mathbf{M}^T = \mathbf{M}^{-1}$): $\mathbf{C}^{-1} = \mathbf{M}^T \mathbf{C}^{-1} \mathbf{M}$. Furthermore $\frac{1}{2}(1 \ 1 \ 1 \ 1)$ is an obvious Eigen vector of \mathbf{C}^{-1} with Eigen value $C_{Q1}^{-1} + 4C_{ES}^{-1}$ or can be found so by noting that $\mathbf{C}^{-1} = C_{Q1}^{-1} \mathbf{I}_4 + C_{ES}^{-1}(\mathbf{1})_4$. The latter also implies that the three remaining normal vectors have components summing to zero and Eigen value C_{Q1}^{-1} . A basis of four orthogonal modes can thus be defined as a linear combination of the four precedent ones and form the matrix \mathbf{M}

below such that $\mathbf{v}' = \mathbf{M}\mathbf{v}$. It appears that there is only one charged (or common) mode V_{CM} and three neutral (or differential) modes $V_{Di}, i \in [1,3]$.

$$\begin{pmatrix} V_{CM} \\ V_{D1} \\ V_{D2} \\ V_{D3} \end{pmatrix} = \frac{1}{2} \begin{pmatrix} 1 & 1 & 1 & 1 \\ 1 & 1 & -1 & -1 \\ 1 & -1 & 1 & -1 \\ 1 & -1 & -1 & 1 \end{pmatrix} \begin{pmatrix} V_{a\uparrow} \\ V_{a\downarrow} \\ V_{b\uparrow} \\ V_{b\downarrow} \end{pmatrix} \quad (185)$$

The same relations are defined for $\rho_{x\uparrow}$ and $I_{x\uparrow}$. \mathbf{M} is orthogonal but also symmetric so we have $\mathbf{M}^{-1} = \mathbf{M}^T = \mathbf{M}$. Hence $\mathbf{v}' = \mathbf{M}\mathbf{v} = \mathbf{M}\mathbf{C}^{-1}\boldsymbol{\rho} = \mathbf{M}\mathbf{C}^{-1}\mathbf{M}\boldsymbol{\rho}' = \mathbf{M}^T\mathbf{C}^{-1}\mathbf{M}\boldsymbol{\rho}' = \mathbf{C}^{-1}\boldsymbol{\rho}'$. Finally we obtain our diagonalized generalized Q=CV:

$$\begin{pmatrix} V_{CM} \\ V_{D1} \\ V_{D2} \\ V_{D3} \end{pmatrix} = \begin{pmatrix} C_{Q1}^{-1} + 4C_{ES}^{-1} & 0 & 0 & 0 \\ 0 & C_{Q1}^{-1} & 0 & 0 \\ 0 & 0 & C_{Q1}^{-1} & 0 \\ 0 & 0 & 0 & C_{Q1}^{-1} \end{pmatrix} \begin{pmatrix} \rho_{CM} \\ \rho_{D1} \\ \rho_{D2} \\ \rho_{D3} \end{pmatrix} \quad (186)$$

Once this basis is adopted Bockrath [94] and Burke [8] respectively derive the transmission line parameters through a Lagrangian or the telegrapher equations. In the latter case the equations are obtained noting that:

$$\frac{\partial \boldsymbol{\rho}'(z, t)}{\partial t} = - \frac{\partial \mathbf{I}'(z, t)}{\partial z} \quad (187)$$

Finally one obtains the propagation speed and characteristic impedance of the common mode of a four channel CNT as follows:

$$v_{p,CM} = \sqrt{\frac{1}{L_{K1} \left(\frac{1}{C_{Q1}} + \frac{4}{C_{ES}} \right)}} = v_F \sqrt{1 + \frac{4C_{Q1}}{C_{ES}}} \equiv \frac{v_F}{g} \quad (188)$$

$$Z_{c,CM} = \sqrt{L_{K1} \left(\frac{4}{C_{ES}} + \frac{1}{C_{Q1}} \right)} = v_F \sqrt{1 + \frac{4C_{Q1}}{C_{ES}}} = \frac{1}{g} \frac{h}{2e^2} \quad (189)$$

Because $V_{CM} = \frac{1}{2}(V_{a\uparrow} + V_{a\downarrow} + V_{b\uparrow} + V_{b\downarrow}) = 2V_{ext}$ while $I_{CM} = \frac{1}{2}I_{ext}$, the measured quantity is not the characteristic impedance of the common mode but one fourth of it. The propagation speed should remain the same as that of the charged mode. Hence the equivalent single transmission line is defined with effective kinetic inductance and quantum capacitance as follows:

$$L_K = \frac{1}{4} L_{K1} = \frac{h}{8e^2 v_F} = \frac{R_0}{4v_F} \quad (190)$$

$$C_Q = 4C_{Q1} = \frac{8e^2}{h v_F} = \frac{4}{R_0 v_F} \quad (191)$$

Which verifies:

$$v_p = \sqrt{\frac{1}{L_K} \left(\frac{1}{C_Q} + \frac{1}{C_{ES}} \right)} = \sqrt{\frac{4}{L_{K1}} \left(\frac{1}{4C_{Q1}} + \frac{1}{C_{ES}} \right)} = v_{p,CM} \quad (192)$$

$$Z_c = \sqrt{L_K \left(\frac{1}{C_{ES}} + \frac{1}{C_Q} \right)} = \sqrt{\frac{L_{K1}}{4} \left(\frac{1}{C_{ES}} + \frac{1}{4C_{Q1}} \right)} = \frac{1}{4} Z_{c,CM} \quad (193)$$

Additional considerations on this model follow in section I.A.1.1).

Appendix 2 – Fortran codes for the complex properties in EMXD

This section presents the Fortran codes used to generate the complex properties in EMXD as reported in section II.C.1.1).

For the surface impedance of a hollow cylinder modeling a SWCNT, file bdlld_sc4.f90:

```

PROGRAM bdlld_sc4
  IMPLICIT NONE

  CHARACTER (LEN=*) , PARAMETER :: PROJET = 'bdld' , &
    NUMERO = '4'

  ! CONSTANTES MATHEMATIQUES ET PHYSIQUES.
  ! -----
  DOUBLE PRECISION , PARAMETER :: CONPI = 3.141592653589793238462643383D+00

  ! VITESSE DE LA LUMIERE DANS LE VIDE (MM/NS).
  ! -----
  DOUBLE PRECISION , PARAMETER :: CONC = 299.792458D+00

  ! PERMEABILITE ET PERMITTIVITE DU VIDE.
  ! -----
  DOUBLE PRECISION , PARAMETER :: CONMU0 = 4.0D-07 * CONPI
  DOUBLE PRECISION , PARAMETER :: CONEPO = 1.0D-12 / ( CONMU0 * CONC * CONC
)
  DOUBLE PRECISION , PARAMETER :: Z0 = CONMU0 * CONC * 1.0D+06

  ! COMPLEXE i.
  ! -----
  DOUBLE COMPLEX , PARAMETER :: CONJ = (0.0D+00,1.0D+00)

```

```

INTEGER,  PARAMETER :: LU = 10

DOUBLE COMPLEX  :: F,ZS

DOUBLE PRECISION  :: SIGMA = 6.0E+02

! VARIABLES.
! -----

DOUBLE PRECISION :: RADIUS = 2.36E-09

! LECTURE DE LA FREQUENCE EN GHZ.
! -----
OPEN (LU,FILE=PROJET//'.f0',ACCESS='SEQUENTIAL',FORM='UNFORMATTED')
REWIND (LU)
READ (LU) F
CLOSE (LU)

! CALCUL DE L'IMPEDANCE.
! -----

ZS = 6.96D+09*RADIUS/Z0 + CONJ*0.1312D+09*F*RADIUS/Z0

print*, 'Freq = ', F, 'ZS = ', ZS

! ECRITURE DE L'IMPEDANCE NORMALISEE.
! -----
OPEN
(LU, FILE=PROJET//'.st'//NUMERO, ACCESS='SEQUENTIAL', FORM='UNFORMATTED')
REWIND (LU)
WRITE (LU) ZS
CLOSE (LU)

OPEN (LU+1, FILE=PROJET//'.ZS'//NUMERO, ACCESS='APPEND', FORM='FORMATTED')
WRITE (LU+1, '(D15.5, D15.5)') F, ZS
CLOSE (LU+1)

END PROGRAM bdld_sc4

```

For the bulk conductivity of a hexagonal bundle of SWCNTs, defined by CNT number and spacing rather than density, file bdld_c1.f90:

```

PROGRAM bdld_c1
  IMPLICIT NONE

  CHARACTER(LEN=*) , PARAMETER :: PROJET = 'bdld', &
    NUMERO = '1'

  ! CONSTANTES MATHEMATIQUES ET PHYSIQUES.
  ! -----
  DOUBLE PRECISION, PARAMETER :: CONPI = 3.141592653589793238462643383D+00
  DOUBLE PRECISION, PARAMETER :: CONE = 1.60217649D-19
  DOUBLE PRECISION, PARAMETER :: CONH = 6.62606896D-34

  ! VITESSE DE LA LUMIERE DANS LE VIDE (MM/NS).
  ! -----
  ! DOUBLE PRECISION, PARAMETER :: CONC = 299.792458D+00

```

```

! PERMEABILITE ET PERMITTIVITE DU VIDE.
! -----
! DOUBLE PRECISION, PARAMETER :: CONMU0 = 4.0D-07 * CONPI
! DOUBLE PRECISION, PARAMETER :: CONEPO = 1.0D-12 / ( CONMU0 * CONC * CONC
)
! DOUBLE PRECISION, PARAMETER :: Z0      = CONMU0 * CONC * 1.0D+06

! CONSTANTES CARACTERISTIQUES DES CNT DE PETIT RAYON.
! -----
DOUBLE PRECISION, PARAMETER :: VF = 9.71D+05
DOUBLE PRECISION, PARAMETER :: NU = (1./3.)*1D+12
DOUBLE PRECISION, PARAMETER :: FNU = NU/(2*CONPI)

! COMPLEXE i.
! -----
! DOUBLE COMPLEX, PARAMETER :: CONJ = (0.0D+00,1.0D+00)

INTEGER, PARAMETER :: LU = 10

! DOUBLE COMPLEX  :: F

! DOUBLE PRECISION  :: SIGMA = 6.0E+02

! VARIABLES.
! -----

DOUBLE PRECISION :: RADIUS = 2.36E-09
DOUBLE PRECISION :: N = 3.0E+00
DOUBLE PRECISION :: DELTAR = 3.4E-09
DOUBLE PRECISION ::
F, NCNT, SURF, DCNT, K, SBULK5, SBULK6, SBULK1, SBULK2, SBULK3, SBULK4

! LECTURE DE LA FREQUENCE EN GHZ.
! -----
OPEN (LU, FILE=PROJET//'.f0', ACCESS='SEQUENTIAL', FORM='UNFORMATTED')
REWIND (LU)
READ (LU) F
CLOSE (LU)

! CALCUL DE L'IMPEDANCE.
! -----

F=F*1.0E+09 !F en GHz convertie en Hz
NCNT = 1+(N+1)*N/2
SURF = ( SQRT(3.0*SQRT(3.0)/2.0)*N*DELTAR +
SQRT(2.0*SQRT(3.0)/3.0)*RADIUS )**2
DCNT = NCNT/SURF
K = 8.0*CONE**2*VF/CONH/NU*(DCNT) !8*(CONE**2/CONH)*(VF/NU)*(DCNT)

SBULK1=0
SBULK2=0
SBULK3=0
SBULK4=0
SBULK5=K/(1+(F/FNU)**2)
SBULK6=-K*(F/FNU)/(1+(F/FNU)**2)

! SBULK = 8*CONE^2*VF/(CONH*NU)*(DCNT)*(1-CONJ*(F/FNU))/(1+(F/FNU)^2)
print*, 'Freq = ', F, 'Re(Sbulk, z) = ', Sbulk5, 'Im(Sbulk, z) = ', Sbulk6

! ECRITURE DE L'IMPEDANCE NORMALISEE.
! -----

```

```

OPEN
(LU,FILE=PROJET//'.t'//NUMERO,ACCESS='SEQUENTIAL',FORM='UNFORMATTED')
REWIND (LU)
WRITE (LU) SBULK1,SBULK2,SBULK3,SBULK4,SBULK5,SBULK6
CLOSE (LU)

OPEN
(LU+1,FILE=PROJET//'.sigma'//NUMERO,ACCESS='APPEND',FORM='FORMATTED')
WRITE (LU+1,'(D15.5, 2(D15.5))') F,SBULK5,SBULK6
CLOSE (LU+1)

END PROGRAM bdld_c1

```

Appendix 3 – Matlab code to enhance contrast in SEM images.

In section II.C.3.2), estimating the number of CNTs in a bundle from SEM images is found difficult due to poor contrast. A Matlab code has been developed to enhance contrast in SEM images with various techniques. It renormalizes the images between either each image's own extreme values or the images set's to extend the range used. It then plots for each image a histogram of grey values, the image with a false color scale to improve visual dynamics for the user, the image filtered with a log scale and with a threshold.

```

N=6; % nb of images
n=5; % first image to read

thresh=0.3.*ones(N);

path='C:\Users\frank\Documents\_Characterisa-
PC\Measurements\110128_SEM\device5-10\selec\device';
fileext='.jpg';
%siz=size(imread(strcat(path,sprintf('%d',n),fileext)));

%siz for crop
siz=[710 1024 3];

imgs=zeros([siz(1) siz(2) N]); %gathers the cropped images along the
3rd dimension
imgthres=zeros([siz(1) siz(2) N]);
maxis=zeros(1,N);
minis=ones(1,N);

%gather the images in imgs and fill maxis and minis to find the global max
%and min of all images to determine the renormalization range
for i=n:n+N-1

    img=double(sum(imread(strcat(path,sprintf('%d',i),fileext)),3))./3;

    % crop
    img=img(1:710,:);

    mini=min(min(img));
    maxi=max(max(img));

```



```

    imgs(:,:,i-n+1)=img;
    minis(i-n+1)=mini;
    maxis(i-n+1)=maxi;

    figure(i),subplot(2,2,1),hist(double(img(:)),0:2:256);
    %subplot(2,2,2),imagesc(img);
    %    subplot(2,2,3),imagesc((img-mini)/(maxi-mini));
    %
    %
    %    img2=((img>thresh(i)).*(img-thresh(i)))/(1-thresh(i));
    %    img2s(:,:,i-n+1)=img2;
    %
    %    subplot(2,2,4), imagesc(img2)
end

maxx=max(maxis);
minn=min(minis);
range=maxx-minn;

% renormalize images before plotting, compute histogram, apply filters
% (log, threshold)
for i=n:n+N-1

    imgn=(imgs(:,:,i-n+1)-minn)./range;

    figure(i),subplot(2,2,1),hist(imgn(:),1/range:1/range:1);
    subplot(2,2,2),imagesc(imgn);
    subplot(2,2,3),imagesc(10.*log10(256.*imgn));
    %subplot(2,2,3),imagesc(exp(3.*imgn));

    imgthre=((imgn>thresh(i)).*(imgn-thresh(i)))/(1-thresh(i));
    imgthres(:,:,i-n+1)=imgthre;
    subplot(2,2,4), imagesc(imgthre)
end

```

Appendix 4 – Radiation resistance

Following [16] (largely based on [243]) the radiation resistance of a short CNT dipole is:

$$R_{r,l_{CNT}} = \left(\frac{\lambda_p}{\lambda}\right)^2 \sqrt{\frac{\mu}{\epsilon}} \xi(kl_{CNT}, k_pl_{CNT}) \quad (194)$$

with:

$$\xi(kl_{CNT}, k_pl_{CNT}) = \frac{1}{2\pi} \int_0^\pi \sin^3 \theta \left(\frac{\cos(kl_{CNT} \cos \theta) - \cos(k_pl_{CNT})}{1 - \left(\frac{k}{k_p}\right)^2 \cos^2 \theta} \right)^2 d\theta \quad (195)$$

Here, we show that, for the odd resonant cases i.e. $l_{CNT} = (2p + 1) \frac{\lambda_p}{4}$, with a relatively short CNT, i.e. $\left(2\pi \frac{(2p+1)\lambda_p}{4\lambda}\right)^2 \ll 1$, ξ is well approximated as a constant, $\xi = \frac{2}{3\pi} \approx 0.21$. Indeed, for $l_{CNT} = (2p + 1) \frac{\lambda_p}{4}$, this becomes:

$$\begin{aligned} \xi \left((2p + 1)k \frac{\lambda_p}{4}, (2p + 1) \frac{\pi}{2} \right) &= \xi_2 \left(\frac{\lambda_p}{\lambda}, p \right) \\ &= \frac{1}{2\pi} \int_0^\pi \sin^3 \theta \left(\frac{\cos \left(2\pi \frac{(2p+1)\lambda_p}{4\lambda} \cos \theta \right)}{1 - \left(\frac{\lambda_p}{\lambda} \right)^2 \cos^2 \theta} \right)^2 d\theta \\ &\equiv \frac{1}{2\pi} \int_0^\pi \xi_3 \left(\theta, \frac{\lambda_p}{\lambda}, p \right) d\theta \end{aligned} \quad (196)$$

Then, for $\left(2\pi \frac{(2p+1)\lambda_p}{4\lambda}\right)^4 \ll 1$, for all $\theta \in [0, \pi]$, we can develop in Taylor series as:

$$\begin{aligned} \left(\frac{\xi_3 \left(\theta, \frac{\lambda_p}{\lambda}, p \right)}{\sin^3 \theta} \right)^{\frac{1}{2}} &= \frac{\cos \left(2\pi \frac{(2p+1)\lambda_p}{4\lambda} \cos \theta \right)}{1 - \left(\frac{\lambda_p}{\lambda} \right)^2 \cos^2 \theta} \\ &\approx \frac{1 - \frac{1}{2} \left(2\pi \frac{(2p+1)\lambda_p}{4\lambda} \right)^2 \left(\frac{\lambda_p}{\lambda} \cos \theta \right)^2 + \frac{1}{24} \left(2\pi \frac{(2p+1)\lambda_p}{4\lambda} \right)^4 \left(\frac{\lambda_p}{\lambda} \cos \theta \right)^4}{1 - \left(\frac{\lambda_p}{\lambda} \cos \theta \right)^2} \\ &= 1 - \left(\frac{\pi^2}{8} (2p+1)^2 - 1 \right) \frac{\left(\frac{\lambda_p}{\lambda} \cos \theta \right)^2}{1 - \left(\frac{\lambda_p}{\lambda} \cos \theta \right)^2} + \frac{\pi^4}{384} (2p+1)^4 \frac{\left(\frac{\lambda_p}{\lambda} \cos \theta \right)^4}{1 - \left(\frac{\lambda_p}{\lambda} \cos \theta \right)^2} \\ &> 1 - \left(\frac{\pi^2}{8} (2p+1)^2 - 1 \right) \frac{\left(\frac{\lambda_p}{\lambda} \cos \theta \right)^2}{1 - \left(\frac{\lambda_p}{\lambda} \cos \theta \right)^2} \geq 1 - \left(\frac{\pi^2}{8} (2p+1)^2 - 1 \right) \left(\frac{\lambda_p}{\lambda} \right)^2 \end{aligned} \quad (197)$$

Then, for $\left(2\pi \frac{(2p+1)\lambda_p}{4\lambda}\right)^4 \ll 1$, for all $\theta \in [0, \pi]$, we obtain:

$$1 \sim \left(1 - \left(\frac{\pi^2}{8}(2p+1)^2 - 1\right)\left(\frac{\lambda_p}{\lambda}\right)^2\right)^2 < \frac{\xi_3\left(\theta, \frac{\lambda_p}{\lambda}, p\right)}{\sin^3 \theta} < 1 \quad (198)$$

Finally, for $\left(2\pi \frac{(2p+1)\lambda_p}{4\lambda}\right)^2 \ll 1$, multiplying the inequation by $\sin^3 \theta$ and integrating over $\theta \in [0, \pi]$, we obtain a value independent of $\frac{\lambda_p}{\lambda}, p$:

$$\xi_2\left(\frac{\lambda_p}{\lambda}, p\right) \approx \xi = \frac{1}{2\pi} \int_0^\pi \sin^3 \theta d\theta = \frac{2}{3\pi} \approx 0.21 \quad (199)$$

Therefore we can write the radiation resistance of a short odd-resonant CNT dipole as:

$$R_{r,(2p+1)\frac{\lambda_p}{4}} = \left(\frac{\lambda_p}{\lambda}\right)^2 \sqrt{\frac{\mu}{\epsilon}} \xi \approx 120\pi \times \frac{2}{3\pi} \left(\frac{\lambda_p}{\lambda}\right)^2 = 80 \left(\frac{\lambda_p}{\lambda}\right)^2 \quad (200)$$

Appendix 5 – Photolithography process

Table 8 relates the standard guidelines for negative and positive photolithography in Cleanroom 2, N2FC, NTU EEE. A few variations can be made on the different process times depending on the UV lamp intensity or on the cleaning (e.g. alternative use of sonication in the solvents at room temperature) and opening procedures depending on what is originally on the wafer. Specifically, in the case where electrodes are fabricated on top of the CNTs, wafer cleaning is either skipped or, if the CNTs are well attached to the substrate, done with a lighter hand by running acetone, IPA then DI water at room temperature along the substrate then drying with an N2 gun. Step 9 is skipped as it would etch away the CNTs in the openings.

Table 8. Standard guidelines for negative and positive photolithography in Cleanroom 2, N2FC, NTU EEE.

No.	Step	Instructions for negative lithography	Positive lithography
1.	Clean maskplate	Clean with acetone then IPA. DI water 5min. 110°C dehydration 5 min. Cool down 2-3 min.	Idem
2.	Clean wafer	Boiling acetone 2 min. Boiling IPA 2 min. DI water 5min. 110°C dehydration 10 min.	Idem

		Cool down 3 min.	
3.	Spin photoresist AZ 5214	Spin speed 4000 rpm 30 sec. 105°C soft bake 1 min.	Idem
4.	Align and expose	14 mW, 3.0 sec. (with mask)	25 sec. (with mask)
5.	Post exposure bake	110°C, 7.5 min.	Idem
6.	Flood expose	25 sec. (no mask)	Nothing
7.	Develop	AZ developer : DI water = 1 : 2 (50 : 100 ml) 120 sec. (approx.) Rinse with DI water to stop the reaction	Idem
8.	Inspect	Check test structures and patterns.	Idem
9.	O ₂ plasma descum	O ₂ gas flow=20sccm, RFpower=30W, 2mins	Idem

Table 9 describes a procedure for metal evaporation and lift-off. In our case the thicknesses are Ti/Au 100nm/1µm. The lift-off procedure was often simplified to soaking in acetone overnight. For very difficult lift-offs on larger patterns, a cleanroom Q tip can be used to softly brush the surface.

Table 9. Procedure for metal evaporation and lift-off.

No.	Step	Instruction
1.	Evaporate metal	Ti / Au 50 nm / 50 nm.
2.	Lift-off	Boil acetone Soak in boiled acetone for 10 min. Spray with acetone. Soak in AZ300T for 10 min. Soak in acetone for ~8mins. Soak in IPA for ~8mins. DI water 5min. 110°C dehydration 10 min.
3.	Inspection	Check test structures.

Appendix 6 – Ethanol CVD runs

Table 10 reports the variations in the various runs of the ethanol CVD recipe reported in section III.B.2.2). The program of the furnace corresponding to this process is as follows for E0.07:

MODE RES
PGM 1
SSP 25
StC 0

SP1	850	TM1	0.18
SP2	900	TM2	0.05
SP3	900	TM3	0.22
SP4	900	TM4	0.40
SP5	25	TM5	0.25
EV1	0		
AL1	9	A1	1010
HY1	1		
EV2	0		
AL2	OFF		
JC	0		
WtZ	OFF		

Table 10. Ethanol CVD recipe runs

Step Process	Flush	Ramp-up	Stabilization	Annealing	Growth	Cool-down	Remarks
E0.01 22/02/ 12	N ₂ and quick through bubbler	N ₂ @1000s ccm 15min	Ar@100s ccm 5+2min	Ar@50sccm H ₂ @100s ccm 10min	Ar@80sccm H ₂ @40sccm Ethanol bubbler 40min	Ar@80sccm H ₂ @40sccm 25min	N ₂ flush Small bubbler
E0.02	idem	18min	No gas	No gas for 4min then as before but 10min then Ar@100s ccm H ₂ @200s ccm 5 min	30min	Ar@100sccm	No gas because only N ₂ open at first
E0.03	idem	idem	Ar@200s ccm 5+2min	Ar@50sccm H ₂ @100s ccm 10min	40min	Idem but Ar+H ₂ until 1h40 (404°C) and bubbler until 1h30 (570°C instead of 200°C)	Growth recipe kept during cool down, furnace closed
E0.04 15/03/ 12	N ₂ @2000sccm through direct Ar@200sccm through bubbler	idem	idem	idem	Idem	Idem	No errors
E0.05 15/05/ 12	Without tube: direct N ₂ 1h,	N ₂ @2000s ccm 18min	idem	idem	Idem	Idem H ₂ @40sccm until	Gas recipe 2 min

	bubbler Ar@200scc m then H ₂ @50scc m then Ar few minutes					cool down to 700°C	late from anneali ng to growth
E0.06 12/10/ 12	Without tube: direct Ar@1000sc cm, bubbler Ar@80scc m H ₂ @50scc m	Ar@500scc cm	idem	idem	Idem	Ar@200sc cm then 1000sccm (at 1:30:00)	No more N ₂ on system
E0.07 02/11/ 12	idem	Ar@2000s ccm	idem	idem	Idem	Ar@1000s ccm	New tall bubbler
E0.08 14/05/ 13	idem	Ar@1000s ccm	idem	idem	Idem	idem	NA
E0.09 16/09/ 13	idem	From room T: air with pump, plateau at 700°C, 10min, then Ar@1000s ccm as usual	idem	idem	Idem	idem	Extra anneali ng in air to burn away any remaini ng resist

Appendix 7 – Additional CPW gap devices and photocurrent investigations

Many devices were fabricated on each sample with variable number of CNTs bridging the gap on the signal line as can be seen from the selection on Fig. 161, Fig. 162, Fig. 163 and Fig. 164. Due to time constraints these have not been characterized yet. They should provide a valuable additional input to the present work. In the legends below, E0.0x is the growth recipe as reported in Appendix 6 and the numbers are the devices name as follows: mnp where mn is the size of the gap in micrometers and p is the repetition number of this size on the sample. The large rectangular pads on the pictures are the gold electrodes, the thin vertical lines are the CNTs.

Measurement was attempted on E0.02 G202 (54 CNTs) in Paris at UPMC-CNRS laboratory L2E with the help of Charlotte Tripon-Canseliet. The setup used was IV

measurement with Kelvin probes under illumination from an 800-nm continuous-wave fiber laser adjusted over the gap through a 60- μm -diameter lensed optical fiber attached to a micromanipulator. The beam can be approximated as having the same diameter as the fiber as the fiber tip is brought down onto the sample. Initial results have shown a decrease in current when the laser was lit on with minutes-long recovery times. This effect is likely due to some thermal inhibition induced by laser heating while photocurrent could not be observed because of a large mismatch between the energy of the laser photons and the bandgap of the semiconducting CNTs. The large number of connected CNTs also suggests there should be about 18 metallic CNTs linking the two electrodes which would dominate the response. Sample E0.02 was left in L2E for further investigation with other lasers, tunable in the telecom range of wavelength which better matches the primary bandgaps of 1-2nm-diameter CNTs.

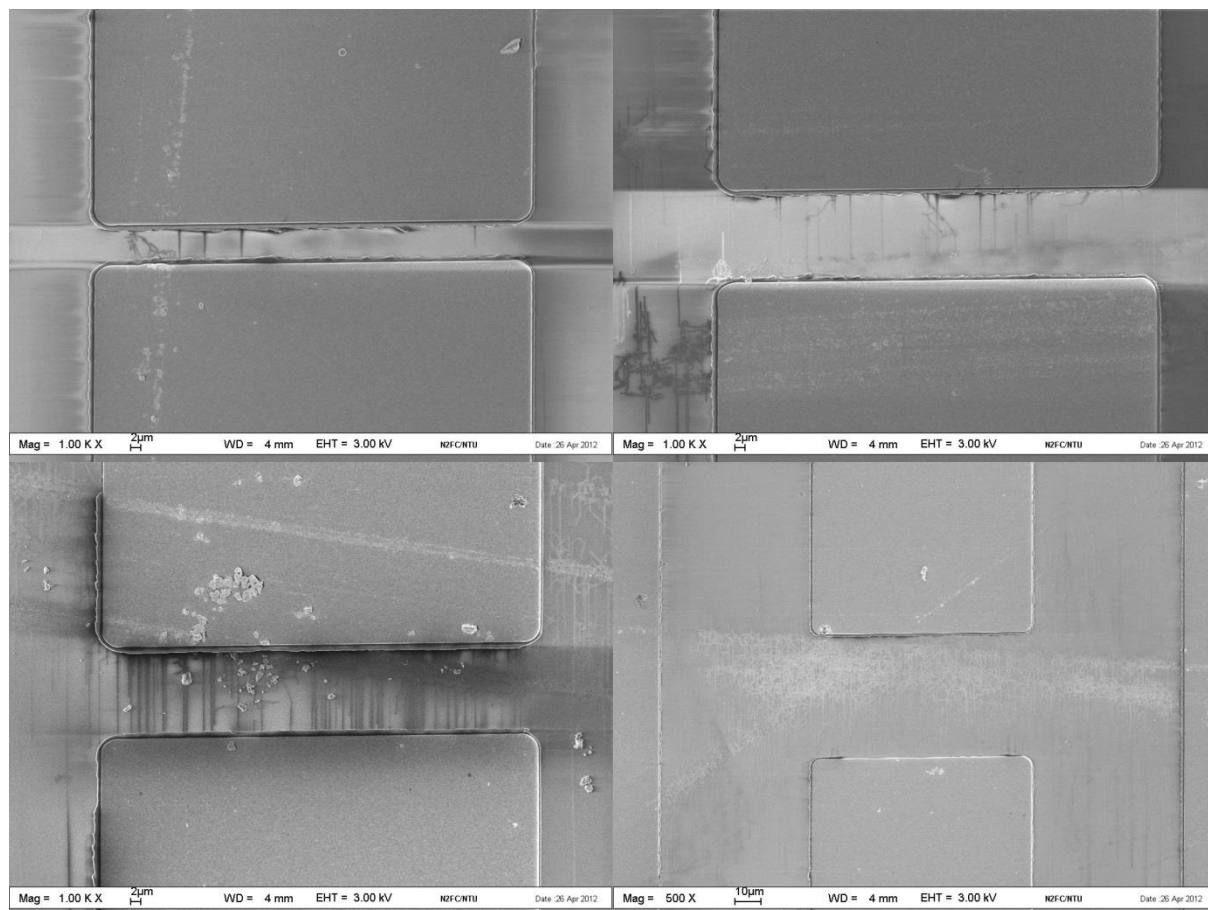


Fig. 161. E0.02: 101, 201, 202, 501 (from left to right, top to bottom).

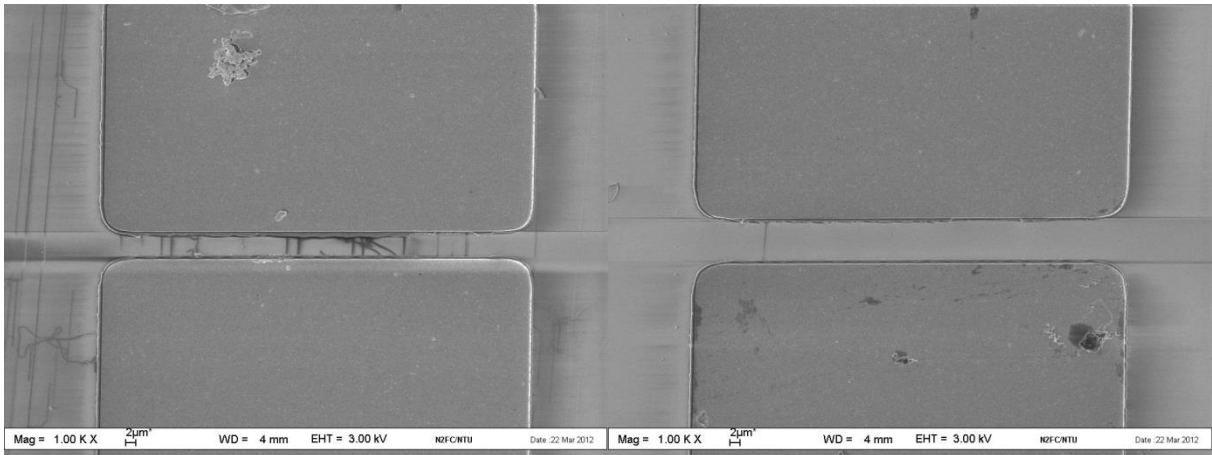


Fig. 162. E0.03: 052, 102 (from left to right).

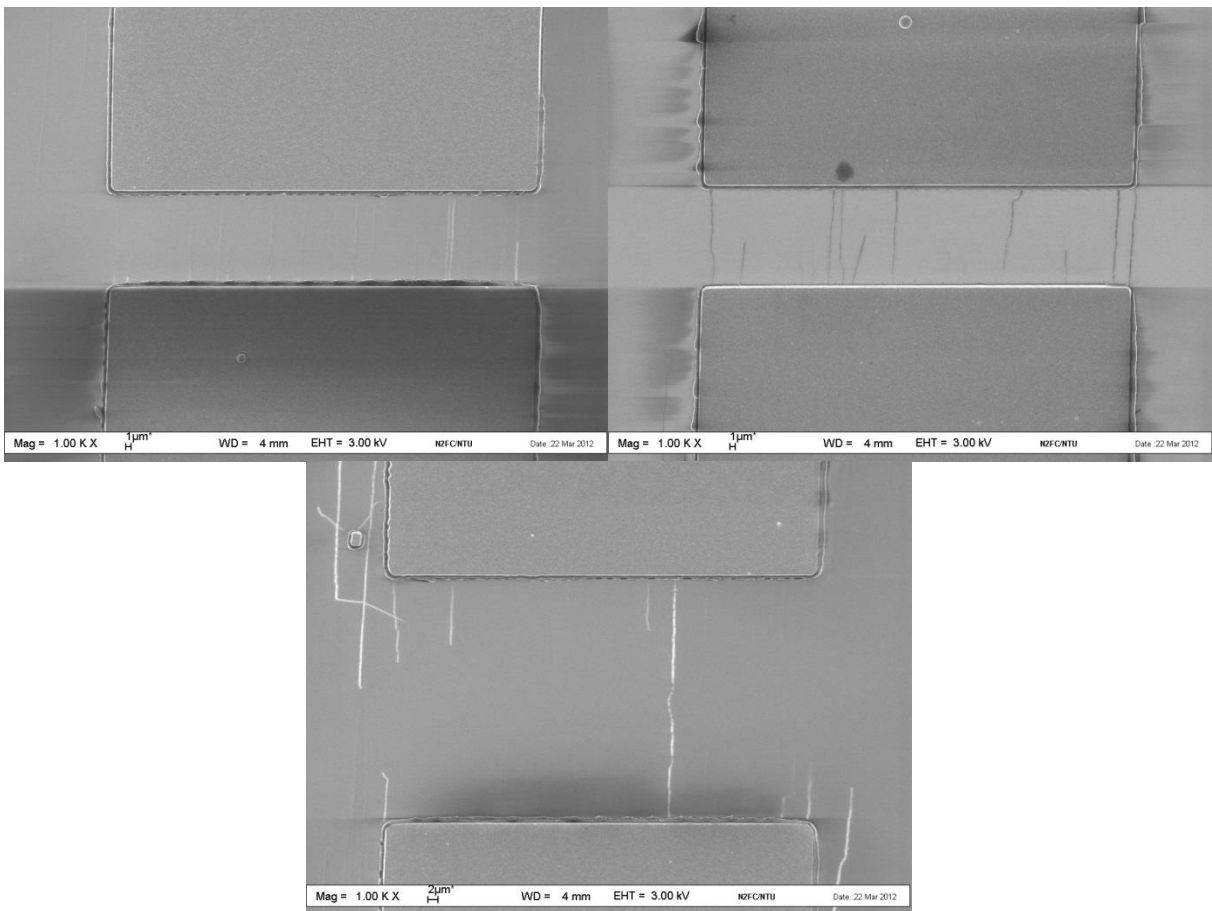


Fig. 163. E0.04: 201, 202, 501 (from left to right, top to bottom).

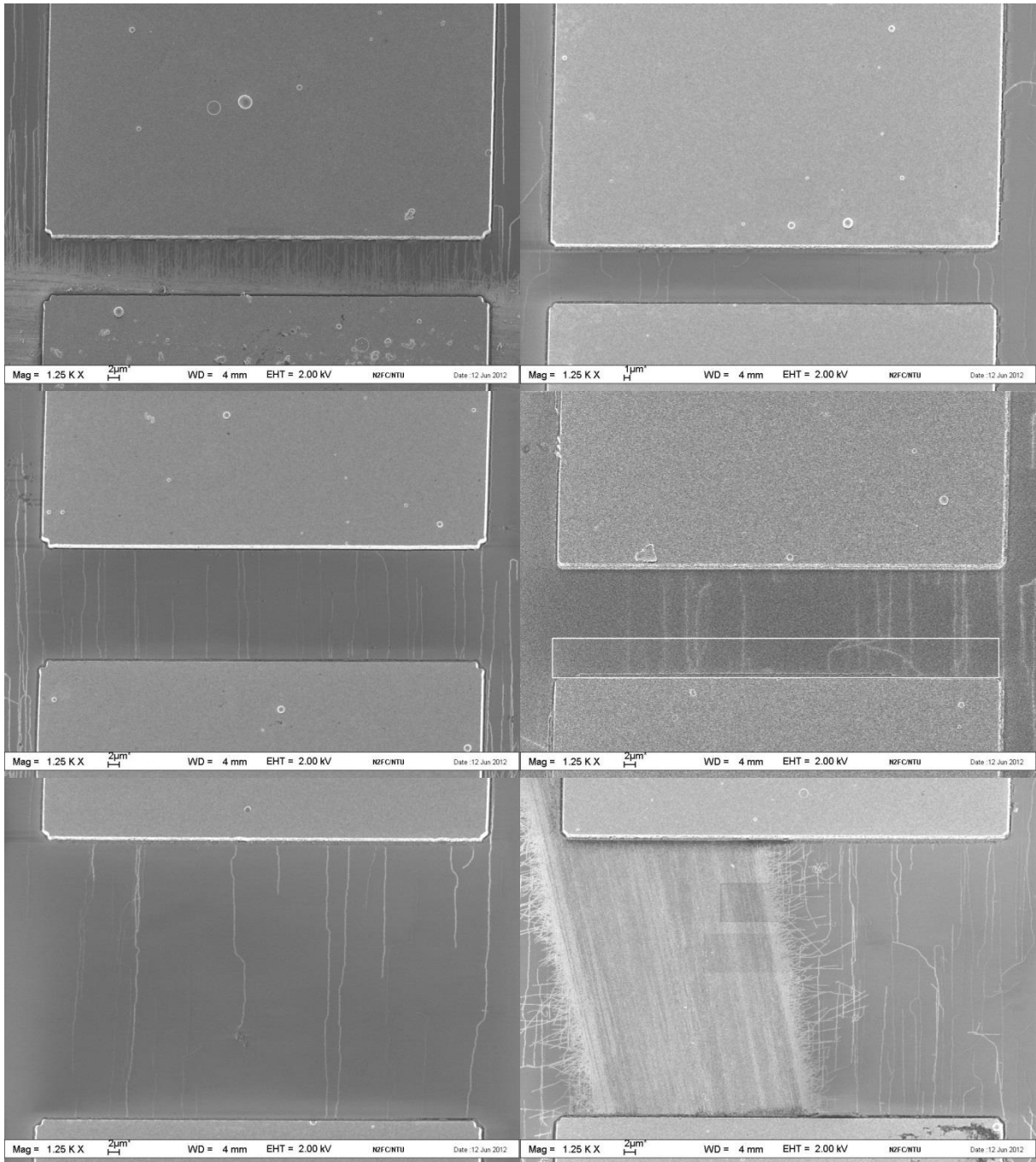


Fig. 164. E0.05A: 102, 103, 201, 203, 502, 503 (from left to right, top to bottom).

Appendix 8 – KOH-based initial vertical monopole designs

Two potentially valid but technologically demanding monopole designs were elaborated and studied before the much simplified final vertical rod design reported in section IV.D.1.1) was adopted. We report the concepts and first validations.

The problematic was to adapt the ideal case presented in section IV.A) to a feasible experimental feed. However, simply using a common microstrip line to feed the monopole is

impractical. Indeed that would imply using full substrate thickness to propagate the wave before reaching the antenna rod. However the thickness of the substrate – a few hundred micrometers – separating the ground plane from the rod would then be about one order of magnitude larger than the length of the rod. The substrate would act as a non-negligible part of the length of the antenna while not confining the currents like a rod would – making design and interpretation very complicated and creating inefficient antennas.

The idea was thus to use KOH (potassium hydroxide commonly known as caustic potash) to etch the substrate and realize a transition between the full substrate thickness and a thin membrane where the antenna would be positioned. Indeed KOH etching of 100 silicon produces has preferential directions producing cavities or pyramids with walls forming an angle of 54.74deg with the surface (see [244] for experimental conditions and modeling).

A8.1) SMP connector in a cavity with capacitive coupling

A first design, illustrated Fig. 165, was conceived. A cavity is wet-etched in a back-metallized silicon substrate by KOH. A CNT rod is grown by patterned-catalyst CVD at the bottom of it. An SMP (coaxial) connector is inserted with its pin coming through the remaining Si membrane at the bottom of the cavity while its ground is connected to the metallized back of the substrate to form the planar ground of the monopole antenna. The CNT rod is capacitively-coupled to the pin which has the advantage to remove the uncertainty over the contact resistance. Indeed the coupling capacity is not dependent of the atomic configuration at the contact and can be modeled in function of the geometry and material parameters.

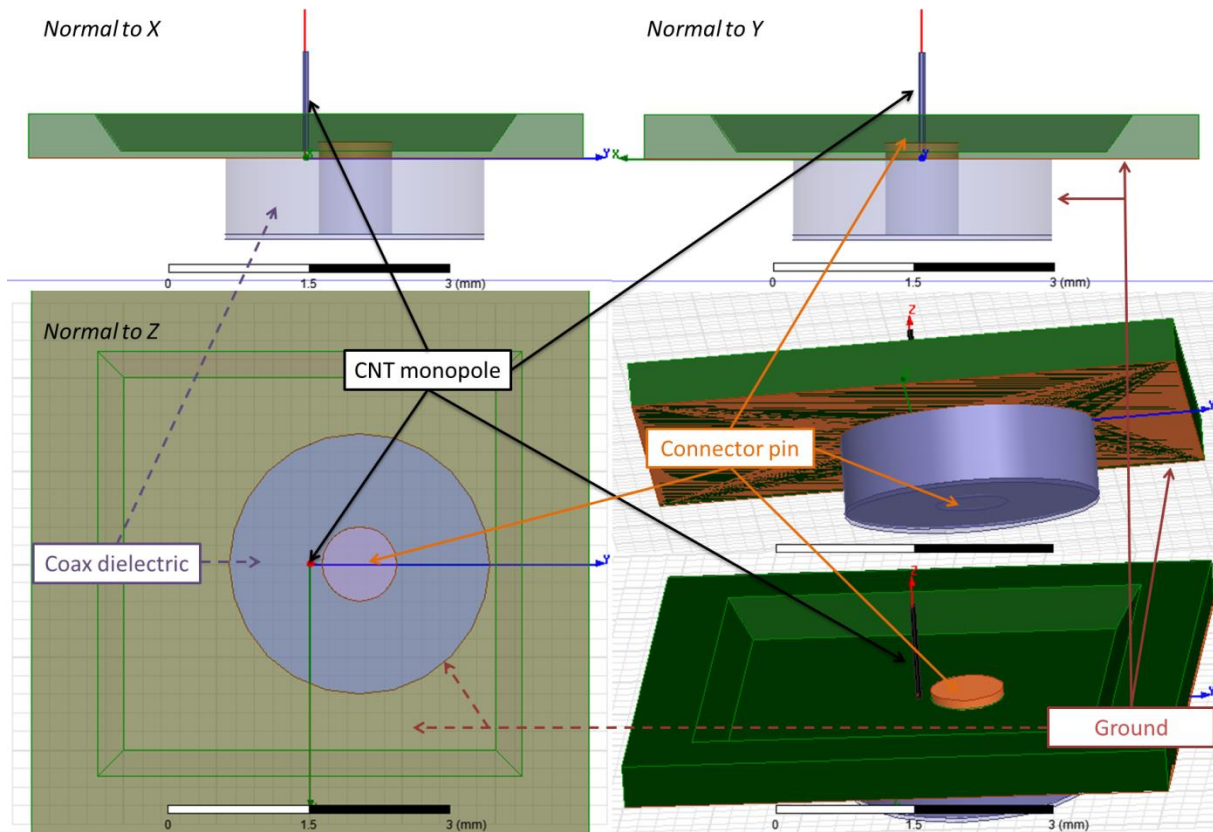


Fig. 165. Capacitively-coupled CNT monopole. Design structure. A cavity is wet-etched in a back-metallized silicon substrate by KOH. A CNT rod is grown at the bottom of it. The CNT rod couples to the pin of an SMA connector that comes through the remaining Si membrane at the bottom of the cavity while the ground of the coaxial connector is connected to the metallized back of the substrate as the planar ground of the monopole antenna.

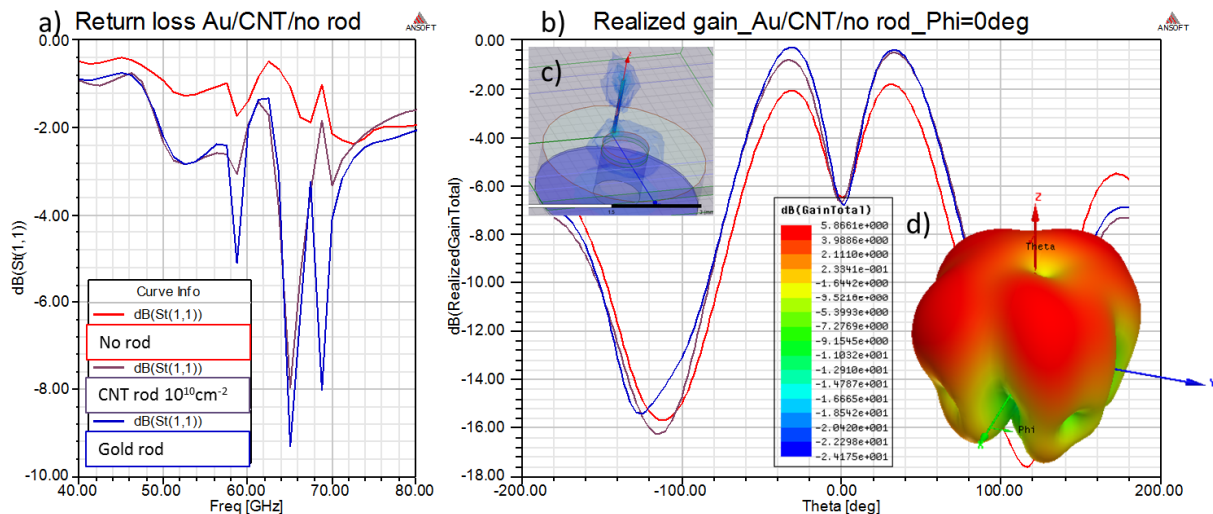


Fig. 166. Capacitively-coupled CNT monopole. a) Return loss shows a resonance at 65GHz for both CNT and gold rods. b) The realized gain, ratio of the power emitted to the power at terminals, is almost 0dB at $\pm 40^\circ$ with rods, 2dB higher than without. c) Electric field plot showing the excitation of a resonance in the CNT rod. d) 3D far-field gain of the structure.

The principle of the design was validated by simulations that showed that a 1.08mm rod resonates around 65GHz provided the conductivity of the rod is sufficient (cf. Fig. 166). There is only resonance for gold and CNTs proving the rod is indeed the radiating part. If the CNT density is divided by 100 or the length randomly made shorter than a quarter-wavelength the resonance disappears. The structure should work with carefully designed electrically-short CNT antennas, but we did study it because the technical challenges for the fabrication seemed too important. Furthermore connectors designed for operation above 110GHz, where CNTs become interesting, are difficult to source.

A8.2) KOH-etched microstrip line.

The second design is a normal microstrip line over a KOH-etched silicon substrate (cf. Fig. 167). The back of the wafer (cavity) is covered with metal to define the ground of the line and of the monopole. Hence the thickness of the substrate is classical at input and adapted to the low thickness needed for the CNT monopole at the center of the cavity where the CNT rod is standing on top of the line. The device can thus be connected by Wiltron fixture or by adding a CPW to microstrip transition. An advantage of the structure is that the CNT rod is aligned with the microstrip electric-field lines.

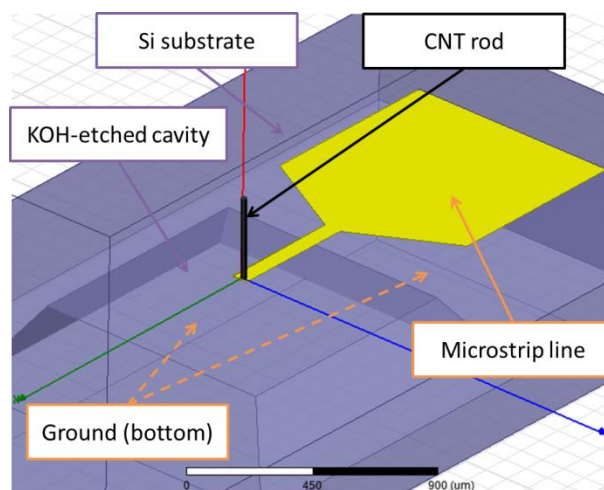


Fig. 167. Structure of the KOH-etched-microstrip-fed monopole antenna.

To keep a given characteristic impedance – like the standard 50Ω – the width of the line can be tapered over the transition slope from the width necessary at full thickness to the width necessary on the Si membrane. Rigorously the taper should follow the non-trivial formula of microstrip line characteristic impedance [245] but, because these transitions are rather short, a linear taper is a sufficient approximation. The transition is actually a steep step.

Maintaining the characteristic impedance constant should prevent return loss but the confinement of the field is increased by a large factor over a fraction of a wavelength. A smoother transmission could be achieved by etching concentric squares to produce steps the spacing of which could be adjusted to obtain a reduced effective slope.

Finally, when needed, an impedance match can be achieved either by introducing a quarter-wavelength line of appropriate characteristic impedance next to the antenna (where it is smaller) or by optimization of the taper and the final line section.

The CPW design was studied by Christophe Brun during his PhD in CINTRA and XLIM [246]. The CNT rod parameters were determined using the CNT Antenna designer spreadsheet elaborated in section IV.A.2). He conceived a full design including 50-Ω CPW probe pads, a CPW-microstrip transition and a final 50-Ω microstrip section as illustrated on Fig. 168. As established with the CNT Antenna designer spreadsheet and simulated with the EM bulk model, using 1027 150-μm-long CNTs packed in a bundle of radius 2.2μm produces an excellent impedance match at 50Ω of -24.5dB at 235GHz while no resonance can be observed for the same rod if it is made of gold around this frequency. Indeed a classical gold wire will need to be more than twice longer – 325μm long with an optimal 11μm radius – to resonate at 232GHz.

However the performance of the CNT rod may not be compared to that of the larger antenna: it has -4dB gain versus +2.8dB gain for the resonant gold monopole. Rather, the performance should be evaluated relative to the short gold wire admitting that the application requires an electrically-short antenna. The gain should then be 2dB higher as evaluated in section IV.A.1.1) while there will be an additional improvement on the realized gain due to the good impedance match at resonance for the CNT antenna.

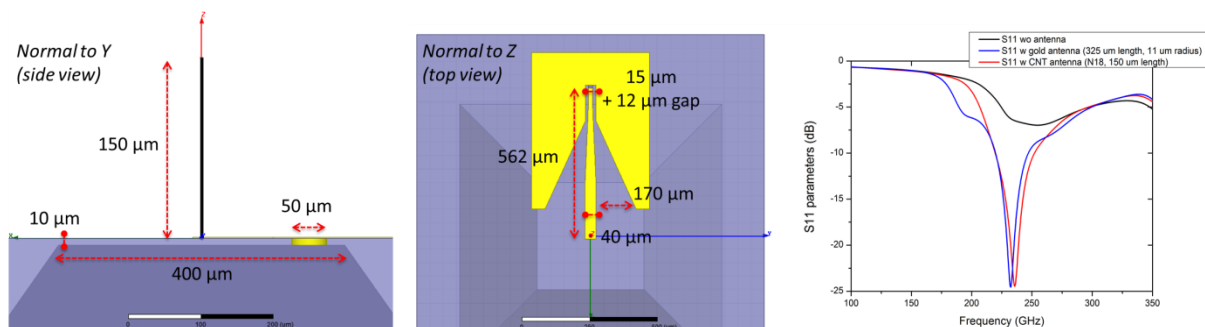


Fig. 168. Design of mixed CPW-microstrip feedline for 50- Ω monopole antennas by Christophe Brun and return loss with a 325- μm -long gold wire (blue), a 150- μm -long rod made of 1027 CNTs (red) and no rod (black).

Initial tests were led by Hong Li at CINTRA/NTU EEE for the KOH etching of the cavity. However a number of the necessary processes presented uncertainties. The KOH etching rate needed to be extremely well calibrated to dig $\sim 450\mu\text{m} \pm 10\mu\text{m}$ in a silicon substrate which itself is given with a $\pm 25\mu\text{m}$ variability on its thickness – thus requiring a pre-measurement of each sample. An additional concern was whether the thus produced 10- μm -thick silicon membrane could sustain the rapid and extreme condition changes involved in the TCVD growth of the CNTs. Finally the technology for metalizing the vias was not available (but the transition may be realized without them). An additional concern was the large number of steps needed which largely increased the failure rate. A simpler design was therefore adopted as described in the next section.

Appendix 9 – Second batch of monopole antennas

As indicated in section IV.F.4), a second much more ambitious batch is underway with the experiment plan exposed below. The fabrication is undertaken at CINTRA/NTU EEE and Aixtron by Chin Chong (Ray) Yap, Wai Leong Chow, Dunlin Tan and Cong Xiang Lu with coordination by Chong Wei Tan. All are part of Beng Kang Tay's group. If fabricated in time this batch could be measured in IEMN together with the initial batch.

A9.1) Catalyst patterns study

Bottom-left dense square of catalyst patterns [16 samples]

- 4 samples on Pt/Ti (full coverage) on SiO₂/Si
 - 4 samples on SiO₂/Si
 - 4 samples on Pt/Ti (full coverage) on Quartz
 - 4 samples on Quartz
- ⇒ 4 varieties
- ⇒ 4 growth times will allow deducing the growth rate and studying the respective stability of each of the 6 catalyst patterns with aspect ratio
- ⇒ target lengths, adapting growth times accordingly from previous experience and first growth, are set at: 20, 50, 100, 200 μm

A9.2) Actual Designs

For CNT lengths targets we indicate three numbers: the antenna is designed for L1 which is assuming, with 1000CNTs, a reduction factor of about 2 of the normal resonant length (L3). However the actual CNT number will be 1700 and more so where possible we could adapt the length to be 60% of L3 (L2). One additional length should be fabricated: the nominal length (L3) where possible or the longest bundle possible according to the catalyst patterns study: $\min(L3, \text{maxstanding})$.

Vertical monopole (300GHz on metal (A) and substrate (B)) <SiO2/Si Wafer> [10 samples]

- (Z, A) [6 samples]
- (Y, B) [3 samples] because the holes in B are matched to Y, not to Z
- (Z, B) [1 sample] anyway for more repeatability of the most interesting patterns

⇒ Length: **100**, 120, 250 μm

Horizontal monopole (200 and 300GHz) <Quartz> [12 samples]

- (Z, 1) [3+1 samples] 300GHz

⇒ Length: **78**, 117, 180 μm

- (Z, 2) [3+1 samples] 200 GHz
- (Z, 3) [3+1 samples] 200 GHz – wider

⇒ Length: **116**, 140, 240 μm

⇒ The +1 samples are to be aligned on metal as explained in section IV.E.1) (the others are aligned normally so in the config 50-50). If this seems too complicated, please replace the +1 samples by 3x (Z M) on quartz.

Vertical monopole (200GHz) <SiO2/Si Wafer> [3 samples]

- (W, C) [3 samples]

⇒ Length: **150**, 180, 350 μm

Horizontal monopole (90GHz) <Quartz> [3 samples]

- (W, 4) [3 samples]

⇒ Length: **272**, 326, 550 μm

TOTAL NUMBER OF SAMPLES [44 SAMPLES]

Appendix 10 – Useful tools

Some designs of CNTs were realized using the Nanotube Modeler by JCrystalsSoft [247].

Detailed Table of Contents

Acknowledgements	3
Contents	7
Introduction	9
Chapter I) Carbon nanotubes for antenna applications	15
I.A) Structure.....	15
I.B) CNT fabrication methods.....	17
I.C) Optical and optoelectronic properties	17
I.D) Applications in electronics and RF	19
I.E) Optical control.....	20
I.F) Methodology	20
Chapter II) Carbon nanotube modeling	25
II.A) Existing models, usage and necessity of a new approach	25
II.A.1) Density Functional Theory	26
II.A.2) Combined Maxwell-Schrödinger approach.....	27
II.A.3) Effective surface conductivity	28
II.A.4) Circuit model	31
II.A.4.1) Lumped-element circuit model for a transmission line.....	32
I.A.1.1) Metallic SWCNT	34
II.A.4.2) MWCNT and bundles	39
II.A.4.3) Implementation.....	41
II.A.5) Bundle modeling and necessity of a new approach	42
II.B) Effective medium approach.....	43
II.B.1) Anisotropic bulk model	44
II.B.1.1) Methodology.....	44
II.B.1.2) Scale considerations	44
II.B.1.3) Bulk nanowire equivalent to a nanotube	45
II.B.1.4) Array of aligned nanowires	46
II.B.2) General derivation	47
II.B.2.1) Axial bulk conductivity	47
II.B.2.2) Transverse bulk conductivity.....	48
II.B.3) Application to carbon nanotubes	50
II.B.3.1) Metallic SWCNTs	50
II.B.3.2) Semi-conducting SWCNTs and mixed SWCNT bundles	53
II.B.3.2.1) General case of mixed SWCNT bundles	53
II.B.3.2.2) Respective influence of semi-conducting and metallic SWCNTs.....	55
II.B.3.3) Multi-wall CNTs.....	57
II.C) Implementation and validation	61
II.C.1) Implementation	61
II.C.1.1) Implementation in EMXD	62
II.C.1.2) Implementation in HFSS	63

II.C.2) Theoretical validation	64
II.C.2.1) Application to dipoles of bundled carbon nanotubes	64
II.C.2.2) Supporting results	65
II.C.2.3) Comparative performance	68
II.C.2.4) Conclusion	69
II.C.3) Experimental retrofitting	69
II.C.3.1) Application to a microstructure	69
II.C.3.1.1) Application to a microstructure	69
II.C.3.1.2) Results.....	71
II.C.3.2) DEP samples.....	72
II.C.3.3) Toppled-CNT samples.....	73
II.D) Conclusion on simulation techniques.....	73
Chapter III) Development of CNT-based electronics fabrication techniques	79
III.A) Conventional fabrication techniques.....	79
III.A.1) Patterning	80
III.A.1.1) Selective-masking-based techniques.....	80
III.A.1.1.1) Photolithography	80
III.A.1.1.2) Shadow mask	81
III.A.1.1.3) Polystyrene beads.....	82
III.A.1.2) Direct writing	83
III.A.1.2.1) Inkjet	83
III.A.1.2.2) Laser writing	84
III.A.1.2.3) Electron-beam lithography.....	84
III.A.1.3) Stamping	85
III.A.2) Deposition and coating.....	86
III.A.2.1) E-beam evaporation and sputtering.....	86
III.A.2.2) Electroplating	87
III.A.2.3) Spin-coating	87
III.A.2.4) Spray coating.....	88
III.A.3) Etching	88
III.A.3.1) Wet etching	88
III.A.3.2) Dry etching.....	89
III.B) CVD growth of CNTs	89
III.B.1) Equipment	89
III.B.1.1) Aixtron BlackMagic II	90
III.B.1.2) TCVD systems	90
III.B.2) Growth recipe	92
III.B.2.1) PE- and TCVD growth of vertical arrays.....	92
III.B.2.2) Ethanol TCVD growth of aligned CNTs.....	92
III.B.3) Catalyst study	94

III.B.3.1) Scratch catalyst.....	95
III.B.3.2) Solution-based catalyst.....	96
III.B.3.3) CNT density control by catalyst lines spacing	97
III.B.4) Additional interesting perspectives: combining CNTs and SiNWs	100
III.C) Structures fabrication	103
III.C.1) DEP-aligned CNTs in CPW gap	103
III.C.2) Sprayed-CNT samples.....	104
III.C.3) Lattice-aligned CNTs in CPW gap.....	106
III.D) Considerations for experimentally-realizable CNT antennas	107
Chapter IV) Resonant electrically-short CNT antennas	111
IV.A) Trade-offs and tools	111
IV.A.1) First observations	111
IV.A.1.1) Single-SWCNT-arm antennas	111
IV.A.1.2) Improving performances: MWCNTs and bundles.....	117
IV.A.1.3) Effect of bundling and trade-offs	118
IV.A.1.3.1) Structure and methodology	118
IV.A.1.3.2) Results.....	119
IV.A.1.3.3) Initial interpretation and conclusions	121
IV.A.2) CNT monopole circuit model	122
IV.A.2.1) Derivation	122
IV.A.2.1.1) Derivation in the general case	123
IV.A.2.1.2) Case of negligible conductance.....	125
IV.A.2.2) Implications for the design of CNT-based antennas.....	127
IV.A.2.2.1) Moderate and low-loss regime	127
I.A.1.1.1.1) Definition	127
IV.A.2.2.1.1) Rigorous effect of the number of CNTs in the bundle	128
IV.A.2.2.1.1.1) Derivation of the phase velocity	129
IV.A.2.2.1.1.2) Discussion	131
IV.A.2.2.1.1.3) Input impedance for moderate and low-loss	132
IV.A.2.2.1.2) Attenuation.....	133
IV.A.2.2.2) High-loss regime	134
IV.A.2.3) Application to the study of CNT monopoles	135
IV.B) THz characterization and THz FSS	137
IV.C) Prototypes from lattice-aligned metallic SWCNTs on quartz	139
IV.C.1) Quartz dipole.....	139
IV.C.1.1) Design and experimental realization.....	139
IV.C.1.2) Parametric study.....	141
IV.C.1.2.1) CNT characteristics	141
IV.C.1.2.2) Antenna geometrical configuration	143
IV.C.1.2.3) Bundle parameters and trade-offs.....	145

IV.C.1.3) Transmission	147
IV.C.1.3.1) Symmetric links	147
IV.C.1.3.2) Dissymmetric links.....	148
IV.C.1.3.2.1) CNT-dipole to conventional dipole.....	148
IV.C.1.3.2.2) Contactless read-out of nanodevices	149
IV.C.1.4) Conclusion of the planar dipole study.....	153
IV.C.2) Coplanar-waveguide-fed dipole and monopole	154
IV.C.2.1) Coplanar-waveguide-fed dipole	154
IV.C.2.2) Coplanar-waveguide-fed monopole	155
IV.C.2.2.1) Feed design and general considerations	155
IV.C.2.2.2) CNT strip design and improved conductivity	156
IV.C.2.2.2.1) CNT density and lengths variation.....	156
IV.C.2.2.2.2) Improved effective conductivity with metal inserts.....	157
IV.C.2.2.3) Initial fabrication results on designed CNT strips.....	158
IV.D) Prototypes from vertically-grown CNTs	159
IV.D.1) Design	160
IV.D.1.1) Vertical monopole.....	160
IV.D.1.2) Aspect ratio issue and monopole cross-sectional shape	162
IV.D.1.3) Toppled-CNT horizontal monopole.....	169
IV.D.1.3.1) Fabrication	169
IV.D.1.3.2) Design and analysis.....	170
IV.D.1.3.2.1) Initial study	170
IV.D.1.3.2.2) Final designs	173
IV.D.1.3.3) Performance	176
IV.D.1.3.4) Transmission.....	179
IV.E) Mask design.....	181
IV.E.1) Feed designs arrangement	183
IV.E.1.1) Arrangement of individual designs	183
IV.E.1.2) Mixed designs arrangement	184
IV.E.2) Catalyst patterns arrangement	187
IV.E.2.1) Vertical CNT rod catalyst patterns.....	187
IV.E.2.2) Horizontal CNT strips patterns	188
IV.F) Fabrication and characterization.....	190
IV.F.1) Design specifications, yield and RF characterization.....	190
IV.F.2) Fabrication of the vertical and toppled monopoles	191
IV.F.3) Visual inspection and material characterization.....	193
IV.F.4) Second batch.....	195
IV.G) Conclusion on CNT-based antenna design	195
Chapter V) Initial characterization towards optical control	197
V.A) Photocurrent samples: sorting metallic and semi-conducting CNTs	197

V.A.1) Selective growth.....	198
V.A.2) Sort in solution	199
V.A.3) Imperfection-immune design	200
V.A.3.1) Concept	200
V.A.3.2) CPW gap samples	200
V.A.3.3) Sprayed-CNT samples with interdigitated electrodes.....	202
V.A.4) Post-processing	205
V.B) Measurement and characterization	207
V.B.1) Physical characterization	207
V.B.1.1) Raman spectroscopy	207
V.B.1.1.1) Sprayed CNT films	209
V.B.1.1.2) CVD-CNT-bridged CPW gaps.....	210
V.B.1.2) Atomic Force Microscopy	213
V.B.2) Photocurrent characterization.....	213
V.B.2.1) Photocurrent setup	213
V.B.2.2) Characterization range.....	216
V.B.2.3) Measurement results	217
V.B.2.3.1) CVD-CNT-bridged CPW gaps.....	217
V.B.2.3.1.1) Gap bridged by 13 to 16 CNTs of mixed chirality	217
V.B.2.3.1.2) Gap bridged by a single semiconducting-SWCNT.....	219
V.B.2.3.2) Sprayed-CNT films.....	223
V.C) Clues for analysis and design	228
V.C.1) Photovoltaic current vs. Photothermoelectric current	229
V.C.2) Antenna designs	229
V.C.2.1) Tunable PIFA	230
V.C.2.2) Rejection-band antenna	230
V.C.2.3) Low profile corrugated antennas	231
Chapter VI) Conclusion and outlook	233
VI.A) Summary of the main achievements	233
VI.A.1) Modeling	234
VI.A.2) Fabrication	235
VI.A.3) Design	235
VI.A.4) Optical control	236
VI.B) Conclusions on CNT-based antennas	236
VI.C) Outlook on related slow-wave technologies	237
VI.C.1) Metamaterial substrate	237
VI.C.2) Graphene and hybrid structures	238
Bibliography	241
Personal publications (17).....	241
Bibliography.....	243
Appendices	257
Appendix 1 – Effective circuit diagram for an SWCNT.....	257
Appendix 2 – Fortran codes for the complex properties in EMXD	259
Appendix 3 – Matlab code to enhance contrast in SEM images.....	262

Appendix 4 – Radiation resistance	263
Appendix 5 – Photolithography process	265
Appendix 6 – Ethanol CVD runs	266
Appendix 7 – Additional CPW gap devices and photocurrent investigations	268
Appendix 8 – KOH-based initial vertical monopole designs.....	271
A8.1) SMP connector in a cavity with capacitive coupling.....	272
A8.2) KOH-etched microstrip line.....	274
Appendix 9 – Second batch of monopole antennas	276
A9.1) Catalyst patterns study	276
A9.2) Actual Designs	277
Appendix 10 – Useful tools.....	278
Detailed Table of Contents	281
List of Figures	289
List of Tables.....	301
List of Equations.....	303
Abstract	309

List of Figures

Fig. 1. Chiral vector of CNTs (adapted from www.sanken.osaka-u.ac.jp).	16
Fig. 2. Structure of the three main types of SWCNTs. Source: http://coecs.ou.edu/Brian.P.Grady/images/nanotube.jpg	16
Fig. 3. Density of states in SWCNTs and bandgaps E_{11} and E_{22} between van Hove singularities. Source: Wikipedia	18
Fig. 4. Kataura plot from [41] (R. B. Weisman et S. M. Bachilo, 2003)	18
Fig. 5. Typical photoluminescence map of a CNT sample. Source: Wikipedia.	19
Fig. 6. Optically-controlled RF-beam stirring would allow the definition of multiple beams and beamshapes with applications in radar, monitoring, or secured transmission by path hopping.	20
Fig. 7 Interrelated conception aspects of an antenna	21
Fig. 8 Block diagram of a self-consistent DFT-NEGF algorithm like TranSIESTA. The DFT algorithm computes the Hamiltonian. It is fed to the NEGF algorithm which in turn computes the electron distribution and passes it to the DFT algorithm.	27
Fig. 9 Block diagram of the self-consistent QM-EM loop – reproduced from [78].	28
Fig. 10 The CNT is discretized in 1D FDTD with nodes connecting to those of the 3D TLM discretized environment – reproduced from [78].	28
Fig. 11 Using tight-binding theory or similar approaches, a SWCNT may be approximated as a hollow cylinder with effective complex conductivity σ . This then allows a classical EM treatment of the problem.	30
Fig. 12 Transmission line. Lumped-equivalent circuit from [98].	32
Fig. 13 Effective circuit diagram for a SWCNT contacted at both ends with a source and a load.	36
Fig. 14 MWCNT circuit model, reproduced from [106]. R_{mc} is the imperfect contact resistance.	41
Fig. 15. Schematic illustration of the anisotropic bulk model.	43
Fig. 16. Cross-sectional cut of a hexagonal array of NWs. In this simple case, NW centers are equidistant and NWs are similar which simplifies geometrical considerations. This cut is a typical inner mesh of the CNT bundles simulated in section II.C.2).	47
Fig. 17. Transverse conductivity as a function of the fraction of cross-sectional area occupied by NWs for various matrix conductivities. 50MS/m is the DC conductivity of the equivalent NW of a SWCNT of radius 2.4nm (cf. section II.B.3)). It is close to the conductivities of bulk gold and bulk copper. For reference, sea water has a conductivity of 4 S/m, polystyrene 0.1 fS/m and metals from 1 to tens of MS/m. Note the threshold at $\delta NW = 12$ for relatively low matrix conductivities.	50
Fig. 18 Linear DC conductivity of zigzag SWCNTs versus their radius. Equivalent linear resistivity and $(m, 0)$ index scales are also indicated. Parameters: $\gamma_0 = 2.7$ eV, $\tau = 3 \times 10^{-12}$ s, $T = 264$ K.	56
Fig. 19. Hexagonal structure used for the bundle definition ($N=6$). Each circle is the cross section of a CNT. The bundle is made of N concentric hexagonal layers of CNTs arranged around a central CNT. $N=0$ corresponds to a single CNT. $N=1,2,3$ are delimited on this figure. Two bundles are then arranged in a dipole as shown on the inset. An EM equivalent configuration is a monopole over a ground plane. We shall use this last configuration because it saves a factor two on mesh complexity. The resulting input impedance is twice lower.	64
Fig. 20. Input impedance of single-CNT dipole antennas as a function of frequency for various CNT lengths. Our results (color dashed lines and big dots) are superimposed over the	

reference results (black continuous lines and small-dot lines) from Hanson. Normalized at $Z_0=10k\Omega$	65
Fig. 21. Reflection coefficient $ S_{11}(f) $ of the dipoles for 0 to 6 layers of CNTs (1 to 127 CNTs) in the case of 40 (a) and 80 (b) μm -long SWCNTs. The two models show excellent agreement for all 13 configurations although we are studying the very sensitive resonance of a monopole. The CNTs are spaced 8.12nm center-to-center and have a radius of 2.36nm.....	66
Fig. 22. Sensitivity of the structure. Uncorrected (left-shifted curves) VS corrected hollow-tube model and bulk model. As little as 5% variation on the perimeter of the tubes shows a difference on the resonance, while the bulk model agrees to near perfection to the corrected model.....	67
Fig. 23. Adaptation peak as a function of CNT radii with a bundle size kept constant ($L_{\text{cnt}}=80\mu\text{m}$ $N=3$). Changing the radius of the tubes by a factor two or three does not affect the resonance as long as the bundle global shape and size are maintained. This confirms that all these configurations can be modeled by the same bulk block.	67
Fig. 24. Electric field magnitude at 120GHz in the cross section (normal to Z axis) of the bundle presented in Fig. 25. Top to bottom: base (metal plane), middle and tip of the bundle. Left: hollow-tube model. Right: bulk model. The scales are logarithmic and identical for tube/bulk comparison but different from top to bottom to stress the field variations in each case. Although the field distribution in the tubes and bulk bundle is different, a skin effect can be observed for both (the field is less intense at the core) and the resulting external fields are similar.....	68
Fig. 25. Electric field magnitude plots for a 3-layer 80 μm -long bundle of CNTs (half dipole) at 120GHz (close to resonance). Section in the XZ plane. Left: hollow-tube model. Right: bulk model. The insets represent the structures actually simulated (radius magnified by 1000, port length by 10).	69
Fig. 26. Bridging the signal line with the CNT bulk model. The yellow boxes are the metallic electrodes. The purple box in the center is the CNT bulk. The red boxes at each end are the material with specific conductivity used to model the contact resistance. They are included in the electrodes and the direct contact of the bundle to the electrodes is only through them. All this lies on a silicon substrate (green).	70
Fig. 27. 20 μm -gap coplanar waveguide structure, from Yang 2011 (cf. inset). Measured (solid lines) and simulated (dashed lines for our results, triangles and circles for Yang's) phase and magnitude of the S21 transmission parameter from one side of the gap to the other for the empty structure. Here the model is not yet under test. The results show good agreement.	70
Fig. 28. 20 μm -gap CPW with (a) one and (b) ten CNTs as shown on the SEM image in each inset. Measured (solid lines) and simulated (dashed lines for our results, triangles and circles for Yang's) phase and magnitude of S21. The results show good agreement both in phase and magnitude.	71
Fig. 29. From left to right: Layout of the simulated and fabricated structure; S21 parameter measured and fitted for different number of CNTs and contact resistances from 1 to 20GHz; SEM images of the CNT bridged gap of a few samples.	72
Fig. 30. Wai Leong Chow's fabrication process flow and fabricated structure; right: (a) as-grown vertically aligned CNT film, (b) horizontally aligned CNT film, (c) plasma-etching-patterned horizontally aligned CNT film, and (d) GSG electrodes formed on patterned horizontally aligned CNT film; left: SEM image of the fabricated horizontal CNT film contacted by GSG electrodes.	73
Fig. 31. Top and bottom view of the currents in the toppled CNTs showing the prevalence of the top layer in transmission.....	73
Fig. 32. Multi-model antenna design process flow.	76

Fig. 33. Two photolithography processes.	81
Fig. 34. Polystyrene (PS) balls of uniform radius r can be deposited as a dense monolayer film where they arrange with maximal density in a periodic diamond structure as illustrated here. The area delimited by green lines is not covered and a metal catalyst can then be deposited. SEM image courtesy of Aliénor Togonal (CINTRA).....	82
Fig. 35. SEM images of MWCNT grown on (a) slot-type (b) patch-type antenna. Inset of (a) is the enlarged view of the area in the red circle, showing typical growth height of 100 – 150 μm . Samples fabricated by Hong Li and Wai Leong Chow	88
Fig. 36. CVD systems in NEL2, School of EEE, NTU.....	89
Fig. 37. Bubbler functioning principle	91
Fig. 38. TCVD gas flow	91
Fig. 39. Ethanol CVD steps.....	93
Fig. 40. Saw scratcher.	95
Fig. 41. SEM images of a CNT growth from photolithography patterned AZ+Fe catalyst lines. From 20000x (top images) to 50x (bottom right).....	96
Fig. 42. SEM images of the catalyst lines at 4 consecutive spacing values. Fix zoom, 1000x. The density in the center is visibly decreasing. On each image the catalyst lines are the vertical ones and the horizontal lines are CNTs.....	98
Fig. 43. SEM images of the catalyst lines at the 12 different spacing values (length indicated in green). Fix zoom, 200x. On each image the catalyst lines are the vertical ones and the horizontal lines are CNTs.....	100
Fig. 44. Thick disorganized CNT film grown by CH_4 TCVD on top of MCEE-fabricated silicon nanowires (sample T0.04B). SEM images zoomed 5000x and 20000x. CNTs are the thin wavy wires and SiNWs the thicker straight vertical pillars.	101
Fig. 45. Optical microscope image and Raman spectrum of sample T0.04B.	102
Fig. 46. Suspended SWCNTs (thin horizontal wires) forming a monolayer net at the tip of silicon nanowires (thicker vertical ones). SEM image, sample E0.03B.	102
Fig. 47. Optical microscope image and Raman spectrum of sample E0.03B.	103
Fig. 48. Dielectrophoresis alignment of CNTs dissolved in solution.	104
Fig. 49. Top-view (left) and 45°-angle-view of a tapered 5- μm CPW gap characterization structure.	104
Fig. 50. Sprayed CNTs observed under SEM. Top (5kx): from Paolo Bondavalli, single pass (left) rather uniform but apparently non-continuous film and 3-pass (right) very uniform and continuous. Bottom (5 and 10kx), hand sprayed CNT ink fabricated in CINTRA; long CNTs or CNT ropes can be observed which are not apparent in P. Bondavalli's samples.	105
Fig. 51. Gold electrodes fabricated by photolithography on sprayed sc-SWCNTs. From left to right: 5000x, 500x and 50x SEM images. The CNT film appears undamaged by the process.	106
Fig. 52. Steps for the fabrication of CPW gap electrodes over horizontally grown CNTs... ..	106
Fig. 53. Same steps illustrated with SEM images of the outcome apart from the skipped step of etching which is also placed in an alternative order.	107
Fig. 54. Current distribution schematic for 3 resonant total lengths: $14\lambda p$, $12\lambda p$, $34\lambda p$. Because the far-field is the coherent sum of the contributions, for odd resonances, the emitted field is the same as the first resonance while the even resonances are actually anti-resonances, they do not emit. A CNT dipole about half-plasmon-wavelength-long is thus the most efficient configuration.	113
Fig. 55. Radiation efficiency of a $\lambda/100$ dipole with resonant m-SWCNT arms and non-resonant NW arms of various radii. Despite its higher R_{rad} , the SWCNT dipole is only a more efficient radiator than the gold NWs if the latter have a radius $a \leq 2\text{nm}$	115

Fig. 56. Radiation efficiency versus diameter for single m-SWCNT and NW dipole antennas.	116
Fig. 57. Return loss plotted against frequency for 80 μ m-long bundled-CNT monopoles with number of CNTs varying from 1 to 2791 (30 hexagonal layers). The best impedance match is achieved with 1261 CNTs \pm 100 (20 layers \pm 1) while -15dB impedance match is achieved with 721 to 2791 CNTs.	119
Fig. 58. Return loss for three different configurations of monopole show that similar impedance or operating frequency can be obtained by varying the parameters. However the lower operating frequency with better impedance match is obtained against a doubled size. The high return loss values are due to the normalization at 50 Ω for these few-CNTs high-impedance antennas and we are only interested in their relative values here.	120
Fig. 59. EM waves propagation velocity ratio between a single tube and a bundle of N tubes. 40 μ m-long (blue diamonds) and 80 μ m-long (orange triangles) bundled-CNT monopoles with varying number of CNTs are used. For both lengths, the velocity ratio rises at 4.4dB/decade.	120
Fig. 60. Size reduction factor K_{red} (compared to a resonant copper monopole) and antenna performance plotted against the number of CNTs in the bundle. Note the shift to the left of the 40 μ m curve with respect to the 80 μ m one. The size gain is only dependent on N_{shells} . By operating at higher frequencies or higher impedance, the relative gain in size is more important for a similar performance.	121
Fig. 61. Resonance frequency (dotted curves) and accepted power at 50 Ω (plain curves) as a function of the monopole antenna geometrical parameters: length and number of tubes. 40 μ m (triangles), 5 μ m (squares) and 1.25 μ m (disks)-long CNTs are plotted.	136
Fig. 62. Size reduction factor (compared to a resonant copper antenna, dotted curves) and accepted power at 50 Ω (plain curves) as a function of the antenna geometrical parameters: length and number of tubes. 40 μ m (triangles), 5 μ m (squares) and 1.25 μ m (disks)-long CNTs are plotted. Note the size gain is only dependent on N_{shells} . By operating at higher frequencies or higher impedance, the relative gain in size will be larger for a similar performance.	136
Fig. 63. Proposed fabrication of a THz FSS. 1) Catalyst is patterned on the substrate and CNTs are grown from it by CVD. 2) Masking with thick resist is patterned by photolithography and developed. 3) The unwanted CNTs are dry-etched by O ₂ plasma then the resist is removed with acetone, leaving patterned CNTs where desired.	138
Fig. 64. CNT dipole on quartz substrate that would be realized by lattice-aligned CVD growth then O ₂ plasma etching.	140
Fig. 65. Demonstration of the fabrication process by the fabrication of Au/Ti CPW gap electrodes over CVD grown CNTs with scratch catalyst.	140
Fig. 66. Effect of γ_0 on the frequency response of a CNT-based antenna. Return loss at 50 Ω plotted from 0 to 300GHz for $\gamma_0 = 2.5, 2.7$ and 3eV. The antenna arms are 78 μ m-long by 4 μ m-wide, made of 80 aligned CNTs each and separated by a 4 μ m gap fed with a 50- Ω lumped port.	142
Fig. 67. Effect of τ on the frequency response of a CNT-based antenna. Return loss at 50 Ω plotted from 0 to 300GHz for $\tau = 0.10ps, 0.32ps, 1.0ps, 3.0ps$ and 3.2ps. The antenna configuration is identical.	142
Fig. 68. Effect of antenna width on the frequency response of a CNT-based antenna. Return loss at 50 Ω plotted from 0 to 300GHz for $W_A = 1, 2, 4, 8, 16$ and 32 μ m.	144
Fig. 69. Effect of feeding port gap width on the frequency response of a CNT-based antenna. Return loss at 50 Ω plotted from 0 to 300GHz for $W_{Gap} = 4, 16, 32, 64$ and 128 μ m. The arms are kept 78 μ m-long each.	144
Fig. 70. Summary of the effect on the primary resonance of a CNT-based antenna of a) Antenna width from Fig. 68; note a slight frequency dip for wider values and relatively	

constant return loss. b) Feeding port gap width, the arms being kept 78- μm -long each, from Fig. 69; note a constant frequency and only slightly increasing mismatch.....	145
Fig. 71. Characteristics of 50- Ω -fed planar SWCNT-based dipoles as a function of <i>NCNT</i> , <i>LCNT</i> a) Resonance frequency and input impedance b) Size reduction and return loss. Dipole lengths are 40 (\blacktriangle), 80 (\bullet), 160 (X), 320 (\blacklozenge), and 640 (\blacksquare) μm with constant 4- μm gap and 4- μm arms width.	146
Fig. 72. Left: Plot of the E-field magnitude at the common resonance of a conventional dipole (top) and a CNT dipole (bottom). Right: idem but zoomed-out and showing the FEM mesh.	148
Fig. 73. Dipole-to-dipole transmission. Inset: Two CNT antennas on a quartz substrate side-to-side.	149
Fig. 74 Scheme of the contactless read-out of nanodevices incorporating CNT dipoles using a horn antenna. The horn is typically one order of magnitude larger than any of the CNT dipoles. Inset: profile view showing the horn is brought very close to the surface and reads only one zone at a time.....	149
Fig. 75. Horn antenna facing a CNT dipole on quartz. The small boxes are larger than the CNT dipole, that they contain, and smaller than the horn antenna. They do not have any physical impact but help guide the automatic refinement of the mesh in HFSS and keep it progressive.	150
Fig. 76. Smith chart of the horn antenna (blue and green) and dipole antenna (red and orange) for frequencies 170-260GHz and 100-180GHz at nominal spacing i.e. quartz substrate stuck to the horn, 1.78mm to the entrance of the waveguide.	152
Fig. 77. Return loss of the horn antenna (dash) and dipole antenna (solid) in the range 100-260GHz for different spacing values: : 1.78mm (orange and red), 2.82mm (grey and dark purple), 7.09mm (purple-blue and blue). Values below -30dB were truncated: horn plotted from 105GHz and values around resonance of the dipole at 220GHz in the nominal configuration (-57dB) truncated.....	152
Fig. 78. Transmission between the dipole and the horn antennas at three different spacing values: 1.78mm (contact), 2.82mm (edge of the horn 1mm from the substrate), 7.09mm (edge of the horn 5.3mm from the substrate). The transmission levels are sufficient for the application we describe. Non-contact read-out is possible by hovering a few millimeters over the substrate but reduces the signal by 10 to 20dB.	153
Fig. 79. Tentative coplanar waveguide (CPW) feed designs for planar dipoles. One arm is connected to the ground (G) and one to the signal (S) of this GSG probe. a) Classical dipole; the feed seems to work but may participate in the resonance. b) Ideal CNT dipole (same width-length ratio as classical one); the line is linearly tapered to accommodate the dimensions of the antenna and realize the impedance matching. c) Realistic design for a CNT dipole with two constant-characteristic-impedance lines connected through a taper and CNT density 1/ μm	155
Fig. 80. Illustration of the design of the CPW horizontal-CNT monopole.....	156
Fig. 81. Steps to fabricate horizontal monopole antennas with CNT strip radiator enhanced with metal inserts. a) Photolithography-defined catalyst lines, b) CNT growth, c) definition of electrodes, d) definition of metal inserts (using the same design as catalyst or denser lines) by second photolithography exposure followed by e-beam deposition of metal and lift-off.	158
Fig. 82. CVD-grown multi-catalyst-lines CNT strips. The strips may be used as such as dipoles in free space or connected with the CPW feed described in this section to form a monopole. The imperfect patterning is due to small issues in the lift-off process. Dipolar behavior and close-up views confirm the good connection of the multiple parts of each strip – that can still be improved by adding metal over the former catalyst lines.	159

Fig. 83. CPW-fed vertical CNT monopole. a) General design. b) Transmission configuration. c) Transmission level vs. antenna spacing at 300GHz. The results of the horizontal CNT dipoles at 220GHz are also included.	161
Fig. 84. Alternative rod designs for the standing monopole. Next to each design are indicated 1) the number of CNTs involved by the cross-section at resolution limit 2) the proportion of CNTs compared to a disk of similar footprint 3) the aspect ratio for this rod for 100 μ m height.	163
Fig. 85. Effect of the pattern on the number of CNTs. Plots are for a CNT density of 10^{14} m ⁻² . Left: N_{CNT} vs. radius of the pattern shows the advantage of the 3-pointed star vs. disk. Right: $\min(N_{\text{CNT}})$ vs. resolution limit for the 3-pointed star	164
Fig. 86. Catalyst patterns as realized by photolithography (after development and before further treatment).....	165
Fig. 87. Below, in this order: bundle tips and bases showing the effect of the catalyst patterns for each $d10(\times 4k)$, $s5.6(\times 13.5k)$, $d2.2(\times 20k)$, $s3.3(\times 20k)$, $s4(\times 10k)$, $s10(\times 5k)$. The fabrication is demonstrated.	165
Fig. 88. A CNT rod may be toppled by blowing a gas at it such as N ₂	170
Fig. 89. Mechanical toppling process by Cary L. Pint. Reproduced from the supplementary information of [182].	170
Fig. 90. Horizontal Monopole design in HFSS as simulated and illustration of a possible realization following the process developed by Wai Leong Chow (SEM image of a fabricated gap structure cropped to show how a monopole could be realized with the existing process).....	171
Fig. 91. A sharp resonance in the return loss (left) matched with a normalized complex impedance of almost perfectly 1 on the Smith Chart (right) show an excellent impedance match at 50 Ω	171
Fig. 92. The fact that the CNT antenna is resonant and impedance-matched to the feed at resonance allows it to have a better realized gain.	172
Fig. 93. A parametric analysis on the number of CNTs in the bundle shows that the design works with variable N_{CNT} (ratio of 2 on total number yielding diameters between 3.5 to 5.1 μ m)	172
Fig. 94. A parametric analysis on the length of the bundles shows that the resonance frequency scales with length as expected and the design works well with a 5-15 μ m tolerance.	173
Fig. 95. CPW monopole feed Design 1. Simple I feed and inverted J for transmission. 50- Ω CPW line. Nominal frequency 300GHz. Acceptable probe pitch 50-150 μ m.	176
Fig. 96. CPW monopole feed Design 2. Simple I feed and inverted J for transmission. 140 μ m 50- Ω pad and $\lambda/4$ 60- Ω CPW line. Nominal frequency 200GHz. Acceptable probe pitch 50-150 μ m.....	176
Fig. 97. CPW monopole feed Design 3. Simple I feed and inverted J for transmission. 140 μ m 50- Ω pad and $\lambda/4$ 60- Ω CPW line. Nominal frequency 200GHz. Acceptable probe pitch 100-150 μ m.....	176
Fig. 98. CPW monopole feed Design 4. Simple I feed and inverted J for transmission. 140 μ m 50- Ω pad and $\lambda/4$ 87- Ω CPW line. Nominal frequency 90GHz. Acceptable probe pitch 100-150 μ m.....	176
Fig. 99. Magnitude return loss of CPW monopole feed Design 1 with (purple solid) and without (red, dot-dashed) CNT rod.	177
Fig. 100. Return loss of Design 2, magnitude in dB (red) and phase (blue).	177
Fig. 101. Return loss of Design 3, magnitude in dB (red) and phase (blue).	177
Fig. 102. Return loss of Design 4, magnitude in dB (red) and phase (blue).	177

Fig. 103. Realized gain for Design 1. Cut at $\phi=0^\circ$: around the axis of the CNT. With (purple solid) and without (red, dot-dashed) CNT rod.	178
Fig. 104. Realized gain for Design 1. Cut at $\phi=90^\circ$: along the axis of the CNT. With (purple solid) and without (red, dot-dashed) CNT rod.	178
Fig. 105. 3D antenna gain for each design. Similar scales: red -4dB to blue -20dB	178
Fig. 106. Realized gain for Design 2. Cuts at $\phi=0^\circ$ (around the CNT axis, red, dashed) and 90° (along the CNT axis, purple solid).	178
Fig. 107. CPW monopole feed Design 3. Simple I feed and inverted J for transmission. $140\mu\text{m}$ $50\text{-}\Omega$ pad and $\lambda/4$ $60\text{-}\Omega$ CPW line. Nominal frequency 200GHz. Acceptable probe pitch 100-150 μm	179
Fig. 108. CPW monopole feed Design 4. Simple I feed and inverted J for transmission. $140\mu\text{m}$ $50\text{-}\Omega$ pad and $\lambda/4$ $87\text{-}\Omega$ CPW line. Nominal frequency 90GHz. Acceptable probe pitch 100-150 μm	179
Fig. 109. Design 1. Return loss for the I and J feed with the CNT rod (-11.3dB and -24.5dB) and without a rod (-1.0dB & -5.6dB).	180
Fig. 110. Design 2. Return loss for the I (Sp1p1) and J (Sp2p2) feeds with the CNT rod, in magnitude (red) and phase (blue).	181
Fig. 111. Transmission at the indicated frequencies between IJ pairs of antennas of the same designs (1, 2 and 3). Transmission levels without the rod are included for comparison. The levels are sufficiently high for measurement.	181
Fig. 112. Global mask layout. The edges representation is chosen to let the patterns appear despite the normally to small patterns.	182
Fig. 113. Effective appearance of the darkfield (left) and brightfield (right) masks.	183
Fig. 114. Zone M: illustration of the common spacing distances of the designs (1,2,3, A,B,E).	185
Fig. 115. Zone M: three simultaneous catalyst alignments are present by design.	186
Fig. 116. Usage of the alignment marks to align the catalyst pattern a) half-half on the signal line (easier to topple), b) fully on the signal line (ohmic contact), c) off the edge by ten micrometer for the centre (capacitive excitation, better growth).	187
Fig. 117. Vertical CNT monopole successfully fabricated with three-pointed star pattern. .	192
Fig. 118. Pair of self-toppled CNT monopoles successfully fabricated with three-pointed star pattern preferentially toppling in the correct direction (1/3 but even more if the pattern is tangent or half-way over the edge of the metallization).	192
Fig. 119. Another pair of self-toppled CNT monopole antennas.	193
Fig. 120. Optical microscope images of a pair of monopole antennas at different focus and FE-SEM image of the same pair. This shows how both techniques can complement each other to allow a good global view and shallow-depth slice-like observation. Here the rods are seen standing which is not the original nature of the design but still provides a working configuration. They could later be toppled to resonate at lower frequencies with the same length as the effective permittivity would be raised by the substrate influence.	194
Fig. 121. Gold CPW gap electrodes fabricated on lattice-aligned CNTs grown by ethanol CVD from scratch catalyst on quartz (E0.03). Left: 4 sizes of gap are fabricated (5, 10, 20, 50 μm) and repeated thrice each; G201 (1 st 20- μm gap) is probed under illumination. Right: SEM images of G201 reveal the CNTs around G201; because the gap is placed quite far from the catalyst line, a single CNT bridges the signal electrodes. Because it is a semiconducting SWCNT it appears faintly contrasted with the dielectric substrate.	201
Fig. 122. G202 is a device on the same sample (E0.03) as G201 on Fig. 121. The gap is aligned next to the scratch and the number of CNTs is thus much higher.	202
Fig. 123. A few of the interdigitated electrode design variations that were fabricated. Left: mask layout. Right: actual sample.	203

Fig. 124. 20- μm -gap (g) interdigitated electrode design, d (inverted). Left: mask layout; the effective connecting width is $L=20 \times l=20\text{mm}$. Right: actual sample with laser spot; note the CNTs are completely invisible.	203
Fig. 125. 20- μm -gap interdigitated electrode design, d (inverted), SEM images.	204
Fig. 126. Optical absorption spectrum of sc-SWCNTs IsoNanotubes-S 99% from NanoIntegris (source: datasheet) fitted with some of the usual continuous-wave-laser wavelengths. A green 532nm laser may be used and is preferable to red lasers but blue and near-infrared lasers around 1 μm may produce better results.	205
Fig. 127. Silver-ink pads deposited on sprayed CNTs on glass. From left to right: optical image and SEM images after electrical breakdown. The CNTs used should be 99% semiconducting but high-scattering regions are observed indicating some metallic content. However the shorter metallic paths linking the two electrodes seem to be cut. The gap is about 740- μm -wide.	206
Fig. 128. Observation of two irreversible electrical breakdown steps while measuring the I-V curve of the CNT film. A voltage source was used as no current source was available.	207
Fig. 129. WITec confocal Raman spectrometry system in Nanoelectronics laboratory 1, School of EEE, NTU.	209
Fig. 130. Raman spectrum measured on the sprayed CNT film over glass of the interdigitated sample. $I_D/I_G=45\%$	209
Fig. 131. Device G202 on sample E0.03. Left to right, top to bottom: SEM image, optical microscope image, Raman map (sum of the signal over the 1550-1630 cm^{-1} band for each position (x,y) to find regions with a high G peak) and representative Raman spectrum for the area.	210
Fig. 132. Optically visible wires and dark regions reveal a CNT spectrum as well but with some more defects and possibly MWCNTs.	211
Fig. 133. Raman mapping of the 1580-1630 cm^{-1} shifts matches the position of the CNTs growing out of a catalyst line by device G501 on sample E0.04. The CNTs are invisible to simple optical microscopy but can be detected and identified through SEM or Raman spectroscopy.	212
Fig. 134. Full Raman spectra acquired on the CNTs characterized on Fig. 133; from I_D/I_G we see that very high quality SWCNTs are obtained.	212
Fig. 135. Left: Raman mapping of the 1580-1630 cm^{-1} shifts (brown color scale) matches the SEM-recorded position of the CNTs in the gap of device G201 on sample E0.04. Right: full Raman spectrum acquired on one of the CNTs (similar for the others in the mapping; very high quality SWCNTs are obtained.	213
Fig. 136. Schematic illustration of the characterization on a CPW gap sample. The laser is chopped before being propagated to the gap where its 100- μm -diameter spot covers the gap. The chopper frequency is fed to the lock-in amplifier connected to the electrodes of the sample.	214
Fig. 137. Experimental photocurrent lock-in amplifier setup using a 532nm CW laser. Top right: lock-in amplifier, top left optical table with freespace laser propagation. Bottom left: going upstream on the optical path, quarter wavelength plate, polarizer, variable density, chopper, laser. Bottom right: Mirror and focusing lens bring the laser to the quartz substrate under the probes.	215
Fig. 138. Principle of the experimental setup. \hat{I} is the incidence angle of the laser on the sample.	216
Fig. 139. IV curve shows a mostly-ohmic response with apparent current saturation above 1-1.5V.	218

Fig. 140. Photocurrent (module) as a function of bias (V_{ds}). There is actually a sign change between negative and positive bias. For lower powers measurements were only recorded with negative bias because of the relative symmetry of the curve.	218
Fig. 141. The photocurrent is dependent on the position of the incident beam on the device. Because of the small dimensions of the device, the position is varied arbitrarily and assigned a pseudoposition number respecting the spatial order.	220
Fig. 142. CNT normal to the plane of incidence, s-polarization parallel to CNT.....	221
Fig. 143. CNT in the plane of incidence, p-polarization parallel to CNT.....	221
Fig. 144. Photocurrent independent of $V_{ds} < 1V$ (measured with CNT normal to the plane of incidence and s-polarization)	221
Fig. 145. Laser power dependence of photocurrent for CNT normal to the plane of incidence and s-polarization (thus parallel to CNT). Different colors correspond to measurement taken at different times thus validating the reproducibility of the measure.....	222
Fig. 146. Laser power dependence of photocurrent for CNT in the plane of incidence and p-polarization (thus parallel to CNT).	222
Fig. 147. CVD single SWCNT polarization and incidence. Laser power: 10mW, chopped.	222
Fig. 148. Photocurrent response of randomly oriented sc-SWCNT films to light intensity at 0V bias (left) and bias at 10mW laser power (right).....	224
Fig. 149. Very high photo-impedance of the film (left) as calculated from the data reported on Fig. 148 and dependence of the photocurrent over the position of the beam illustrated (right) by a sample of positions over the grid (as shown on the inset) and the measured current.....	224
Fig. 150. Incidence parallel to propagation in the gaps.	225
Fig. 151. Incidence normal to propagation in the gaps.	225
Fig. 152. Photocurrent dependence in polarization at incidence parallel to the gap propagation, 0V and 10mW.	225
Fig. 153. Photocurrent dependence in polarization at incidence normal to the gap propagation, 0V and 60mW.	225
Fig. 154. Schema of same spot used in incidence both parallel and normal to the gaps.	226
Fig. 155. Using the exact same spot be it with incidence plane parallel (bottom to top) or normal (left to right) to the gap the response is the same. However p-polarization is systematically more efficient than s.	226
Fig. 156. Direct current measurement shows a clear ΔI but a slow response; at 130Hz the modulation is limited by the time response and only varies by 10% instead of +200% at 63.7mW and 0V bias.....	227
Fig. 157. Signal dependence on chop frequency. If the signal is modulated too fast the modulation amplitude decreases because the current does not rise or fall fast enough to reach its minimum and maximum values.	227
Fig. 158. Improve uniformity of coating: 3 devices have quite similar but still different performance.....	228
Fig. 159. Concept of a CPW-fed PIFA antenna with a horizontal CNT shorting loop realized by lattice-aligned CVD grown CNTs or spray-coated/inkjet-printed CNTs.....	230
Fig. 160. Sprayed CNTs in the slot of a notched trapezoidal monopole (adapted from Antenna Magus online repository). The CNTs could allow switching on and off the notch filter.	231
Fig. 161. E0.02: 101, 201, 202, 501 (from left to right, top to bottom).	269
Fig. 162. E0.03: 052, 102 (from left to right).....	270
Fig. 163. E0.04: 201, 202, 501 (from left to right, top to bottom).	270
Fig. 164. E0.05A: 102, 103, 201, 203, 502, 503 (from left to right, top to bottom).	271

Fig. 165. Capacitively-coupled CNT monopole. Design structure. A cavity is wet-etched in a back-metallized silicon substrate by KOH. A CNT rod is grown at the bottom of it. The CNT rod couples to the pin of an SMA connector that comes through the remaining Si membrane at the bottom of the cavity while the ground of the coaxial connector is connected to the metallized back of the substrate as the planar ground of the monopole antenna. 273

Fig. 166. Capacitively-coupled CNT monopole. a) Return loss shows a resonance at 65GHz for both CNT and gold rods. b) The realized gain, ratio of the power emitted to the power at terminals, is almost 0dB at $\pm 40^\circ$ with rods, 2dB higher than without. c) Electric field plot showing the excitation of a resonance in the CNT rod. d) 3D far-field gain of the structure. 273

Fig. 167. Structure of the KOH-etched-microstrip-fed monopole antenna..... 274

Fig. 168. Design of mixed CPW-microstrip feedline for 50- Ω monopole antennas by Christophe Brun and return loss with a 325- μm -long gold wire (blue), a 150- μm -long rod made of 1027 CNTs (red) and no rod (black). 276

List of Tables

Table 1. Transmission line parameters for a SWCNT adapting from [98].	38
Table 2. Typical circuit parameter values. We take $\gamma_0 = 2.7$ eV hence $v_F = 8.74 \times 10^5$ m/s. Then we have $LK = 3.69$ nH/ μ m and $CQ = 355$ aF/ μ m independently of the two factors varied in the table. For <i>Rground</i> we take $a = 0.7$ nm and $\delta_{min} = 100$ nm.	39
Table 3. Comparison of techniques of EM simulation of CNTs for antenna design and simulation	74
Table 4. Different CNT types for the fabrication of an electrically-short resonant antenna.	108
Table 5. Selected patterns for the mask in this order top to bottom. All lengths in μ m. The estimated number of CNTs is based on a CNT density of 10^{14} m ⁻² and takes the rounded edges due to diffraction limit into account for the three-pointed-star patterns.	164
Table 6. Dimensions of the CPW feeds for horizontal monopoles. All lengths are in μ m. For all designs, we have $L3 = 3 \times \max(2\mu\text{m}, G2 - G1, W2 - W1, W2 + 2G2 = W1 + 2G1, L2 \approx \lambda/4$ and $L1 = 4 \times l_{probe}$.	174
Table 7. CNT strips length and density variations included in zone X and U.	189
Table 8. Standard guidelines for negative and positive photolithography in Cleanroom 2, N2FC, NTU EEE.	265
Table 9. Procedure for metal evaporation and lift-off.	266
Table 10. Ethanol CVD recipe runs	267

List of Equations

(1)	29
(2)	29
(3)	30
(4)	30
(5)	31
(6)	32
(7)	32
(8)	32
(9)	33
(10)	33
(11)	33
(12)	33
(13)	33
(14)	33
(15)	33
(16)	33
(17)	33
(18)	34
(19)	34
(20)	34
(21)	34
(22)	34
(23)	35
(24)	35
(25)	35
(26)	35
(27)	35
(28)	35
(29)	35
(30)	36
(31)	37
(32)	37
(33)	37
(34)	37
(35)	37
(36)	40
(37)	40
(38)	40
(39)	40
(40)	40
(41)	40
(42)	40
(43)	41
(44)	44
(45)	45
(46)	45

(47)	46
(48)	46
(49)	46
(50)	47
(51)	48
(52)	48
(53)	48
(54)	48
(55)	49
(56)	49
(57)	49
(58)	49
(59)	49
(60)	49
(61)	50
(62)	51
(63)	51
(64)	51
(65)	51
(66)	51
(67)	52
(68)	52
(69)	52
(70)	52
(71)	53
(72)	53
(73)	53
(74)	53
(75)	53
(76)	54
(77)	54
(78)	54
(79)	54
(80)	55
(81)	55
(82)	56
(83)	56
(84)	56
(85)	57
(86)	57
(87)	58
(88)	58
(89)	58
(90)	58
(91)	59
(92)	59
(93)	59
(94)	59
(95)	60
(96)	60

(97)	60
(98)	60
(99)	60
(100)	61
(101)	61
(102)	61
(103)	63
(104)	63
(105)	64
(106)	64
(107)	64
(108)	64
(109)	112
(110)	112
(111)	112
(112)	112
(113)	112
(114)	114
(115)	114
(116)	115
(117)	115
(118)	117
(119)	122
(120)	122
(121)	122
(122)	123
(123)	123
(124) (125).....	123
(126) (127).....	123
(128)	123
(129)	123
(130)	124
(131)	124
(132)	124
(133)	124
(134)	124
(135)	124
(136)	125
(137)	125
(138)	125
(139)	125
(140)	125
(141)	125
(142)	126
(143)	126
(144)	126
(145)	126
(146)	126
(147)	126
(148)	126

(149)	127
(150)	127
(151)	127
(152)	127
(153)	127
(154)	128
(155)	128
(156)	129
(157)	129
(158)	129
(159)	129
(160)	130
(161)	130
(162)	130
(163)	130
(164)	131
(165)	131
(166)	131
(167)	131
(168)	132
(169)	132
(170)	132
(171)	133
(172)	133
(173)	133
(174)	133
(175)	133
(176)	133
(177)	133
(178)	134
(179)	134
(180)	134
(181)	163
(182)	237
(183)	257
(184)	257
(185)	258
(186)	258
(187)	258
(188)	258
(189)	258
(190)	259
(191)	259
(192)	259
(193)	259
(194)	263
(195)	263
(196)	264
(197)	264
(198)	265

(199) 265
(200) 265

Abstract

Modèle électromagnétique et procédés technologiques pour les ensembles mésoscopiques de nanotubes de carbone appliqués à la fabrication d'antennes innovantes

Nous présentons une étude de faisabilité d'antennes innovantes basées sur les propriétés particulières des nanotubes de carbone (NTC). Celles-ci pourraient permettre une amélioration des performances des antennes électriquement courtes mais aussi le développement de systèmes innovants tels que des réseaux réflecteurs à commande optique. Ce pourrait aussi être une technologie intéressante pour les applications en plein essor dans les domaines des ondes millimétriques et terahertz. Des avancées significatives ont été réalisées suivant les quatre axes interdépendants qui régissent ces antennes : modélisation des NTC, analyse des antennes basées sur les NTC, fabrication à partir de NTC et caractérisation. Ceci nous a permis d'une part de concevoir et de fabriquer les premiers prototypes d'antennes électriquement courtes à base de NTC et d'autre part de mettre en évidence des tendances dans la réponse des NTC sous illumination. En effet, en utilisant une approche mésoscopique, nous avons développé un modèle électromagnétique original pour les ensembles de nano-éléments alignés, en particulier les NTC, permettant leur intégration dans des logiciels de simulation électromagnétique classiques et donc la mise en correspondance des possibilités de fabrication et de simulation. En parallèle nous avons reproduit et développé des méthodes de croissance et de dépôt de NTC et établi des procédés de fabrication pouvant être adaptés à grande échelle. De plus, un modèle analytique des antennes monopôles à base de NTC a été établi à partir d'une approche ligne de transmission. Ces techniques nous ont permis de mettre en avant les compromis nécessaires dans la conception d'antennes de taille réduite à base de NTC et ainsi de concevoir et fabriquer de premiers prototypes. Elles ont aussi été appliquées à la fabrication de structures de test pour une caractérisation des NTC sous illumination. Ceci nous a permis de mettre en évidence les conditions optimales pour générer un courant photoélectrique dans les NTC et d'évaluer les performances pouvant être attendues comme base pour de futurs systèmes.

Mots clés : Nanotubes de carbone, Antennes, Modélisation électromagnétique, Croissance CVD, Courant photoélectrique, Nanofabrication, Micro- et nanoélectronique, Electronique haute fréquence

Mesoscopic electromagnetic model of carbon-nanotube arrays and scalable technological processes: application to the fabrication of novel antennas

We report the efforts lead in the design and fabrication of novel antennas from carbon nanotubes (CNTs) to assess their practicality in diverse usage scenarios. CNT-based antennas could help improve the performance of electrically-small antennas but may also allow the development of novel structures such as optically-controlled reflectarrays. They also represent an interesting technology for millimeter-wave and THz applications. Significant progress has been made on each of the four intertwined axes pertaining to these special antennas, modeling, analysis, fabrication and characterization. This has allowed designing and fabricating the first electrically-short CNT antenna prototypes and determining preliminary photocurrent trends. Indeed, we have derived an original mesoscopic model for the electromagnetic properties of aligned arrays of nano-elements with a special focus on CNTs to match simulation and fabrication capabilities. In parallel, we have reproduced and developed CNT growth and deposition techniques and established scalable fabrication processes. Additionally, an analytical model for CNT-based monopole antennas has been derived from transmission line theory. By combining modeling, analysis, simulation and fabrication, we have finally achieved the design and fabrication of CNT-based monopole antenna prototypes. The techniques have also been applied to the fabrication of CNT-based photocurrent samples which have been extensively characterized to highlight optimal illumination conditions and assess expectable performances as a base for future designs.

Keywords : Carbon nanotubes, Antennas, Electromagnetic modeling, CVD growth, Photocurrent, Nanofabrication, Micro- and nano-electronics, RF Engineering